IntechOpen

Recent Advances in Porous Ceramics

Edited by Uday M. Basheer Al-Naib

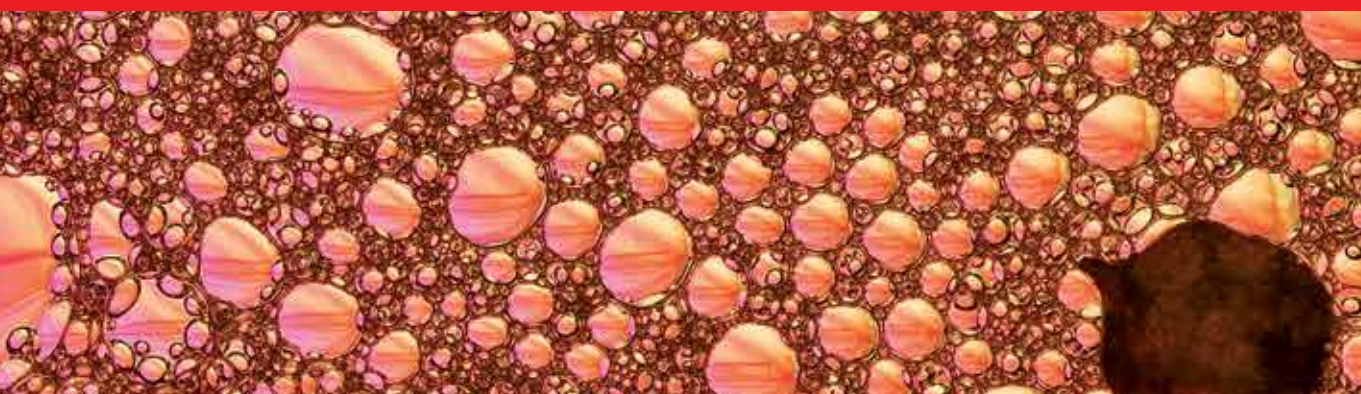

RECENT ADVANCES IN POROUS CERAMICS

Edited by **Uday M. Basheer Al-Naib**

Recent Advances in Porous Ceramics
http://dx.doi.org/10.5772/68104
Edited by Uday M. Basheer Al-Naib

Contributors

Uday M. M. Basheer Al-Naib, Takeshi Yabutsuka, Hongliang He, Emmanuel J. Ekoi, Denis Dowling, Muhammad Awais, Sijo A. K., Yibran Perera-Mercado, Griselda Castruita-De Leon, Geanette Polanco, Xiaojian Mao, Tamara Ivetić, Umaru Ahmadu, Alhassan Muaazu, Sadiq Umar, Ru Ji, Xidong Wang, Yang He, Vânia Salvini, Victor Pandolfelli, Dirceu Spinelli

Notice

First published in London, United Kingdom, 2018 by IntechOpen
eBook (PDF) Published by IntechOpen, 2019
IntechOpen is the global imprint of INTECHOPEN LIMITED, registered in England and Wales, registration number: 11086078, The Shard, 25th floor, 32 London Bridge Street
London, SE19SG – United Kingdom
Printed in Croatia

British Library Cataloguing-in-Publication Data
A catalogue record for this book is available from the British Library

Additional hard and PDF copies can be obtained from orders@intechopen.com

Recent Advances in Porous Ceramics
Edited by Uday M. Basheer Al-Naib

p. cm.

Print ISBN 978-1-78923-652-1

Online ISBN 978-1-78923-653-8

eBook (PDF) ISBN 978-1-83881-280-5

Meet the editor

Dr. Uday M. Basheer Al-Naib is a senior lecturer at Universiti Teknologi Malaysia (UTM). He held a postdoctoral associate position at Universiti Sains Malaysia (USM) between 2013 and 2014. He received his PhD degree in Materials Engineering from USM in 2013. He obtained his BS and MS degrees in chemical engineering from the University of Baghdad and University of Technology, Iraq, respectively. He has over 25 years of academic and practical experience in the field of ceramic and metal composites, advanced ceramics, porous ceramics, ceramic-metal joining, materials characterizations, ceramic insulators, ceramic membranes, and thermoelectric and ceramic coating. He was recognized at the practical level of solving specific problems in ceramic industries. This was evident when he published his research work with different publishers and in international material engineering journals with high impact factors. Currently, he supervises five international PhDs and three masters by research students related with different fields of materials engineering.

Contents

Preface

Porous ceramics are now expected to be adopted for a wide range of industrial applications such as lightweight structures, membranes, heat insulators, scaffolds and support structures of catalyst applications. During the last decade, tremendous efforts have been devoted for the researches on innovative processing technologies of porous ceramics, resulting in better control over porous structures and significant improvements of the properties. Generally, porous ceramics have good properties such as high mechanical strength, low density, chemical and thermal stability, abrasion resistance, and high thermal shock resistance. Furthermore, permeability is one of the most important properties of porous ceramics for filters because this property directly relates to the pressure drop during filtration. Thus, the development of porous ceramics requires sufficient mechanical and chemical stability as well as permeability. This book, however, focuses on preparation, structures, properties, and testing of porous ceramic materials.

This book is proposed to share recent research and knowledge related to porous ceramics and it consists of 11 chapters. Chapter 1 is an introduction of this book; it briefly explains the introduction to porous ceramics. Chapter 2 introduces novel biomaterials utilizing porous bone-like apatite coating formation by using apatite nuclei, and Chapter 3 presents the ceramic foams process by using foaming technology. Chapter 4 discusses the production of porous ceramic sensors for hydrocarbon leak detection under diverse environmental conditions. Chapter 5 shows the research results of synthesized Zn_2SnO_4 ceramics on their structure, morphology, and properties with large open porosity, as well as the results obtained during their solid-state processing optimization.

Chapter 6 explains tailoring of magnetic and structural properties of some spinel ferrites through different fabrication methods. Chapter 7 presents the sintering of porous ceramic by using microwave plasma technique. Chapter 8 deals with the preparation and numerical modeling of ceramic foam insulation for energy-saving applications. Chapters 9, 10, and 11 are related to the physical and mechanical properties of porous ceramic with different objectives such as physical properties of porous barium titanate after doping with zinc and tin oxides, as well as the mechanical properties and shock compression of porous ceramic, respectively.

We hope that the knowledge and objectives of recent research achievements on porous ceramic that we shared in this book will be useful for researchers, students, engineers, and others that work in this kind of ceramics.

I would like to express my thanks to all authors who contributed their findings related to porous ceramic in this book. Without their expertise and contributions, this book could not have been compiled.

Dr. Uday M. Basheer Al-Naib
Faculty of Mechanical Engineering
UTM Centre for Low Carbon Transport
In Cooperation with Imperial College London
Institute for Vehicle Systems and Engineering
Universiti Teknologi Malaysia
81310 Skudai Johor Malaysia

Chapter 1

Introductory Chapter: A Brief Introduction to Porous Ceramic

Uday M. Basheer Al-Naib

Additional information is available at the end of the chapter

http://dx.doi.org/10.5772/intechopen.74747

1. Introduction

Porous ceramics have grown in importance in the industry recently because of their many applications like filters, absorbers, dust collectors, thermal insulation, hot gas collectors, dielectric resonators, bioreactors, bone replacement and automobile engine components [1–4]. Generally, porous ceramics have good properties such as mechanical strength, abrasion resistance, chemical and thermal stability. These porous network ceramic structures also have relatively low density, low mass and low thermal conductivity [5]. Furthermore, permeability is one of the most important properties of porous ceramics for different applications such as membranes because this property directly relates to the pressure drop during filtration. Pore size control is the one key factor in fabrication of porous ceramics [6]. As well as the size of particles and their distribution of the raw materials, manufacturing techniques, types of binder used, distribution of binder and sintering affect the final porosity and pore connectivity important factors that must be considered during the manufacturing of the porous ceramic body. Therefore, the development of porous ceramics research requires sufficient mechanical and chemical stability as well as permeability. This book covers a wide range of topics such as porous ceramic structure and properties, preparation, simulation and fabrication, 3D printer fabrication, porous ceramic composites, honeycombs, membranes, bioceramic, automotive and aerospace porous ceramic.

2. What are porous ceramics?

Porous ceramics are categorized as those ceramics having high percentage porosity between 20 and 95%. These materials composed of at least two phases like solid ceramic phase, and the gas-filled porous phase [7]. The gas content of these pores usually regulates itself to the environment, as an exchange of gas with the environment is possible through pore channels.

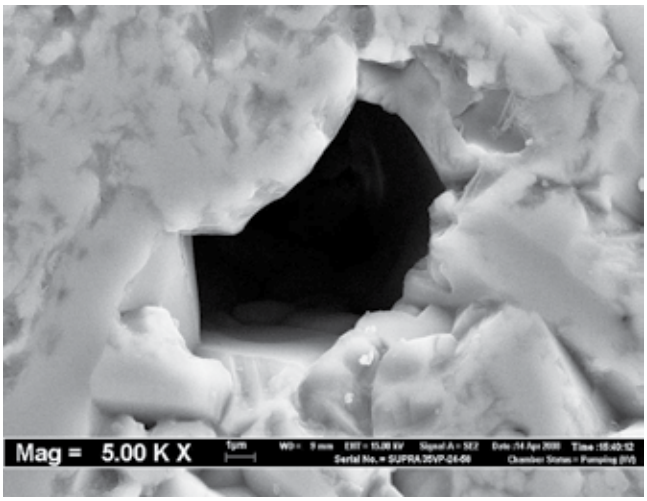

Figure 1. Magnification of a single open pore in the alumina ceramic body.

Closed pores can contain a composition of gases that is independent of the environment [8]. When porosity is determined for any ceramic body, porosity can be distinguished for several types such as open (accessible from the outside) porosity (**Figure 1**) and closed porosity. Where open porosity can be further categorized into open dead-end pores and open pore channels. The presence of porosity depends on the specific application, so a more open porosity may be needed to be permeable such as a closed porosity or filters/membrane such as thermal insulator may be wanted. The sum of the open and closed porosity is mentioned to as the total porosity [9]. If the fractional porosity of a material is relatively low, then the closed porosity will dominate; at the fractional porosity increases, the open porosity level increases.

The porous ceramics have been classified on the basis of nature of porosity, volume fraction and size of these pores [10]. The nature of porosity in natural ceramics depend on their genesis while in synthetic ceramics, it depends on their manufacturing and generally, it can be controlled. The pore size of these materials can be classified into three grades depending on the pore diameter: microporous (less than 2 nm), mesoporous (between 2 and 50 nm) and macroporous (more than 50 nm). The pore size distributions are usually measured by mercury intrusion porosimetry technique. The pore size distribution of the closed porosity is not determinable using this technique, but may occur, for example, by optical and electronic examination of a polished cross section. The pore size distribution represents the pore volume in function of pore size and commonly is given as percentage or a derivative [11].

3. Methods and techniques for fabrication of porous ceramics

In recent years, with the development of new needs and technologies, there was an increasing request for porous ceramic. Hence their fabrication methods are being widely studied and the subject of inclusive research. Partial sintering of ceramic powder compacts is one of the methods used to fabricate porous ceramic bodies, but this method mostly yields low porosities (less than 50%) and few options to significantly alter the pore size distribution [12].

http://dx.doi.org/10.5772/intechopen.74747

Honeycombs also with well-defined unidirectional channels can be paste extruded from a variety of ceramic powders and more complex three-dimensional porous ceramics can be made by rapid prototyping techniques, such as 3D printing. Apart from these methods, it is possible to distinguish many different types of fabrication routes (**Figure 2**) for producing

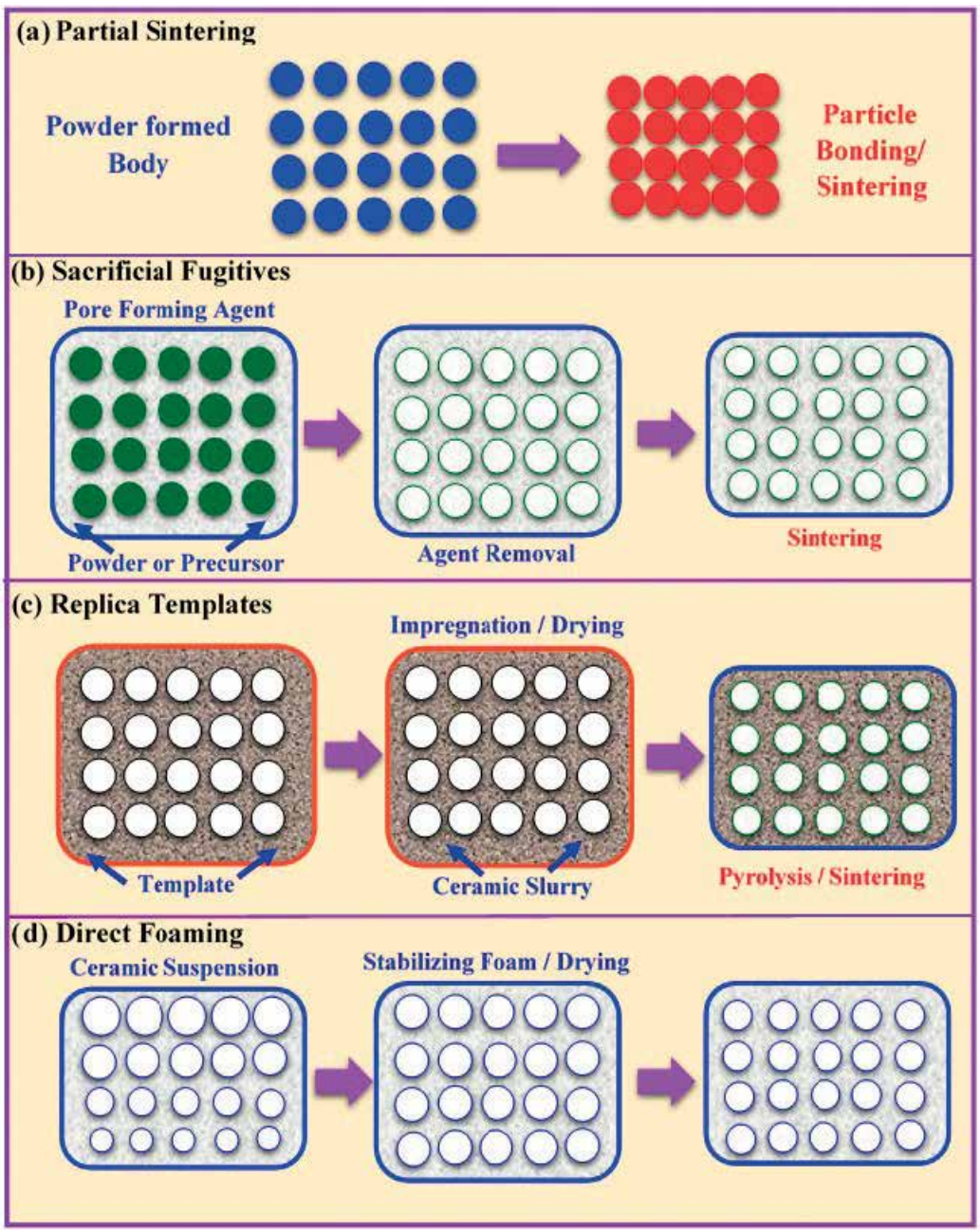

Figure 2. Schematic of porous ceramic processing methods: (a) partial sintering, (b) sacrificial fugitives, (c) replica templates, and (d) direct foaming [1].

porous ceramics such as the replica method, the sacrificial phase technique, direct foaming methods, paste extrusion and most recently developed rapid prototyping technique [13].

The fields of application and specific forms of porous ceramics are wide and varied according to their manufacturing processes [14]. Some of its useful applications are in the manufacture of filter. As these porous structures are used to filter high-pressure gas at high temperature and are used as an aid to remove the contaminants. In the field of petroleum treatment, porous ceramics are used as a substrate for catalysts in the process of filtration. They are also used in recovering hydrogen from the crude oil. Other applications are thermal insulators in filter membrane to separate metal impurities from molten metals such as steel, iron and aluminum. Today, porous ceramic structures prepared from different materials based on their application are used widely in biomedical field. For example, porous calcium phosphate materials can be used to replicate bone architecture and allow the growth of osseous tissue on an artificial substrate, thereby forming an artificial living bone structure. There porous hydroxyapatite can be used to replace bone and also as a drug delivery system [15].

4. Porous ceramic structure and properties

Porous ceramics possess a number of suitable properties, which combine the features of ceramics, and porous materials such as low density, lightweight, low thermal conductivity, low dielectric constant, thermal stability, high specific surface area, high specific strength, high permeability, high resistance to chemical attack and high wear resistance [13]. Either porous ceramics are reticulate (interconnected voids surrounded by a connection of ceramic) or foam (closed voids within a continuous ceramic matrix). Reticulated porous ceramics are usually used for molten metal, industrial hot-gas filters, catalyst supports, and diesel engine exhaust filters.

Pore size and porosity percentage are controlled by the particle size distribution of starting ceramic powders, fabrication techniques, types of binder used, concentration of binder and sintering conditions respectively [1]. Generally, the particle size of raw ceramic powder should be geometrically in the range between two to five times larger than that of pores in order to provide the desired pore size. The Porosity percentage reductions with increased making conditions such as pressure, sintering temperature and time. Furthermore, the fabrication influences such as the amount and type of additives, green densities, and sintering conditions (temperature, pressure atmosphere, etc.) significantly affect for the porous ceramics microstructures.

5. Mechanical behavior of porous ceramic

The general properties for porous ceramics can be designed for specific environmental application by controlling their composition and microstructure [16]. Changes in open and closed porosity, distribution of pore size and shapes of pore can have a main effect on the properties of porous ceramics. All of these microstructural features are in turn greatly affected by the processing way used to produce of the porous ceramic. For mechanical properties of porous ceramics, they are determined by their structural parameters, such as percentage of porosity, pore size, and shape. Furthermore, the solid microstructure phase of grain growth and solid phase continuity greatly affect the mechanical properties. Several important issues relating to

the growth of the neck touching particles by surface and volume diffusion can significantly increase the mechanical properties with minimal increase in density. The microstructure in porous ceramics can be controlled not only by adjusting the particle size and shape of the initial raw powders, but also through the process of sintering.

6. Classification of porous ceramic

Classification of pores is one of the basic requirements of inclusive characterization of porous ceramics (**Figure 3**). There are different classes of pores described porous ceramic in the literature,

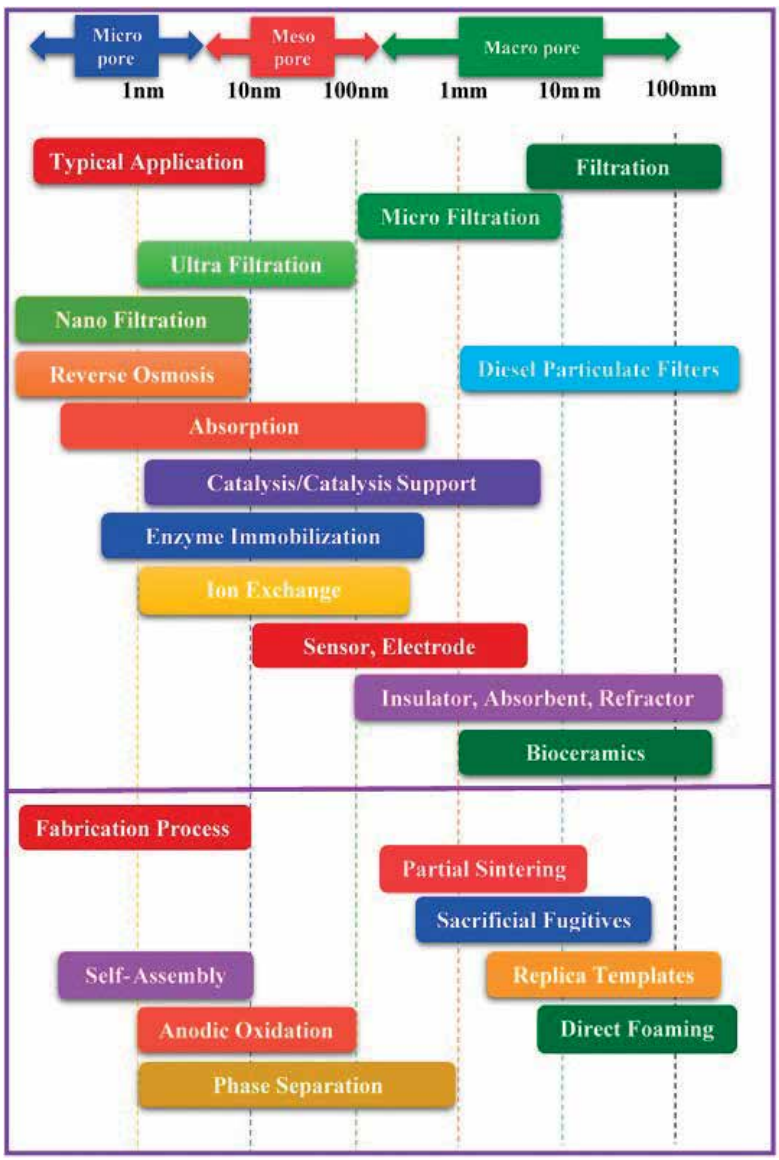

Figure 3. Schematic of classification of porous ceramic [1].

but they are difficult to give a consistent general classification of porous ceramics including catalyst carriers in various chemical processes, electrolyte carriers in fuel elements, adsorbents. As well as filtration of liquids, hot gases, melted metals and alloys, membranes for separation and purification of gas and liquids etc. The purpose of these classifications is to organize pores in classes by grouping them based on their common characteristics like structure, size, shape, accessibility etc. Therefore, porous ceramics can be classified according to the different characteristic attributes such as chemical composition of initial ceramic materials, porosity percentage, physical state of these products, refractoriness correlated to service temperatures, destination and application area [1].

7. Ceramic foams

Ceramic foams are porous brittle materials with closed, open-celled structures or partially interconnected porosity [17]. Ceramic foams are a special class of porous materials included of large voids with linear dimensions in the range between 10 and 5 mm. Foams are also called cellular ceramic materials because their structure can be represented by a lattice of a repeatable unit called "cell". They are fabricated from a broad kind of ceramic materials; specifically both oxide and non-oxide, which includes pure oxides, aluminosilicates and carbides that are being considered for the whole range of possible applications. These include filtration, catalysis, impact-absorbing structures, thermal insulation, performs for metal-ceramic composites, biomechanical implants, high specific strength materials and high efficiency combustion burners. The ceramic foams have been produced in a variety of materials with different shape sizes, densities and degree of interconnectivity. Foams or cellular are usually made with the density between 10 and 40% of theoretical and the pore sizes less than 1 mm. Ceramic foams can be made with a variety of microstructures with controlled properties through several versatile and simple methods, such as direct foaming, replica, sacrificial template techniques [5].

8. Porous ceramics using additive manufacturing techniques

The manufacturing of complex porous ceramic parts with defined microstructure is a challenge today [18]. Concerning this issue, additive manufacturing technology is a promising alternative to conventional manufacturing procedures. Various additive manufacturing technologies like laminated object manufacturing (LOM), stereolithography (SLA), fused deposition modeling (FDM), selective laser sintering (SLS) and three-dimensional printing (3D printing) have already been used to fabricate different porous ceramic shapes [19]. One of the fastest and most efficient technologies is 3D printing. The introduction of 3D printing technology into the porous ceramic industry provides greater speed and flexibility, eliminates tool constraints, needs only low cost investment, and enables the sustainability of the additive manufacturing process. The 3D printing can be used in the making of porous ceramics in a different of applications. For example, it is widely used for catalysis chemical reactors, biomedical applications and filtration technologies. It can also be used to produce porous ceramic membranes, energy storage and heat exchangers, because of the good thermal properties and relative strength of ceramic materials.

9. Porous hydroxyapatite ceramic and its biomedical applications

Hydroxyapatite (HA) porous ceramics are substitute materials for bone and teeth in repairing and regeneration applications due to their chemical and biological similarity to human hard tissue [20]. In the design of these porous ceramic for bone repairing or regeneration, it is important to control their pore structures. Pore ceramic structure can be designed using the size and morphology of the Hydroxyapatite particles that are utilized to build these porous ceramics. Porous hydroxyapatite ceramic exhibits strong joining to the bone, the pores provide a strong mechanical interlock leading to a firmer fixation of the structure. Porous hydroxyapatite is more resorbable and osteoconductive than HA dense counterpart [21]. The surface area of porous Hydroxyapatite form is greatly increased which allows more bone cells to be carried in comparison with dense hydroxyapatite. The most common techniques used to make porosity in a biomaterial are gas foaming, salt leaching, freeze-drying, phase separation and sintering depending on the material used to make the scaffold. The minimum pore size required to regenerate mineralized bone is generally considered to be around 100 μm.

10. Porous ceramics and catalyst carriers

Porous ceramics have a good activity and high absorption materials. The reaction rate and conversion increase significantly for the reactive fluid that flows through the porous ceramic networks [22]. The ceramic catalyst carrier plays a major role in promoting the chemical reaction. Due to the chemical corrosion resistance and thermal shock of porous ceramics, they can be used in highly required service conditions, like the reactor in chemical engineering and the vehicles gas exhaust treatment. As well as the fine metal particles are usually supported on the heterogeneous catalyst carriers, which are generally ceramic. Catalysis becomes also progressively more important in environmental pollution control. The catalyst effectively reduced pollution from automotive and industries applications. The ceramic used must have connected porosity and the pore size can differ between 6 nm and 500 μm. Alumina, titania, zirconia silica and silicon carbide are the most popular choices for catalyst supports. These ceramic powders are formed into a variety of shapes such as cylinder bars or hollow beads or clover-leaf shaped sections. They are then sintered to their final density. Porous ceramics also can be used as carriers in the recycling of steam, oxidation of ammonia, recombination of methane, destruction of volatile organic compounds (VOCs) by incineration and decomposition of organics by photocatalysis.

11. Porous ceramics and membranes

Porous ceramic membranes can be used to separate water, oil, liquids, solids, dust in gas, yeast or thallus and blood cells and to clarify alcohol in the food, chemical and medical industries. In addition, these membranes act as biological reactors in the recovery of fermented fluid. During the last few decades, the ceramic membrane applications have increased because of their excellent chemical, mechanical and thermal stability, and high separation efficiency [23]. High-permeability ceramic membranes can only be obtained in an asymmetric multilayer

arrangement with microporus support, providing mechanical strength and reducing flow resistance. Commercially porous ceramic membranes of oxides such as alumina and zirconia are not suitable for large-scale application because these kind of oxide membranes are very expensive. Recently, the natural minerals such as zeolite, apatite, dolomite and clays have received increasing attention due to their cheap fabrication and multiple applications. The development of ceramic membranes made of natural minerals could lead to a new critical technological revolution that would add significant economic value to the natural minerals found all over the world.

12. Porous ceramics and piezoelectric materials

The piezoelectric materials contain crystalline structures that do not overlap the positive and negative charge centers, leading to bipolar moments. When subjected to mechanical vibrations or movement, the mechanical strain of this material is applied and leads to distortion of the electrode, creating electrical charge [24, 25]. The electrical energy can be harvested by storing it in capacitors or rechargeable batteries. The piezoelectric material has been widely recognized with unique electromechanical coupling properties for its potential benefits in a large number of sensors and application engines. Moreover, it has also been shown that the microstructure of a piezoelectric material can be modified by adding a second phase (as in piezoelectric composites) or by introducing porosity (as in piezoelectric foams), in order to improve the piezoelectric materials properties for specific applications [26]. For example, by introducing porosity into piezoelectric material, the signal-to-noise ratio, sensitivity properties and impedance matching can be improved, thus the piezoelectric material can be made more suitable for the applications of hydrophone.

Author details

Uday M. Basheer Al-Naib

Address all correspondence to: ummb2008@gmail.com

Faculty of Mechanical Engineering, UTM Centre for Low Carbon Transport in Cooperation with Imperial College London, Institute for Vehicle Systems and Engineering, University of Technology Malaysia, Johor, Malaysia

References

[1] Ohji T, Fukushima M. Macro-porous ceramics: processing and properties. International Materials Reviews. 2012;**57**(2):115-131

[2] Gaudillere C, Serra JM. Freeze-casting: Fabrication of highly porous and hierarchical ceramic supports for energy applications. Boletín de la Sociedad Española de Cerámica y Vidrio. 2016;**55**(2):45-54

[3] Obada DO et al. Pressureless sintering and gas flux properties of porous ceramic membranes for gas applications. Results in Physics. 2017

[4] Korjakins A, Upeniece L, Bajare D. High efficiency porous ceramics with controllable porosity in Civil Engineering. International Scientific Conference. Proceedings (Latvia). 2013. Latvia University of Agriculture

[5] Eom J-H, Kim Y-W, Raju S. Processing and properties of macroporous silicon carbide ceramics: A review. Journal of Asian Ceramic Societies. 2013;**1**(3):220-242

[6] Sakka Y et al. Fabrication of porous ceramics with controlled pore size by colloidal processing. Science and Technology of Advanced Materials. 2005;**6**(8):915-920

[7] German RM. Liquid Phase Sintering. New York: Springer Science & Business Media, LLC, Plenum Press; 2013

[8] Misyura SY. The influence of porosity and structural parameters on different kinds of gas hydrate dissociation. Scientific Reports. 2016;**6**:30324

[9] Yurkov A. Refractories for Aluminum: Electrolysis and the Cast House. Springer; 2017

[10] Gaydardzhiev S et al. Gel-casted porous Al_2O_3 ceramics by use of natural fibers as pore developers. Journal of Porous Materials. 2008;**15**(4):475-480

[11] Nimmo J. Porosity and pore size distribution. Encyclopedia of Soils in the Environment. 2004;**3**:295-303

[12] Ishizaki K, Nanko M. A hot isostatic process for fabricating porous materials. Journal of Porous Materials. 1995;**1**(1):19-27

[13] Studart AR et al. Processing routes to macroporous ceramics: A review. Journal of the American Ceramic Society. 2006;**89**(6):1771-1789

[14] Werr U. Porous ceramics manufacture–properties–applications. In: CFI-Ceramic Forum International. 2014. 8, D-76532 Baden Baden, Germany: Goller Verlag GmbH Aschmattstrasse

[15] Yoshikawa H et al. Interconnected porous hydroxyapatite ceramics for bone tissue engineering. Journal of the Royal Society Interface. 2009:p. rsif. 2008.0425. focus

[16] Korjakins A, Upeniece L, Bajare D. Heat insulation materials of porous ceramics, using plant filler. Civil Engineering'13. 2013: p. 169

[17] Rahman HA, Guan YC. Preparation of Ceramic Foam by Simple Casting Process. 2007

[18] Tofail SAM et al. Additive manufacturing: Scientific and technological challenges, market uptake and opportunities. Materials Today. 2017

[19] Hwa LC et al. Recent advances in 3D printing of porous ceramics: A review. Current Opinion in Solid State and Materials Science. 2017

[20] Prakasam M et al. Fabrication, properties and applications of dense hydroxyapatite: A review. Journal of functional biomaterials. 2015;**6**(4):1099-1140

[21] Zhou K et al. Porous hydroxyapatite ceramics fabricated by an ice-templating method. Scripta Materialia. 2011;**64**(5):426-429

[22] Julbe A, Farrusseng D, Guizard C. Porous ceramic membranes for catalytic reactors—overview and new ideas. Journal of Membrane Science. 2001;**181**(1):3-20

[23] Wu P et al. A review of preparation techniques of porous ceramic membranes. Journal of Ceramic Processing Research. 2015;**16**:102-106

[24] Bowen C et al. Processing and properties of porous piezoelectric materials with high hydrostatic figures of merit. Journal of the European Ceramic Society. 2004;**24**(2):541-545

[25] Li H, Tian C, Deng ZD. Energy harvesting from low frequency applications using piezoelectric materials. Applied physics reviews. 2014;**1**(4):041301

[26] Zhang Y et al. Enhanced pyroelectric and piezoelectric properties of PZT with aligned porosity for energy harvesting applications. Journal of Materials Chemistry A. 2017; **5**(14):6569-6580

Chapter 2

Biomimetic Porous Bone-Like Apatite Coatings on Metals, Organic Polymers and Microparticles

Takeshi Yabutsuka

Additional information is available at the end of the chapter

http://dx.doi.org/10.5772/intechopen.71390

Abstract

When pH and temperature of simulated body fluid (SBF) are raised, fine particles of calcium phosphate are precipitated. Recently, the authors' research group found that these fine particles were highly active to induce formation of porous bone-like apatite in SBF, or body fluid, and named them 'apatite nuclei.' By using apatite nuclei, the author successfully imparted high bioactivity, that is, apatite-forming ability, to various kinds of bioinert biomaterials such as metals and organic polymers in a series of recent studies. These materials spontaneously formed porous bone-like apatite layer on their surfaces in SBF in a short time and showed high bioactivity in vitro. In addition, thWe author also successfully fabricated microcapsules consisted of porous bone-like apatite by using apatite nuclei.

Keywords: porous bone-like apatite, apatite nuclei, bioactive metals, bioactive organic polymers, apatite microcapsules

1. Introduction

1.1. Bioactive materials

When artificial materials such as metals, ceramics and organic polymers are implanted in the body, these materials are generally encapsulated with noncalcified fibrous tissue and separated from the surrounding living tissue. Such biological response is known as a normal immune reaction of the living body with respect to exogenous materials. In early 1970s, L.L. Hench found that Na_2O-CaO-SiO_2-P_2O_5-type glass (bioglass®) showed bone-bonding ability without the isolation from surrounding living tissue [1]. Since the discovery of bioglass®, ceramic materials such as glass-ceramic Ceravital® containing crystalline apatite [2], sintered

hydroxyapatite ($Ca_{10}(PO_4)_6(OH)_2$) [3], glass-ceramics Cerabone® A-W containing crystalline apatite and wollastonite ($CaO{\cdot}SiO_2$) [4, 5], and so on have been found to bond with living bone. Most of the ceramics mentioned above forms apatite layer on their surface and can bond with living bone through the apatite layer in living body [6, 7]. This apatite layer consists of minute crystallites containing carbonate ions in chemical composition [8] and is similar to apatite, which contains living bone [9, 10]. On the apatite layer, osteoblast actively proliferates and differentiates [6, 11]. Hence, bone tissue is formed on the apatite layer and the artificial materials can be also found to bond with the surrounding bone tissue through the apatite layer. Such material property is often defined as 'bioactivity' in the research field of ceramic biomaterials.

1.2. Simulated body fluid

In early 1990s, T. Kokubo proposed an acellular simulated body fluid (SBF) with ion concentrations similar to those of human blood plasma [12–14]. It is possible to reproduce the abovementioned apatite formation reaction on most of the bioactive materials by soaking the materials in SBF. Hence, we can predict bioactivity, that is, apatite-forming ability, of specimens by soaking them in SBF and evaluating apatite formation on their surface. **Table 1** shows the ion concentrations of simulated body fluid and human blood plasma. The SBF can be prepared by dissolving NaCl, $NaHCO_3$, KCl, $K_2HPO_4{\cdot}3H_2O$, $MgCl_2{\cdot}6H_2O$, $CaCl_2$ and Na_2SO_4 in pure water and maintaining the pH value at 7.40 with $(CH_2OH)_3CNH_2$ and 1 mol dm^{-3} HCl solution at 36.5°C. The details of preparation method of SBF and the bioactivity test are certified by ISO 23317 [14]

1.3. Apatite nuclei

When pH and temperature of SBF are raised, fine particles of calcium phosphate are precipitated. Generally, calcium phosphate formation in an aqueous solution can be described as shown in (Eq. (1)) by applying hydroxyapatite as a representative calcium phosphate.

$$10\,Ca^{2+} + 6PO_4^{3-} + 2OH^- = Ca_{10}(PO_4)_6(OH)_2 \quad (1)$$

Ion	Ion concentration/mM	
	SBF	Blood plasma
Na^+	142.0	142.0
K^+	5.0	5.0
Mg^{2+}	2.5	2.5
Ca^{2+}	1.5	1.5
Cl^-	147.8	103.0
HCO_3^-	4.2	27.0
HPO_4^{2-}	1.0	1.0
SO_4^{2-}	0.5	0.5

Table 1. Ion concentrations of simulated body fluid (SBF) and human blood plasma.

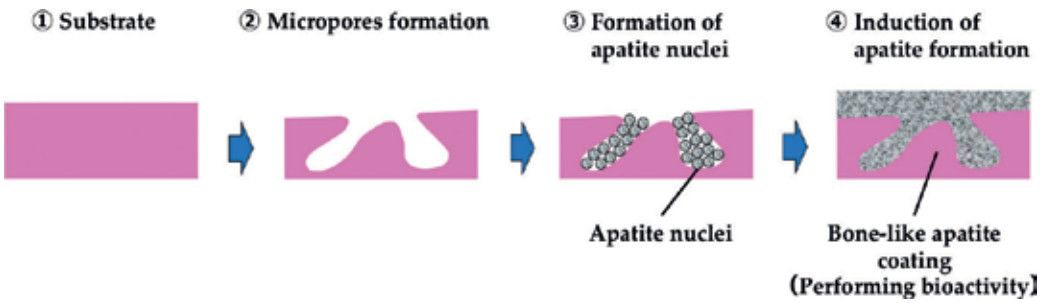

Figure 1. Bioactive materials' design by utilizing the function of apatite nuclei.

When pH value or concentration of the aqueous solution increases, apatite formation is promoted from a viewpoint of the abovementioned chemical equilibrium because of an increase of OH^- or Ca^{2+} and PO_4^{3-}. In addition, the reaction is accelerated under high-temperature environment because of an increase of chemical reaction rate of calcium phosphate formation. Yao et al. found that thus-precipitated fine particles of calcium phosphate showed high activity for induction of porous bone-like apatite formation in SBF and named the particles 'apatite nuclei' [15].

1.4. Bioactive materials' design by utilizing the function of apatite nuclei

As described in Section 1.3, apatite nuclei, precipitated by raising pH or temperature of SBF, actively induce apatite formation in SBF or body environment. By using apatite nuclei, excellent implant materials possessing various mechanical properties as well as high bioactivity and bioaffinity can be developed by combining it with various kinds of bioinert materials such as metals and organic polymers. Recently, we found that high apatite-forming ability can be imparted by the following method [16].

- Micropores are formed on the surface of the substrate by acid treatment or sandblasting process.
- The abovementioned micropores-formed substrate or porous substrate is soaked in SBF, and pH and temperature of SBF is increased. By this treatment, apatite nuclei are precipitated in the pores of the substrate.

When this material is implanted into a bone defect, it is thought that apatite nuclei induce apatite formation and this material subsequently bonds with living bone through the formed bone-like apatite layer (**Figure 1**). As a result, it is expected that the materials can bond with living bone through the formed apatite layer.

2. Fabrication of bioactive metals by incorporation of apatite nuclei as precursors of apatite

2.1. Bioactive metals

Metals have high mechanical strength and high fracture toughness. Among them, stainless used steel (SUS), cobalt-chromium (Co-Cr) alloys, titanium (Ti) and its alloys have

been widely used as implant materials. However, most of them do not have bioactivity or have extremely poor bioactivity. Hence, these materials without any pretreatment cannot spontaneously form apatite coatings in living body in most cases. For this reason, effective methods for imparting high bioactivity to these metallic biomaterials are desired. As a representative surface modification of metals for bioactivity, hydroxyapatite coating by plasma spray method has been widely used in practical use as artificial hip joint [17]. However, this method required heating process at a temperature over 10,000°C and it is difficult to optimize the composition and crystallinity of hydroxyapatite for the bone conduction in living body. Kokubo et al. reported that NaOH and heat treatment are an effective way to impart bioactivity to the surface of Ti metal and its alloys [5, 18, 19]. In fact, the NaOH- and heat-treated Ti metal showed apatite formation within 1 day in SBF and attained high bioactivity. From these properties, the Kokubo's method has been already used in clinical use as a surface modification for artificial hip joint. However, this method cannot be applied to SUS and Co-Cr alloys [19]. As one of the most effective method for solving this problem, incorporation of apatite nuclei described in Section 1.4 can become an effective candidate to impart bioactivity to various kinds of bioinert metallic biomaterials. Recently, the author successfully imparted bioactivity to pure Ti metal [20–22], Ti-6Al-4 V alloy [23], Ti-15Mo-5Zr-3Al alloy [22, 24, 25], Ti-12Ta-9Nb-3 V-6Zr-O alloy [22], pure zirconium (Zr) metal [23], Co-Cr alloy [26] and SUS [27, 28] by incorporation of apatite nuclei on their surfaces based on the materials' design described in Section 1.4. Among them, the author introduces the details of bioactive SUS as a representative case of bioinert metallic biomaterials in this chapter.

2.2. SUS as an orthopedic material

SUS is a typical biomaterial with high mechanical strength and high-corrosion resistance and has been already used as orthopedic implants such as artificial hip joint. However, SUS has no bioactivity. If an effective bioactivity treatment for SUS is established, range of its application is largely extended. Bioactivity treatment utilizing apatite nuclei described in Section 1.4 is one of the effective methods used for surface modification of SUS to impart bioactivity. As a novel micropores formation process, the authors established a formation process of roughened surface with fine pores on metals and organic polymers by doubled sandblasting process [29] by using the grinding particles with 14 μm of average particle size as first process, and then using the particles with 3 μm of average particle size as second process. The authors clarified that thus-formed fine pores contributed to the improvement of adhesion property of porous bone-like apatite layer formed on the bioactive materials in SBF in the process shown in **Figure 1** because of an improvement of mechanical interlocking effect. As described in this section, the authors formed micropores on the surface of SUS plates by the doubled sandblasting process. Then the authors precipitated apatite nuclei in the pores of SUS to impart bioactivity.

2.3. Fabrication process of bioactive SUS

2.3.1. Micropores formation by the doubled sandblasting process

First, in order to prepare micropores on the surface, the SUS plates (JIS SUS 316 L) were treated by a sandblasting process using alumina-grinding particles with 14 μm (JIS #800) of

average particle size. Then, the plates were treated by that with 3 μm (JIS #4000) of average particle size. **Figure 2** shows the SEM micrograph of the surface of the SUS plate after the sandblasting process. It can be seen that the SUS plate possessed the roughened surface with fine pores formed by the sandblasting process.

2.3.2. Impartation of apatite-forming ability: incorporation of apatite nuclei as precursors of apatite

After the micropores formation, the following process was conducted for apatite nuclei precipitation in the pores to impart bioactivity to the surface of the SUS plate. First, the pH value of SBF was increased to 8.40 by dissolving tris(hydroxymethyl)aminomethane at 25°C. Subsequently, the SUS plates were soaked in the SBF and the solution was pressed by cold isostatic pressing machine to make the solution penetrate into the pores. In order to precipitate apatite nuclei in the pores of the specimens, the solution was heated by using electromagnetic induction at 2.5 kW for 2 hours while soaking the specimens in the solution. Hereafter, the authors denote these treatments as 'alkaline SBF treatment'. **Figure 3** shows the SEM micrograph and the EDX profile of the surface of the SUS plate after the alkaline SBF treatment. It can be seen that the surface morphologies were slightly rounded off in comparison with just after the doubled sandblasting process shown in **Figure 2** and some types of coatings were formed on the plates. In the EDX profile, peaks of P and Ca were detected. It is considered that the SUS plate has been effectively heated in SBF by electromagnetic induction because the iron, which is a main chemical component of SUS, has high magnetic susceptibility. As a result, nucleation and growth of calcium phosphate were further promoted and the apatite nuclei formed under alkaline condition grew to some types of calcium phosphate coating on the surface of the SUS plate in the alkaline SBF treatment. Hereafter, the SUS plate after the alkaline SBF treatment is denoted as 'bioactive SUS'

2.4. Apatite-forming ability of bioactive SUS: porous bone-like apatite coatings in biomimetic environment

Next, bioactivity of thus-obtained bioactive SUS was evaluated by soaking in SBF at pH 7.40, 36.5°C, which is corresponded to physiological environment. **Figure 4** shows the thin-film

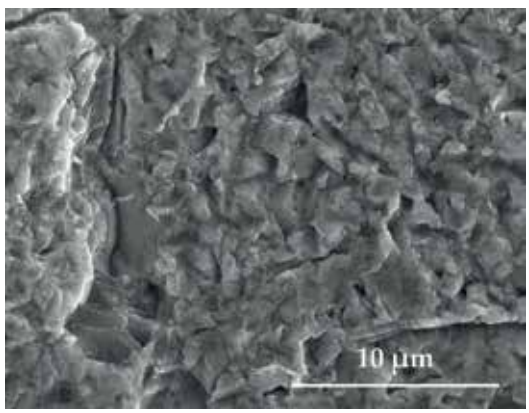

Figure 2. SEM micrograph of the surface of the SUS plate after the sandblasting process.

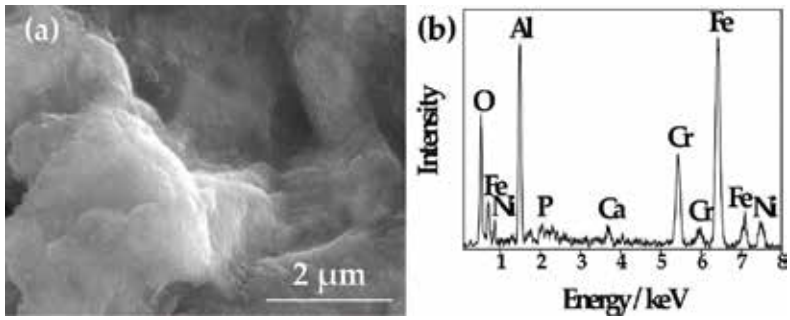

Figure 3. (a) SEM micrograph and (b) EDX profile of the surface of the SUS plate after the alkaline SBF treatment.

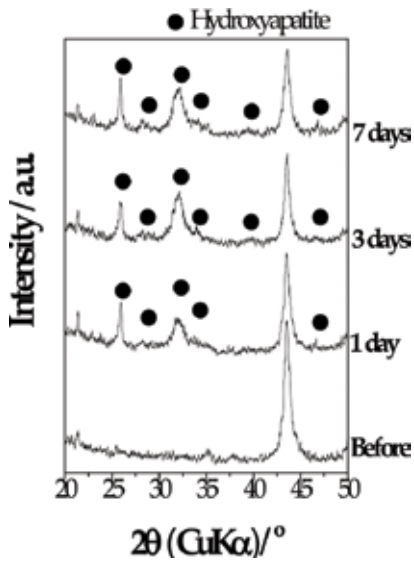

Figure 4. TF-XRD profile of the surface of the bioactive SUS after the soaking in SBF for 0 day, 1 day, 3 days and 7 days.

X-ray diffraction (TF-XRD) profiles of the surface of the bioactive SUS after soaking in SBF for 0 day (i.e., before soaking in SBF), 1 day, 3 days and 7 days. Before soaking in SBF, diffraction peaks of apatite were not detected. This result suggested that the calcium phosphate coating formed in the alkaline SBF treatment was consisted of amorphous calcium phosphate (ACP). After soaking in SBF for 1 day, 3 days and 7 days, diffraction peaks of apatite were clearly detected. **Figure 5** shows the SEM micrograph and the EDX profile of the surface of the bioactive SUS after soaking in SBF for 1 day. It was observed that the whole surface was covered with porous coating, which consisted of needle-like crystallites, which characterize bone-like apatite, in the SEM observation. In the EDX profile, the intensity of the peaks of P and Ca was relatively increased in comparison with those after the alkaline SBF treatment shown in **Figure 3**. From these results, it is indicated that apatite formation was induced within 1 day and high bioactivity was imparted to the SUS by the alkaline SBF treatment.

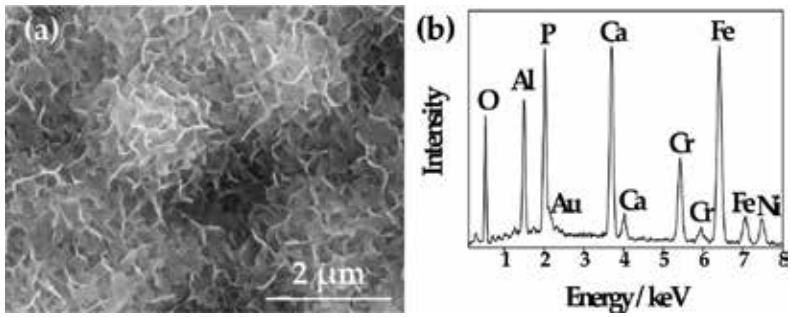

Figure 5. (a) SEM micrograph and (b) EDX profile of the surface of the bioactive SUS after the soaking in SBF for 1 day.

2.5. Adhesion property of porous bone-like apatite coating formed on the bioactive SUS

The adhesive strength between the bioactive SUS and the porous bone-like apatite coating formed by soaking in SBF for 14 days was measured by a modified ASTM C-633 method [30–33]. For the reference, the author prepared the specimens, which were applied same treatments without the doubled sandblasting treatment. The average adhesive strength between the formed apatite layer and the bioactive SUS with alkaline SBF treatment was 15.4 MPa, and for the SUS without the sandblasting treatment was 1.5 MPa. The SUS treated with doubled sandblasting treatment showed higher adhesive strength than untreated ones. This is because a mechanical interlocking effect between the SUS plate and the porous bone-like apatite coating was attained by the formation of micropores.

2.6. Case of the other types of metals

As described in Section 2.1, the author reported that this bioactivity treatment was applicable not only to SUS but also to other kinds of metallic biomaterials such as Ti metal and its alloys, Zr metal and Co-Cr alloy by optimizing the condition of micropores formation and apatite nuclei precipitation according to the kinds of materials. Also in the case of these metals, apatite formation was induced within 1 day in SBF [20–26]. In addition, it is reported that most of the bioactive ceramics show apatite formation within 1 week in SBF [34]. Hence, it is suggested that the alkaline SBF treatment was an effective method to impart high bioactivity to bioinert or poorly bioactive metals.

3. Fabrication of bioactive organic polymers by incorporation of apatite nuclei as precursors of apatite

3.1. Bioactive organic polymers

Organic polymers have various mechanical properties and are easily processed in various shapes such as sticks, plates, films, sponges and fibers. Because of these properties, organic polymers have been widely used as various implant materials such as artificial hip joint,

artificial knee joint, artificial knuckle joint and artificial ligament. Generally, however, organic polymers are not bioactive and cannot bond with living bone in living body. If organic polymers acquire bioactivity, implant materials with various mechanical properties as well as high bioactivity can be developed. As a conventional method to impart bioactivity to organic polymers, the method that bioactive ceramics particles such as sintered hydroxyapatite are dispersed in polymeric matrix have been mainly applied. Among them, HAPEX™, which contains 40 vol% of hydroxyapatite in high density polyethylene matrix [35], has been already in practical use as an orbital implant and a middle ear implant. However, such method is difficult to control bioactivity of the materials because most of ceramics particles are buried inside the polymeric matrix and bioactivity was performed by only the particles exposed to the surface of the materials [36]. As one of the most effective method for solving this problem, the alkaline SBF treatment described in Section 1.4 can act as an attractive candidate to impart bioactivity also to polymeric biomaterials, similar to the case of metals. Recently, the author successfully established the surface modification technique to impart bioactivity to ultrahigh-molecular weight polyethylene (UHMWPE) [37], polyethyleneterephthalate (PET) [24], poly-L-lactic acid (PLLA) [38], polyetheretherketone (PEEK) [39–41], carbon fiber-reinforced PEEK (CFR-PEEK) [42], glass fiber-reinforced PEEK (GFR-PEEK) [42] and glass fiber-reinforced poly(m-Xylyleneadipamide)-6 (GFR-MXD6) [43]. Among them, the author introduces the details of bioactive PEEK as representative cases of polymeric biomaterials in this chapter.

3.2. PEEK as orthopedic materials

PEEK is well known as one of the next-generation polymeric materials with high mechanical toughness. In addition, PEEK is in the spotlight of orthopedic or dental fields because of its more similar elastic modulus with cortical bone than metallic biomaterials such as Ti alloys, SUS and Co-Cr alloys and ceramic biomaterials such as alumina, zirconia and sintered hydroxyapatite. From these mechanical properties, it is expected that PEEK becomes a candidate for replacing conventional metallic or ceramic bone substitutes in clinical use [44]. Although PEEK has biocompatibility, bioactivity of PEEK is extremely poor. If high bioactivity is imparted to PEEK, the range of its clinical or dental use such as minimally invasive orthopedic treatment will be largely extended. As described in this section, micropores were formed on PEEK by sulfuric acid treatment. Then apatite nuclei were precipitated in the pores and bioactivity was imparted to PEEK by incorporation of apatite nuclei.

3.3. Fabrication process of bioactive PEEK

3.3.1. Micropores formation by sulfuric acid treatment

First, in order to form micropores on the surface of the PEEK, PEEK plates were treated with 98% sulfuric acid at room temperature. **Figure 6** shows the SEM micrograph of the surface of the PEEK after the sulfuric acid treatment. It can be seen that cancellous micropores around 500 nm in diameter were formed on the whole surface of the plate.

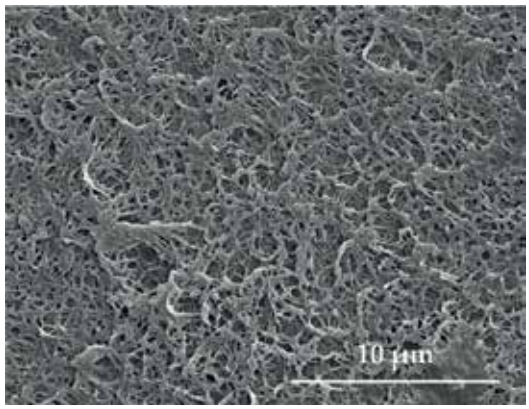

Figure 6. SEM micrograph of the surface of the PEEK plate after the sulfuric acid treatment.

3.3.2. Impartation of apatite-forming ability: incorporation of apatite nuclei as precursors of apatite

Next, the author conducted surface modification to impart bioactivity to PEEK by incorporation of apatite nuclei. As a pretreatment for the apatite nuclei incorporation, the surfaces of the micropores-formed PEEK were treated with glow-discharge in O_2 gas atmosphere. By this treatment, reactive functional groups, which have hydrophilic property, were supplied on the surfaces of organic polymers [45]. The pH value of SBF was increased to 8.4 by dissolving tris(hydroxymethyl)aminomethane at 25°C. In order to precipitate apatite nuclei in the micropores, the micropores-formed PEEK was soaked in this SBF and kept at 70°C for 24 hours. Hereafter, this treatment is denoted as 'alkaline SBF treatment'. **Figure 7** shows the SEM micrograph and the EDX profile of the surface of the micropores-formed PEEK after the alkaline SBF treatment. It can be seen that the surface morphology was different from **Figure 6**, after the sulfuric acid treatment. In the EDX profile, peaks of P and Ca were detected. In the SEM micrograph, spherical particles of apatite nuclei were observed on the whole surface. It is considered that apatite nuclei were precipitated on the surface or inside the pores by the alkaline SBF treatment. Hereafter, this material is denoted as 'bioactive PEEK'

3.4. Apatite-forming ability of bioactive PEEK: formation of porous bone-like apatite coatings in biomimetic environment

Next, bioactivity of the bioactive PEEK was evaluated by SBF test similar to the case of SUS as described in Section 2.4. **Figure 8** shows the TF-XRD profiles of the surface of the bioactive PEEK after the soaking in SBF for 0 day, 1 day, 3 days, 7 days and 14 days. After soaking in SBF for 1 day, diffraction peaks of apatite were detected. As elapse of soaking time, the intensity of the diffraction peaks increased and those of PEEK decreased. **Figure 9** shows the SEM micrograph and the EDX profile of the surface of the bioactive PEEK after soaking in SBF for 1 day. It can be seen that the whole surface of the plate was covered with porous coatings consisted of needle-like crystallites, which characterize bone-like apatite, in the SEM observation

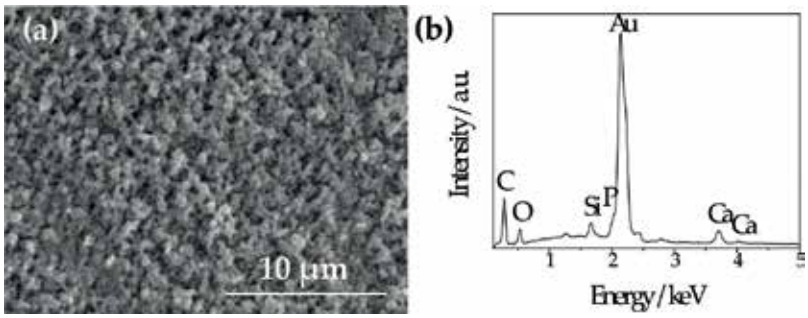

Figure 7. (a) SEM micrograph and (b) EDX profile of the surface of the PEEK plate after the alkaline SBF treatment.

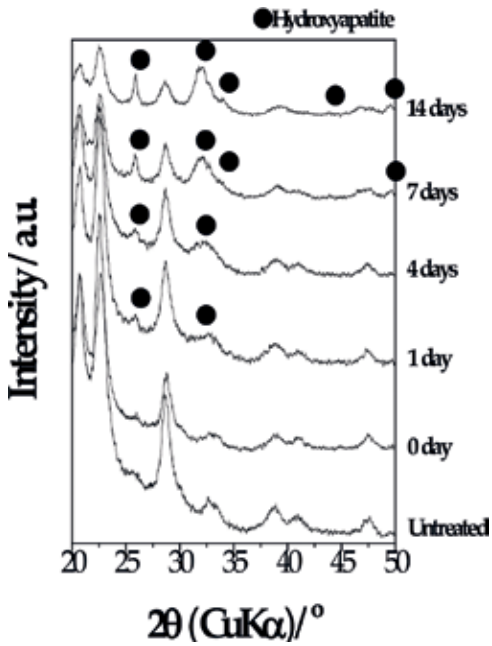

Figure 8. TF-XRD profiles of the surface of the untreated PEEK and the bioactive PEEK after the soaking in SBF for 0 day, 1 day, 3 days, 7 days and 14 days.

and peaks of P and Ca were strongly detected in the EDX analysis. By considering the results of TF-XRD, SEM and EDX, it is revealed that porous bone-like apatite, which was induced by apatite nuclei, covered the whole surface of the bioactive PEEK within 1 day and the apatite layer grew thick as elapse of the soaking time.

3.5. Adhesion property of porous bone-like apatite coating formed on the bioactive PEEK

Similar to the case of metals, adhesive strength between the bioactive PEEK and the porous bone-like apatite coating formed by soaking in SBF for 14 days was measured by a modified ASTM C-633 method [30–33]. For the reference, the author prepared the specimens, which

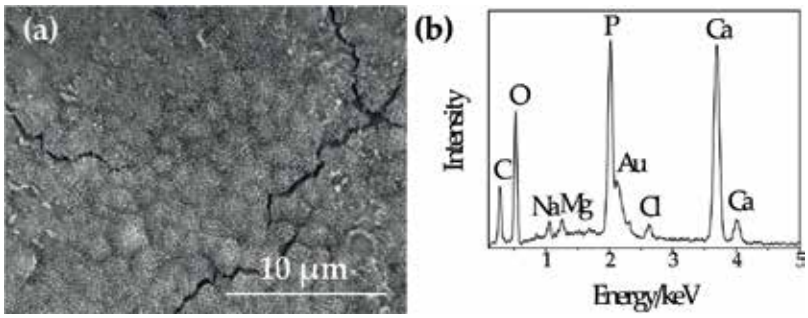

Figure 9. (a) SEM micrograph and (b) EDX profile of the surface of the bioactive PEEK after the soaking in SBF for 1 day. The generation of cracks observed in **Figure 9** (a) was caused when the specimen was air-dried after the SBF test.

were applied same treatments without sulfuric acid treatment. The average value of adhesion strength of the porous bone-like apatite coating for the bioactive PEEK with the pores formed by the sulfuric acid treatment was 6.7 MPa. In contrast, PEEK without pores formation was 2.1 MPa. The PEEK with pores formed by the sulfuric acid treatment presented higher adhesion strength. This difference was caused by a mechanical interlocking effect between the PEEK and porous bone-like apatite layer by existence of the micropores, similar to the case of the SUS.

3.6. Case of the other types of polymers

As described in Section 2.1, the author reported that this bioactivity method was applicable not only to PEEK but also to other kinds of polymeric biomaterials such as UHMWPE, PET, PLLA, CFR-PEEK, GFR-PEEK and GFR-MXD6 by optimizing the condition of micropores formation and apatite nuclei precipitation according to the kinds of materials, similar to the case of the metals [24, 37, 38, 42, 43]. Also in the case of these polymers, apatite formation was induced within 1 day in SBF in most cases. Hence, it is suggested that the alkaline SBF treatment was an effective method to impart high bioactivity not only to metals but also to polymeric implant materials.

4. Fabrication of apatite microcapsules consisted of biomimetic porous bone-like apatite coatings by using apatite nuclei as precursors of apatite

4.1. Fabrication of microcapsule consisted of porous bone-like apatite

Drug delivery system (DDS) is one of the most attractive techniques in the medical and pharmaceutical fields. DDS can contributes to chemotherapy that can achieve low side effects because it can achieve an efficient local or controlled release of pharmaceutical drugs. The microcapsules can be filled with pharmaceutical drugs. Hence, the DDS carriers consisted of microcapsules have a possibility to be applied in many kinds of pharmaceutical fields. Apatite has high bioaffinity because it forms bone-like apatite coatings consisted of needle-like fine crystallites on its surface in living body and can avoid immune reaction. From the above idea, it is thought that microcapsules possessing high biocompatibility can be obtained by applying apatite. The porous bone-like apatite microcapsules can be fabricated by the following process [46, 47]:

- Apatite nuclei are attached to the surfaces of core particles.
- The microspheres are soaked in SBF.

By this treatment, apatite formation is induced by the apatite nuclei and grows over the whole surface area of the core particles. As a result, porous bone-like apatite coats the whole surface of the particles and apatite microcapsules can be obtained (**Figure 10**). By this method, it is expected to encapsulate various kinds of functional particles or pharmaceutical drugs with apatite.

The development of sustained-release of drug is expected to contribute to have effects of the drug without side effects and reduce the burdens of patients. Porous bone-like apatite formed in SBF has flake-like crystalline structure and porous body [46, 47]. Focusing on these features of porous bone-like apatite, the author has intended to fabricate porous bone-like apatite microcapsules encapsulating various kinds of substances such as PLLA [48], silver [48], silica gel [48, 49], magnetite [50], maghemite [51, 52], agarose gel [53, 54] and corn oil [55]. Among them, the author introduces the details of encapsulation of corn oil in the porous bone-like apatite microcapsules as representative cases in this chapter.

4.2. Porous bone-like apatite microcapsules encapsulating corn oil

By utilizing surfactant such as albumin, oil droplets in micrometer level can be stabilized in water phase or water droplets in micrometer level can be stabilized in oil phase. The microencapsulation techniques by forming oil or water droplets can achieve an intravenous injection of the droplets containing pharmaceutical drug. As described in this section, the author fabricated porous bone-like apatite microcapsules encapsulating corn oil droplets containing ibuprofen, hydrophobic drug and nonsteroidal anti-inflammatory drug and evaluated the temporal change in release of the ibuprofen in vitro.

4.3. Preparation process of porous bone-like apatite microcapsules encapsulating corn oil

4.3.1. Fabrication of porous bone-like apatite microcapsules

Corn oil and ibuprofen were mixed. In order to dissolve ibuprofen in corn oil sufficiently, ethyl acetate was added in the mixture. After albumin aqueous solution was poured, the mixture was treated by ultrasonic vibration, so emulsion was formed. The emulsion was mixed

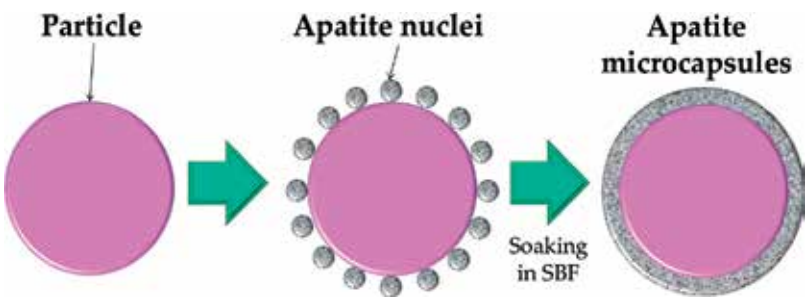

Figure 10. Fabrication process of apatite microcapsules by using apatite nuclei.

with 1.5 SBF, whose ion concentrations are 1.5 times in comparison with those of SBF, and apatite nuclei, thereafter, the mixture was treated by ultrasonic vibration to attach apatite nuclei on the surface of the oil droplets. After ethyl acetate was evaporated and removed from the mixture, the solution was kept at 36.5°C for 4 days. **Figure 11** shows SEM micrograph and EDX profile of thus-obtained microcapsules. Spherical particles consisted of needle-like crystals, which characterize bone-like apatite, were observed. In the EDX measurement, phosphorus and calcium, main consistent of apatite, were detected. It is suggested that the apatite nuclei attached on the oil droplets induced formation of bone-like apatite and then the crystal growth of apatite was caused on the surface of the oil droplets. **Figure 12** shows the powder X-ray diffraction (XRD) profile of the obtained apatite microcapsules. It can be seen that the peak positions of the apatite microcapsules corresponded to those of apatite, but shape of the pattern was broad. From this result, it was indicated that bone-like apatite covered the corn oil droplets during soaking in SBF.

4.4. Function of porous bone-like apatite microcapsules: drug release behavior

The author evaluated the release behavior of ibuprofen contained in corn oil droplets. **Figure 13** shows the temporal change in the concentration of ibuprofen released from porous bone-like apatite microcapsules in phosphate buffer (pH 7.40 at 36.5°C) measured by high-performance liquid chromatography (HPLC). It can be seen that the concentration of

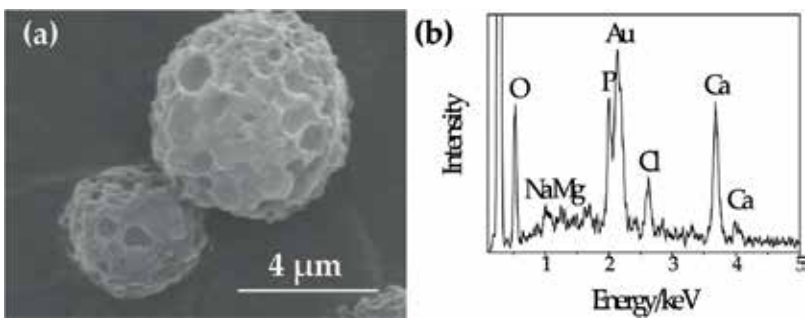

Figure 11. (a) SEM micrograph and (b) EDX profile of the porous bone-like apatite microcapsules encapsulating corn oil.

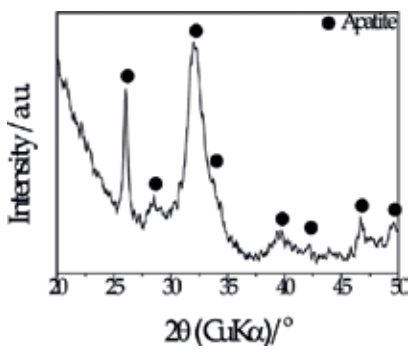

Figure 12. XRD profile of the porous bone-like apatite microcapsules encapsulating corn oil.

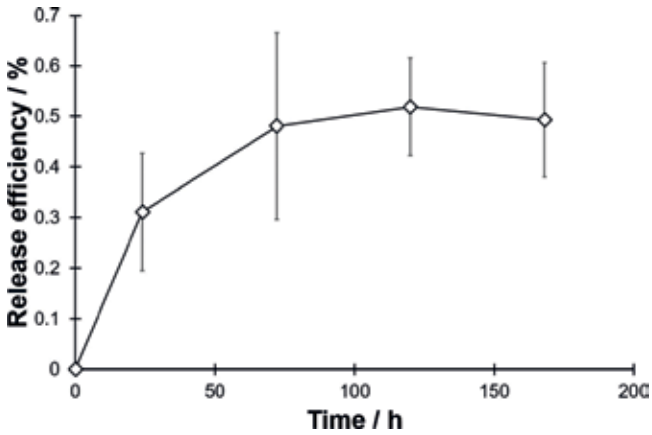

Figure 13. Release behavior of ibuprofen from bone-like apatite microcapsules.

ibuprofen in the buffer did not increase rapidly in a short time but increased gradually. This profile suggested that the porous structure of bone-like apatite microcapsules can gradually release ibuprofen contained in corn oil through the micropores of the apatite coatings.

4.5. Other types of porous bone-like apatite microcapsules

As described in Section 4.1, this fabrication method for porous bone-like apatite microcapsules was applicable to other kinds of core materials such as encapsulating various kinds of substance such as PLLA [48], silver [48], silica gel [48, 49], magnetite [50], maghemite [51, 52] and agarose gel [53, 54] by optimizing the fabrication condition. In the case of silver, sustained release of silver was attained by existence of porous coatings of bone-like apatite. In the case of silica gel, sustained release of insulin was attained by conducting absorption of insulin solution into the silica-gel matrix [56]. In the case of magnetite, release of magnetite was inhibited in water by existence of the porous apatite coatings. In the case of agarose gel, sustained release of vitamin B_{12} was attained by conducting insertion of vitamin B_{12} solution in the apatite microcapsules [53]. In the case of maghemite, in addition, the author successfully achieved enzyme immobilization and collection by combination of bioaffinity of apatite with ferrimagnetism of maghemite.

5. Conclusion

In this chapter, the author introduced novel biomaterials utilizing porous bone-like apatite formation from apatite nuclei from a viewpoint of bioactive metals, bioactive organic polymers and apatite microcapsules. This methodology has high materials selectivity, and function of apatite nuclei enables us to impart bioactivity to various kinds of materials or to coat microparticles with porous bone-like apatite coating. It is expected that the porous bone-like apatite coating technique are promising methodology to be useful to fabricate novel medical, pharmaceutical and environmental materials by combination of bone-like apatite with various kinds of functional materials in micron scale.

Author details

Takeshi Yabutsuka

Address all correspondence to: yabutsuka@energy.kyoto-u.ac.jp

Department of Fundamental Energy Science, Graduate School of Energy Science, Kyoto University, Japan

References

[1] Hench LL. Bioceramics: From concept to clinic. Journal of the American Ceramic Society. 1991;**74**(7):1487-1510. DOI: 10.1111/j.1151-2916.1991.tb07132.x

[2] Gross UM, Müller-Mai C, Voigt C. Ceravital® bioactive glass-ceramics. In: Hench LL, editor. An Introduction to Bioceramics. 2nd ed. London: Imperial College Press; 2013. pp. 209-214. DOI: 10.1142/9781908977168_0015

[3] Jarcho M, Kay JF, Gumaer KI, Doreus RH, Drobeck HP. Tissue, cellular and subcellular events at bone-ceramic hydroxylapatite interface. Journal of Bioengineering. 1977;**1**(2): 79-92

[4] Kokubo T, Shigematsu M, Nagashima Y, Tashiro M, Yamamuro T, Higashi S. Apatite- and wollastonite-containing glass-ceramics for prosthetic application. Bulletin of the Institute of Chemical Research, Kyoto University. 1982;**60**(3-4):260-268

[5] Kokubo T, Yamaguchi S. Novel bioactive materials derived by bioglass: Glass-ceramic A-W and surface-modified Ti metal. International Journal of Applied Glass Science. 2016;**7**(2):173-182. DOI: 10.1111/ijag.12203

[6] Neo M, Kotani S, Fujita Y, Nakamura T, Yamamuro T, Bando Y, Ohtsuki C, Kokubo T. Differences in ceramics-bone interface between surface-active ceramics and resorbable ceramics: A study by scanning and transmission electron microscopy. Journal of Biomedical Materials Research. 1992;**26**(2):255-267. DOI: 10.1002/jbm.820260210

[7] Neo M, Nakamura Ohtsuki C, Kokubo T, Yamamuro T. Apatite formation on three kinds of bioactive material at an early stage in vivo: A comparative study by transmission electron microscopy. Journal of Biomedical Materials Research. 1993;**27**(8):999-1006. DOI: 10.1002/jbm.820270805

[8] Kokubo T, Ito S, Huang ZT, Hayashi T, Sakka S, Kitsugi T, Yamamuro T. Ca,P-rich layer formed on high-strength bioactive glass-ceramic A-W. Jounal of Biomedical Materials Research. 1990;**24**(3):341-343. DOI: 10.1002/jbm.820240306

[9] Kim HM, Kishimoto K, Miyaji F, Kokubo T, Yao T, Suetsugu Y, Tanaka J, Nakamura T. Composition and structure of the apatite formed on PET substrates in SBF modified with various ionic activity products. Journal of Biomedical Materials Research. 1999;**46**(2):228-235. DOI: 10.1002/(SICI)1097-4636(199908)46:2<228::AID-JBM12>3.0.CO;2-J

[10] Kim HM, Kishimoto K, Miyaji F, Kokubo T, Yao T, Suetsugu Y, Tanaka J, Nakamura T. Composition and structure of apatite formed on organic polymer in simulated body fluid with a high content of carbonate ion. Journal of Materials Science: Materials in Medicine. 2000;**11**(7):421-426. DOI: 10.1023/A:1008935924847

[11] Loty C, Sautier JM, Boulekbache H, Kokubo T, Kim HM, Forest N. In vitro bone formation on a bone-like apatite layer prepared by a biomimetic process on a bioactive glass-ceramic. Journal of Biomedical Materials Research. 2000;**49**(4):423-434. DOI: 10.1002/(SICI)1097-4636(20000315)49:4<423::AID-JBM1>3.0.CO;2-7

[12] Kokubo T, Kushitani H, Sakka S, Kitsugi T, Yamanuro T. Solutions able to reproduce in vivo surface-structure changes in bioactive glass-ceramic A-W. Journal of Biomedical Materials Research. 1990;**24**(6):721-734. DOI: 10.1002/jbm.820240607

[13] Kokubo T, Takadama H. How useful is SBF in predicting in vivo bone bioactivity? Biomaterials. 2006;**27**(15):2907-2915. DOI: 10.1016/j.biomaterials.2006.01.017

[14] ISO 23317. Implants for Surgery—In Vitro Evaluation for Apatite-Forming Ability of Implant Materials. International Organization for Standardization; 2014

[15] Yao T, Hibino M, Yamaguchi S, Okada H. Method for stabilizing calcium phosphate fine particles, process for production of calcium phosphate fine particles by utilizing the method, and use thereof. U.S. Patent. 2012;8178066, Japanese Patent. 2013;5261712

[16] Yao T, Hibino M, Yabutsuka T. Method for Producing Bioactive Composites. U.S. Patent. 2013;8512732, Japanese Patent. 2013;5252399

[17] de Groot K, Geesink RGT, Klein CPAT, Serekian P. Plasma sprayed coatings of hydroxyapatite. Journal of Biomedical Materials Research. 1987;**21**(12):1375-1387. DOI: 10.1002/jbm.820211203

[18] Kokubo T, Yamaguchi S. Novel bioactive materials developed by simulated body fluid evaluation: Surface-modified Ti metal and its alloys. Acta Biomaterialia. 2016;**44**:16-31. DOI: 10.1016/j.actbio.2016.08.013

[19] Kim HM, Miyaji F, Kokubo T, Nakamura T. Preparation of bioactive Ti and its alloys via simple chemical surface treatment. Journal of Biomedical Materials Research. 1996;**32**(3):409-417. DOI: 10.1002/(SICI)1097-4636(199611)32:3<409::AID-JBM14>3.0.CO;2-B

[20] Yabutsuka T, Hibino M, Yao T. Development of bioactive titanium-apatite nuclei composite. Key Engineering Materials. 2007;**361-363**:709-712. DOI: 10.4028/www.scientific.net/KEM.361-363.709

[21] Yabutsuka T, Hibino M, Yao T, Tanaka K, Takemoto M, Neo M, Nakamura T. Fabrication of bioactive apatite nuclei precipitated titanium by using electromagnetic induction heating. Bioceramics Development and Applications. 2011;**1**:D110122. DOI: 10.4303/bda/D110122

[22] Mizuno H, Yabutsuka T, Yao T. Fabrication of bioactive apatite nuclei-precipitated titanium alloys by using sandblasting. Key Engineering Materials. 2012;**529-530**:553-558. DOI: 10.4028/www.scientific.net/KEM.529-530.553

[23] Kidokoro Y, Yabutsuka T, Takai S, Yao T. Bioactivity treatments for zirconium and Ti-6Al-4V alloy by the function of apatite nuclei. Key Engineering Materials. 2017;**720**:175-179. DOI: 10.4028/www.scientific.net/KEM.720.175

[24] Yabutsuka T, Yao T. Fabrication of bioactive apatite nuclei-precipitated composites. Key Engineering Materials. 2012;**493-494**:545-550. DOI: 10.4028/www.scientific.net/KEM.493-494.545

[25] Yabutsuka T, Mizuno H, Karashima R, Yao T. Fabrication of bioactive apatite nuclei precipitated Ti-15Mo-5Zr-3Al alloy by using doubled sandblasting process. Key Engineering Materials. 2015;**631**:231-235. DOI: 10.4028/www.scientific.net/KEM.631.231

[26] Yabutsuka T, Mizutani H, Takai S, Yao T. Fabrication of bioactive cobalt-chromium alloys by incorporation of apatite nuclei. Key Engineering Materials. 2017;**720**:180-184. DOI: 10.4028/www.scientific.net/KEM.720.180

[27] Yabutsuka T, Karashima R, Takai S, Yao T. Fabrication of bioactive stainless steel by the function of apatite nuclei. Key Engineering Materials. 2016;**696**:151-156. DOI: 10.4028/www.scientific.net/KEM.696.151

[28] Yabutsuka T, Karashima R, Takai S, Yao T. Effects of sandblasting conditions in preparation of bioactive stainless steels by the function of apatite nuclei. Phosphorus Research Bulletin. 2016;**31**:15-19. DOI: 10.3363/prb.31.15

[29] Yao T, Yabutsuka T. Material having pores on surface, and method for manufacturing same. Japanese Patent. 2017;6071895

[30] Lacefield WR. Hydroxyapatite coatings. In: Hench LL, editor. An Introduction to Bioceramics. 2nd ed. London: Imperial College Press; 2013. pp. 331-347. DOI: 10.1142/9781908977168_0021

[31] Kim HM, Miyaji F, Kokubo T, Nakamura T. Bonding strength of bonelike apatite layer to Ti metal substrate. Journal of Biomedical Materials Research. 1997;**38**(2):121-127. DOI: 10.1002/(SICI)1097-4636(199722)38:2<121::AID-JBM6>3.0.CO;2-S

[32] Miyazaki T, Kim HM, Kokubo T, Ohtsuki C, Kato H, Nakamura T. Enhancement of bonding strength by graded structure at interface between apatite layer and bioactive tantalum metal. Journal of Materials Science: Materials in Medicine. 2002;**13**(7):651-655. DOI: 10.1023/A:1015729507800

[33] Juhasz JA, Best SM, Kawashita M, Miyata N, Kokubo T, Nakamura T, Bonfield W. Bonding strength of the apatite layer formed on glass-ceramic apatite-wollastonite–polyethylene composites. Journal of Biomedical Materials Research. 2003;**67A**(3):952-959. DOI: 10.1002/jbm.a.10131

[34] Kokubo T. Bioceramics and their Clinical Applications. Cambridge: Woodhead Publishing and CRC Press; 2008

[35] Bonfield W, Grynpas MD, Tully AE, Bowman J, Abram J. Hydroxyapatite reinforced polyethylene—A mechanically compatible implant material for bone replacement. Biomaterials. 1981;**2**(3):185-186. DOI: 10.1016/0142-9612(81)90050-8

[36] Ohtsuki C. Bioactive composite materials. Journal of Adhesion Science of Japan. 2003;**39**(3):125-130

[37] Yabutsuka T, Yamaguchi S, Hibino M, Yao T. Development of bioactive polyethylene-apatite nuclei composite. Key Engineering Materials. 2007;**330-332**:467-470. DOI: 10.4028/www.scientific.net/KEM.330-332.467

[38] Yabutsuka T, Mizono H, Yao T. Fabrication of bioactive apatite nuclei precipitated polylactic acid by using sandblasting process. Key Engineering Materials. 2014;**587**:165-170. DOI: 10.4028/www.scientific.net/KEM.587.165

[39] Fukushima K, Yabutsuka T, Takai S, Yao T. Development of bioactive PEEK by the function of apatite nuclei. Key Engineering Materials. 2016;**696**:145-150. DOI: 10.4028/www.scientific.net/KEM.696.145

[40] Fukushima K, Yabutsuka T, Takai S, Yao T. Investigation of effective procedures in fabrication of bioactive PEEK using the function of apatite nuclei. Phosphorus Research Bulletin. 2016;**31**:31-37. DOI: 10.3363/prb.31.31

[41] Yabutsuka T, Fukushima K, Hiruta T, Takai S, Yao T. Effect of pores formation process and oxygen plasma treatment to hydroxyapatite formation on bioactive PEEK prepared by incorporation of precursor of apatite. Materials Science and Engineering: C. 2017;**81**:349-358. DOI: 10.1016/j.msec.2017.07.017

[42] Yabutsuka T, Fukushima K, Kidokoro Y, Matsunaga T, Takai S, Yao T. Fabrication of bioactive fiber reinforced polyetheretherketone by the function of apatite nuclei. Key Engineering Materials. 2017;**720**:246-251. DOI: 10.4028/www.scientific.net/KEM.720.246

[43] Yabutsuka T, Fukushima K, Kidokoro Y, Matsunaga T, Takai S, Yao T. Fabrication of bioactive glass Fiber reinforced polyamide with high mechanical performance by the function of apatite nuclei. Key Engineering Materials. 2017;**720**:241-245. DOI: 10.4028/www.scientific.net/KEM.720.241

[44] Kurtz SM, Devine JN. PEEK biomaterials in trauma, orthopedic, and spinal implants. Biomaterials. 2007;**28**(32):4845-4869. DOI: 10.1016/j.biomaterials.2007.07.013

[45] Tanahashi M, Yao T, Kokubo T, Minoda M, Miyamoto T, Nakamura T, Yamamuro T. Apatite coated on organic polymers by biomimetic process: Improvement in its adhesion to substrate by glow-discharge treatment. Journal of Biomedical Materials Research. 1995;**29**(3):349-357. DOI: 10.1002/jbm.820290310

[46] Yao T, Yabutsuka T. Biomimetic fabrication of Hydroxyapatite microcapsules by using apatite nuclei. In: Mukherjee A, editor. Biomimetics, Learning from Nature. Vukovar: InTech; 2010. pp. 273-288. DOI: 10.5772/8786

[47] Yao T, Yabutsuka T, Shimada Y, Yamane S. Calcium phosphate microcapsule. PCT Patent. 2012;PCT/JP2012/059689.

[48] Yabutsuka T, Tsuboi S, Hibino S, Yao T. Fabrication of encapsulated Ag microsphere with hydroxyapatite for sustained-release. Key Engineering Materials. 2008;**361-363**:1199-1202. DOI: 10.4028/www.scientific.net/KEM.361-363.1199

[49] Yamane S, Yabutsuka T, Hibino M, Yao T. Fabrication of encapsulated silicagel microsphere with hydroxyapatite for sustained-release. Key Engineering Materials. 2009; **396-398**:519-522. DOI: 10.4028/www.scientific.net/KEM.396-398.519

[50] Yabutsuka T, Yao T. Preparation of encapsulated magnetite microparticles with hydroxyapatite. Energy Procedia. 2011;**9**:532-538. DOI: 10.1016/j.egypro.2011.09.061

[51] Kumazawa S, Hisashuku D, Yabutsuka T, Yao T. Fabrication of magnetic hydroxyapatite microcapsule for protein collection. Key Engineering Materials. 2014;**587**:160-164. DOI: 10.4028/www.scientific.net/KEM.587.160

[52] Yabutsuka T, Kumazawa S, Hisashuku D, Mizutani H, Fukushima K, Takai S, Yao T. Enzyme immobilization by using apatite microcapsules with magnetic properties. Key Engineering Materials. 2016;**696**:259-264. DOI: 10.4028/www.scientific.net/KEM.696.259

[53] Yabutsuka T, Iwahashi K, Nakamura H, Yao T. Fabrication of hydroxyapatite microcapsule containing vitamin B12 for sustained-release. Key Engineering Materials. 2015;**631**:326-331. DOI: 10.4028/www.scientific.net/KEM.631.326

[54] Nakamura H, Sakaguchi M, Yabutsuka T, Takai S, Yao T. The effects of SBF conditions on encapsulation of agarose gel with hydroxyapatite microcapsules. Phosphorus Research Bulletin. 2016;**31**:9-14. DOI: 10.3363/prb.31.9

[55] Matsunaga T, Yabutsuka T, Takai S, Yao T. Fabrication of hydroxyapatite microcapsules for controlled release of hydrophobic drug. Key Engineering Materials. 2017;**720**:12-16. DOI: 10.4028/www.scientific.net/KEM.720.12

[56] Yamane S, Yabutsuka T, Hibino M, Yao T. Fabrication hydroxyapatite microcapsule containing insulin in silicagel microsphere. Bioceramics. 2009;**22**:551-554

Chapter 3

Processing of Ceramic Foams

Xiaojian Mao

Additional information is available at the end of the chapter

http://dx.doi.org/10.5772/intechopen.71006

Abstract

The ceramic foams have great importance in many industry fields. This chapter introduces the processing of ceramic foams by direct foaming technology. The structure of the precursor foams which attributes the final properties of the ceramic foams is described. Two different methods for foaming the ceramic slurry, as well as the techniques for foam consolidation, are presented in detail.

Keywords: ceramic foams, processing, foaming, stabilization, porosity

1. Introduction

Ceramic foams are tough foams made from ceramics, or ceramics with foam-like structure. It is a kind of porous ceramics with high porosity and sometimes called as cellular ceramics. Because of high amount of pores and surface, ceramic foams are especially suitable for filtering molten metals or hot gases, thermal protection systems, and heat exchangers [1].

The basic structural unit of the ceramic foams is composed of solid struts or walls and the empty cells surrounded by them. If the ceramic phase surrounds entire cells so that each cell is isolated from its adjacent ones, it is called as closed cell structure. If all cells are connected to each other with ceramic phase only in cell edges, it is called as open structure. In fact, ceramic foams often appear in a semi-open structure between the two ideal structures. The basic cell unit is the essential difference between the ceramic foams and general porous ceramics, which is actually a solid with isolated pores. And high porosity is its important characteristic. Gibson and Ashby [2] deem that there is a transition from ceramic foams to general porous ceramics with the relative density at about 0.3.

The earliest and still most common method for creating ceramic foams is the polymeric sponge replication method [3], with the products sometimes called as reticulated porous ceramics. In this

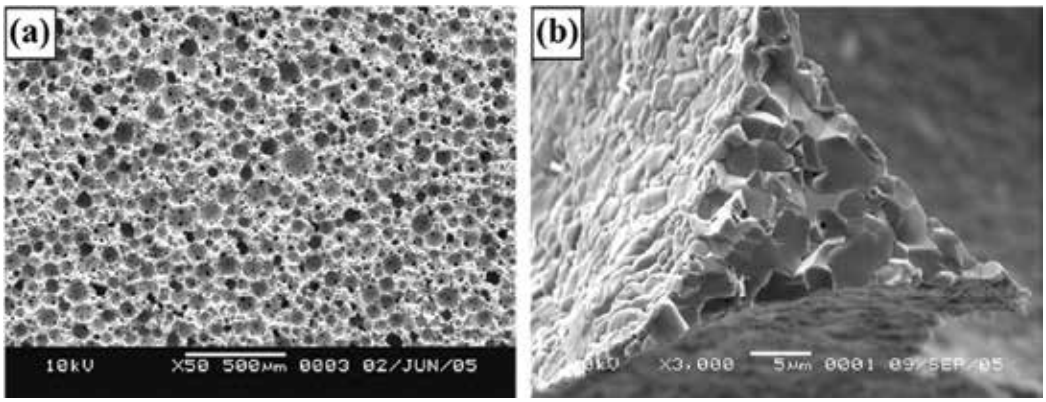

Figure 1. SEM photographs of ceramic foams consisted of (a) spherical cells and windows and (b) dense triangular struts.

method, a polymeric sponge with open pores is immersed into ceramic slurry, and after rolling to remove redundant slurry, the coated sponge is dried and pyrolyzed, leaving only the porous ceramic structure. Then, the resultant foam will be sintered for final densification to get required mechanical strength. This method is widely used because it is effective with most kinds of ceramic materials, such as silicon carbide, zirconia, silicon nitride, alumina, silica, mullite, and cordierite. However, large amount of gaseous by-product is released during pyrolysis, and consequently, leaving triangle hollows inside the ceramic struts. Cracking due to difference in thermal expansion coefficient is easy to occur [4]. Hence, there would be defects in ceramic foams fabricated by such polymeric foam replication technique, which led to lower mechanical strength [5].

Another technique to fabricate ceramic foams is direct foaming method. Ceramic foams are produced by incorporating air into a suspension or liquid media, which is subsequently set in order to keep the structure of air bubbles created. Then, the consolidated foams are afterwards sintered at high temperature to obtain high-strength foams [4]. This method can result in full dense struts without defects by polymeric sponge replication method. Hence, the mechanical strengths of the products are generally higher than those of reticulated porous ceramics. The characteristic of foams by this technique is that most cells are closed or semi-closed, depending on the air bubbles incorporated [6, 7]. **Figure 1(a)** shows the typical morphology of the ceramic foams prepared by the direct foaming method [8], and **Figure 1(b)** is a cross-sectional photograph of the dense struts. This chapter describes the processing of ceramic foams by direct foaming method.

2. Liquid precursor foams

2.1. Structure of foams

A bulk foam is a substance formed by trapping gas air bubbles in liquid or solid. A bath sponge and the top of fresh beer are examples of foams. In most cases, the volume of gas is

large, with thin films of liquid or solid separating the regions of gas. The equilibrium structure of foam is an elegant and well-defined arrangement of films, plateau borders, and junctions. The bubbles which are pressed together to form the foam are separated by thin films. The films meet along a line or curve, forming a liquid-filled interstitial channel called a plateau border. Where several plateau borders meet to form an interconnected network, they do so at a junction [9].

2.2. Liquid foams

Liquid foams are thermodynamically unstable systems due to their high gas-liquid interfacial area. Several physical processes take place in wet foams to decrease the system free energy, leading to foam destabilization. The main destabilization mechanisms are drainage (creaming) and coarsening (Ostwald ripening). Drainage is the physical separation between the gaseous and liquid phases of the foam because of the effect of gravity. In draining foams, light gas bubbles move upwards, forming a denser foam layer on the top, while the heavier liquid phase is concentrated on the bottom, as illustrated in **Figure 2** [4]. Coarsening is the gradual change of the foam structure due to gas diffusion through the films. This diffusion is driven by the pressure differences between bubbles. Small bubbles have high pressure, so they lose gas and disappear. Thus, the average bubble size increases with time.

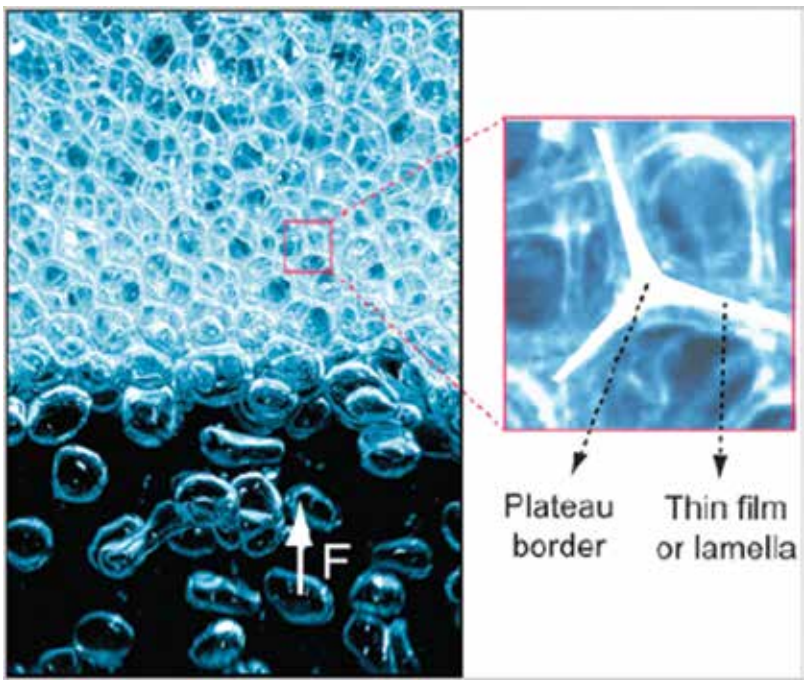

Figure 2. Photograph of foam drainage and foam structure [4].

Generally, real liquid foams are only stable if they contain surfactants. Good foams usually contain complex molecules that toughen the walls of the bubbles. Milk fat, for instance, serves this purpose in whipped cream. The way the bubbles stick together or slip past one another determines how the foam behaves.

2.3. Particle-stabilized wet foams

Solid particles with tailored surface chemistry have lately been shown to efficiently stabilize gas bubbles upon adsorption at the air-water interface. The attachment of particles at gas-liquid interfaces occurs when particles are not completely wet in the liquid phase or, in other words, are partially lyophobic (hydrophobic if the liquid is water). The position of the particles at the interface is ultimately determined by a balance between the gas-liquid, gas-solid, and solid-liquid interfacial tensions, as shown in **Figure 3** [10]. A simple way to describe the particle position at the interface is through the contact angle formed at equilibrium through the liquid phase. Slightly lyophobic particles remain predominantly in the liquid phase and exhibit a contact angle <90°, leading to the formation of air in water mixture, that is, foams [4].

In this method, the amphiphiles added to the suspension let the particles partially hydrophobic by adsorbing with its polar anchoring group on the surface and leaving a short hydrophobic tail in contact with the aqueous phase. Studart et al. [4] summarized some amphiphilic compounds, such as valeric acid, propyl gallate, butyl gallate, and hexyl amine, for surface modification for different particles. After surface modification, air can be easily incorporated by mechanical whipping, injection of gas stream, or initiation of a chemical reaction that releases gaseous by-products directly into the initially fluid suspension.

However, the particle-stabilized wet foams are not strong enough to resist the stress during drying. Hence, they still need to be strengthened before water evaporation, either by coagulating the particles within the foam films or by chemically gelling the foam liquid phase [11].

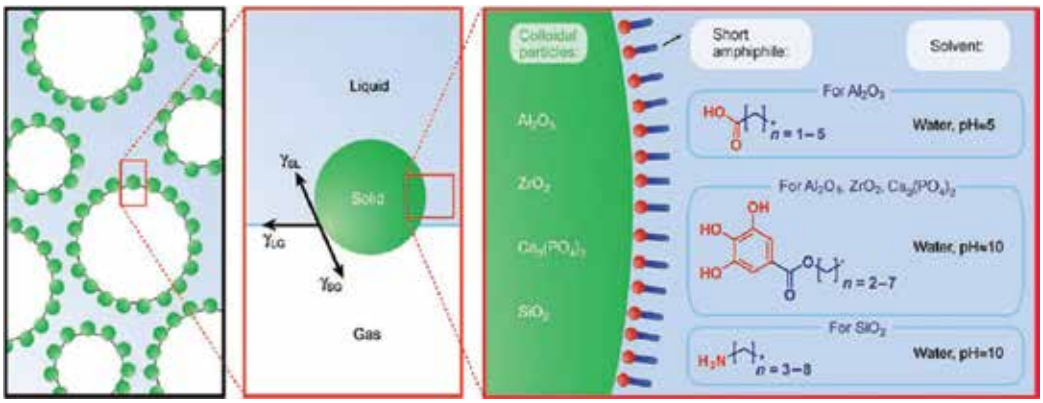

Figure 3. Diagrammatic sketch of the particle-stabilized foams [10].

http://dx.doi.org/10.5772/intechopen.71006

2.4. Foams of ceramic slurry

In order to manufacture ceramic foams, the liquid foams have to contain abundant ceramic particles in the liquid phase, which are going to be sintered as the main component of the corresponding ceramic foams. **Figure 4** shows the diagram of the related structures for precursor foams and the resulting ceramic foams. The bubbles, which occupy the most volume of liquid foams, turn into cells of the ceramic foams. The films, which comprise liquid and ceramic particles, transform into the cell walls. Generally, the central part of the films is too thin to keep intact during sintering. Hence, there are commonly windows in the cell walls between two neighbor cells. This kind of common constitution is called as semi-open structure. If the films are extremely thin or the solid contents are too low, only plateau border is survived after sintering corresponds to the struts between three or more cells. That generates the strict open pore structure.

Generally, the solid content influences the rheology of ceramic suspension. High solid content contributes to high viscosity and shear thin behavior. And the solid content would also associate with the final structure of the ceramic foams. Consequently, it is a practical way to adjust the porosity and structure of ceramic foams by controlling the solid content of the original suspension. Mao et al. [12] manufactured alumina foams with different morphology by changing the solid content using direct foaming and gelcasting method. **Figure 5** shows the rheological flow curves of suspensions with different solid contents. All suspensions reveal pseudoplastic behavior, and the viscosity increases with solid content at the measured shear rate range. In the fabrication of ceramic foams, a slight pseudoplasticity could favor the generation of foams since lower viscosities are obtained under high speed whipping, and the foam stability would be improved because the viscosity recovery under static condition delays the collapse of fluid films around the bubbles.

The relative density of final alumina foams increases with the solid loading, while other processing conditions are constant, as indicated in **Figure 6**. The reason is that high solid content results in high viscosity, corresponding to low foaming capacity and high relative density. It

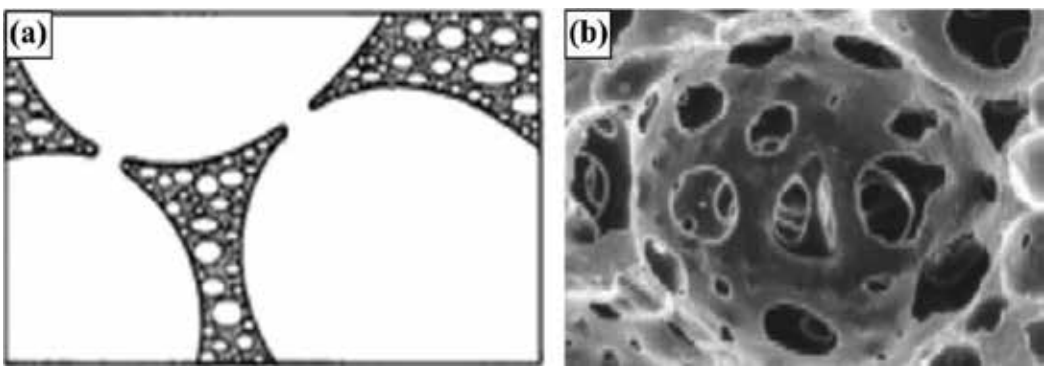

Figure 4. Structural diagram of (a) precursor foams and (b) the sintered ceramic foams.

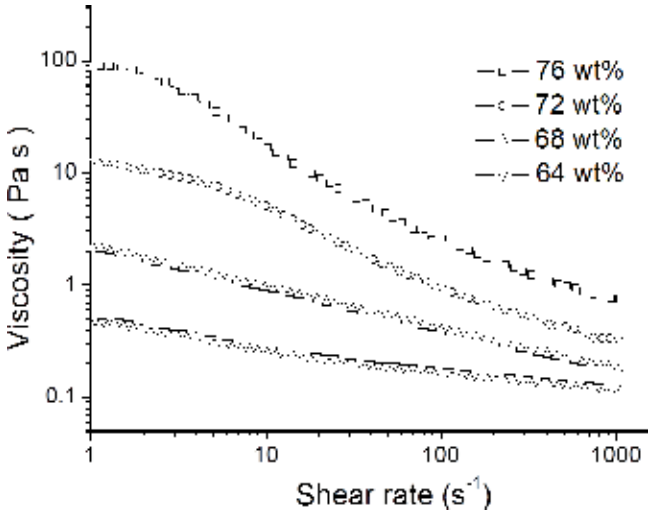

Figure 5. Rheological flow curves of suspensions with different solid contents [12].

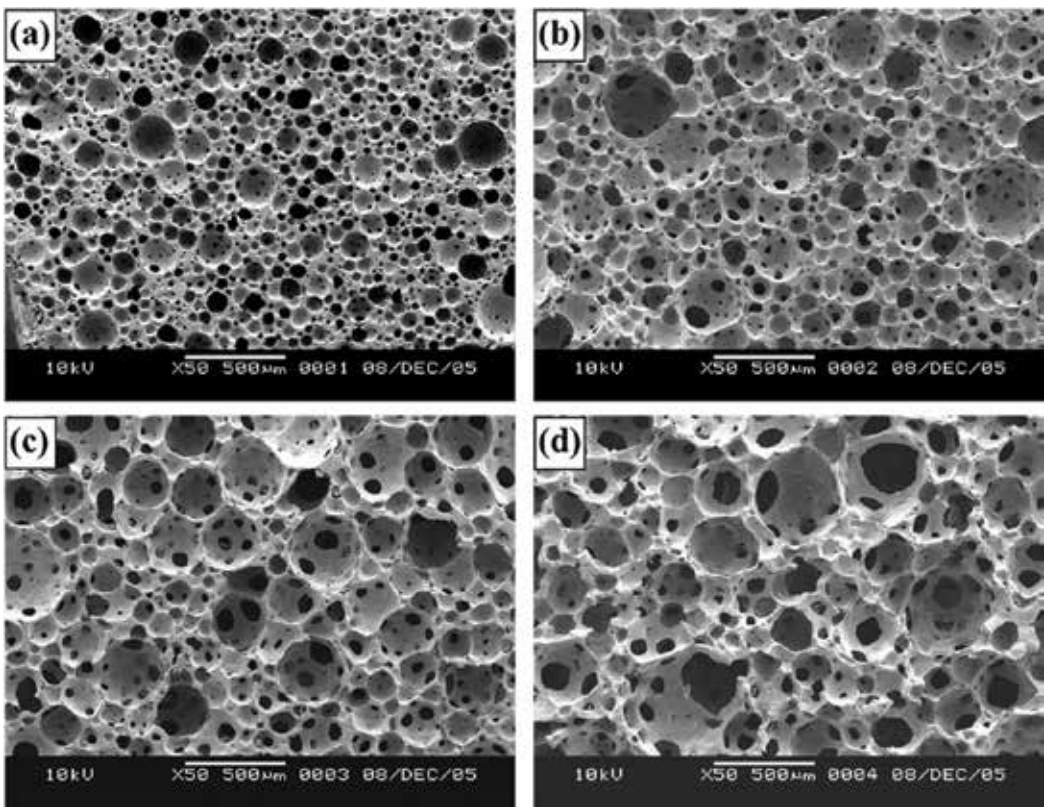

Figure 6. SEM micrographs of alumina foams with suspension solid content of (a) 76 wt%, (b) 72 wt%, (c) 68 wt%, and (d) 60 wt% [12].

can also be seen from **Figure 6** that with the decrease of the relative density, both the mean cell size and the window size are increased.

In order to evaluate the influence of the size of ceramic particles, Mao et al. [13] introduced granule particles into the original powders to manufacture the alumina foams. The coarse powder was manufactured by grinding the presintered foams obtained by the fine powder, in order to keep similar sintering ability to fine powder. The flexural strength of the sintered foams with the coarse powder is 25% lower than that by original powder. And the permeability of foams using the coarse powder is about 30% higher than that by original powder. The drop of flexural strength and the rise of permeability are related to high degree of open pores.

3. Foaming techniques

Foams and foaming phenomena are common and important in our daily lives. While putting some shaving cream or soap on our faces, and rub gradually, we will create a truly bizarre substance, which are most gas and little bit of liquid. When we whisk air into egg white or cream, bubbles form and linger because the proteins present in these viscous liquids stretch around bubbles and trap them. The foams spout out from the compressed bottle, when we style our hair with mousse.

All these techniques would be applied in the manufacture of ceramic foams. The foaming of ceramic slurries involves dispersing gas in the form of bubbles into ceramic suspension. There are two basic approaches for achieving this: (1) incorporating an external gas by mechanical frothing, or injection of a gas stream and (2) evolution of a gas in situ [14]. In order to stabilize the bubbles developed within the slurry, the surface tension of the gas-liquid interface need to be reduced by, in most cases, adding surfactant or by sometimes partially hydrophobic particles. In some cases, water-soluble polymers are added into the slurry to modify the viscosity, which will affect the foaming results and the stability.

3.1. Incorporation of an external gas phase

One of the ways foam is created is through dispersion, where a large amount of gas is mixed with a liquid. Mechanical stirring is the most common technique for gas dispersion. Electric beater or household whisk is convenient choice for foaming of ceramic slurries [15]. The whisking procedure involves incorporating with air-forming bubbles, and at the same time, the bubbles flow up and break because of drainage and coalescence. Hence, generally, surfactant is necessary to reduce the surface tension to stabilize the bubbles. When the speed of bubble generation and burst become equilibrium, the maximum volume of the foam is obtained.

Figure 7 shows the foam volume versus stirring time for alumina suspensions containing two different foaming agents, Triton X114 and Tween 80 [16]. The foam volume increases gradually up to a maximum after approximately 4 min of agitation. During this initial stirring period, gas is entrained into the suspensions and liquid is drawn around each bubble until a thin film is formed. Subsequently, the surfactant molecules of the foaming agent transfer from

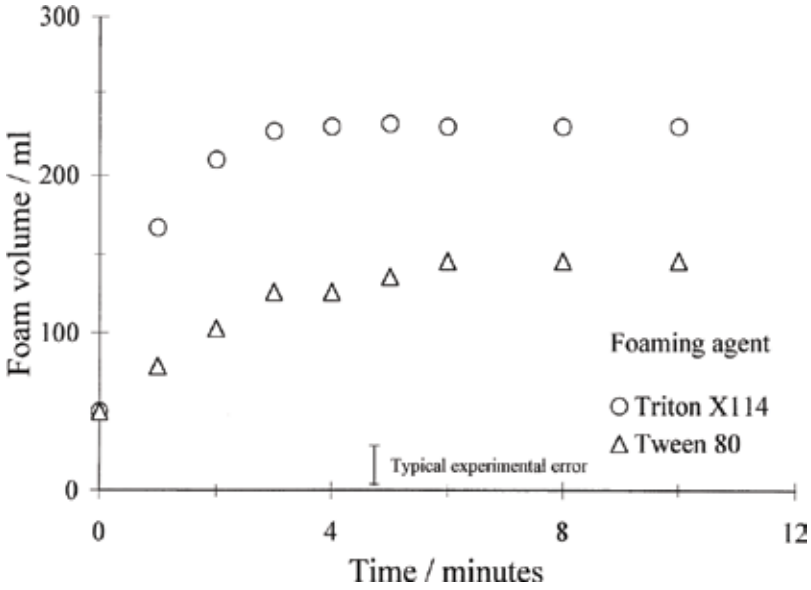

Figure 7. Foam volume generated with two different foaming agents [16].

interior of the suspension toward the newly created surface, decreasing the surface tension. Increasing the surfactant concentration accelerates this transfer and hence increases the foaming capacity [17]. Sepulveda considers that the maximum foam volume is associated with a minimum thickness of film that can sustain a stable foam. When most surfactant molecules have attached themselves to the gas-liquid interface, the stabilization of new films is no longer possible and the volume increase becomes negligible.

3.2. In situ gas evolution

The foaming technology of this theme is the presence of a foaming agent that decomposes due to heat or a chemical reaction to generate a gas within a ceramic suspension. Kim [18, 19] used the mixture of the cross-linked polycarbosilane and polysiloxane as the preceramic polymers to manufacture the SiOC foams, which were pressed into disks and CIPed at 340 MPa. The green compacts were placed in a pressure chamber to saturate with gaseous CO_2 under a pressure of 5.5 MPa. Then, a thermal dynamic instability was introduced by rapidly dropping the pressure at a rate of 2.9 MPa/s. The foamed preceramic specimens were further cross-linked, then pyrolyzed, and sintered at 1200°C in nitrogen. Takahashi et al. [20] used the blend of methylsilicone resin and polyurethane precursor to prepare the SiOC foams. The foamed blend was prepared in two steps. The first step was the addition of methylsilicone resin dissolved in CH_2Cl_2 to the mixture of the polyols, the amine catalysts, the surfactant, and the additional dichloromethane. The second step was the addition of polyisocyanate to the solution obtained in the first step. The expansion started during mechanical stirring by the evaporation of the solvent caused by the exothermal reactions occurring in the solution.

4. Foam consolidation

In direct foaming method, ceramic foams are prepared by introducing large amounts of air bubbles into the slurry. The foam is essentially a metastable system, with some bubbles shrinking and others gathering. It is important to consolidate the foams in certain period, to keep the cellular structure during further heating procedure [21]. In order to prevent the foams from drainage or coarsening, it is necessary to accelerate the consolidation speed and obtain a higher strength. Suitable consolidation method would bring uniform and dense struts, which is a benefit for mechanical properties of the resulting ceramic foams.

4.1. Freezing

Freezing method is one of the practical methods to consolidate the foamed slurry [22]. Verma et al. [23] manufactured silica foams with 85 vol% porosity content from ceramic slurries containing ovalbumin as binder along with additives of sucrose and colloidal silica by combination of direct foaming and freeze-casting routes. The foamed slurries were poured into vaseline-coated aluminum molds and cooled using liquid nitrogen for instant freezing of porous structure. The frozen samples were freeze-dried at a low temperature for 24 h. After drying, the dried foam was heated to 1150°C to remove the binder and sinter the pore walls. The advantage of the freezing method is that extra consolidation agent is unnecessary. However, during freezing procedure, the liquid solvent, for example, water, will transfer to solid crystals which entrapped between the agglomerated ceramic particles at the films. These crystals will leave micropores after the evaporation of solvent. Rapid freezing of the solvent leads to formation of fine ice crystals, while long-time freezing procedure would enlarge the size of the crystals. The corresponding large pores may not be removed during sintering and, hence, lead to lower mechanical strength. The freezing time has to be prolonged to cool down the temperature of inside parts for large-sized bulk foams since the foamed slurry is a thermal insulator, which indicates that the frozen crystals will grow during consolidation of large-scale products. Thus, the freezing technique might not be good for high-strength foam production.

4.2. Natural polymer denaturation

Some natural polymers from animal and plant sources have the properties of liquid-solid transition due to denaturation which has potential applications in the consolidation of foamed slurries. Protein and polysaccharide including starch, agar, and cellulose are often used to manufacture ceramic foams and porous ceramics [23–25]. Proteins are high molecular compounds, which are formally understood as condensation products of amino acids. The amphiphilic character of these molecules causes a decrease of surface tension, therefore good foaming properties. These foaming properties are influenced by the amino acid sequence or rather the number of polar and apolar side chains as well as molecule flexibility [26]. After foaming, the foamed slurries are consolidated by changing conditions, for example, adding acid or heating over 60°C, which would trigger the irreversible changes in the spatial structure of the protein molecule.

Garrn et al. [26] used albumin, a major constituent of blood, as a model binder to an aqueous powder suspension to produce ceramic foams. Foaming was done in a planetary mill using PE-milling pots for 15 min. A fine cellular foam structure with approximate diameter of 50–300 μm was formed. Thermal consolidation was done in a conventional household microwave oven with a maximum microwave power of 900 W. After burn out and sintering, final densities in the range from 8 to 20% were achieved. Fish collagen and egg white [27, 28] are other specific examples of protein applied for ceramic foams. They were added into ceramic slurries which would be stirred to become foams. The foamed slurries were then heated at 80°C or higher for consolidation, attributing to the gelation of protein.

Methylcellulose and polysaccharide, which have similar transformation as protein in case of heating, are also typical agents for consolidation of foamed ceramic slurries. Mao et al. [17] manufactured silica foams based on the generation of foams from composite slurries with cassava starch. These slurries combined with surfactant were vigorously whisked for about 5 min to make foam structure. The as-foamed slurries were then preheated in a microwave oven with a power of 400 W for 60 s, followed by setting in a 70°C oven for 30 min to consolidate the foam structure. After sintering, the resulting silica foams with the relative density of 18–30% were obtained. Because the cassava starch is not soluble in water, the particles will residual pores inside cell walls and struts after debindering and sintering. Hence, the direct foaming and starch consolidation method can produce porous ceramics with hierarchical structures, as shown in **Figure 8**. **Figure 8(a)** shows clearly the spherical cells with the average size of about 50 μm, while **Figure 8(b)** reveals the pores averaging about 10 μm in the cell walls. **Figure 8(c)** further indicates small voids inside ceramic matrix. It can be inferred that the large-sized cells, moderate-sized pores, and small-sized voids were originated from bubbles, elimination of starch particles, and interstices among the silica grains, respectively.

These natural polymers which can be operated in laboratory environment, for example, simply heated at 50–80°C, are excellent agents for ceramic foams. They are environmentally friendly and low cost and, hence, are widely used. However, the consolidation procedure needs heating of the foamed slurries, which would lead to the expansion of air bubbles. The metastable structure would change during the temperature change, which should remain some defects in final ceramic foams.

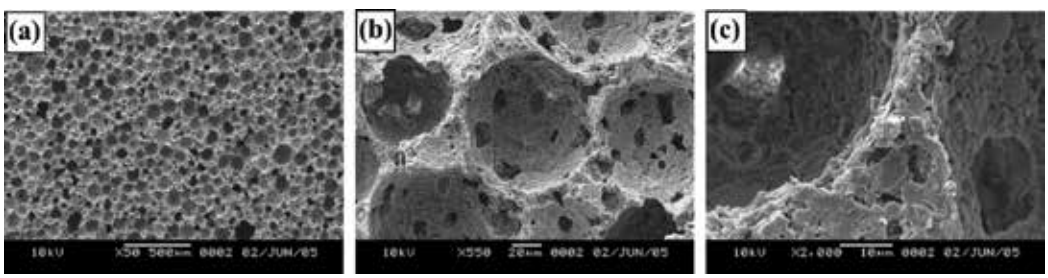

Figure 8. SEM micrographs of sintered ceramics with details of (a) large-sized cells, (b) moderate-sized pores in cell wall, and (c) small-sized voids among silica grains [17].

4.3. Gelcasting

In recent years, the gelcasting method was developed to manufacture ceramic foams by solving the shortcomings of the mentioned natural polymer substances which need heating for denaturation. The water-soluble small molecule compounds are added into the slurries, which will form a gel through radical polymerization. The method was first proposed by Smith [29], which combines the foaming and gelcasting processes, resulting in wet foams with high strength for drying and further handling. Sepulveda and Binner have done a lot of work on the gelcasting of foams, which has been shown to be useful in a variety of ceramic systems such as zirconia, alumina, and hydroxyapatite [30]. The benefit compared with using polymers is the ability to formulate slurries with a lower viscosity, because the size of the organic molecule is smaller, so that higher solid contents can be achieved with good packing densities and excellent green strengths [31]. Such a process yields cellular structures with porosity varying from 40% to >90%, with pores closed or open depending on pore fraction. Mechanical strength of sintered foams is higher than that obtained by other routes, because of the spherical pore shape associated with fully dense matrix [15].

Figure 9 shows the flow chart for production of ceramic foams by gelcasting of foams. Ceramic slurries with monomers and surfactants are vigorously whisked under inert gas atmosphere to form foams. Afterwards, catalyst and initiator are added to trigger the polymerization reaction, forming a strong three-dimensional gel net. The concentration of these reagents is designed to produce an induction period such that polymerization will be initiated immediately after casting. Within the time allowed by the induction period, the foams could be placed in a desiccator with the pressure reduced using a vacuum pump to produce foams with cell size larger than those obtained directly through foaming [16]. The excellent green body strength is the main advantage of the gelcasting of ceramic foams, which may maintain a porous structure with the porosity up to 90%, compared with other consolidation methods. The investigation to the sintered foams confirms that the solid matrix has very high density, which is much perfect than those by polymeric sponge replication method. Sepulveda produced alumina foams with the bending strength in the range of 2–26 MPa, while their relative density varied in 8–30% [30].

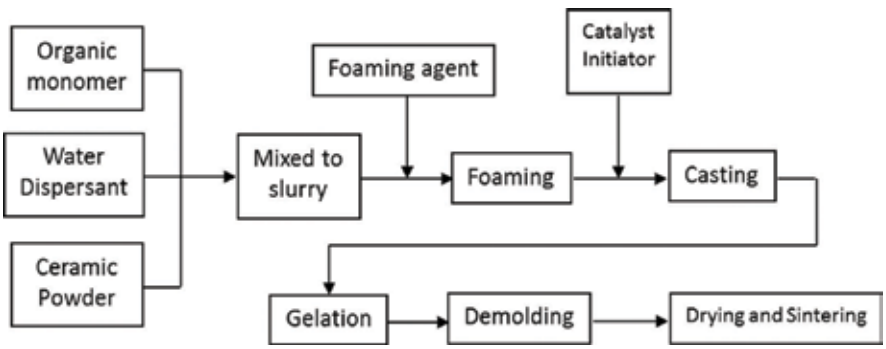

Figure 9. Flow chart for production of ceramic foams by gelcasting of foams.

However, the usual monomers are acrylamide derivatives, and the polymerization is a free radical reaction which is inhibited by oxygen. For example, just 0.2% oxygen was sufficient to inhibit the reaction completely in foamed suspensions [30]. Thus, the foaming and polymerization procedures have to be carried out in a N_2-filled chamber to insulate oxygen.

Mao et al. [32] developed a novel gelcasting system based on epoxy resin and polyamine hardener, which could be operated in air atmosphere, because the polymerization between the epoxide group of the epoxy resin and active hydrogen of amine is a nucleophilic addition reaction which is not affected by oxygen in atmosphere. This gelcasting system was then applied to manufacture ceramic foams with some modification [12]. Aqueous suspensions with solids loading of 60–76 wt% were prepared by mixing alumina powder, dispersant, and 5 wt% polyethyleneimine solution. Vigorous stirring about 5 min was applied after adding the surfactant to generate foams. For setting the fluid foams, 10 wt% sorbitol polyglycidyl ether based on the premix solution was added with further stirring about 30 s. The foamed suspensions were immediately poured into plastic molds and sealed at room temperature for gelation.

Yang et al. reported a novel single-component water-soluble copolymer of isobutylene and maleic anhydride, with a commercial name of Isobam, which could be used as both surfactant and gelling agent with the addition much lower than normal gelation systems [33]. Yang et al. developed this system for the consolidation of ceramic foams. A small addition of 0.3 wt% Isobam based on alumina powder is sufficient to consolidate liquid foams and maintain the wet foams for further treatments [34]. Small additive amount is benefit for further heat treatment because the exhaust gaseous by-product can be dramatically reduced. It was confirmed that Isobam could be applied to manufacture variety of ceramic materials, such as mullite and $Yb_3Al_5O_{12}$ [35].

4.4. Sol-gel

Sol-gel method has been widely used in the preparation of powder, film, and bulk materials. Since the processing of sol-gel is actually a liquid-solid transformation, it can be used to consolidate the liquid foams without any other additive. The advantage of this route is that no contamination is involved, which is suitable for producing high-purity ceramic foams. Silica foams and silica-contained ceramic foams have been manufactured [36–38]. Commercial SiO_2 sol or the hydrolyzate of the precursor tetraethoxysilane was modified by adding acid to the pH value in the range of 5–6. After adding surfactant, the sol is incorporated with air by mechanical stirring or in situ gas evolution. Then, the foamed sol will be gradually consolidated with the sol transfer to gel. The porosity and the pore size distribution may be controlled by changing the viscosity and foaming technology. The silica-based sol-gel system has been used in many ceramic foams, such as silica, boehmite, and zirconia [21]. Pereira et al. [37] manufactured bioactive glass and hybrid scaffolds for bone tissue engineering by sol-gel method. TEOS and calcium chloride were used as the silica and calcium precursors, respectively. The starting sol was prepared by hydrolysis of TEOS in the presence of 1 N hydrochloric acid solution with subsequent addition of calcium chloride. PVA solution, Teepol surfactant, and 5 vol% hydrofluoric acid solution were added to a 40-ml aliquot of the

sol, and the mixture was foamed by vigorous agitation. HF was added in order to catalyze the gelation. The foamed gels were cast, aged at 40°C for 72 h, and dried at 40°C for 120 h. Final glass and hybrid foams can be obtained with a high porosity varying from 60 to 95% and macropore diameters ranging from 10 to 600 μm.

5. Drying and sintering

The consolidated wet foams are a mixture of gas, liquid, and solid, which need to be dried and debindered before sintering to final ceramic foams. Since there are large amount of bubbles dispersed in the bodies, the green strength is much lower than that of normal ceramics. Hence, both drying and debindering procedures should be carried out carefully. However, the bubbles, especially the connected bubbles, would become channels for water, solvent, or pyrolyzate to escape. Generally, the drying and calcination speed should be slowed down to avoid possible crack.

The foamed green bodies need to be sintered to get sufficient strength for further applications. It is important to modify the sintering schedules to get dense and strong struts and cell walls, to increase the mechanical properties of the ceramic foams. The sintering for ceramic foams is not get equivalent research intension as for foaming and consolidation, since the sintering behavior is dominantly decided by the powders. Especially for the particles inside the struts and the cell walls, the coordination particles are same within normal ceramics. However, for those particle located on the surface of cell walls or in the tip of the strut edges, their coordination particles are less than in dense green bodies. **Figure 10** shows the SEM microstructures of the fracture surface of the struts and the edge of the cell window. We can see clearly that grain size inside the struts is larger than that near the cell wall surface. And the gran size becomes much smaller when the location shifts to the tip of the triangle. The ceramic sintering theory seems not simply suitable to describe the ceramic foams. The difference for grain size

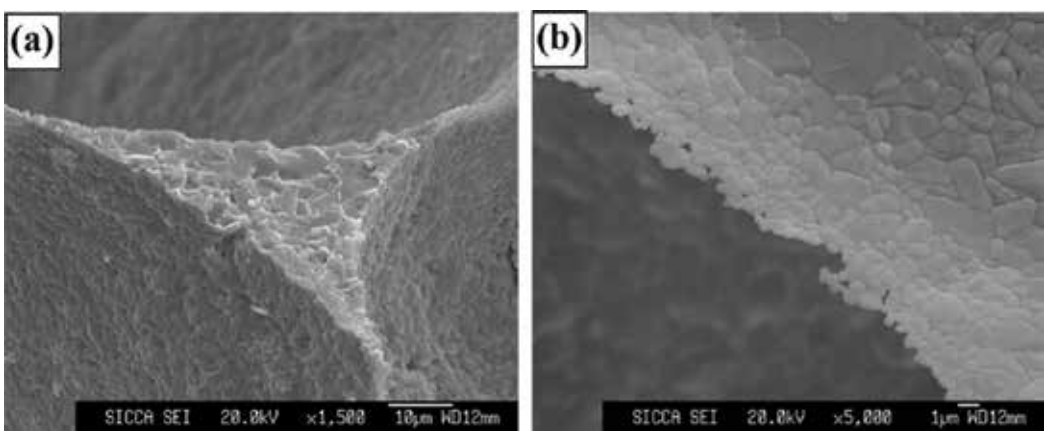

Figure 10. Microstructure of alumina foams: (a) fracture surface of the struts and (b) edge of the cell window.

is related to the particle coordination, where large coordination number corresponds to large grain size. The possible reason is that more coordination particles indicate abundant mass resource for grain growth.

6. Summary

Due to its current and potential great application, ceramic foams attracted distinct attentions in past decades with new process routs constantly being developed and reported in the scientific literature and at conferences. As a kind of porous ceramic with special structure, the ceramic foams gradually play irreplaceable roles in many industry fields, such as diesel particulate filters, interpenetrating composites, high-temperature thermal insulators, and biomedical applications. It is very important and valuable to explore novel manufacture routes and continuously improve the performance of ceramic foams. Whereas the polymer replication process is advanced to be in commercial use for decades, now the slurry foaming techniques are developed rapidly, which yields ceramic foams with different morphologies, and hence different properties and potential applications. This provides much greater choice for the end user and far greater potential for the tailoring of structures to meet specific end-sue requirement.

Acknowledgements

The author would like to acknowledge Prof. Shiwei Wang, Shunzo Shimai, and Dr. JinZhao for their work contributed to this chapter.

Author details

Xiaojian Mao

Address all correspondence to: xmao@siom.ac.cn

Key Lab of Transparent Opto-Functional Inorganic Materials, Shanghai Institute of Ceramics, Chinese Academy of Sciences, Shanghai, China

References

[1] Available from: http://www.cenlon.net/article_image.php?cid=13&id=4

[2] Gibson LJ, Ashby MF, editors. Cellular Solids Structure and Properties. 2nd ed. UK: Cambridge University Press; 1997. 2-6 p

[3] Schwartzwalder K, Somers AV. Method of Making Porous Ceramic Articles. US Pat. 1963; (No. 3090094)

[4] Studart AR, Gonzenbach UT, Tervoort E, Gauckler LJ. Processing routes to macroporous ceramics: A review. Journal of the American Ceramic Society. 2006;**89**(6):1771-1789. DOI: 10.1111/j.1551-2916.2006.01044.x

[5] Oliveira FAC, Dias S, Vaz MF, et al. Behavior of open-cell cordierite foams under compression. Journal of the European Ceramic Society. 2006;**26**:179-186

[6] Jiang PQ, Li SZ. Fabrication of high porosity ceramic material. Advances in Ceramics. 2003;**2**:37-40

[7] Ashish P, Dong NS, Seung TL, Ik JK. Processing of porous ceramics by direct foaming: A review. Journal of the Korean Ceramic Society. 2013;**50**(2):93-102

[8] Mao XJ, Wang SW. Method for porous ceramics with high porosity. CN Patent. 2005; (200510027545.2)

[9] Weaire D, Cox S, Brakke K. Liquid foams-precursors for solid foams. In: Scheffler M, Colombo P, editors. Cellular Ceramics: Structure, Manufacturing, Properties and Applications. Weinheim: Wiley-VCH; 2005. p. 21

[10] Gonzenbach UT, Studart AR, Tervoort E, Gauckler LJ. Ultrastable particle-stabilized foams. Angewandte Chemie International Edition. 2006;**45**(21):3526-3530. DOI: 10.1002/anie.200503676

[11] Gonzenbach UT, Studart AR, Tervoort E, Gauckler LJ. Macroporous ceramics from particle stabilized wet foams. Journal of the American Ceramic Society. 2007;**90**(1):16-22. DOI: 10.1111/j.1551-2916.2006.01328.x

[12] Mao X, Shimai SZ, Wang S. Gelcasting of alumina foams consolidated by epoxy resin. Journal of the European Ceramic Society. 2007;**28**(1):217-222

[13] Mao X, Shimai SZ, Wang S. Effects of coarse particles on the gelcasting of ceramic foams. Journal of the American Ceramic Society. 2008;**91**(7):2412-2414. DOI: 10.1111/j.1551-2916.2008.02451.x

[14] Binner J. Ceramic foams. In: Scheffler M, Colombo P, editors. Cellular Ceramics: Structure, manufacture, Properties and Applications. 1st ed. Weinheim: Wiley-VCH; 2005. p. 42

[15] Sepulveda P, Ortega FS, Innocentini MDM, Pandolfelli VC. Properties of highly porous hydroxyapatite obtained by the gelcasting of foams. Journal of the American Ceramic Society. 2000;**83**(12):3021-3024. DOI: 10.1111/j.1151-2916.2000.tb01677.x

[16] Sepulveda P, Binner JGP. Processing of cellular ceramics by foaming and in situ polymerisation of organic monomers. Journal of the European Ceramic Society. 1999;**19**(12):2059-2066. DOI: 10.1016/S0955-2219(99)00024-2

[17] Mao X, Wang S, Shimai SZ. Porous ceramics with tri-modal pores prepared by foaming and starch consolidation. Ceramics International. 2008;**34**:107-112

[18] Kim YW, Kim SH. Fabrication of microceramic foams using gaseous carbon dioxide. Journal of the American Ceramic Society. 2003;**86**(12):2231-2233

[19] Kim YW, Kim SH. Processing of closed-cell silicon oxycarbide foams from a preceramic polymer. Journal of Materials Science. 2004;**39**:5647-5652

[20] Takahashi T, Munsted H, Modesti M, Colombo P. Oxidation resistant ceramic foams from a silicone preceramic polymer/polyurethane blend. Journal of the European Ceramic Society. 2001;**21**(16):2821-2828

[21] Sepulveda P. Gelcasting foams for porous ceramics. American Ceramic Society Bulletin. 1997;**76**(10):61-65

[22] Carn F, Colin A. Rational design of marcocellular silica scaffolds obtained by a tunable sol-gel foaming processing. Advanced Materials. 2004;**16**(2):140-144

[23] Verma J, Vijayakumar M, Mitra R. Processing and microstructure of freeze-cast silica foams. Materials Letters. 2015;**153**:168-170. DOI: 10.1016/j.matlet.2015.04.019

[24] Dhara S, Pradhan M, Ghosh D, et al. Nature inspired novel processing routes for ceramic foams. Advances in Applied Ceramics. 2005;**104**(1):9-21

[25] Cyster LA, Grant DM, Howdle SM. The influence of dispersant concentration on the pore morphology of hydroxyapatite ceramics for bone tissue engineering. Biomaterials. 2005;**26**:697-702

[26] Garrn I, Reetz C, Brandes N, et al. Clot-forming: The use of proteins as binders for producing ceramic foams. Journal of the European Ceramic Society. 2004;**24**:579-587

[27] Yin LY, Zhou XG, JS Y, Wang HL, Zhao S, Luo Z, et al. Preparation of Si3N4 ceramic foams by simultaneously using egg white protein and fish collagen. Ceramics International. 2013;**39**(1):445-448

[28] Tuck C, Evans JRG. Porous ceramics prepared from aqueous foams. Journal of Materials Science Letters. 1999;**18**:1003-1005

[29] Smith R. Processing of Engineering Porous Ceramics [thesis]. UK: Nottingham Univ; 1994

[30] Sepulveda P, Binner JGP. Evaluation of the in situ polymerization kinetics for the gelcasting of ceramic foams. Chemistry of Materials. 2001;**13**:3882-3887

[31] Binner J. Ceramic foams. In: Scheffler M, Colombo P, editors. Cellular Ceramics: Structure, manufacture, Properties and Applications. 1st ed. Weinheim: Wiley-VCH; 2005. p. 50

[32] Mao XJ, Shimai SZ, Dong MJ, Wang SW. Gelcasting of alumina using epoxy resin as a gelling agent. Journal of the American Ceramic Society. 2007;**90**(3):986-988

[33] Yang Y, Shimai SZ, Wang SW. Room temperature gelcasting of alumina with a water-soluble co-polymer. Journal of Materials Research. 2013;**28**(11):1512-1516. DOI: 10.1557/jmr.2013.132

[34] Yang Y, Shimai SZ, Sun Y, Dong MJ. Fabrication of porous Al_2O_3 ceramics by rapid gelation and mechanical foaming. Journal of Materials Research. 2013;**28**(15):2012-2016. DOI: 10.1557/jmr.2013.170

[35] Wang X, Xiang H, Wang G, Zhou Y. A green fabrication strategy for porous $Yb_3Al_5O_{12}$ ceramics with high strength and tunable gas permeability. Journal of Materials Research. 2016;**31**(19):3078-3087. DOI: 10.1557/jmr.2016.319

[36] Tomita T, Kawasaki S. A novel preparation method for foamed silica ceramics by sol-gel reaction and mechanical foaming. Journal of Porous Materials. 2004;**11**:107-115

[37] Pereira MM, Ions JR, Hench LL. Bioactive glass and hybrid scaffolds prepared by sol-gel method for bone tissue engineering. Advances in Applied Ceramics. 2005;**104**(1):35-42

[38] Fujiu T, Messing G, Huebner W. Processing and properties of cellular silica synthesized by foaming sol-gels. Journal of the American Ceramic Society. 1990;**73**(1):85-90

Chapter 4

Porous Ceramic Sensors: Hydrocarbon Gas Leaks Detection

Yibran A. Perera-Mercado,
Griselda Castruita-de Leon and
Geanette Polanco Piñerez

Additional information is available at the end of the chapter

http://dx.doi.org/10.5772/intechopen.72315

Abstract

According to the American National Standards Institute (ANSI), a sensor is a device which provides a usable output in response to a specified measurement of a physical quantity converted into a signal suitable for processing (e.g., optical, electrical, or mechanical signals). On the other hand, porous ceramic materials play an important role as sensor materials, because by selecting a suitable base ceramic material for the intended use and then adjusting their overall porosity, pore size distribution, and pore shape, they can cover different applications such as liquid-gas filters, insulators, catalytic supports, mixed of gases separators and sensors, among others. In addition, they have controlled permeability, high melting point, high superficial area, high corrosion and wear resistance, low expansion coefficient, tailored electronic properties, etc. Currently, a few niche areas demand sensors for compact electronic device design, e.g., leak inspections for oil and gas dispositive, flammable and/or toxic gas detection in waste storage areas and confined spaces, hydrocarbons and their associated gas detection at low temperatures and high humidity conditions, among others. In this chapter, the advances in porous ceramic production for hydrocarbons and associated gas detection will be presented and discussed.

Keywords: porous ceramic materials, sensors, hydrocarbons, mesoporosity, microporosity, macroporosity, nanomaterials, hydrocarbon leaks

1. Introduction

Sensors are key elements in the rapidly evolving fields of instrumentations, measurements, and automated systems. Different functions and materials have been investigated, and several devices have been put on the market or have become part of sophisticated instrumentations.

Among these materials, porous ceramics have played an important role because of their intrinsic physicochemical properties. They have also been widely used to satisfy diverse needs for sensing devices, and consistent results have been obtained in the field of atmospheric sensors, i.e., temperature, humidity, and presence of hydrocarbon gases sensors. In addition, the management of risk in oil and gas industrial installations is a priority task, especially when exploration and exploitation activities of the petroleum and gas sector in remote places and fragile environments are increasing rapidly. In particular, due to the nature of the working fluids in the oil industry, the risks associated to plant operations are considered as a high-risk activity. The risk management activity begins at the study and understanding of the hazards involved in a particular industrial activity, in order to establish security zones and secure procedures to be followed.

On the other hand, the current tendency of porous ceramic materials used in hydrocarbon leaks detection is shown in **Figure 1a**. The technological advances in this field indicate that 31% of these materials are based on tin oxide (SnO_2), followed by indium oxide (In_2O_3) with 23% and by zinc oxide (ZnO) that represents the 18%. These three metal oxides are the most common porous ceramic materials that have been using for sensing hydrocarbon and/or associated gases such as liquefied petroleum gas (LPG), methane, H_2, NO_2, ethanol, methanol, acetone, H_2S, CO, toluene, among others. However, several researchers have been testing additional oxides such as chromium oxide (Cr_2O_3), cobaltic oxide (Co_3O_4) tungsten trioxide (WO_3), and silicon dioxide (SiO_2) as potential porous ceramics with sensing properties. In addition, diverse elements are adding to the ceramic porous materials in order to improve their sensing capabilities. **Figure 1b** shows that palladium (Pd) with 32% is the most used element for doping the porous ceramic sensors for hydrocarbon leaks detection, followed by platinum (Pt), and vanadium (V) with 16%. Other elements such as cerium (Ce), gold (Au), tungsten (W), etc., were also identified as important secondary compounds of these kinds of sensing materials. These statistic data were generated based on the state-of-the-art developed for this specific book chapter and will be explained extensively in the following sections.

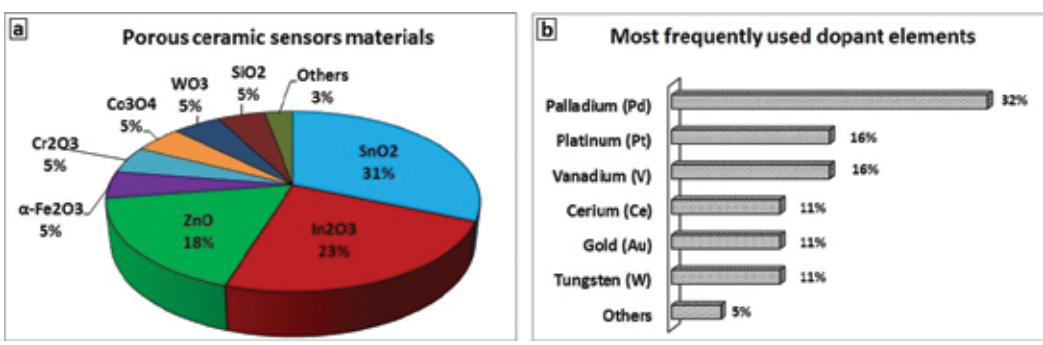

Figure 1. (a) Percentage distribution of the most used porous ceramic materials for sensing hydrocarbons and (b) percentage of elements most used for doping the porous ceramic sensor materials.

http://dx.doi.org/10.5772/intechopen.72315

Therefore, the present chapter focuses on a complete review on the application of porous ceramic materials, as an important part of the new materials' generation, to detect leakages of hydrocarbons and their associated gases.

2. Porous ceramic materials: synthesis methods and characterization

A porous material is identified by the presence of channels, holes, or interstices. Ceramic materials with either ordered or disordered porosity in different size ranges have attracted the attention as sensing materials in the fields of hydrocarbon leaks detection and other important gases such as CO, CO_2, H_2, NH_3, NO_x, SO_x, and H_2S. Typical classification of porous materials is given by IUPAC depending on the pore size as follows: micropores (less than 2 nm), mesopores (2–50 nm), and macropores (more than 50 nm). The application and performance of porous materials in such fields lies in their physical, morphological, and textural properties. For example, high-specific surface area is of great importance, especially to interact with gases. Pore properties, such as pore size, porosity, and pore shape, also strongly influence on the desired performance of the material. Through different synthesis methods, the formation of porous ceramic materials is possible. Typical methods that are widely practiced are sol-gel synthesis, wet synthesis, impregnation, co-precipitation, and hydrothermal synthesis. Hydrothermal synthesis is the most common method to obtain a variety of nanostructured materials with different shapes, such as spheres, roads, wires, sheets, tubes, and so on. Others are sponge method, foam method, leaching, sintering of particles, emulsion templating, gel casting, and injection molding. More sophisticated methods have been developed to produce complex ceramic materials, for example, solution-combustion method. Many kinds of materials have received attention regarding gas sensors field. In the following text, a description of some relevant porous materials, their synthesis methods, and main characterization that determine their potential application in hydrocarbon and gas sensors is presented.

Zeolites are versatile materials that have found industrial applications in several fields such as water purification, catalysis, adsorption, and more recently in sensors for different hydrocarbons and gases [1–3]. Synthetic zeolites by hydrothermal method are obtained from Si and Al sources dissolved in water into an autoclave. Here, the growth of crystals is developed under high pressure and temperature in a closed system by controlling reaction temperature and time, precursors, and chemical composition of reaction mixture [4]. Novel strategy to synthesize nanozeolite LTA (Linde Type A) in its sodium form by hydrothermal method was reported by Anbia et al. [5]. In this report, pore size of 6–7 nm and BET surface areas around 500 m^2/g were calculated by N_2 adsorption-desorption analysis. Novel approach of *in-situ* hydrothermal synthesis was applied to glass fibers coated with zeolite for chemical sensors toward ethane and propane [6]. SEM images showed homogeneous layer of zeolite crystals and XRD patterns confirmed the zeolite type structure.

ZnO has been successfully loaded into mesoporous ZSM-5 zeolites by simple wet impregnation method, which consists on the immersion of sample in solution of the corresponding metal oxide at determined concentration, temperature, and stirring [7]. In this way, sensors based on

ZnO particles have been fabricated toward CO, H_2, and H_2S, showing high preference to ethanol detection [8]. Additionally, zeolite has been used as layer support and overlay onto metal oxides as filters for modified gas sensors. In this regard, the sorption and catalytic properties of zeolites can improve the response of sensor and make it sensitive or insensitive to specific species. Layers of different porous zeolites such as silicalite, zeolite A, ZSM-5, LTA onto metal oxides (SnO_2, WO_3, and Cr_2O_3) have been assessed [9–12]. Seeding process and screen printing deposition seem to be common methodologies for fabrication of zeolite films onto metal oxides. The results of this investigation indicated an excellent discriminatory behavior when zeolite overlays were used, making the sensor more selective to specific gases even humidity or mixture-gas environments were tested. Nevertheless, in all cases, the sensor sensitivity was very dependent on the zeolite structure.

The combination of zeolite and conductive polymers has resulted in gas sensors lighter and less expensive with favorable operation on extreme conditions in comparison with metal sensors. Polythiophene (PT), polypyrrole (PPr), polyphenylene (PP), polyphenylenevinylene (PPV), and mainly polyaniline (PANI) have been taken into account for these purposes [13]. PANI/clinoptilolite and PT/zeolite 13X composites for CO sensors have been included by chemical oxidative polymerization of the respective monomer solution in presence of zeolite dispersion to promote the polymer penetration into zeolite pores [14]. The electrical conductivity sensitivity to CO increased significantly when zeolite content increased too, suggesting the higher amount of zeolite pores and surface area, the better interaction with gas molecules.

Since the discovery in 1990, mesoporous silica has had wide and varied field of application in catalysis, sorption, drug delivery, oil and gas industry, sensor fabrication, and so forth. Ordered mesoporous silica molecular sieves are produced widely by sol-gel method and also under hydrothermal conditions using a surfactant (cationic, anionic, or non-ionic) as template and either tetraethyl orthosilicate (TEOS) or sodium silicate as silica source [15, 16]. The first stage of sol-gel process involves the formation of colloidal suspension (sol) and then the gelation of the sol to form a network. Particularly, the synthesis of silica comprising the hydrolysis and condensation of silica source at specific pH conditions (acidic or basic pH) as catalyst of the reaction to form silica particles that precipitate after a nucleation and growth process [17]. The regulation of reaction conditions has been decisive in order to obtain well-ordered pore structure with defined morphology. During synthesis processes, time and temperature aging, pH of solution, type of surfactant, and co-surfactant have been evaluated to investigate the effect of reaction conditions on the structural and textural properties of silica particles [18]. Micelles

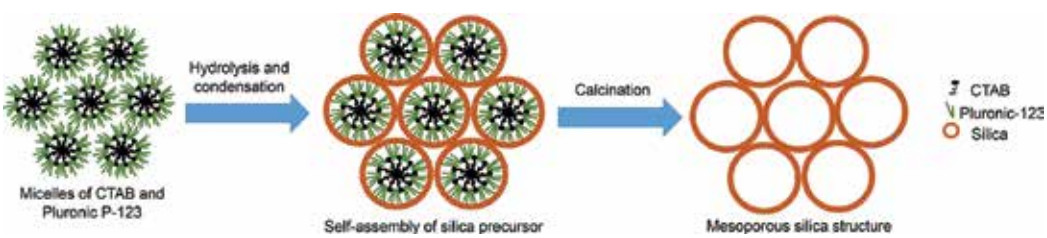

Figure 2. Proposed mechanism for synthesis of spherical SBA-15.

formed by Pluronic 123 and cetyltrimethylammonium bromide (CTAB) as template and co-template, respectively, induced the co-assembling of hydrolyzed silicate species from TEOS to synthesize spherical SBA-15 mesoporous silica with potential application in gas adsorption processes (**Figure 2**) [19]. Silica particles were not obtained when Pluronic 123/CTAB molar ratio was less than 0.31. After synthesis, samples were calcined for surfactant and co-surfactant elimination. Samples calcined at 540°C showed narrow pore size distribution with an average pore size of 3 nm and BET surface area of 667 m^2/g. The analysis of thermally treated samples at 850°C indicated the structural order and spherical morphology were maintained.

Mesoporous MCM-41 silica was synthesized by hydrothermal method at several pH values [20]. Well-ordered hexagonal mesoporous structure was validated by TEM (transmission electron microscopy) images and XRD patterns which showed the characteristic reflection peaks indexed to the planes [100, 110, 200] of this type of silica. Yang et al. [21] synthesized hierarchical porous wheat-like silica particles by sol-gel method and co-hydrothermal aging. Bimodal mesoporous structure (average pore size of 2–10 nm) determined by N_2 adsorption-desorption measurements was achieved through controlling the templates ratio and pH solution. Microwave-assisted hydrothermal methodology has allowed the preparation of mesoporous silica particles in shorter reaction time with similar structural and textural properties to those obtained by conventional hydrothermal route [22].

On the other hand, sol-gel method has been also applied for silica synthesis with no hydrothermal conditions. Spherical mesoporous MCM-48 silica have been successfully obtained at room temperature conditions from TEOS [23]. High structural ordering of mesoporous evidenced by XRD patterns and TEM images was achieved by varying the reaction time, surfactant/TEOS, and water/ethanol ratios. Uniform spherical MCM-48 silica particles with high surface area (900–1800 m^2/g) and average pore diameter of 2 nm were obtained by modulating reaction conditions and initial gel composition [24]. SEM and HR-TEM images of *in-situ* amino-functionalized MCM-48 mesoporous silica are shown in **Figure 3**. Spherical particles with well-ordered pore structure were achieved at 7 h of reaction time with particle size between 200 and 500 nm [25].

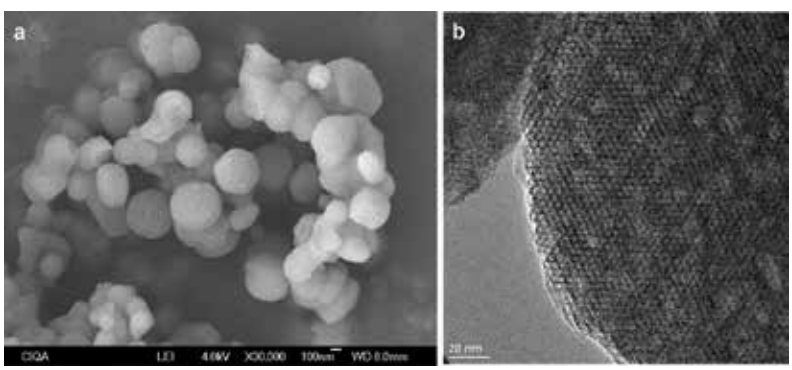

Figure 3. SEM (a) and HR-TEM (b) images of in-situ amino-functionalized mesoporous MCM-48 silica synthesized by sol-gel at room temperature.

Due of the high-specific surface area and low density, silica aerogels prepared by sol-gel method have received attention for gas sensing purposes [26]. Nanofibers embedded in hydrophobic silica aerogel synthesized from a sol comprising tetramethyl orthosilicate, methanol, and water in basic medium were investigated by Xiao et al. for acetylene detection [27]. SEM images showed the nanofibers 200 mm long and 0.8 μm diameter well-embedded in the aerogel. The porosity of aerogel allowed the fiber performance as evanescent-field gas sensor. Silica can be used as template or coating for other components such as metal oxides. ZnO nanoparticles coated with mesoporous silica through a simple sol-gel method were reported by El-Nahhal et al. [28]. The change on the displacement of XRD peaks and the elemental analysis by EDX (energy-dispersive X-ray spectroscopy) confirmed the presence of silica. Additional evidence through TEM images was provided, where a worm-like silica structure coated the dark ZnO nanoparticles. Li et al. [29] reported the use of SBA-15 (Santa Barbara Amorphous-15) silica as template for mesoporous NiO nanowires to be assessed as sensor toward ethanol. In this work, SBA-15 silica was prepared by hydrothermal method, after that, NiO nanowires was synthesized by nanocasting method which consisted on the dissolution and dispersion of the NiO precursor ($Ni(NO_3)_2$) and the silica particles under stirring and heating. After, the resulting powder was calcined and SBA-15 silica was removed with NaOH aqueous solution. Mesoporous NiO nanowires with high surface area (111 m^2/g) and average pore size of 3.6 nm were achieved. These characteristics make them more sensitive to ethanol gas in the range of 50–3000 ppm.

Porous alumina (Al_2O_3) is other kind of material that has had an important role as ceramic support of metal oxides for gas sensors due to its insulating properties and inert chemical behavior [30]. A conventional method used to prepare it is by means of solid-phase transformation through thermal decomposition of aluminum hydroxides. Alumina precursors can be synthesized by sol-gel process where an aluminum salt, such as $AlCl_3$, $AlNO_3$, $Al_2(SO_4)_3$, is hydrolyzed to form the corresponding aluminum hydroxide which precipitates [31]. The thermal treatment at different temperatures leads several transition alumina and α-alumina with highly porous vermicular microstructure as can be appreciated in **Figure 4**.

On the other hand, γ-alumina loaded at 20 wt% with various metal oxides (CeO_2, CuO, Fe_2O_3, Mn_2O_3, NiO, and RuO_2) were prepared by Hyodo et al. [32] for VOC sensing. The mesoporous γ-alumina was synthesized by microwave-assisted solvothermal method from hydrolysis of

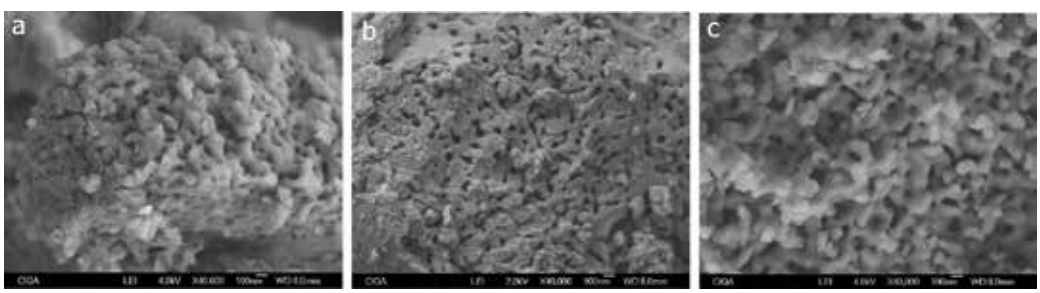

Figure 4. SEM images of α-alumina synthesized by sol-gel method from different aluminum salts. (a) Precursor of $AlNO_3$; (b) precursor of $AlCl_3$; (c) precursor of $Al_2(SO_4)_3$.

aluminum butoxide in propanol/water solution under heating to form a white precipitate. The precipitate was impregnated with the solution of the corresponding metal oxide precursor and the mixture was treated by firing at 700°C to obtain the loaded γ-alumina powder. The metal oxide-alumina powders showed high specific surface areas (around 200 m^2/g) and were able to detect ethanol, and other VOC such as acetone, ethyl acetate, benzene, toluene, and o-xylene. Porous alumina synthesized via anodic oxidation of aluminum, denoted as porous anodic alumina, has been object of numerous studies as template on which metal oxides are deposited for the development of gas sensor systems. The anodizing process consists of exposure the aluminum specimens to certain voltage conditions in an electrolyte solution. Anodization conditions, such as type of electrolyte, anodizing potential, temperature, and duration of process, determine the morphology and microstructure of porous film. Sharma and Islam [33] found that the increasing voltage caused an increase of pore size due to greater dissolution of the oxide layer. Likewise, the porous structure of alumina provided the nucleation sites for uniform growth of Pd-capped Mg when was deposited on it, and a finer film was obtained as was appreciated in XRD patterns and SEM images. Norek et al. [34] argued that the pores of alumina provided enough space for free expansion of metallic film, avoiding the accumulation of stress and resulting in a greater H_2 absorption capacity. In the same way, active layers of WO_3 and NbO_2 were deposited onto anodic porous alumina by sputter-deposition [35]. The critical combination of the high quality and reproducible porous structure of alumina film significantly influenced the sensor response to H_2 in a range of 5–1000 ppm and operating temperatures of 20–350°C.

3. Porous ceramic materials for sensors. Operational principles for gases detection

The complex operational mechanism of porous ceramic sensors for hydrocarbon gases is affected by factors, such as chemical composition, humidity, temperature, morphology, and so on. This mechanism is determined by chemical and electronic interactions between the porous ceramic and the specific gas resulting in a resistance change. The main operational principles of sensing devices are shown in **Table 1** [36].

There are three principal reasons for monitoring hydrocarbon gases: (1) combustible/flammable gas, (2) toxic/irritant gases and (3) oxygen levels control. As is well known, any hydrocarbon leaks is a potential explosive hazard, where to avoid an explosion, atmospheric levels must be maintained below the lower explosive limit (LEL) for each gas, or purged of oxygen. In addition, for a flame to exist, three conditions must be met: (1) a source of fuel (any hydrocarbon source, e.g., methane or gasoline vapors), (2) enough oxygen (greater than 10–15%) to oxidize or burn the fuel, and (3) a source of heat (ignition) to start the process [36]. Moreover, combustion can occur at both extreme low-end and high-end gas concentrations. These extremes are called the lower explosive limit (LEL) also known as lower flammability limit (LFL), and the upper explosive limit (UEL) or upper flammability limit (UFL). Any gas or vapor concentration that falls between these two limits is in the flammable (explosive) range [36]. Therefore, the control and knowledge about the sensors' operational conditions

Gas detection technology	Operational description	Gas type detected
Catalytic bead	A wire coil is coated with a catalyst-coated glass or ceramic material, and is electrically heated to a temperature that allows it to burn (catalyze) the gas being monitored, releasing heat, and increasing the temperature of the wire. As the temperature of the wire increases, so does its electrical resistance. This resistance is measured by a Wheatstone Bridge circuit and the resulting measurement is converted to an electrical signal used by gas detectors. A second sensor, the compensator, is used to compensate for temperature, pressure and humidity	Combustible gas
Metal oxide semiconductor (also known as "solid state")	A semiconducting material (metal oxide) is applied to a non-conducting substrate between two electrodes. The substrate is heated to a temperature at which the presence of the gas can cause a reversible change in the conductivity of the semi-conducting material. When no gas is present, oxygen is ionized onto the surface and the sensor becomes semi-conductive; when molecules of the gas of interest are present, they replace the oxygen ions, decreasing the resistance between the electrodes. This change is measured electrically and is proportional to the concentration of the gas being measured	Combustible gas; toxic gas
Point infrared (IR) short path	Uses an electrically modulated source of IR energy and two detectors that convert the IR energy into electrical signals. Each detector is sensitive to a different range of wavelengths in the IR portion of the spectrum. The source emission is directed through a window in the main enclosure into an open volume. A mirror may be used at the end of this volume to direct the energy back through the window and onto the detectors. The presence of a combustible gas will reduce the intensity of the source emission reaching the analytical detector, but not the intensity of emission reaching the reference detector. The microprocessor monitors the ratio of these two signals and correlates this to a %LEL reading	Combustible gas
Open (long path) infrared	Open-path IR monitors expand the concepts of point IR detection to a gas sampling path of up to 100 m. Like point IR monitors, they utilize a dual beam concept. The "sample" beam is in the infrared wavelength which absorbs hydrocarbons, while the second "reference" beam is outside this gas absorbing wavelength. The ratio of the two beams is continuously compared. When no gas is present, the signal ratio is constant; when a gas cloud crosses the beam, the sample signal is absorbed or reduced in proportion to the amount of gas present while the reference beam is not. System calculates the product of the average gas concentration and the gas cloud width, and readings are given in %LEL/meter.	Combustible gas
Photoacoustic infrared	The gas sample is exposed to infrared light; as it absorbs light, its molecules generate a pressure pulse. The magnitude of the pressure pulse indicates the gas concentration present	Combustible gas; toxic gas
Electrochemical for toxic gas or/and oxygen detection	Sensor is a chamber containing a gel or electrolyte and two active electrodes—the measuring (sensing/working) electrode (anode) and the counter electrode (cathode). A third electrode (reference) is used to build up a constant voltage between the anode and the cathode. The gas sample enters the casing through a membrane; oxidation occurs at the anode and reduction takes place at the cathode. When the positive ions flow to the cathode and the negative ions flow to the anode, a current proportional to the gas concentration is generated	Toxic gas or oxygen deficiency/ enrichment

Gas detection technology	Operational description	Gas type detected
Thermal conductivity	Two sensors (detecting and compensating sensors) are built into a Wheatstone Bridge. The detecting sensor is exposed to the gas of interest; the compensating sensor is enclosed in a sealed compartment filled with clean air. Exposure to the gas sample causes the detecting sensor to cool, changing the electrical resistance. This change is proportional to the gas concentration. The compensating sensor is used to verify that the temperature change is caused by the gas of interest and not by other factors	Combustible gas; toxic gases
Photoionization	A photoionization detector (PID) uses an ultraviolet lamp to ionize the compound of interest. Ions are collected on a "getter," a current is produced and the concentration of the compound is displayed in parts per million on the instrument meter	Toxic (organic compounds)

Table 1. Types of gas detection technologies and their operational descriptions [36].

are the master key to understand the hydrocarbon gases monitoring process in order to get alarms before a potential explosive condition occurs. On the other hand, the developments of low cost and power efficient devices that can selectively detect hazardous analytes with very high sensitivity have evolved constantly. Two main operating principles have been intensely investigated: catalytic sensors and metal oxide semiconductor (MOS) have been investigated in sensors for wide range of chemical analytes [37].

Catalytic sensors are very common to detect combustible gases. These consist of two elements: a detector element which contains the sensitive material and an inert compensator element. The operating principle is based on the oxidation reaction of the combustible gas with the detector element. The heat released by this exothermic reaction changes the electrical resistance of the detector element. Combustible gas does not burn on the compensator element, so its temperature and resistance are maintained unchanged. When sensor is located at combustible gas-free atmosphere, a balance of the bridge circuit is maintained. On the contrary, when combustible gases are present, the resistance of the detector element increases and causes an imbalance in the bridge circuit producing an output voltage signal, which is proportional to the combustible gas concentration. This kind of sensors is very sensitive to environmental conditions such as temperature, humidity, and pressure. On the other hand, basic electrochemical-type sensors consist on a working electrode, a counter electrode, and an ion conductor. An electrical signal is produced by the chemical reaction (oxidation or reduction) of the analyte (gas) with the working electrode, giving a current proportional to the gas concentration that flows between electrodes [38]. This kind of sensor depends on establishment of an electrochemical potential which is not affected by surface morphology. Electrochemical sensors are minimally affected by pressure, but they are very sensitive to temperature.

In MOS sensors, a metal oxide is used as sensing material. In a typical MOS sensor, oxygen is adsorbed onto the surface of the sensing material (i.e., SnO_2, ZnO, In_2O_3, TiO_2, and WO_3). These oxygen molecules attract free electrons from the metal oxide which forming a potential barrier to prevent electron flow. If sensor is exposed to certain gas atmosphere, the gas reacts with the

oxygen molecules through a reducing reaction which causes the release of electrons and allows that a current flows freely through the sensor. Consequently, the gas concentration is detected by the resistance change of MOS [4]. This kind of sensor seems to be the most important because the huge amount of investigation regarding to them. Pt nanoparticles-modified Al-doped ZnO (AZO) porous macro/mesoporous nanosheets prepared by solution combustion method were assessed for butane gas sensor at low temperature. The large surface area of 50.17 m^2/g and the broad pore size distribution between 3 and 110 nm calculated by BJH method provided a good contacting interface between sensing material and gas molecules allowing a maximum response of 56–3000 ppm of butane. The gas sensitivity is related to the electron flow through the interface from AZO to Pt. An oxidation-reduction reaction happened when Pt nanoparticles-modified AZO nanosheets were exposed to reducing gas. A large amount of electrons are released which back to the conduction band of AZO leading a decrease of resistance [39]. Hierarchical flower-like structure composite formed by combination of metal oxides with high surface area and porous structure have shown improved gas sensing performance in comparison with pure metal oxide. NiO:CuO nanocomposites (molar ratio 1:1) showed 2 s response time to 100 ppm NO_2 at room temperature and relative humidity of 42%. The heterojunction formed at the interface between NiO and CuO could accelerate the speed response. O_2 molecules are absorbed on the surface of sensor when it is exposed to air. These O_2 molecules capture electrons from conduction band of sensing material forming ions O_2^-. At NO_2 atmosphere, these gas molecules are adsorbed onto the surface by extracting electron from conduction band. Because electrons are transferred to NO_2, the resistance is decreased [40].

The combination of p-type Sb_2O_5 with n-type SnO_2 in composite sensor for NO_2 have also evaluated thought output voltage measurements and the sensing response was defined by the ratio of sensor resistance in NO_2 and air atmospheres. Relevant results indicate low operation temperature (100°C) and high response (800–5 ppm NO_2) at short time (5 s) of composite sensor. The existence of p-n junction in composite sensor which induced a new potential barrier when electrons transfer between SnO_2 particles, large surface area and porous structure of Sb_2O_5 and SnO_2 particles gave benefits to exhibit superior gas sensing performance. The reduction of operating temperature was attributed to lower energy required for electron transition derived from the decrease of band gap of p- and n-type semiconductor [41]. In another work, porous hollow balls formed by self-assembly of α-Fe_2O_3 nanoparticles were synthesized by hydrothermal method and were evaluated for sensing ethanol, CO, and NH_3 in a temperature range from 250 to 450°C. Sensor response (S) was determined following the equation $S = R_{air}/R_{gas}$, where R_{air} and R_{gas} are the sensor resistances recorded in presence of test gas and dry air, respectively. The initial resistance of α-Fe_2O_3 hollow balls sensor decreasing when operating temperature increasing, leading 85 kΩ at 250°C and 18 kΩ at 450°C in ethanol sensing test. In addition, the sensor response increased from 1.77 to 3.29 with increasing ethanol concentration from 50 to 500 ppm at 400°C. Low sensor response to CO and NH_3 was detected, thus, this sensor is suggested only for ethanol detection [42]. In order to improve its ethanol sensing capability at the temperature range between 25 until 125°C, other researchers have been introduced Au nanoparticles into ZnO nanostructures by sputtering technique. The sensing mechanism is based on the surface electron density changes of the semiconductor. The oxygen molecules in air react to the surface electrons of ZnO forming oxygen species determined by the constant reaction k_{oxy} as follows:

O_2 (ads) + e^- (surface) ↔ O_2 (ads) [43]. The Au nanoparticles act as the catalyst leading oxygen dissociation. In this way, the k_{oxy} in chemical reaction allows an improved sensor response. The resistance values showed a reduction when sensor was exposed to ethanol vapor. If the ethanol exposition is stopped, the sensor resistance returned to the initial state. Moreover, the resistance response is improved when UV illumination is included in tests. This behavior is associated to the large density of active photoelectrons due to the UV excitation [10]. Novel approaches toward ethanol sensor enhancement using decorated metal oxides have recently studied [44]. Improved ethanol sensing at operating temperature of 160°C and response of 70.2–100 ppm was reported by using porous SnO_2 nanosheets loaded with Au nanoparticles, which means a response three times higher than those obtained with SnO_2-based sensor. The response curves increased with increasing ethanol concentration and returned to baseline when ethanol supply was stopped inside test chamber, indicating quick response and recovery time. The synergistic effect of 2D porous structure of SnO_2 which allowed facile gas diffusion and the catalytic activity of Ag particles allowed superior ethanol-detection properties [45]. The fabrication of NiO/ZnO nanoplates by solvothermal method and thermal treatment is also reported. The ratio of the electrical resistance in air Ra, and electrical resistance in ethanol-air mixed gas was used to determine the sensor performance. The response to ethanol in NiO/ZnO sensor is better than those in NiO gas sensor. A short response of 2.1 s and time recovery of 4 s promised good sensor performance for ethanol sensing [8]. Colloidal ZnO quantum dots treated with $ZnCl_2$ and annealing at 200–300°C were used to fabricate gas sensor toward H_2S. Nearly, no response (1.07–50 ppm H_2S) was obtained with untreated ZnO sensor whereas $ZnCl_2$-treatment ZnO sensor showed a response up to 5 with very slow recovery. Recovery properties were improved by annealing at 300°C for 1 h. Sensor under that conditions at room temperature reached a response of 113.5 and recovery time of 820 s. Based on results, the fast and sensitive response makes this sensor very attractive in comparison with others [46]. Changes in resistance of porous $BiNbO_4$ nanostructures-based sensors were reported for selective NH_3 sensing. The complete oxidization of NH_3 onto the sensor surface makes changes on the conductivity sensor. The maximum response of 16 s and recovery time less than 17 s were attributed to the large surface area (41.27 m^2/g) and high porosity that increase the accessible sites for adsorption of gas molecules [47].

4. Specific application: hydrocarbon leak sensors. The thermomechanics principles

Diverse fluids used in the petrochemicals processes such as propane, liquid petroleum gas (LPG), butane, propylene; and other organics and inorganics fluids are widely stored, transported, or used in a pressure-liquefied state. Therefore, these fluids are very important in the industry when leak sensing technology is needed. Specifically, pressure-liquefied gas (PLG have a high probability of ending in a fatal accidental leak due to its own fluid properties and behavior [48, 49]. So, sensing technology needed must cover a range of fluids; however, there are some clear examples where the widely and frequently used of some fluids highlight some extra needs for specially design sensors or sensing technology.

4.1. Theoretical basis of the problem: phenomenon involved

Flashing depends on the initial parameter values of the fluid as pressure and temperature as well as the type of fluid. A particular combination of those variables can create, for some cases, a complete breaking of the liquid core into droplets at the same time that it is going out of container like unstable two phase jet or liquid jet. The major difficulty in the understanding of this flashing phenomenon and the parameters interactions within it belongs to the existence of a compromise between the physical and thermodynamics mechanism that acts on the released fluid [50]. Specific behavior and characteristics of these liquid-gas mixtures and the potential for the formation of vapor-liquid aerosols during a superheated liquid release due to the breaking of the metastable state can significantly affect the hazard zone and the mitigation steps that can be taken to minimize the release impact for the hydrocarbon industry [49, 51, 52].

High complexity level of the whole process in combination with the need of more information based on experimental, analytical, or numerical models is the main difficulty to be overcome in order top developed new sensing technology. Different authors have concentrated efforts of the jet characterization. The developed information about the jet can help to understand the parameters that can be used as key indicators of accidental release of hydrocarbons.

Flashing phenomenon complexity required calculation of the velocity discharge, void fraction, and mass flow of a flashing jet together with the estimation of the temperature. Due to the nature of the nucleation process, the assumptions of adiabatic flow with non-reversible work for the surface tension forces are made. Those considerations are found to be more realistic that the isentropic condition used until now by different authors. Dynamics conditions usually considered include the mixture velocity after flashing as critical conditions. Frequently numerical modeling techniques are only applied after the flashing jet is formed. No droplets generation or vapor generation are included in the modeling. Droplets are imposed as part of the boundary condition of a gas jet. Droplets transport mechanics and their interaction and momentum exchange with the gas current is made using droplet interaction models as for example Disperse Model (DDM). Geometrical aspects as nozzle dimension, as well as, turbulent model used have a large impact on the core region length of the velocity profile. The numerical results are compared based on the centerline or cross section velocity profiles [53].

In general, centerline, the temperature profile presents an initial decay from the exit of the nozzle until a certain distance, where a minimum value is achieved presumably connected with the location of cessation of boiling and completion of nucleation as main interaction mechanics of energy exchange. After that point, mechanical and evaporation mechanisms become the main driving mechanisms for energy exchange instead. The position at which the minimum temperature occurs is known as Minimum Temperature Distance (MTD). Previous works have not report major observations on this particular parameter. However, other related concepts as Cold Spray Distance (CSD), which refers to the spray distance where the spray maintains a specific temperature considered "cold" and the Spray Thermal Length (STL) refers to a total spray length where liquid droplets exist [54]. Similar behavior of the temperature profiles at the centerline has been observed several experimental settings [55–58].

Geometrical characteristics as diameter of the nozzle, length of the nozzle in the experimental system have influence on the dynamics behavior of the system, driving the velocity profile as well as the temperature profile. Evaporation and convection processes are also involved and their relevance along the leaking fluid properties as well as the characteristics of the jet is not well determined yet. Even so, in more recent works, some authors applied the jump condition analysis to the shock waves in the discharge of a superheated liquid [59]. Due to the metastable liquids supply the energy stored within them via the latent heat of vaporization, the evaporation wave was assumed as an adiabatic phase transition.

4.2. Identification of key parameters for sensing technology: viability for sensing based on the concept

As direct consequence of the understanding of the process, it is possible to evaluate the potential of different variables or parameters to detect in the best possible way any leak, keeping in mind that the primary purpose of leak detection systems is to assist pipeline operators in detecting and locating leaks. The first aspect to consider is the magnitudes of the scale of mass discharge, the critical explosion limits, change in temperature of the surrounding, the time scale of the process, or any other parameters that be used to catch this phenomenon. Mass discharge directly seems to be no a convenient parameter to be measured directly but based on the amount of mass going out concentration of the leaked fluid in the surrounding will change. As described, this variable will depend on several physical parameters such as pressure difference, temperature, and fluid properties that will determine the discharge velocity.

Time scale of the leak is related with the jet velocity; however, the thermodynamics process of phase change are under the influence of another parameter as the fluid properties, which can be described based on the temperature variation along the centerline of the yet. Initially, there is a time lag of the initiation of flashing, followed by a drop of temperature driven by a phenomenon of sudden change of phase and finally an increment of the temperature to the ambient condition driven mainly by the mechanics mechanism of energy exchange. Characteristics of centerline droplets temperature of a R134a flashing jet by using and exponential function, which started with an almost exponential decay with the fastest drop in the temperature taking place near the nozzle exit, explained by the presence of rapid evaporation of the droplets and the insufficiency of the convective heat transfer from the surrounding [54]. This exponential decay of droplets average temperature can be described by an exponential function followed by less rapid temperature decay. Meanwhile, experimental data have pointed out that for different substances that there is a visible minimum in the temperature profile that can be related with the factor the mechanics mechanisms take over the thermodynamics mechanics of energy exchange [60]. Mentioned time scales are not commonly reported, however, it is possible to be calculated using the equilibrium model [61].

A different approach described that the flashing process can be detected based on the fact that rapid vaporization or phase change of superheated fluid produced an acoustic pulse that can detect by an acoustic sensor [62, 63]. Nucleation of vapor bubble requires a minimum amount of energy related to the vibrating media that will be traduced in pressure waves (noises). As mentioned in Section 3, the ceramics porous materials (e.g., catalytic and MOS sensors) are other available options for sensing hydrocarbon vapors and this will be discuss in details on the next section.

5. Porous ceramic materials (micro- and nano-materials) for sensing hydrocarbons

Wherever there is a leak at a hydrocarbon facility (e.g., pipeline), there will be hydrocarbon vapors that may be detected. *In situ* detection of hydrocarbon plumes from leakages involves reading of a variety of environmental variables and combination of techniques that will allow to detect the leak in the air, soil, or water. when a gaseous hydrocarbon leaks takes place and it migrates to the environment; this would require an immediate detection procedure of hydrocarbon vapors in order to take the respectively actions to control any catastrophic accident. This section extensively reviews the recent development of porous ceramic gas sensor materials for hydrocarbon gas leaks including LPG [64, 65], CH_4 [66–68], H_2 [69–71], ethanol [29, 84–88], methanol [89–92], and associated gases such as NO_2 [41, 73–77], H_2S [78–83], and CO [72]. Basically, the discussion will be focused on the specific overlapped section between three interesting areas such as (1) porous ceramic materials, (2) hydrocarbon gas leaks detection, and (3) sensor materials giving the opportunity to explore the interesting niche area for sensing hydrocarbons and their associated gases leaks by porous ceramic materials. In addition, promising materials for sensitive detection of diverse hydrocarbons and/or their associated gases have been identified and are summarized in **Table 2**.

The detection effectivity of hydrocarbons gases by porous ceramic sensor materials (e.g., metal-oxide semiconductor—MOS) have a great influence on the chemical composition of the ceramics, the doping type by specific elements, the porosity type, how morphology-affect the gas sensing properties, etc. According to the information in **Table 2**, the most used porous ceramic materials for hydrocarbon sensing application are (1) the porous tin oxide (SnO_2) which have been applied to detect LPG, methane, H_2, NO_2, ethanol, methanol, toluene, etc.; (2) the porous indium oxide (In_2O_3) that shows a great potential to sensing ethanol, methanol and other associated gases to the hydrocarbon field such as NO_2, H_2S, etc.; and (3) the porous zinc oxide (ZnO) that has been used to sensing ethanol, acetone, NO_2, H_2S, etc. On the other hand, the catalyst elements mostly used as doping materials in order to improve the sensing properties of the porous ceramics are palladium (Pd) [65, 66, 85], gold (Au) [77], tungsten (W) [76, 95], vanadium (V) [71], cerium (Ce) [90], platinum (Pt) [69], and/or combinations thereof [70, 76, 91]. The Pd could be used to explain the principle of operation of these doping elements which is based on the fact that Pd is a catalytic metal that dissociates the ambient gas to ions. These travel by diffusion to the metal-oxide interface where an electrically polarized layer is formed (according to the ambient gas used). This layer stimulates a change in the electrical characteristics of the MOS device, and hence a sensing mechanism is established [97]. In addition, other compounds such as Sb_2O_5 [41], NiO [70], and graphene [88] have been also evaluated as doping or as secondary materials in advanced composite sensors.

There are only few papers devoted to investigation of sensor properties of porous ceramic materials toward low temperature at high humidity sensing conditions. As humidity is a permanent environmental factor, its control and measurement are particularly important not only for human comfort but also for many industries and technologies. It has been found that the ambient humidity plays a crucial role in the response of the porous ceramic materials based sensor to different hydrocarbons and their associated gases at room temperature. Therefore,

Substance	Porous ceramic materials	Reference
LPG	SnO_2 nanoflowers and porous nanospheres	[64]
	Porous nanoparticles of α-Fe_2O_3 doped with Pd	[65]
Methane (CH_4)	Mesoporous SnO_2 doped with Pd	[66]
	Porous Ga_2O_3	[67]
	Nanoporous SnO_2	[68]
H_2	Pt-WO_3 porous composite ceramics	[69]
	Porous SiO_2 films doped with NiO and Au nanocrystals	[70]
	Vanadium-doped SnO_2 oxide porous nanofibers	[71]
CO	SnO_2 coated with amorphous microporous Si–B–C–N layers	[72]
NO_2	Mesoporous In_2O_3 nanospheres	[73]
	Sb_2O_5 modified SnO_2 porous nanocomposites	[41]
	CuO/p-porous silicon	[74]
	Porous corundum-type In_2O_3 nanosheets	[75]
	W- and V-modified mesoporous MCM-41 SiO_2	[76]
	Au-functionalized porous ZnO nanosheets	[77]
H_2S	Porous In_2O_3 nanotubes and nanowires	[78]
	Porous ZnO nanosheet-built network film	[79]
	CuO nanostructures with porous nanosheets	[80]
	In_2O_3 micro/nanostructured porous thin film	[81]
	Porous $ZnFe_2O_4$ nanosheets	[82]
	Porous α-Fe_2O_3	[83]
Ethanol (C_2H_6O)	Porous SnO_2 hollow nanospheres	[84]
	Porous indium oxide (In_2O_3) nanostructured with Pd	[85]
	Porous ZnO-Co_3O_4 hollow polyhedrons heterostructures	[86]
	Mesoporous nickel oxides nanowires	[29]
	Mesoporous Co_3O_4 nanoneedle arrays	[87]
	Mesoporous In_2O_3-reduced graphene oxide (rGO)	[88]
Methanol (CH_3OH)	Porous hierarchical SnO_2	[89]
	Ce-doped In_2O_3 porous nanospheres	[90]
	Pd-Pt-In_2O_3 composited nanocrystalline SnO_2	[91]
	Macropore and mesopore SnO_2	[92]
Toluene (C_7H_8)	Porous Pd-loaded flower-like SnO_2 microspheres	[93]
	Cr_2O_3 porous microspheres	[94]
Acetone (C_3H_6O)	Porous WO_3-Cr_2O_3 thin films	[95]
	Porous ZnO crystals	[96]

Table 2. Porous ceramic materials for hydrocarbon leaks detection.

ceramic metal oxides are found to be a good choice as humidity sensing materials due to their properties such as high mechanical strength, good physical and chemical stabilities, fast response and recovery times, and wide range of operating temperatures. Semiconducting metal oxide sensors are the widely studied chemiresistive sensors. Recently, nanostructures of semiconductor metal oxides have received considerable interest in the fabrication of humidity and gas sensors due to their high surface-to-volume ratio of atoms, excellent surface reactivity, and the ability to tailor their surface and charge transport properties. Hence, they are considered as ideal candidates as humidity sensors. SnO_2 nanowires, ZrO_2 nanorods, Al_2O_3 nanowires, TiO_2 nanotubes, $BaTiO_3$ nanofibers, $ZnSnO_3$ nanocubes, among others constitute the recently explored nanostructured metal oxides to this effect [98].

Tin oxide (SnO_2) is the most versatile oxide used as porous ceramics for sensing hydrocarbon leaks and/or their associated gases. For instance, Wagner et al. [66] produced mesoporous SnO_2 doped with Pd species to be exposed to different gas mixtures at high temperature (600°C) and simulate long term usage. The Pd oxidation state was directly associated to the resistive change of the SnO_2 sensor at different concentrations of methane gas. An important reduction of Pd(II) to Pd(0) was registered for samples evaluated at 5000 ppm of methane in air. The resistive response is affected by the temperature 300°C or 600°C evaluated during the test, and the type of gas used, i.e., synthetic air, pure N_2, etc. On the other hand, Waitz et al. [68] reveals that mesoporous SnO_2 synthesized by structure replication (nanocasting) from ordered mesoporous KIT-6 silica shows a high thermal stability with no structural loss up to 600°C and only minor decrease in specific surface area by 18% at 800°C. In particular, the samples turn out to be much more stable than porous SnO_2 materials prepared by sol-gel-based synthesis procedures for comparison. The thermal stability facilitates the utilization of the materials as sensors for combustible gases showing promising behavior for the methane (CH_4) sensing methodologies. In addition, Ho et al. [64] synthetized SnO_2 with two different microstructures: (1) hierarchical SnO_2 flowers assembled by numerous one-dimensional tetragonal prism nanorods, and (2) SnO_2 sphere architectures formed by numerous smaller particles. The results show that the nanoflowers exhibited higher sensitivities to ethanol than the nanospheres, whereas the typical responses of these sensors to H_2 and LPG indicated that the porous spheres demonstrated better sensing performance than the hierarchical flowers [64]. This research is a main example about how the material's microstructure/morphology could affect the sensing properties of the same material; the results demonstrated the great effect that the microstructures could have on the final gas sensing properties of this metal oxide.

Indium oxide (In_2O_3), as a typical n-type semiconductor with a band gap of 3.55–3.75 eV, has been investigated extensively in last decade for its applications in diverse areas. For instance, Gong et al. [85] successfully synthesized porous In_2O_3 nanocuboids on a large scale and the sensors made with them exhibit enhanced sensitivity and stability to reducing gases including H_2S, acetone, ethanol and methanol vapors, after modified with Pd nanoparticles. The results indicate the existence of abundant pores for the aggregations of particles in the materials. The BET surface area of the materials is 36.2 $m^2\ g^{-1}$. As was mentioned, the In_2O_3 and $Pd@In_2O_3$ nanocuboids were used to produce two different types of chemical sensors. The sensor fabricated with $Pd@In_2O_3$ was more stable with a higher response to the reducing vapors

in comparation to the In_2O_3 nanocuboids sensor. The results also indicate that Pd nanoparticles have a positive effect on the sensing mechanism of In_2O_3 nanocuboids. On the other hand, hydrogen sulfide (H_2S) is a toxic, flammable, colorless, and malodorous gas that has been getting strong attention in the industrial gases sensing field for several years. Therefore, In_2O_3-based sensing film and its sensing performances to H_2S (especially at low working temperature) have been much studied and received superior attentions [99]. In the same order of idea, In_2O_3 nanoparticle film synthetized by hydrothermal method and studied its gas sensing performances to H_2S at different temperatures above125°C. Such film exhibited a strong and selective sensing to H_2S at 268°C among the normal gas molecules. In addition, nanocrystalline In_2O_3-based films had a high response to H_2S gas at 150°C. Also, the nanostructured In_2O_3 thin films, induced by spray pyrolysis technique, showed a good sensitivity to H_2S at a lower temperature of 50°C [99]. Wang et al. [99] reported the sensing properties of In_2O_3 micro/nanostructured orderly porous thin film produced by solution-dipping monolayer organic colloidal template. This sensing material was used for H_2S detection at room temperature. The results indicated that the humidity has a great effect on the sensing properties of the In_2O_3 porous film where H_2S was not detected in ambient without humidity. This sensing material shows an ultra-high response value to H_2S at room temperature with a significant humidity-induced enhanced sensing performance. The results also indicate that the sensing mechanism of the In_2O_3 film for the H_2S at room temperature is due to three potential effect such as (1) the ambient humidity-induced H_2S hydrolyzation, (2) the hydrolyzation-induced desorption of the chemisorbed oxygen and adsorption of water, or (3) even formation of water thin film on the In_2O_3 surface produced by the effect of the ambient humidity. This research team also proposed a design of an In_2O_3 porous thin film-based sensor array with potential uses for the H_2S detection under environmental operational conditions.

Zinc oxide (ZnO) is one of the most auspicious materials for a large number of applications because of its physicochemical properties, where its chemical sensitivity permits to be used as a sensing material for many gases including H_2, NO_2, O_2, CH_3CH_2OH, NH_3, and LPG [100]. Accordingly, Al-Salmana et al. [100] produced ZnO nanostructure deposited on the PET and quartz substrates, and found that ZnO sensor based on PET substrate has a sensitivity valor of 24.8% for H_2 gas tested at room temperature with an increase until 99.53% at 200°C with a response of 224. Otherwise, ZnO sensor based on quartz substrate showed high sensitivity (96.29%) at 100°C, with an increase until 99.95% at 250°C and a response value of 2254. The ZnO gas sensors based on PET and quartz substrates showed high sensitivity, stability, and recovery to the initial value of the sensor signal when they were operating at temperatures between 100 and 200°C. These sensing materials used for H_2 gas detection and based on ZnO nanostructures were stable over several cycles and had a fast response at different operating temperatures. On the other hand, Wagner et al. [101] produced mesoporous ZnO and evaluated its sensing properties for CO and NO_2 detection in a concentration range of 2–10 ppm at a relative humidity of 50%. It is well known that the long-term permit-exposure values for the human race without health damage are about 30 ppm for CO and 5 ppm for the NO_2. This research group indicated that their mesoporous sensing materials can be used for the detection of these gases under concentration bellow of the legal thresholds register in most countries and showed previously.

Other kind of porous ceramics materials have been investigated for hydrocarbons gases detection. For instance, Picasso et al. [65] have produced sensors based on nanoparticles of α-Fe_2O_3 doped with different amounts of Pd ranging from 0.1 to 1.0 wt.% for liquefied petroleum gas (LPG) detection. They demonstrated that the sample of Pd-doped sensors showed much higher sensitivity than the undoped one revealing the promotion electronic effect of Pd^{2+} on the surface reaction. Among all samples, the sensor with 0.75 wt.% Pd presented the highest gas response at 300°C in all gas tested concentrations, likely due to the highest BET surface, well-defined hematite crystalline structure and best surface contact over Pd surface via electronic mechanism. On the other hand, Xiaoqing Li et al. [29] produced mesoporous NiO NWs by using SBA-15 silica as the hard templates with the nanocasting method under the calcination temperature between 550 and 750°C. All results showed that all samples exhibited the best response to ethanol gas. The specific surface area decreased with the increasing calcination temperature, while crystallization degree and bandgap increased. Owing to the suitable specific surface area, crystallization degree and bandgap at the calcination temperature of 650°C, mesoporous NiO NWs-650 exhibited the best gas-sensing performance. For ethanol detection Co_3O_4 nanoneedle arrays were successfully fabricated via a facile two-step approach, including the formation of needle-shaped $Co(CO_3)0.5(OH)\cdot 0.11H_2O$ followed by thermal conversion to mesoporous Co_3O_4. The highest sensitivity reached ~89.6 for 100 ppm ethanol vapor and the optimal working temperature was as low as 130°C [87].

In addition, some of the most sensing materials used for humidity conditions are based on metal oxides, spinel- and perovskite-type oxides and/or thereof combination. Basically, the physicochemical properties of these materials allow them to detect humidity in gaseous media. The sensing mechanism of ceramic humidity sensors is based on water adsorption on the ceramic surface. The microstructure of these ceramic materials integrated by grains, porous, and their crystalline or non-crystalline phases support the sensing mechanism process. Hence, these kinds of sensors are based on the mechanical or electrical change due to bulk and/or surface modifications of the sensing materials with water adsorption [102]. Finally, the present state-of-art indicates that there are just a few publications related to the sensing hydrocarbons and/or their associated gases at low temperature and high humidity indicating a great niche for future researches.

6. Conclusion

In the recent past, a great deal of research efforts were directed toward the development of advanced ceramics porous materials due to their sensing properties and potential application for sensing hydrocarbons and/or their associated gases leaks. Among the various techniques that are available for gas detection, solid state metal oxides offer a wide spectrum of materials and their sensitivities for different gaseous species, making it a better choice over other options. The oxides that are covered in this study include oxides of aluminum, silicon, bismuth, cerium, chromium, cobalt, copper, indium, iron, nickel, niobium, tin, titanium, tungsten, vanadium, zinc, zirconium, and the mixed or multi-component metal oxides. The cover hydrocarbons and their associated gases are liquefied petroleum gas (LPG), CH_4, ethanol (C_2H_6O), methanol (CH_3OH), acetone (C_3H_6O), H_2, NH_3, CO, H_2S, NO_x, among others.

The book chapter mentions the principle of the hydrocarbon leaks and the advances in the production and applications of micro- and nanoporous ceramics for hydrocarbon leaks under diverse environmental conditions (e.g., humidity and low temperatures) that also affects the sensing capability of these materials. Finally, sensing of hydrocarbon leaks at low temperatures and high humidity conditions is clearly identified as niche area that requests future research efforts.

Acknowledgements

Dr. Y.A. Perera-Mercado is grateful to the West Houston Center for Science and Engineering Center (WHC) at Houston Community College System (HCCS); and Dr. G. Castruita-de Leon is thankful to Cátedras-CONACYT for the support received from both organizations in order to write this book chapter. Finally, the publication charges for this article have been funded by a grant from the publication fund of UiT The Arctic University of Norway.

Author details

Yibran A. Perera-Mercado[1]*, Griselda Castruita-de Leon[2] and Geanette Polanco Piñerez[3]

*Address all correspondence to: yibranpereramercado@gmail.com

1 West Houston Center for Science & Engineering (WHC) at Houston Community College System (HCCS), Houston, Texas, USA

2 CONACYT—Research Center for Applied Chemistry (CIQA), Saltillo, Coahuila, México

3 The Arctic University of Norway, Faculty of Engineering and Technology, Institute of Industrial Technology, Narvik, Norway

References

[1] Salmasi SSZ, Abbas-Abadi MS, Haghighi MN, Abedini H. The effect of different zeolite based catalysts on the pyrolysis of polybutadiene rubber. Fuel. 2015;**160**:544-548. DOI: 10.1016/j.fuel.2015.07.091

[2] Sahner K, Hagen G, Schönauer S, Reiß S, Moos R. Zeolites-versatile materials for sensors. Solid Sate Ionics. 2008;**179**:2416-2423. DOI: 10.1016/j.ssi.2008.01.024

[3] Masoudi-Nejad M, Fatemi S. Thermodynamic adsorption data of CH_4, C_2H_6, C_2H_4 as the OCM process hydrocarbons on SAPO-34 molecular sieve. Journal of Industrial and Engineering Chemistry. 2014;**20**:4045-4053. DOI: 10.1016/j.jiec.2013.12.107

[4] Boyjoo Y, Wang M, Pareek VK, Liu J, Jaroniec M. Synthesis and application of porous non-silica metal oxides submicrospheres. Chemical Society Reviews. 2016;**45**:6013-6047. DOI: 10.1039/c6cs00060f

[5] Anbia M, Koohsaryan E, Borhani A. Novel hydrothermal synthesis of hierarchically-structured zeolite LTA microspheres. Materials Chemistry and Physics. 2017;**193**: 380-390. DOI: 10.1016/j.matchemphys.2017.02.048

[6] Snelders DJM, Valega Mackenzie FO, Boersma A, Peeters RHM. Zeolites as coating materials for Fiber Bragg Grating chemical sensors for extreme conditions. Sensors and Actuators B. 2016;**235**:689-706. DOI: 10.1016/j.snb.2016.05.133

[7] Cheng XW, Meng QY, Chen JY, Long YC. A facile route to synthesize mesoporous ZSM-5 zeolite incorporating high ZnO loading in mesopores. Microporous and Mesoporous Materials. 2012;**153**:198-203. DOI: 10.1016/j.micromeso.2011.12.041

[8] Deng X, Zhang L, Guo J, Chen Q, Ma J. ZnO enhanced NiO-based gas sensors towards ethanol. Materials Research Bulletin. 2017;**90**:170-174. DOI: 10.1016/j.materresbull.2017.02.040

[9] Vilaseca M, Coronas J, Cirera A, Cornet A, Morante JR, Santamaria J. Gas detection with SnO_2 sensors modified by zeolite films. Sensors and Actuators B. 2007;**124**:99-110. DOI: 10.1016/j.snb.2006.12.009

[10] Varsani P, Afonja A, Williams DE, Parkin IP, Binions R. Zeolite-modified WO_3 gas sensors-enhanced detection of NO_2. Sensors and Actuators B. 2011;**160**:475-482. DOI: 10.1016/j.snb.2011.08.014

[11] Hagen G, Dubbe A, Retting F, Jerger A, Birkhofer T, Müller R, Plog C, Moos R. Selective impedance based gas sensors for hydrocarbons using ZSM-5 zeolite films with choromiun (III) oxide interface. Sensors and Actuators B. 2006;**119**:441-448. DOI: 10.1016/j.snb.2005.12.052

[12] Tarttelin-Hernández P, Hailes SMV, Parkin IP. Hydrocarbon detection with metal oxide semiconducting gas sensors modified by overlayer or admixture of zeolites Na-A, H-Y and H-ZSM-5. Sensors and Actuators B. 2017;**242**:1281-1295. DOI: 10.1016/j.snb.2016.09.00

[13] Mir MA, Bhat MA, Naikoo RA, Bhat RA, Khan M, Shaik M, Kumar P, Sharma PK, Tomar R. Utilization of zeolite/polymer composites for gas sensing: A review. Sensors and Actuators B. 2017;**242**:1007-1020. DOI: 10.1016/j.snb.2016.09.152

[14] Olad A, Khatamian M, Naseri B. Preparation of polyaniline nanocomposite with natural clinoptilolite and investigation of its special properties. International Journal of Nanoscience and Nanotechnology. 2010;**6**:43-52

[15] Sun B, Zhou G, Zhang H. Synthesis, functionalization and applications of morphology-controllable silica-based nanostructures: A review. Progress in Solid State Chemistry. 2016;**44**:1-19. DOI: 10.1016/j.progsolidstchem.2016.01.001

[16] Fakoya MF, Shah SN. Emergence of nanotechnology in the oil and gas industry: Emphasis on the application of silica nanoparticles, In Petroleum. 2017;**3**(4):391-405. ISSN 2405-6561. https://doi.org/10.1016/j.petlm.2017.03.001

[17] Rahman IA, Padavettan V. Synthesis of silica nanoparticles by sol-gel: Size-dependent properties, surface modification, and applications in silica-polymer nanocomposites—A review. Journal of Nanomaterials. 2012:1-15. DOI: 10.1155/2012/132424

[18] Meléndez-Ortiz HI, Mercado-Silva A, García-Cerda LA, Castruita G, Perera-Mercado YA. Hydrothermal sythesis of mesoporous silica MCM-41 using commercial sodium silicate. Journal of the Mexican Chemical Society. 2013;**57**:73-79

[19] Meléndez-Ortiz HI, Puente-Urbina B, Castruita-de León G, Mata-Padilla JM, García-Uriostegui L. Synthesis of spherical SBA-15 mesoporous silica. Influence of reaction conditions on the structural order and stability. Ceramics International. 2016;**42**:7564-7570. DOI: 10.1016/j.ceramint.2016.01.163

[20] Golezani AS, Fateh AS, Mehrabi HA. Synthesis and characterization of mesoporous silica material produced by hydrothermal continues pH adjusting path way. Progress in Natural Science. 2016;**26**:411-414. DOI: 10.1016/j.pnsc.2016.07.003

[21] Yang L, Wu H, Jia J, Ma B, Li J. Synthesis of bimodal mesoporous silica with coexisting phases by co-hydrothermal aging route with P123 containing gel and F127 containing gel. Microporous and Mesoporous Materials. 2017;**253**:151-159. DOI: 10.1016/j.micromeso.2017.06.037

[22] Dudarko OA, Gunathilake C, Sliesarenko VV, Zub YL, Jaroniec M. Microwave-assisted and conventional hydrothermal synthesis of ordered mesoporous silicas with P-containing functionalities. Colloids and Surfaces, A: Physicochemical and Engineering Aspects. 2014;**459**:4-10. DOI: 10.1016/j.colsurfa.2014.06.036

[23] Meléndez-Ortiz HI, Perera-Mercado YA, García-Cerda LA, Mercado-Silva JA, Castruita G. Influence of the reaction conditions on the thermal stability of mesoporous MCM-48 silica obtained at room temperature. Ceramics International. 2014;**40**:4155-4161. DOI: 10.1016/j.ceramint.2013.08.072

[24] Meléndez-Ortiz HI, García-Cerda LA, Olivares-Maldonado Y, Castruita G, Mercado-Silva JA, Perera-Mercado YA. Preparation of spherical MCM-41 molecular sieve at room temperature: Influence of the synthesis conditions in the structural properties. Ceramics International. 2012;**38**:6353-6358. DOI: 10.1016/j.ceramint.2012.05.007

[25] Castruita-de León G, Perera-Mercado YA, García-Cerda LA, Mercado-Silva JA, Meléndez-Ortiz HI, Olivares-Maldonado Y, Alvarez-Contreras L. Synthesis of amino-functionalized MCM-48 silica via direct co-condensation at room temperature. Microporous and Mesoporous Materials. 2015;**204**:156-162. DOI: 10.1016/j.micromeso.2014.11.023

[26] Amonette JE, Matyás J. Functionalized silica aerogels for gas-phase purification, sensing, and catalysis: A review. Microporous and Mesoporous Materials. 2017;**250**:100-119. DOI: 10.1016/j.micromeso.2017.04.055

[27] Xiao L, Grogan MDW, Wadsworth WJ, England R, Birks TA. Stable-low optical nanofibers embedded in hydrophobic aerogel. Optics Express. 2011;**19**:764-770

[28] El-Nahhal IM, Salem JK, Kuhn S, Hammad T, Hempelmann R, Al Bhaisi S. Synthesis & characterization of silica coated and functionalized silica coated zinc oxide nanomaterials. Powder Technology. 2016;**287**:439-446. DOI: 10.1016/j.powtec.2015.09.042

[29] Li X, Li D, Xu J, Jin H, Jin D, Peng X, Hong B, Li J, Yang Y, Ge H, Wang X. Calcination-temperature-dependent gas-sensing properties of mesoporous nickel oxides nanowires as ethanol sensors. Powder Technology. 2017;**318**:40-45. DOI: 10.1016/j.powtec.2017.05.020

[30] Kita J, Schubert F, Retting F, Engelbrecht A, Groß A, Moos R. Ceramic alumina substrates for high-temperature gas sensors-implications for applicability. Procedia Engineering. 2014;**87**:1005-1508. DOI: 10.1016/j.proeng.2014.11.584

[31] Castruita G, Perera-Mercado YA, Saucedo-Salazar EM. Sol-gel aluminum hydroxides and their thermal transformation studies for the production of α-alumina. Journal of Inorganic and Organometallic Polymers. 2013;**23**:1145-1152. DOI: 10.1007/s10904-013-9905-y

[32] Hyodo T, Hashimoto T, Ueda T, Nakagoe O, Kamada K, Sasahara T, Tanabe S, Shimizu Y. Adsorption/combustion-type VOC sensors employing mesoporous γ-alumina co-loaded with noble-metal and oxide. Sensors and Actuators B. 2015;**220**:1091-1104. DOI: 10.1016/j.snb.2015.06.065

[33] Sharma K, Islam SS. Optimization of porous anodic alumina nanostructure for ultra-high sensitive humidity sensor. Sensors and Actuators B. 2016;**237**:443-451. DOI: 10.1016/j.snb.2016.06.041

[34] Norek M, Stepniowski WJ, Polánski M, Zasada D, Bojar Z, Bystrzycki JA. Comparative study on the hydrogen absorption of thin films at room temperature deposited on non-porous glass substrate and nano-porous anodic aluminum oxide (AAO) template. Inter. J. Hydrogen Energy. 2011;**36**:11777-11784. DOI: 10.1016/j.ijhydene.2011.06.046

[35] Mozalev A, Calavia R, Vázquez RM, Gracia I, Cané C, Correig X, Vilanova X, Gispert-Guirado F, Hubálek J, Llobet E. MEMS-microhotplate-based hydrogen gas sensor utilizing the nanostructured porous-anodic-alumina-supported WO_3 active layer. International Journal of Hydrogen Energy. 2013;**38**:8011-8021. DOI: 10.1016/j.ijhydene.2013.04.063

[36] MSA Safety Company. Gas Detection Handbook. Key Concepts & Reference Materials for Permanently Installed Gas-monitoring Systems. 5th ed. US: MSA Instrument Division; 2007. 145 p

[37] Maduraiveeran G, Jin W. Nanomaterials based electrochemical sensor and biosensor platforms for environmental applications. Trends in Environmental Analytical Chemistry. 2017;**13**:10-23. DOI: 10.1016/j.teac.2017.02.001

[38] Fergus JW. Solid electrolyte based sensor for measurement of CO and hydrocarbon gases. Sensors and Actuators B. 2007;**122**:683-693. DOI: 10.1016/j.snb.2006.06.024

[39] Xinxin X, Chen T, Zhao R, Wang Z, Wang Y. A low temperature butane gas sensor used Pt nanoparticles-modified AZO macro/mesoporous nanosheets as sensing material. Sensors and Actuators B. 2018;**254**:227-238. DOI: 10.1016/j.snb.2017.07.091

[40] Xu H, Zhang J, Rehman AU, Gong L, Kan K, Li L. Synthesis of NiO@CuO nanocomposites as high-performance gas sensing for NO_2 at room temperature. Applied Surface Science. 2017;**412**:230-237. DOI: 10.1016/j.apsusc.2017.03.213

[41] Ni Y, Du W, Fang W, Chen X, liu W, Wang Y, Liu J. High response to nitrogen dioxide derived from antimony peroxide modified tin oxide porous nanocomposites serving as gas sensing material. Sensors and Actuators B. 2017;**247**:216-223. DOI: 10.1016/j.snb.2017.03.019

[42] Hung CM, Hoa ND, Duy NV, Toan NV, Le DTT, Hieu NV. Synthesis and gas-sensing characteristics of α-Fe_2O_3 hollow balls. Journal of Science: Advanced Materials and Devices. 2016;**1**:45-50. DOI: 10.1016/j.jsamd.2016.03.003

[43] Wongrat E, Chanlek N, Chueaiarrom C, Samransuksamer B, Hongsith N, Choopun S. Low temperature ethanol response enhancement of ZnO nanostructures sensors decorated with gold nanoparticles exposed to UV illumination. Sensors and Actuators B. 2016;**251**:188-197. DOI: 10.1016/j.sna.2016.10.022 0924-4247

[44] Karaduman I, Er E, Celikkan H, Erk N, Acar S. Room-temperature ammonia gas sensor based on reduced graphene oxide nanocomposites decorated by Ag, Au and Pt nanoparticles. Journal of Alloys and Compounds. 2017;**722**:569-578. DOI: 10.1016/j.jallcom.2017.06.152

[45] Liu L, Song P, Wei Q, Yang Z, Wang Q. Synthesis of porous SnO_2 hexagon nanosheets loaded with Au nanoparticles for high performance gas sensor. Materials Letters. 2017;**201**:211-215. DOI: 10.1016/j.matlet.2017.05.024

[46] Zhang B, Li M, Song Z, Kan H, Yu H, Liu Q, Zhang G, Liu H. Sensitive H_2S gas sensor employing colloidal zinc oxide quantum dots. Sensors and Actuators B. 2017;**249**:558-563. DOI: 10.1016/j.snb.2017.03.098

[47] Balamurugan C, Lee DW, Maheswari AR, Parmar M. Porous wide band gap $BiNbO_4$ ceramic nanopowder synthesized by low temperature solution-based method for gas sensing applications. RSC Advances. 2014;**4**:54625-54630. DOI: 10.1039/c4ra08898k

[48] Authority PS. Petroleum Safety Authority Norway [Internet]. 2017. Available from: http://www.psa.no/risk-level/category876.html [Accessed: 2016-06-15]

[49] Abbasi T, Abbasi SA. Accidental risk of superheated liquids and a framework for predicting the superheat limit. Journal of Loss Prevention in the Process Industries. 2007;**20**:165-181. DOI: 10.1016/j.jlp.2005.11.002

[50] Polanco G. Phase Change within Flows from Breaches of Liquiefied Gas Pipelines. Coventry, UK: Coventry University; 2008

[51] Deaves DM, Gilham S, Mitchell BH, Woodburn P, Shepherd AM. Modelling of catastrophic flashing releases. Journal of Hazardous Materials. 2001;**88**(1):1-32. DOI: 10.1016/S0304-3894(01)00284-9

[52] Demichela M, Piccinini N, Poggio A. Analysis of an LPG accidental release. Safety and Environmental Protection. 2004;**82**(2):128-131. DOI: 10.1205/095758204322972762

[53] Polanco G, Holdo AE, Munday AG. General review of flashing jet studies. Journal of Hazardous Materials. 2010;**173**:2-18. DOI: 10.1016/j.jhazmat.2009.08.138

[54] Zhifu Z, Weitao W, Bin C, Guoxiang W, Liejin G. An experimental study on the spray and thermal characteristics of R134a two-phase flashing spray. International Journal of Heat and Mass Transfer. 2012;**55**:4460-4468. DOI: 10.1016/j.ijheatmasstransfer.2012.04.021

[55] Allen JT. Laser-based Velocity Measurement in Two-phase Flashing Propane Jet Releases. Health and Safety Laboratory; 1996

[56] Allen JT. Laser-based Droplet Size measurEments in Two-phase, Flashing Propane Jets. Health and Safety Laboratory; 1996

[57] Allen JT. Laser-Based Measurements in two-Phase Flashing Propane Jets. University of Sheffield; 1998

[58] Yildiz D, Rambund P, Van Beeck JPJA, Buchlin J-M. Thermal characterization of a R134A two-phase flashing jet. In: ICLASS 2003—9th International Conference on Liquid Atomization and Spray Systems; July 2003; Sorrento, Italy

[59] Moreira JRS, Bullard CW. Pressure drop and flashing mechanisms in refrigerant expansion devices. International Journal of Refrigeration. 2003;**26**:840-848. DOI: 10.1016/S0140-7007(03)00070-7

[60] Yildiz D, Beeck JPJA, Riethmuller ML. Global rainbow thermometry applied to a flashing two-phase R134-A Jet. In 11th International Symposium on Application of Laser Techniques to Fluid Mechanics; 2002; Lisbon, Portugal

[61] Friedel SKL. Assessment of the maximum possible liquid superheat during flashing leak flow. Journal of Loss Prevention in the Process Industries. 1997;**10**(**54**):345-350

[62] Sarkar R, Mondal PK, Chatterjee BK. Study of acoustic emission due to vaporisation of superheated droplets at higher pressure. Physics Letters A. 2017;**381**:2531-2537

[63] Mondal PK, Sarkar R, Chatterjee BK. Response of superheated droplet detector (SDD) and bubble detector (BD) to interrupted irradiations. Nuclear Instruments and Methods in Physics Research A. 2017;**857**:111-114

[64] Ho LT, Cuong ND, Hoa TT, Khieu DQ, Long HT, Quang DT, Hoa ND, Hieu NV. Synthesis, characterization, and comparative gas sensing properties of tin dioxide nanoflowers and porous nanospheres. Ceramics International;**10**:14819-14825. DOI: 10.1016/j.ceramint.2015.08.003

[65] Picasso G, Sun Kou MR, Vargasmachuca O, Rojas J, Zavala C, Lopez A, Irusta S. Sensors based on porous Pd-doped hematite (α-Fe_2O_3) for LPG detection. Microporous and Mesoporous Materials. 2014;**185**(1):79-85. DOI: 10.1016/j.micromeso.2013.11.014

[66] Wagner T, Bauer M, Sauerwal T, Kohl CD, Tiemanna M. X-ray absorption near-edge spectroscopy investigation of the oxidation state of Pd species in nanoporous SnO_2 gas sensors for methane detection. Thin Solid Films. 2011;**520**(3):909-912. DOI: 10.1016/j.tsf.2011.04.187

[67] Flingelli GK, Fleischer MM, Meixner H. Selective detection of methane in domestic environments using a catalyst sensor system based on Ga_2O_3. Sensors and Actuators B: Chemical. 1998;**48**(1-3):258-262. DOI: 10.1016/S0925-4005(98)00054-9

[68] Waitz T, Becker B, Wagner T, Sauerwald T, Kohl C-D, Tiemann M. Ordered nanoporous SnO_2 gas sensors with high thermal stability. Sensors and Actuators B: Chemical. 2010;**150**(2):788-793. DOI: 10.1016/j.snb.2010.08.001

[69] Song C, Wu G, Sun B, Xiong Y, Zhu S, Hu Y, Gu H, Wang Y, Chen W. Pt-WO_3 porous composite ceramics outstanding for sensing low concentrations of hydrogen in air at room temperature. International Journal of Hydrogen Energy. 2017;**42**(9):6420-6424. DOI: 10.1016/j.ijhydene.2016.12.101

[70] Gaspera ED, Busu D, Guglielmi M, Martucci A, Bello V, Mattei G, Post ML, Cantalini C, Agnoli S, Granozzi G, Sadek AZ, Kalantar-Zadeh K, Wlodarski W. Comparison study of conductometric, optical and SAW gas sensors based on porous sol–gel silica films doped with NiO and Au nanocrystals. Sensors and Actuators B: Chemical. 2010;**143**(2):567-573. DOI: 10.1016/j.snb.2009.09.060

[71] Xu X, Yin M, Li N, Wang W, Sun B, Liu M, Zhang D, Li Z, Wang C. Vanadium-doped tin oxide porous nanofibers: Enhanced responsivity for hydrogen detection. Talanta. 2017;**167**(15):638-644. DOI: 10.1016/j.talanta.2017.03.013

[72] Prasad RM, Gurlo A, Riedel R, Hübner M, Barsan N, Weimar U. Microporous ceramic coated SnO_2 sensors for hydrogen and carbon monoxide sensing in harsh reducing conditions. Sensors and Actuators B: Chemical. 2010;**149**(1):105-109. DOI: 10.1016/j.snb.2010.06.016

[73] Xiao B, Wang D, Song S, Zhai C, Wang F, Zhanga M. Fabrication of mesoporous In_2O_3 nanospheres and their ultrasensitive NO_2 sensing properties. Sensors and Actuators B. 2017;**248**:519-526. DOI: 10.1016/j.snb.2017.04.022

[74] Liu X, Hu M, Wang Y, Liu J, Qin Y. High sensitivity NO_2 sensor based on CuO/p-porous silicon heterojunction at room temperature. Journal of Alloys and Compounds. 2016;**685**:364-369. DOI: 10.1016/j.jallcom.2016.05.215

[75] Gao L, Cheng Z, Xiang Q, Zhang Y, Xu J. Porous corundum-type In_2O_3 nanosheets: Synthesis and NO_2 sensing properties. Sensors and Actuators B. 2015;**208**:436-443. DOI: 10.1016/j.snb.2014.11.053

[76] Yuliarto B, Honma I, Katsumura Y, Zhou H. Preparation of room temperature NO_2 gas sensors based on W- and V-modified mesoporous MCM-41 thin films employing surface photovoltage technique. Sensors and Actuators B: Chemical. 2006;**114**(1):109-119. DOI: 10.1016/j.snb.2005.04.016

[77] Mun Y, Park S, An S, Lee C, Kim HW. NO_2 gas sensing properties of Au-functionalized porous ZnO nanosheets enhanced by UV irradiation. Ceramics International. 2013; **9**(8):8615-8622. DOI: 10.1016/j.ceramint.2013.04.035

[78] Xu L, Dong B, Wang Y, Bai X, Liu QQ, Song H. Electrospinning preparation and room temperature gas sensing properties of porous In_2O_3 nanotubes and nanowires. Sensors and Actuators B: Chemical. 2010;**147**(2):531-538. DOI: 10.1016/j.snb.2010.04.003

[79] Zhu Y, Wang Y, Duan G, Zhang H, Li Y, Liu G, Lei X, Cai W. In situ growth of porous ZnO nanosheet-built network film as high-performance gas sensor. Sensors and Actuators B: Chemical. 2015;**221**(31):350-356. DOI: 10.1016/j.snb.2015.06.115

[80] Li Z, Wang J, Wang N, Yan S, Liu W, Qing FY, Wang Z. Hydrothermal synthesis of hierarchically flower-like CuO nanostructures with porous nanosheets for excellent H_2S sensing. Journal of Alloys and Compounds. 2017;**725**:1136-1143. DOI: 10.1016/j.jallcom.2017.07.218

[81] Wang Y, Duan G, Zhu Y, Zhang H, Xu Z, Dai Z, Cai W. Room temperature H_2S gas sensing properties of In_2O_3 micro/nanostructured porous thin film and hydrolyzation-induced enhanced sensing mechanism. Sensors and Actuators B: Chemical. 2016;**228**(2):74-84. DOI: 10.1016/j.snb.2016.01.002

[82] Gao X, Sun Y, Zhu C, Li C, Ouyang Q, Chen Y. Highly sensitive and selective H_2S sensor based on porous $ZnFe_2O_4$ nanosheets. Sensors and Actuators B: Chemical. 2017;**246**:662-672. DOI: 10.1016/j.snb.2017.02.100

[83] Huang Y, Chen W, Zhang S, Kuang Z, Ao D, Alkurd NR, Zhou W, Liu W, Shen W, Li Z. A high performance hydrogen sulfide gas sensor based on porous α-Fe_2O_3 operates at room-temperature. Applied Surface Science. 2015;**351**:1025-1033. DOI: 10.1016/j.apsusc.2015.06.053

[84] Qiang Z, Ma SY, Jiao HY, Wang TT, Jiang XH, Jin WX, Yang HM, Chen H. Highly sensitive and selective ethanol sensors using porous SnO_2 hollow spheres. Ceramics International. 2016;**42**:8983-18990. DOI: 10.1016/j.ceramint.2016.09.053

[85] Gong F, Gong Y, Liu H, Zhang M, Zhang Y, Li F. Porous In_2O_3 nanocuboids modified with Pd nanoparticles for chemical sensors. Sensors and Actuators B. 2016;**223**:384-391. DOI: 10.1016/j.snb.2015.09.053

[86] Xiong Y, Xu W, Zhu Z, Xue Q, Lu W, Ding D, Zhu L. ZIF-derived porous ZnO-Co_3O_4 hollow polyhedrons heterostructure with highly enhanced ethanol detection performance. Sensors and Actuators B: Chemical. 2017;**253**:523-532. DOI: 10.1016/j.snb.2017.06.169

[87] Wen Z, Zhu L, Li Y, Zhang Z, Ye Z. Mesoporous Co_3O_4 nanoneedle arrays for high-performance gas sensor. Sensors and Actuators B: Chemical. 2014;**203**:873-879. DOI: 10.1016/j.snb.2014.06.124

[88] Xue P, Yang X, Lai X, Xia W, Li P, Fang J. Controlling synthesis and gas-sensing properties of ordered mesoporous In_2O_3-reduced graphene oxide (rGO) nanocomposite. Science Bulletin. 2015;**60**(15):1348-1354. DOI: 10.1007/s11434-015-0852-6

[89] Zhang C, Wang J, Hu R, Qiao Q, Li X. Synthesis and gas sensing properties of porous hierarchical SnO_2 by grapefruit exocarp biotemplate. Sensors and Actuators B: Chemical. 2016;**222**:1134-1143. DOI: 10.1016/j.snb.2015.08.016

[90] Han D, Song P, Zhang S, Zhang H, Xu Q, Wang Q. Enhanced methanol gas-sensing performance of Ce-doped In_2O_3 porous nanospheres prepared by hydrothermal method. Sensors and Actuators B: Chemical. 2015;**216**:488-496. DOI: 10.1016/j.snb.2015.04.083

[91] Li Y, Deng D, Xing X, Chen N, Liu X, Xiao X, Wang YA. High performance methanol gas sensor based on palladium-platinum-In_2O_3 composited nanocrystalline SnO_2. Sensors and Actuators B: Chemical. 2016;**237**:133-141. DOI: 10.1016/j.snb.2016.06.088

[92] Wang J, Xu Y, Xu W, Zhang M, Chen X. Simplified preparation of SnO_2 inverse opal for methanol gas sensing performance. Microporous and Mesoporous Materials. 2015;**208**:93-97. DOI: 10.1016/j.micromeso.2015.01.038

[93] Tian J, Wang J, Hao Y, Du H, Li X. Toluene sensing properties of porous Pd-loaded flower-like SnO_2 microspheres. Sensors and Actuators B: Chemical. 2014;**202**:795-802. DOI: 10.1016/j.snb.2014.05.048

[94] Ma H, Xu Y, Rong Z, Cheng X, Gao S, Zhang X, Zhao H, Huo L. Highly toluene sensing performance based on monodispersed Cr_2O_3 porous microspheres. Sensors and Actuators B: Chemical. 2012;**174**:325-331. DOI: 10.1016/j.snb.2012.08.073

[95] Gao P, Ji H, Zhou Y, Li X. Selective acetone gas sensors using porous WO_3–Cr_2O_3 thin films prepared by sol-gel method. Thin Solid Films. 2012;**520**(7):3100-3106. DOI: 10.1016/j.tsf.2011.12.003

[96] Xie X, Wang X, Tian J, Song X, Wei N, Cui H. Growth of porous ZnO single crystal hierarchical architectures with ultrahigh sensing performances to ethanol and acetone gases. Ceramics International. 2017;**43**(1):1121-1128. DOI: 10.1016/j.ceramint.2016.10.050

[97] Wilson SA, Jourdain RPJ, Zhang Q, Dorey RA, Bowen CR, Willander M, Wahab QU, Al-hilli SM, Nur O, Quandt E, Johansson C, Pagounis E, Kohl M, Matovic J, Samel B, Van der Wijngaart W, Jager EWH, Carlsson D, Djinovic Z, Wegener M, Moldovan C, Iosub R, Abad E, Wendlandt M, Rusu C, Persson K. New materials for micro-scale sensors and actuators an engineering review. Materials Science and Engineering. 2007;**56**(1-6):1-129. DOI: 10.1016/j.mser.2007.03.001

[98] Divya T, Nikhila MP, Anju M, Arsha KTV, Akhila AK, Ravikiran YT, Renuka NK. Nanoceria based thin films as efficient humidity sensors. Sensors and Actuators A. 2017;**261**:85-93. DOI: 10.1016/j.sna.2017.05.008

[99] Wang Y, Duan G, Zhu Y, Zhang H, Xu Z, Dai Z, Cai W. Room temperature H_2S gas sensing properties of In_2O_3 micro/nanostructured porous thin film and hydrolyzation-induced enhanced sensing mechanism. Sensors and Actuators B. 2016;**228**:74-84. DOI: 10.1016/j.snb.2016.01.002

[100] Al-Salmana HS, Abdullaha MJ. Hydrogen gas sensing based on ZnO nanostructure prepared by RF-sputtering on quartz and PET substrates. Sensors and Actuators B. 2013;**181**:259-266. DOI: 10.1016/j.snb.2013.01.065

[101] Wagner T, Waitz T, Roggenbuck J, Fröba M, Kohl CD, Tiemann M. Ordered mesoporous ZnO for gas sensing. Thin Solid Films. 2007;**515**(23):8360-8363. DOI: 10.1016/j.tsf.2007.03.021

[102] Blanka TA, Eksperiandova LP, Belikov KN. Recent trends of ceramic humidity sensors development: A review. Sensors and Actuators B. 2016;**228**:416-442. DOI: 10.1016/j.snb.2016.01.015

Chapter 5

Zinc-Tin-Oxide-Based Porous Ceramics: Structure, Preparation and Properties

Tamara Ivetić

Additional information is available at the end of the chapter

http://dx.doi.org/10.5772/intechopen.71581

Abstract

Zinc-tin-oxide-based ceramics have been extensively investigated especially regarding the synthesis of zinc stannate (Zn_2SnO_4), a spinel structure ternary compound with a wide range of possible applications. Among all of those, the best-known use of this material is in the combustion gas and moisture sensors. This chapter presents the research results review on the structure, morphology, and properties of mechanochemically synthesized Zn_2SnO_4 ceramics with large open porosity, as well as the results obtained during its solid-state processing optimization. Also shown is the review of the results obtained in the study of the influence of addition of the small amounts of bismuth oxide (Bi_2O_3) on the obtained Zn_2SnO_4 structure, microstructure, and electrical properties, as it provides the condition for the liquid phase sintering and creates a new dynamics in the zinc-tin-oxide reaction sintering process.

Keywords: ZnO-SnO_2 ceramics, spinels, zinc stannate, mechanical activation, sintering

1. Introduction

Zinc stannate is a non-toxic transparent n-type semiconducting oxide material whose electrical conductivity is sensitive to the changes of oxygen stoichiometry and environmental atmosphere, so it is mostly known for its gas-sensing (detection of combustion gases, CO, H_2, NO, NO_2, and moisture) applications [1–3]. However, the unique electrical and optical properties of the zinc stannate, which has been manufactured so far in different forms (thin and thick films, polycrystalline powders, composite and porous sintered ceramics) [4–7], makes it a suitable material for the various other applications as well (as functional coatings, flat panel displays, thin film solar cells, windows coatings, transparent conducting electrodes, as anode material in Li-ion batteries, as various photoelectrical devices, in photocatalysis) [8–20]. Zinc stannate is a spinel compound with a general formula Zn_2SnO_4 and a band gap of 3.6 eV. The spinel

Zn_2SnO_4 in the bulk form is stable in the inverse spinel structure, with a face-centered cubic unit cell (space group Fd3m), where Zn^{2+} occupy the 8a sites, and both Zn^{2+} and Sn^{4+} cations occupy the 16d sites, while O is placed in the 32e sites. Its unit cell parameter has a value of a = 8.6574 Å (JCPDS PDF 24-1470). The spinel-type structures can have big cation disorders in the crystal lattice and certain nonstoichiometry. Nevertheless, the disorders in spinels are not conventional so there is no change in the symmetry. The most general spinel formula is AB_2O_4, where A is two valent or four valent metal ions, and B are two valent or tree valent metal ions. To this day, there have been synthesized over 200 different types of spinel oxide compounds. Some spinel compounds are known to have the characteristic sensor and catalytic properties, like Zn_2SnO_4, and exhibit complex disordering phenomena related to the redistribution of cations over (B) and [A] sublattices in their structure. The partly inverse spinels like Zn_2SnO_4 have four valent ions on octahedral positions [A] and two valent ions in some ration distributed over tetrahedral (B) and octahedral coordination [A]. The zinc stannate compound may then be presented as $(Zn^{2+})[Sn^{4+}Zn^{2+}]O_4$ to emphasize the site occupancy at the atomic level.

The previous solid-state synthesis investigations established that complete Zn_2SnO_4 formation needs prolonged mechanical activation of the starting reaction precursors (ZnO and SnO_2 powders) and considerable high temperature of sintering (in the range from 1000 to 1280°C). The solid-state chemical reaction between the ZnO and SnO_2 starts relatively slow at 1000°C while the monophase polycrystalline zinc stannate is formed at 1280°C.

2. Mechanochemical activation and consolidation of ZnO-SnO_2 powder system

Finding optimal conditions of mechanochemical activation is the first and foremost important processing step for obtaining the right texture, particle size distribution and chemical reactivity of the starting powders in the solid-state synthesis of the polycrystalline Zn_2SnO_4 ceramics and the achievement of the wide range of its applications [21]. The mechanochemical activation consists of several processes that are usually divided into four stages: the material destruction, new surface formation, fine grinding and transformation to a completely different material structure. The optimal powder processing is a way to lower the sintering temperature necessary in the further steps of the ceramics production, which is very important fact from the stand point of the cost-effectiveness. When the starting powders of zinc oxide and tin oxide in the 2:1 molar ratio (ZnO:SnO_2 = 2:1) are mechanically activated in a planetary ball mill (Fritsch Pulverisette) in time intervals 0–160 min (with 320 rpm, ball to powder mass ratio of 40:1, in zirconium grinding media of a 500 ml vial and 10 mm diameter balls) the two stages of the grinding process occurs (**Figure 1**). The investigated samples were marked further in the text as ZSO-00, ZSO-10, ZSO-40, ZSO-80, and ZSO-160, and these marks are related to the not-activated, 10, 40, 80, and 160 min activated 2ZnO-SnO_2 powder mixtures, respectively. The first stage, up to 10 min of mechanical activation, is the increase in the powders specific surface area (S_{BET}, calculated by BET method from the linear part of N_2 adsorption isotherms [21–23]) which is related to the breaking of the powder particles and formation of the new surfaces (**Figure 2a** and **b**). The second stage brings the cold-welding and chemical reaction between the starting precursors (ZnO and SnO_2 powders),

http://dx.doi.org/10.5772/intechopen.71581

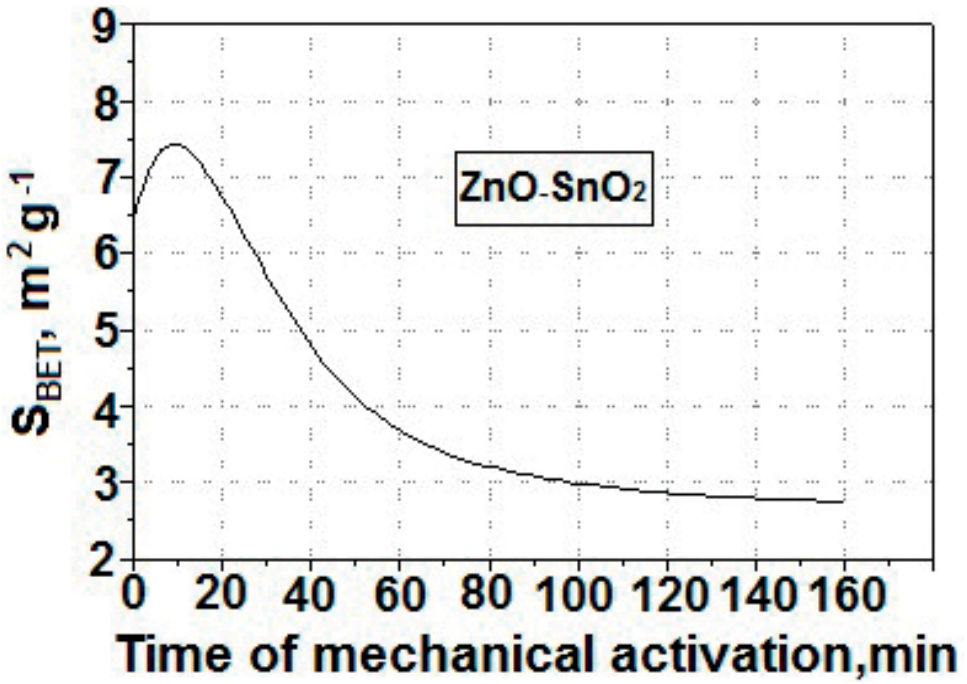

Figure 1. The specific surface area vs. the time of mechanical activation for the ZnO-SnO_2 powder system.

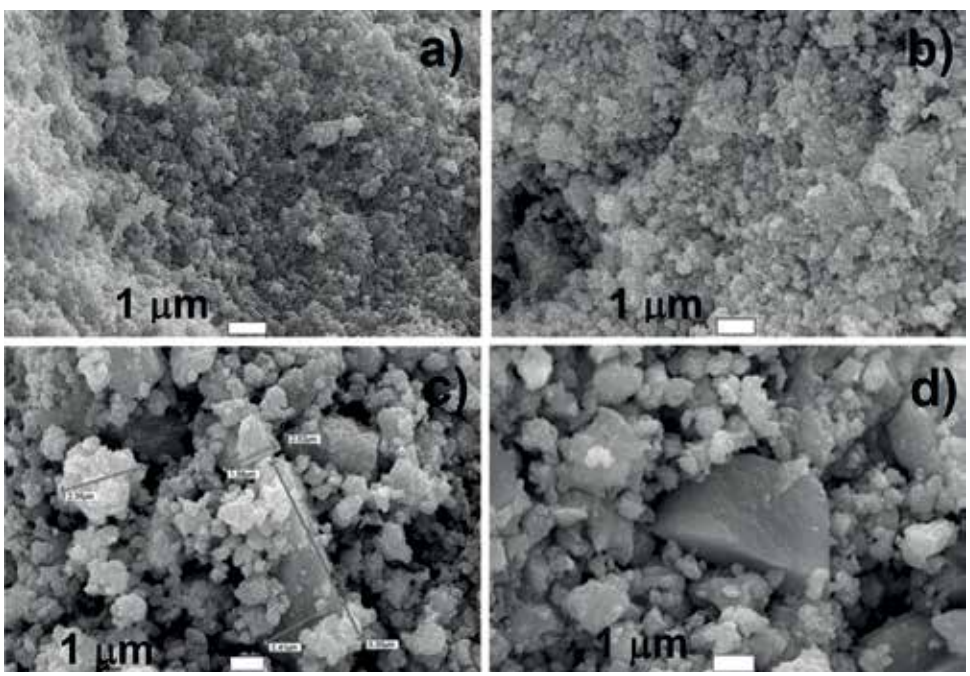

Figure 2. SEM micrographs of ZnO-SnO_2 powder mixtures activated, (a) 0, (b) 10, (c) 40, and (d) 80 min.

a formation of a new phase and a decrease in the S_{BET} (**Figure 2c** and **d**). The first sign of the spinel zinc stannate formation was noticed after 40 min of mechanical activation (results obtained by X-ray diffraction, XRD [21]). By increasing the activation time the intensities of the XRD peaks of the starting phases ZnO and SnO_2, become lower while XRD peaks of the spinel Zn_2SnO_4 phase dominates. After 160 min of mechanical activation, the Zn_2SnO_4 becomes a major phase in the system. Together with the progression of the mechanochemical reaction and formation of the zinc stannate spinel a secondary agglomeration occurs as well, which contributes mostly to a continuous decrease of S_{BET} during the second stage of the grinding process (**Figure 2c** and **d**). The microstructure of the starting ZnO and SnO_2 powder mixture characterizes in the homogeneously distributed particles of two kinds, the smaller ones with a spherical shape that belongs to ZnO and the longer ones with a polygonal shape, which belongs to the SnO_2. After 10 min of activation, there is a noticeable decrease in a number of the spherical particles because ZnO is more than six times softer material than SnO_2 (microhardness of ZnO and SnO_2 is 1.5 and 10 GPa, respectively) so firstly the drastic changes induced by mechanical activation addresses the ZnO (**Figure 2**).

The shape of the adsorption isotherms (example shown in **Figure 3a**) of all the investigated samples (different mechanically activated powder mixtures) confirms mono-multi layered adsorption on the clear and stable powder surfaces with a morphology that suffered fragmentation and aggregation during the mechanical activation and is characterized by macropores or even limited number of the micropores [21]. According to the IUPAC classification, these adsorption–desorption isotherms belong to the aggregated particles that form slit-shaped

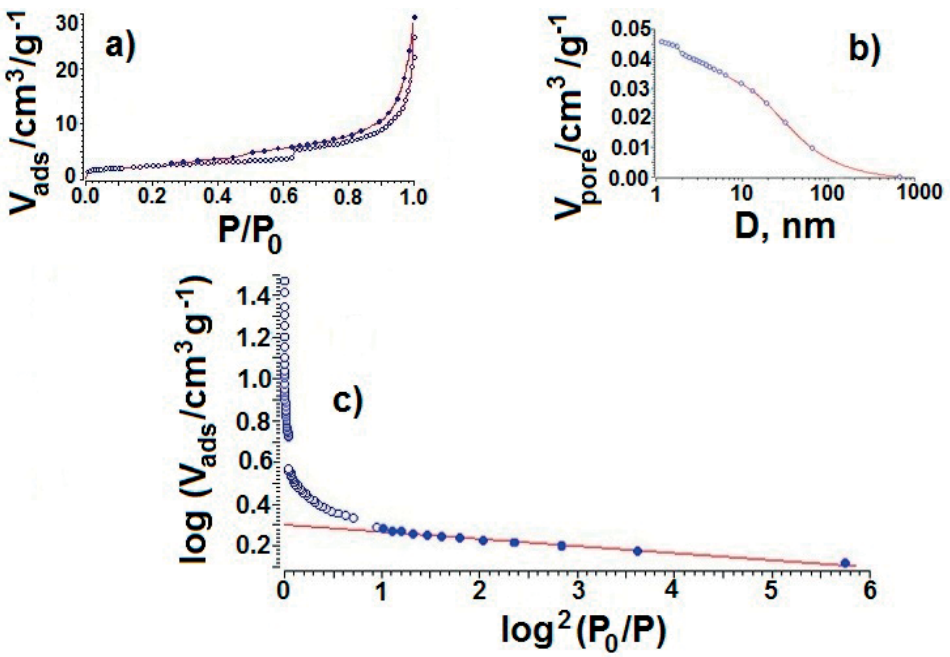

Figure 3. The nitrogen adsorption–desorption isotherm (a), the pore size distribution (b), and the pore volume distribution by Dubinin Radushevich line method (c), for the 10 min activated ZnO-SnO_2 powder mixture.

pores [22–24]. Isotherms have a reversible part (as physical adsorption is namely reverse) at the low relative pressures, when desorption is happening along the same isotherm path as adsorption, and hysteresis loops at higher relative pressures which happen because the desorption is harder when in very porous adsorbents, like in this material system, the condensation occurs inside fine pores and capillaries at lower than equilibrium pressure. The N_2 isotherm analysis (pore size distribution by Dollimore-Heal Poresizes [25] and Dubinin-Radushkevich Line [26] methods, an example shown in **Figure 3b** and **c**) gave the textural properties of the investigated different activated powder mixtures, and have shown that pores with the biggest total bulk volume were found in the powder mixture activated for 10 min, while lower total porosity (volume) was determined for the 40 min of activation, and the lowest for the other activation times (80 and 160 min) that had a smaller amount of the big pores (mesopores), like ZSO-40. The average mesopore diameters varied in the range from 22 nm (ZSO-10) to 79 nm (ZSO-80). The increase of the activation time, from 80 to 160 min, did not bring further texture-porosity evolution [21].

The second most important step in the ceramics processing is the consolidation of a mechanically activated power mixture by pressing. The microstructure of the sintered pellets (i.e. thermally treated consolidated powder mixtures) extremely depends on the quality of the green body (pressed mechanically activated powder mixture before the sintering process). It is very crucial to the whole technology of the ceramics production to establish the mathematical–physical correlation between the pressure of the compaction (consolidation), and the main macroscopic features of the investigated material (density or porosity), that is, to determine the compressibility of the investigated powders (dependence of the green body density vs. the compaction pressure). These compressibility investigations have actually a very practical nature, that is, to determine the pressing pressure needed for each of the investigated powder mixtures to obtain a specifically desired density. Different mechanochemically activated ZnO-SnO_2 powders were pressed under 49–392 MPa into 10 mm pellets. The green body density (green density) was determined for each of the samples by measuring the weight and dimensions of the obtained pellets with an error not bigger than 1% [27]. **Figure 4** shows the influence of the consolidation pressure vs. relative green density for differently activated powders from the ZnO-SnO_2 system.

The green densities of the nonactivated ZnO-SnO_2 powder mixture obtained under several applied pressures are significantly lower compared to the green densities of the 10, 40, 80 and 160 min activated ZnO-SnO_2 powder mixtures. The highest densities are obtained for the lowest activation time (10 min). Because the green densities of the 80 and 160 min activated powder mixtures have really close values, for clarity, the relative green densities of the 160 min activated powder mixture were left out in **Figure 4**. All dependency curves in **Figure 4** have the same shape, while their relationships point out to the general rule that the longtime of mechanical activation and the same applied compaction pressure results in a green density decrease. This is probably a consequence of the formation of a larger number of harder agglomerates (**Figure 2**) with prolonged activation and is actually a typical compressibility behavior of the powder materials. In other words, longer mechanical activation demands higher pressure force to obtain the green body with approximately same density. For the 80 min (and 160 min) activated ZnO-SnO_2 powder system, it is necessary to apply four times higher pressure than for 10 min

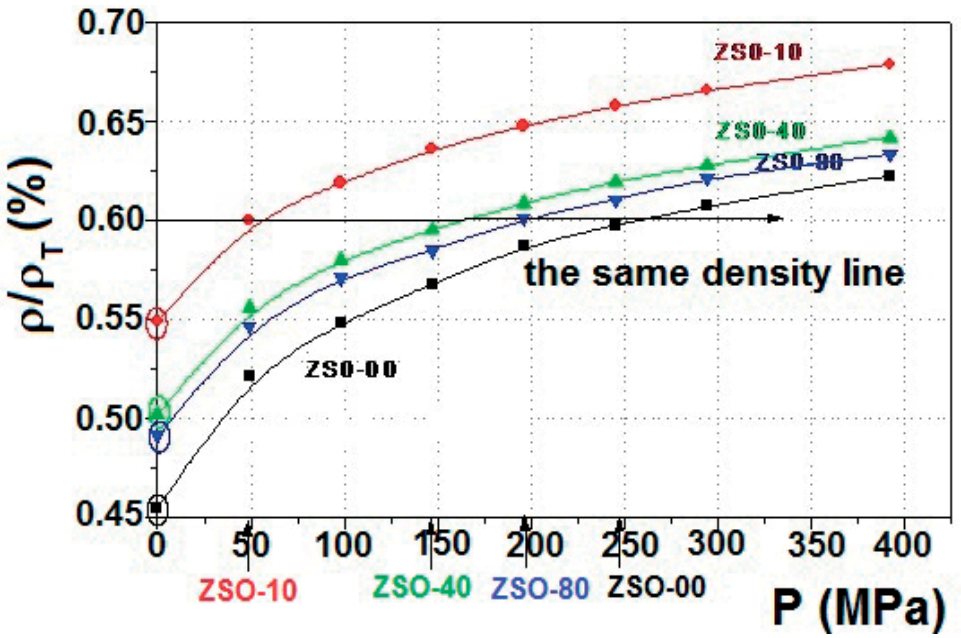

Figure 4. The pressing pressure vs. green density for the ZnO-SnO_2 system [27].

activated powder mixture to have the green body with the same density. It is easy to spot on the so-called, "the same density line" in **Figure 4**, that shows the values of the pressure that have to be applied in order to obtain the green body that has the same density (60% of the theoretical density), no matter how activated ZnO-SnO_2 powder mixture is.

3. Mechanism and kinetics of sintering, and the porosity of consolidated ZnO-SnO_2 system

In order to investigate the influence of the mechanical activation on ZnO-SnO_2 systems densification, the green bodies of the different activated ZnO-SnO_2 powder mixtures were prepared by uniaxial pressing with different pressures (250, 50, 150, 200, 200 MPa was applied for ZSO-00, ZSO-10, ZSO-40, ZSO-80, and ZSO-160, respectively) in accordance with the findings in **Figure 4**, so the starting sintering density would be the same (3.769 g/cm^3) [27, 28] for all the investigated samples. Non-isothermal sintering kinetics was determined by monitoring the relative shrinkage of the green body by sensitive dilatometer, in the air up to 1200°C, with three different heating rates (5°C/min in **Figure 5a**, 10°C/min in **Figure 5b**, and 20°C/min in **Figure 5c**). All the results are shown in **Figure 5**.

The dilatometric results point to 800°C as the temperature when the densification process starts in ZSO-40, ZSO-80, and ZSO-160 samples. The dilatometric behavior of ZSO-00 and ZSO-10 is somehow different. The initial expansion in the ZSO-00 and ZSO-10 samples starts around 1000°C and continues in shrinkage. It is very important to determine the origin of this

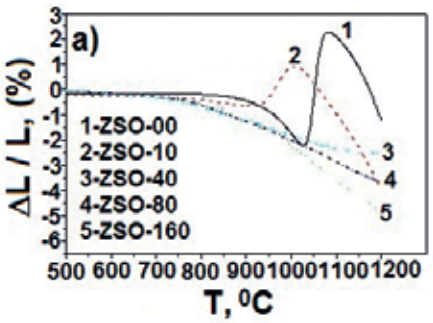

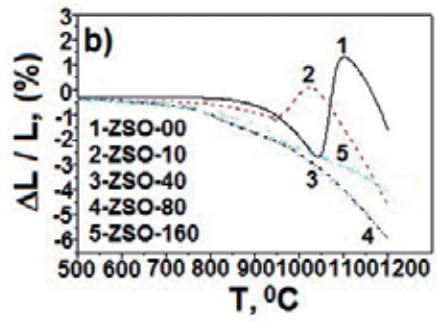

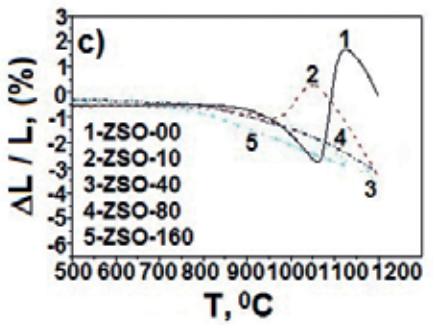

Heating speed, 5 °C/min	ZSO-00	ZSO-10
$T_{MIN.}$, °C	1026	916
$T_{MAX.}$, °C	1082	1008
Heating speed, 10 °C/min		
$T_{MIN.}$, °C	1044	945
$T_{MAX.}$, °C	1100	1025
Heating speed, 20 °C/min		
$T_{MIN.}$, °C	1060	957
$T_{MAX.}$, °C	1126	1050

Figure 5. The dilatometric curves of differently activated ZnO-SnO_2 samples obtained by non-isothermal sintering in air, at different heating rates: (a) 5°C/min, (b) 10°C/min, and (c) 20°C/min, and up to 1200°C [28–30]. The inset table shows the minimum and maximum temperatures where the expansion and the shrinkage start, respectively, for the ZSO-00 and ZSO-10 samples.

deviation and its impact on the process of densification and further evolution of the material microstructure. This expansion cannot be explained just by the simple differences in the molar volumes of the samples because the theoretical density of zinc stannate spinel (6.42 g/cm^3) is very close to the theoretical density of the equimolar mixture of ZnO and SnO_2 (6.24 g/cm^3). Several mechanisms are described in the literature to explain phenomena like this, that is, the expansion of the powders during the solid-state reactions. In the oxide systems as ZnO-SnO_2, it is explained by to the separation of the particles when the reaction product is formed. The chemical reaction starts at 1026°C (when the heating speed is 5°C/min), 1044°C (when the heating speed is 10°C/min) and 1060°C (when the heating speed is 20°C/min) in the ZSO-00 sample, and at 916°C (heating speed, 5°C/min), 945°C (heating speed, 10°C/min) and 957°C (heating speed, 20°C/min) for the ZSO-10 sample (Inset Table in **Figure 5**). During the chemical reaction, the product, zinc stannate, causes the expansion of the ZSO-00 and ZSO-10 samples because the starting powder grains are being separated in the way that is illustrated in **Figure 6**.

The reaction sintering is a process during which the chemical reaction and the densification happen simultaneously. The temperature of the reaction sintering beginning is obviously lower for the longer mechanically activated ZnO-SnO_2 powder mixtures and higher when higher heating speeds were used during the thermal treatment. Some believe that the most important fact for the reaction sintering process is a defect degree of the formed microstructure during the chemical reaction. For the systems where the chemical reaction does not induce the

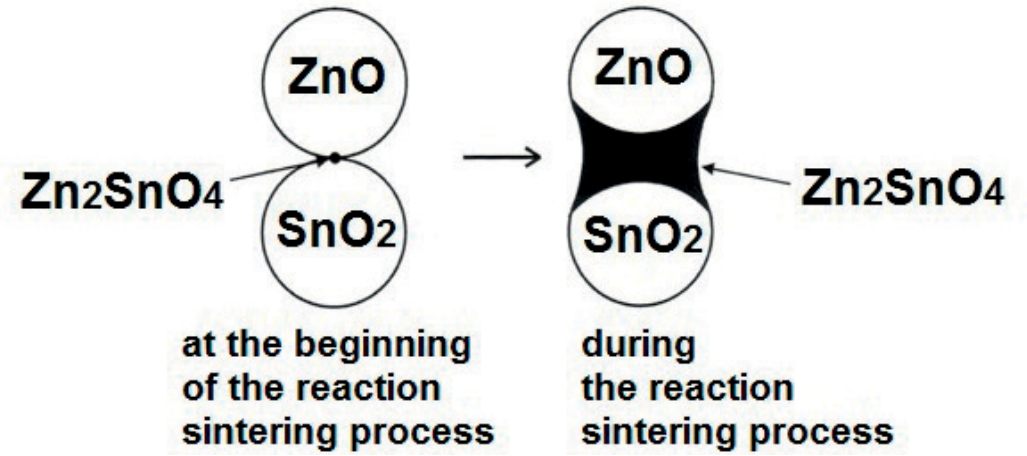

Figure 6. The schematic illustration of the solid-state reaction in the ZnO-SnO_2 system.

huge microstructure changes, obtaining higher densities and controlled grain growth does not depend on the fact whether the chemical reaction begins before or after the densification process. However, if the volume change during the reaction sintering is large, the densification should occur before the reaction if the high density and controlled grain growth are desired. The results obtained for ZSO-00 and ZSO-10 samples imply that the reaction between the ZnO and SnO_2 and formation of the Zn_2SnO_4 spinel in these samples begins before the process of sintering and it is accompanied by a very large expansion of the samples. In samples activated for 40 min and more, the shrinkage is dominant. The XRD results confirmed that in these samples zinc stannate spinel is a major phase so the process of densification prevails. The slope of the dilatometer curves of ZSO-40, ZSO-80, and ZSO-160 samples point to the possibility of the spinel phase formation in the shape of the agglomerates that progress by the increased activation time because the agglomeration inhibits the densification. The calculated green and sintered densities were 3.74 and 4.14 g/cm^3 (ZSO-40), 3.78 and 4.12 g/cm^3 (ZSO-80) and 3.79 and 3.86 g/cm^3 (ZSO-160), respectively. The densification is the highest for the sample activated for 40 min and the lowest for the longest activated sample (ZSO-160). The densities of all the samples increase during sintering but the highest value is obtained for the ZSO-40 sample. Hence, the relative shrinkage during sintering is primarily dependent on a distribution of the starting particles, their consolidation, and activity. The densities of all the sintered samples are lower than 70% of the theoretical density of zinc stannate. It is obvious that this structure is difficult to sinter. The porosity present in starting powder mixtures is preserved in the sintered samples as well. The starting powders are mainly made of the agglomerates, which are the reason why the packing of the particles during consolidation step is not ideal, and then it is so difficult to reach the high densification degree during sintering. This, together with the formation of the agglomerated spinel, is the main reason for the slow sintering process in this system. The moving force of the reaction sintering is the low free energy of the system as a result of the spinel phase formation through the diffusion mechanisms. The additional force is the high surface free energy induced by the process of mechanical activation of the starting powders, but only after the system gains the chemical balance.

The isothermal sintering was performed at 900 to 1200 °C (**Figure 7a**) for different time intervals (30–120 min) (**Figure 7b**). The relative densities were determined and used to calculate the obtained ceramics porosities (**Table 1**). The isothermal sintering is usually analyzed by investigating the shrinkage degree, which is described by the so-called Lanel parameter. This parameter connects the after sintering Π_S and starting porosity Πo, that is, the green ρ_0, sintered ρ_S, and theoretical ρ_T density of the investigated material: $L = 1-(\Pi_S/\ \Pi_0) = (\rho_S - \rho_0)/(\rho_T - \rho_0)$. The joint structural characteristic of all the sintered samples is a large open porosity, ~40% and inhomogeneity which is a consequence of the powders "history" (the presence of the agglomerates and aggregates) (**Figure 2**), porosity in the starting powder mixtures and the solid-state reaction with the spinel formation (**Figure 6**). The formal sintering kinetic analysis by Lanel parameter (**Figure 8**) confirmed that mechanical activation of the starting powder mixtures influences the sinterability, but having all the results in mind, longer activation than 40 min is not necessary because the

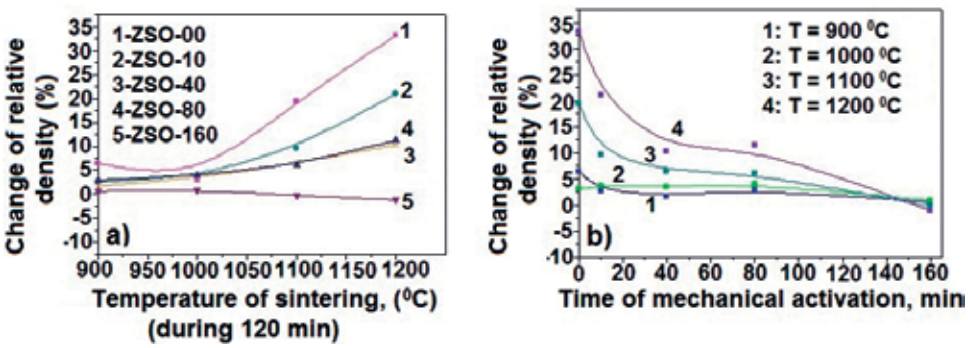

Figure 7. The change of the relative density vs. a) Temperature of the isothermal sintering and b) time of the mechanical activation, of the ZnO-SnO_2 system.

Sample	$\Pi_0 = 1-\rho_0/\rho_T$ (%)	$\Pi_S = 1-\rho_S/\rho_T$ (%)	Sample	$\Pi_0 = 1-\rho_0/\rho_T$ (%)	$\Pi_S = 1-\rho_S/\rho_T$ (%)
		$T_{SINTER.}$ = 900 °C			$T_{SINTER.}$ = 1100 °C
ZSO-00	48.6	45.3	ZSO-00	48.6	38.6
ZSO-10	41.9	46.4	ZSO-10	43.1	37.7
ZSO-40	45.3	44.4	ZSO-40	44.7	41.1
ZSO-80	45.8	44.2	ZSO-80	46.1	42.8
ZSO-160	46.4	46.1	ZSO-160	46.4	46.6
		$T_{SINTER.}$ = 1000 °C			$T_{SINTER.}$ = 1200 °C
ZSO-00	46.9	45.3	ZSO-00	48.4	31.3
ZSO-10	43.8	41.7	ZSO-10	42.8	30.8
ZSO-40	45.3	43.5	ZSO-40	45.3	39.7
ZSO-80	45.6	43.5	ZSO-80	46.4	40.3
ZSO-160	45.6	45.1	ZSO-160	46.6	47.2

Table 1. Porosity (%) for the green and isothermally sintered ZnO-SnO_2 samples.

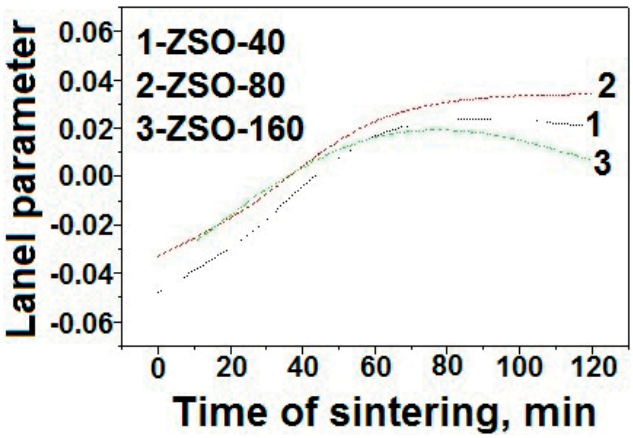

Figure 8. The Lanel parameter vs. time of sintering for the ZnO-SnO_2 samples activated 40, 80, and 160 min and sintered at 900°C for 2 hours.

effects of longer mechanical activation have a very little impact on the sinterability improvement. The mechanical activation longer than 40 min, on the other hand, is needed for more efficient zinc stannate synthesis.

The behavior of the differently activated samples of ZnO-SnO_2 system during the heat treatment was complemented with differential thermal analysis (DTA). From the shape of the exothermal peak of the nonactivated ZnO-SnO_2 powder mixture, it is obvious that starting from 400°C, the serious of exothermic, poorly separated changes (processes) occur. These processes lead to the formation of zinc stannate phase, which is confirmed by the XRD analysis [29, 30]. The exothermal effect in ZSO-10 is a consequence of the two processes: formation of the zinc stannate at lower temperatures and spinel crystal growth at higher temperatures.

The XRD analysis confirms the existence of the spinel peaks in ZSO-40, ZSO-80, and ZSO-160 samples, so the exothermal effect in these samples is only a result of the spinel growth during the thermal treatment [30]. With the higher activation times used in the preparation of the starting powder mixtures, the temperature of the exothermal peak is lowering (ZSO-00: 1135, ZSO-10: 1031, ZSO-40: 941, ZSO-80: 892, and ZSO-160: 849°C). The specific reaction enthalpy values were 1.69 (ZSO-10), 3.10 kJ/g (ZSO-40), and for the ZSO-80 and ZSO-160 samples, had the same value of 3.69 kJ/g, so the conclusion could be that the good condition for mechanochemical synthesis of the zinc stannate spinel is obtained already with 80 min of mechanical activation. The obtained results imply also the possibility of zinc stannate solid-state synthesis already at 900°C, which is a much lower temperature of Zn_2SnO_4 synthesis than previously found (1280°C) [31].

4. Morphology, optical and acoustic characterization of sintered ZnO-SnO_2 system

The influence of mechanical activation on the morphology, optical and thermal properties of the solid-state synthesized Zn_2SnO_4 was investigated by the scanning electron microscopy,

room temperature far infrared and photoacoustic spectroscopy [28, 32–34]. The reflectivity of near normal incidence light in the range between 100 and 1400 cm^{-1} as a function of the wave number showed the existence of eight ionic oscillators for all the investigated samples. The intensity of the reflectivity peaks was the highest for the sample activated for 10 min and gradually decreased with longer mechanical activation (40, 80 and 160 min, respectively). As confirmed by microstructural analysis longer times of activation lead to the increase of porosity and defects (**Figure 2**). The specificity of the obtained results is the two extra oscillators from the six that are expected to show for the known Wyckoff sites for zinc stannate structure and calculated by nuclear site group analysis, which is obviously the result of mechanical activation and sintering [32, 33]. It is known that the mechanical activation is responsible for the formation of the defects and after sintering a structure that contains pores, aggregates and intergranular material besides crystalline grains [32] (**Figure 9a–d**). As shown previously, the activation of 10 min brings the significant refinement in the crystallite size of the initial oxides, while the beginning of the spinel zinc stannate phase formation starts after 40 min of activation [21, 30]. The agglomeration and high porosity is a feature of all the mechanically activated samples, and it increases with the longer activation times and remains also after the sintering process (**Figure 9**). The ceramic materials with a large open porosity like zinc stannate obtained by the reaction sintering processing described in this review paper are convenient for the application in the humidity sensors. Atmospheric water can be absorbed on the grain surfaces inside pores or condensed in the small channels and pores [28]. Humidity sensor has to have features like high sensitivity, reversibility, fast response, the broad range of moisture selectivity, chemical, and thermal stability, which depends on the microstructure formed

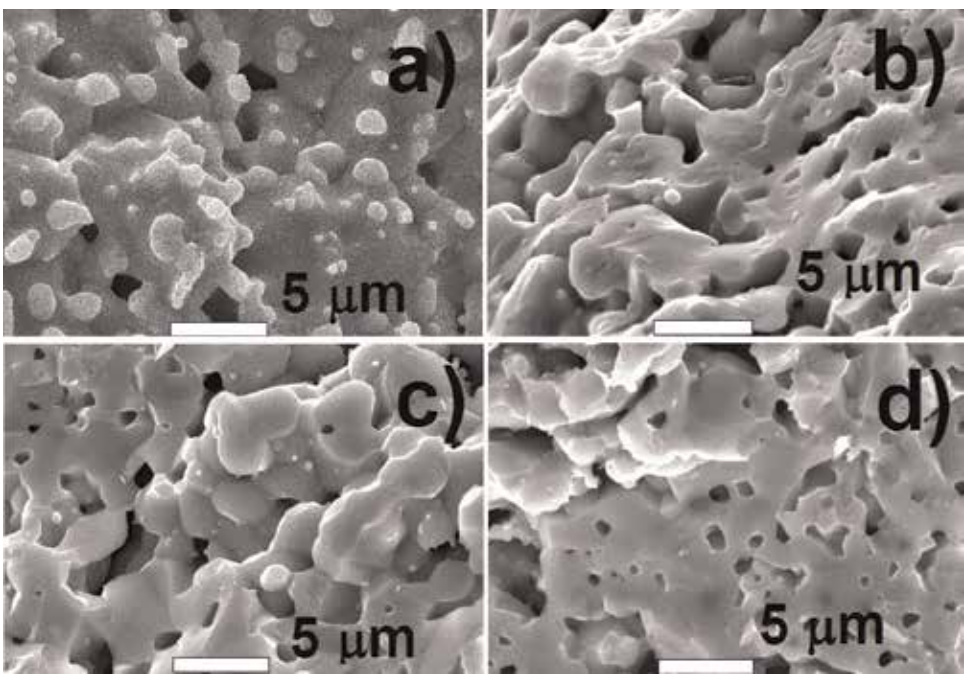

Figure 9. SEM micrographs of ZnO-SnO_2 ceramics prepared by mechanical activation for, (a) 10, (b) 40, (c) 80 and (d) 160 min and isothermal sintering at 1300°C for 2 hours.

during the synthesis procedure. The thermal characterization of these materials is very important. Photoacoustic spectroscopy was used to determine the thermal and transport properties of 40, 80, and 160 min activated and non-isothermally sintered up to 1200°C samples (heating rate of 5°C/min) [28] and the 10, 40, 80 and 160 min activated and isothermally sintered at 1300°C for 2 hours samples [34]. The experimental photoacoustic phase and amplitude spectra were recorded as a function of the chopped frequency of the laser beam (red laser with power of 25 mW, λ = 632 nm) in a thermal-transmission detection configuration and analyzed by theoretical Rosencwaig-Gersho thermal-piston model [35], which enable determination of the materials thermal properties including thermal diffusivity, diffusion coefficient of the minority free carriers and optical absorption coefficient.

The differences in thermal-electrical characteristics that were obtained again indicated that the changes in the material are induced by the differences in the processing routes of the powders before sintering. With the increase of the activation time and the formation of a single phase zinc stannate the thermal diffusivity value increases. The thermal diffusivity of zinc stannate material obtained by non-isothermal sintering route (0.21×10^{-7}, 1.80×10^{-7} , and 10.06×10^{-7} m^2 s^{-1}, for the ZSO-40, ZSO-80, and ZSO-160 samples, respectively) are to our best knowledge the first time ever measured values of this kind [28]. The photoacoustic analysis for differently activated and isothermally sintered ceramic samples shown differences in photoacoustic spectra, especially specific are the results obtained for the ZSO-10 sample. The frequency dependence photoacoustic phase has an explicit minimum for the samples prepared with higher activation times [34]. In the amplitude diagrams, at critical frequencies where phase diagram has the explicit minimum, a knee like a change of the curve rate occurs. It is obvious that at those frequencies in the samples activated longer than 10 min, the significant changes in the material properties appear. Those samples act as thermally thick at frequencies higher than the critical, and thermally thin at the frequencies lower than critical. In the area of lower frequencies, the dominant role in the generation of the photoacoustic signal has the thermal diffusivity and optical absorption coefficient. In the frequency range when the samples are thermally thick, the intensity and phase of the photoacoustic signal depend primarily upon the electrical transport properties of the investigated samples. The increase in the thermal diffusivity value with the increase of the activation time is confirmed in these samples as well which again points to the fact that higher activation times are responsible for the formation of porous, defect and low-density microstructure. This confirms, once more, that the grain growth of the spinel phase slows down the densification process, and together with the agglomerates formed during the mechanical activation, causes the appearance of a highly porous microstructure [34].

5. Liquid phase sintering of the ZnO-SnO_2 system

The effect of small amounts of bismuth oxide (Bi_2O_3) on the microstructure, optical, structural and electrical properties of the spinel-type ZnO-SnO_2 (zinc-tin-oxide) ceramics was investigated [36–39] to complement the above-shown research on the zinc-tin-oxide porous ceramics. Two series of samples were made for this purpose. Samples of the first series were used as the reference and were prepared by mechanical activation in different time intervals (10, 40, 80,

and 160 min), pressing under 980 MPa in 10 mm diameter pellets, and isothermal sintering at 1300°C, for 2 hours. They were used for selecting the optimal conditions for the preparation of Bi-doped ZnO-SnO_2 samples (the second series samples). The infrared spectra of the first series samples were used also as the reference spectra to compare with infrared spectra's of samples of the second series. XRD analysis of the first series samples confirmed the presence of only Zn_2SnO_4 spinel phase [36, 37]. The density measurements, however, show that the slightly higher density was obtained for the starting powder mixture activated for 10 min (**Table 2**). Comparing the obtained relative densities of the sintered samples at temperatures from 900 to 1200°C (**Table 1**, where the values were in the range from 52.8–69.2%), and the ones in **Table 2**, it is easy to conclude that by increasing the sintering temperature the relative density of the ZnO-SnO_2 ceramic material is increased. Because of the slightly higher densities obtain for the 10 min activated sample; this parameter of synthesis (10 min of activation) was applied in the preparation of the samples from the second series. Samples of the second series were then prepared with the same starting powder mixtures, with the molar ratio of ZnO:SnO_2 = 2:1, but with the addition of 0.5, 1.0 and 1.5 mol.% of Bi_2O_3 (samples marked as ZSO-0.5, ZSO-1, and ZSO-1.5, respectively), mechanical activation for 10 min, pressing under 980 MPa and isothermal sintering at 1300°C for 2 hours. The highest relative density was obtained for the 1.0 mol.% of Bi_2O_3 (~92%) (**Figure 10a**), while the increasing concentration of Bi_2O_3 in the system (1.5 mol.%) lead to the decrease of the relative density (~87) probably because of the further grain growth and problematic packing of the bigger particles that are now more present in the system (**Figure 10b**). These conclusions are confirmed by the scanning electron microscopy measurements shown in **Figure 10**.

Samples of the first series	ρ_S/ρ_T (%)	Samples of the second series	ρ_0 (g/cm^3)	ρ_0/ρ_T (%)	ρ_S (g/cm^3)	ρ_S/ρ_T (%)
ZSO-10	75.9	ZSO	3.92	62.96	5.25	84.44
ZSO-40	75.7	ZSO-0.5	4.12	65.79	5.63	89.93
ZSO-80	75.5	ZSO-1.0	4.12	65.19	5.81	92.21
ZSO-160	75.3	ZSO-1.5	4.22	66.51	5.49	86.58

Table 2. The sintered relative densities of the samples from the first series, and relative densities before and after the sintering for the Bi_2O_3 doped ZnO-SnO_2 samples.

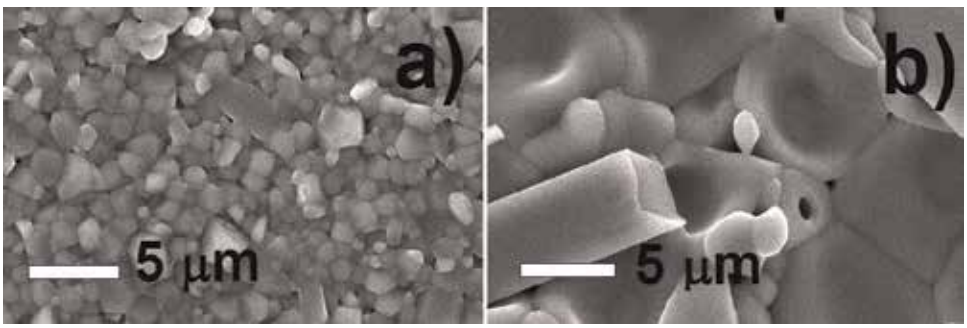

Figure 10. SEM micrographs of (a) 1 and (b) 1.5 mol.% Bi_2O_3 doped ZnO-SnO_2 ceramics.

Addition of the small amounts of Bi_2O_3 to the ZnO-SnO_2 system creates conditions for the liquid phase sintering and enhances the densification process. The obtained structure and morphology was examined using XRD and SEM-EDS [36–39]. FTIR and impedance spectroscopy were used to investigate the optical and electrical properties [38, 39]. Bi_2O_3 doping creates the conditions for the liquid phase sintering. Bismuth oxide forms $Bi_2Sn_2O_7$ pyrochlore phase with SnO_2 and in the presence of ZnO leads to the formation of Zn_2SnO_4 spinel and Bi_2O_3 liquid phase between 1000 and 1100°C, according to the following reaction [36]: $Bi_2Sn_2O_7 + 4ZnO \rightarrow 2Zn_2SnO_4 + Bi_2O_3(l)$. This brings a new dynamic into the ZnO-SnO_2 sintering mechanism. The base system mixture (2ZnO-SnO_2) grains are completely surrounded by the thin film of liquid Bi_2O_3, which directly influence the densification, grain growth and the solid-state reaction between the ZnO and SnO_2. No XRD proof of Bi_2O_3 was found in the sintered samples, either because the amount of Bi_2O_3 was under the XRD detection limit, or such high temperature of sintering (1300°C) caused the Bi_2O_3 to evaporate (evaporation of Bi_2O_3 starts at 825°C) [37]. The addition of Bi_2O_3 stimulates the ion substitution between Sn^{4+} and Zn^{2+} which results in ZnO/SnO_2 solid solution formation with rather limited regions of pure Zn_2SnO_4 [36, 38] (**Figure 11**). Probably the diffusion-evaporation mechanisms are responsible for the reaction between the ZnO and SnO_2 in this case of this material sintered at such high temperatures, and not just the ordinary diffusion processes that happen in the usual solid-state chemical reactions. A limited evaporation of ZnO is also inevitable [37]. The ZnO evaporation opens up larger pores in places where the SnO_2 was not available for the reaction due to the incomplete mixing. The zinc oxide condenses unreacted on the walls of the cavities upon cooling. The residual SnO_2 appears to balance the evaporated ZnO. As said previously, the Zn_2SnO_4 has a cubic inverse spinel (AB_2O_4) structure so the A and B sites can substitute for each other during sintering based on the following reaction: $AB_2O_4 \rightarrow (AB)BO_4$. Even though the valance of the Sn^{4+} is higher than of the Zn^{2+} ion the substitution is mutual [38] and according to the obtained results [36–39] the Bi-doping strongly promoted this substitution and contribute to the Zn_2SnO_4-SnO_2 solid solution formation, along with the larger regions of pure spinel Zn_2SnO_4 (**Figure 11**) and smaller areas of residual SnO_2. In Bi-doped ZnO-SnO_2 system, the liquid phase assisted sintering mechanism is obviously responsible for these dramatic microstructural changes and the deviation from the expected formation of single phase cubic spinel Zn_2SnO_4. The enhancement of the densification process and higher bulk

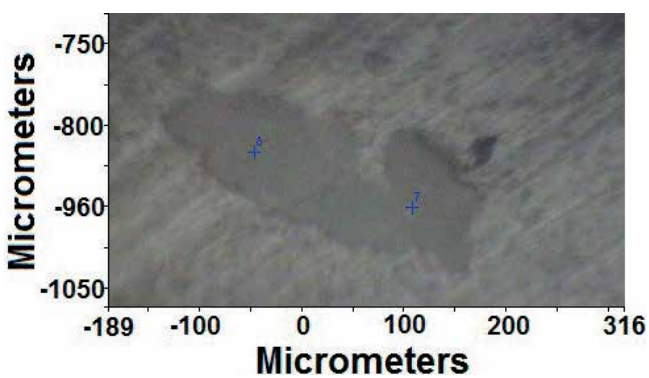

Figure 11. The ZSO-1 sample image taken with an optical microscope. The dark-gray area belongs to the pure Zn_2SnO_4 phase and it is surrounded by the "matrix" region composed of Zn_2SnO_4-SnO_2 solid solution (noticeable recording points 6 and 7, marks the positions where the additional IR and EDS analysis were performed and shown elsewhere [36, 38]).

relative densities are expected. The influence of the addition of Bi_2O_3 on the densification process was investigated by monitoring the change in the relative density vs. the molar percentage of the Bi_2O_3 added, and it shows an increase in relative density of sintered samples (~ 92%) with the addition of Bi_2O_3 up to 1.0 mol%, while further addition of 1, 5 mol% Bi_2O_3 leads to a decrease in relative density (~ 87%) [37]. This is probably due to further grains growth and packaging problem of much larger particles. The general conclusion is that the optimal amount of Bi_2O_3 under applied sintering conditions (1300°C, 2 hours) for achieving the best possible densification is 1.0 mol%.

The agglomeration and high porosity present in the starting mixtures are also retained in the sintered samples (porosity ~25%) (**Table 2**). The general microstructure of the sintered samples of the second series is characterized by the denser sintered areas compared to the reference sample (**Figures 9** and **10**). The "matrix" consists more of the non-stoichiometric zinc stannate, $Zn_{2-x}Sn_{1+x}O_4$ and represent some kind of a solid-solution, where dark-gray regions are closer to the composition of pure Zn_2SnO_4, while smaller areas are composed of the residual SnO_2 whose polygonal grains are like inserted into the spinal structure (**Figure 10b**) [36–38].

The Bi-addition to the ZnO-SnO_2 system reflected on its optical properties as well. Although, the FTIR spectra [38] were similar to the previously obtained for Zn_2SnO_4 spinel [30, 32, 33] and were characterized by two extra oscillators (eight in total) attributed to the cation disorder in the crystal lattice induced by preparation procedure, compared to the six predicted by group theory analysis that belongs to the zinc stannate structure, it showed also the additional three more peaks that belong to SnO_2 phase (ω_{TO}) found at 244 and 288 cm^{-1}, and the most intensive bulk mode of SnO_2 at 613 cm^{-1}, which position was shifted to higher frequency in ZSO-1 sample [36, 38].

The impedance spectroscopy measurements provided evidence of the intrinsic features of the grain-boundary phenomenon in this kind of ceramic material and point to its possible application in the nonohmic devices [39]. Impedance diagrams of SnO_2-Zn_2SnO_4 ceramics showed Cole-Cole type behavior, where complex impedance data resulted in the semi-circles with the high degree of overlapping which is consistent with the reported semiconductor properties of this kind of ceramic material.

6. Summary

The optimal conditions for the best zinc stannate synthesis by reaction sintering of the mechanically activated ZnO and SnO_2 powder mixtures in a high-energy planetary ball mill, in the time intervals from 0 to 160 min, were obtained. The mechanochemical activation of 40 min and more creates the conditions for the beginning of the Zn_2SnO_4 formation. The pure stannate phase was obtained in the sample activated for 160 min and sintered at 1200 °C and higher. A joint structural feature of all the polycrystalline sintered bulk samples is a large open porosity. Formal analysis of the sintering kinetics using Lanel parameter confirmed that mechanical activation affects the sinterability only for the activation less than 40 min, while longer milling intervals have no more effect on the obtained Zn_2SnO_4 large porosity. In the materials characterization, it was shown that thermal diffusivity increases with the activation

time and progression of the zinc stannate formation. SEM and FTIR results agree well in the conclusion that longer times of mechanical activation lead to increased porosity and defects. The FTIR spectra were numerically analyzed and oscillator parameters were calculated. Two more oscillators were observed compared to six predicted by the group theory for the single crystal Zn_2SnO_4, as a result of the synthesis procedure. The obtained defect structure of the Bi-doped ZnO-SnO_2 system is a direct consequence of the structural changes in all the hierarchy levels induced by the liquid phase sintering mechanism, which strongly influences the optical and electrical properties of the obtained material as well. By selecting the conditions and the ways of the sample preparation during the process of mechanical activation and sintering, it is possible to alter the microstructure, phase composition, optical and electrical properties of the resulting zinc-tin-oxide ceramics to fit the best the desired applications.

Acknowledgements

The author is grateful to the Ministry of Education, Science and Technological Development of the Republic of Serbia for the support (Project No. ON 171022).

Author details

Tamara Ivetić

Address all correspondence to: tamara.ivetic@df.uns.ac.rs

University of Novi Sad, Faculty of Sciences, Department of Physics, Trg Dositeja Obradovića, Novi Sad, Serbia

References

[1] Peiteado M, Iglesias Y, Fernández JF, De Frutos J, Caballero AC. Microstructural development of tin-doped ZnO bulk ceramics. Materials Chemistry and Physics. 2007;**101**:1-6

[2] Šepelák V, Becker SM, Bergmann I, Indris S, Scheuermann M, Feldhoff A, Kübel C, Bruns M, Stürzl N, Ulrizh AS, Ghafari M, Hahn H, Grey CP, Becker KD, Heitjans P. Nonequilibrium structure of Zn_2SnO_4 spinel nanoparticles. Journal of Materials Chemistry. 2012;**22**:3117-3126

[3] Baruah S, Dutta J. Zinc stannate nanostructures: Hydrothermal synthesis. Science and Technology of Advanced Materials. 2011;**12**:013004 (18pp)

[4] Yuan H-L, Li J-C. Effect of annealing temperature on the growth of Zn-Sn-O nanocomposite thin films. Journal of Alloys and Compounds. 2017;**714**:114-119

[5] Salohub AO, Voznyi AA, Klymov OV, Safryuk NV, Kurbatov DI, Opanasyuk AS. Determination of fundamental optical constants of Zn_2SnO_4 films. Semiconductor Physics, Quantum Electronics & Optoelectronics. 2017;**20**:79-84

[6] Ivetić T, Nikolić MV, Young DL, Vasiljević-Radović D, Urošević D. Photoacousic and optical properties of zinc-stannate thin films. Materials Science Forum. 2006;**518**:465-470

[7] Liu X, Niu C, Meng J, Xu X, Wang X, Wen B, Guo R, Mai L. Gradient-temperature hydrothermal fabrication of hierarchical Zn_2SnO_4 hollow boxes stimulated by thermodynamic phase transformation. Journal of Materials Chemistry A. 2016;**4**:14095-14100

[8] Lehnen T, Zopes D, Mathur S. Phase-selective microwave synthesis and inkjet printing applications of Zn_2SnO_4 (ZTO) quantum dots. Journal of Materials Chemistry. 2012;**22**: 17732-17736

[9] Young DL, Williamson DL, Coutts TJ. Structural characterization of zinc stannate thin films. Journal of Applied Physics. 2002;**91**:1464-1471

[10] Young DL, Moutinho H, Yan Y, Coutts TJ. Growth and characterization of radio frequency magnetron sputter-deposited zinc stannate, Zn_2SnO_4, thin films. Journal of Applied Physics. 2002;**92**:310-319

[11] Rong A, Gao XP, Li GR, Yan TY, Zhu HY, Qu JQ, Song DY. Hydrothermal synthesis of Zn_2SnO_4 as anode materials for Li-ion battery. The Journal of Physical Chemistry. B. 2006;**110**:14754-14760

[12] Alpuche-Aviles MA, Wu Y. Photoelectrochemical study of the band structure of Zn_2SnO_4 prepared by the hydrothermal method. Journal of the American Chemical Society. 2009;**131**:3216-3224

[13] Fu X, Wang X, Long J, Ding Z, Yan T, Zhang G, Zhang Z, Lin H, Fu X. Hydrothermal synthesis, characterization, and photocatalytic properties of Zn_2SnO_4. Journal of Solid State Chemistry. 2009;**182**:517-524

[14] Lana-Villarreal T, Boschloo G, Hagfeldt A. Nanostructured zinc stannate as semiconductor working electrodes for dye-sensitized solar cells. Journal of Physical Chemistry C. 2007;**11**:5549-5556

[15] Wang X, Wang Y-F, Luo Q-P, Ren J-H, Li D-J, Li X-F. Highly uniform hierarchical Zn_2SnO_4 microspheres for the construction of high performance dyesensitized solar cells. RSC Advances. 2017;**7**:43403-43409

[16] Li Y, Pang A, Zheng X, Wei M. CdS quantum-dot-sensitized Zn_2SnO_4 solar cell. Electrochimica Acta. 2011;**56**:4902-4906

[17] Stambolova I, Konstantinov K, Kovacheva D, Peshev P, Donchev T. Spray pyrolysis preparation and humidity sensing characteristics of spinel zinc stannate thin films. Journal of Solid State Chemistry. 1997;**128**:305-309

[18] Jiang Y-Q, Chen X-X, Sun R, Xiong Z, Zheng L-S. Hydrothermal synthesis and gas sensing properties of cubic and quasi-cubic Zn_2SnO_4. Materials Chemistry and Physics. 2011;**129**:53-61

[19] Yang HM, Ma SY, Yang GJ, Chena Q, Zeng QZ, Ge Q, Ma L, Tie Y. Synthesis of La_2O_3 doped Zn_2SnO_4 hollow fibers by electrospinning method and application in detecting of acetone. Applied Surface Science. 2017;**425**:585-593

[20] Movahedi M, Hosseinian A, Bakhshaei M, Rahimi M, Arshadnia I. Micro-spherical SnO_2/Zn_2SnO_4: Synthesis, heat treatment and photocatalytic efficiency for decolorization of two dye mixture in wastewater. Journal of Applied Chemistry. 2017;**11**:11-16

[21] Ivetić T, Vuković Z, Nikolić MV, Pavlović VB, Nikolić JR, Minić D, Ristić MM. Morphology investigation of mechanically activated ZnO-SnO_2 system. Ceramics International. 2008;**34**:639-643

[22] Gregg SH, Sing KS. Adsorption, Surface Area and Porosity. New York: Academic Press; 1967

[23] Rouquerol F, Rouquerol J, Sing K. Adsorption by Powders and Porous Solids. London: Academic Press; 1999

[24] Sing KS, Everett DH, Haul RAW, Moscou L, Pierotti RA, Rouguero J, Siemieniewska T. Reporting physisortion properties data for gas/solid systems with special reference to the determination of surface area and porosity. Pure and Applied Chemistry. 1985;**57**:603-619

[25] Dollimore D, Heal GR. An improved method for the calculation of pore size distribution from adsorption data. Journal of Applied Chemistry. 1964;**14**:109-114

[26] Dubinin MM. Physical adsorption of gases and vapors in microspores. In: Cadenhead DA, editor. Progress in Surface and Membrane Science. New York: Academic Press; 1975. pp. 1-70

[27] Ivetić TB, Vojisavljević KM, Srećković T. Influence of mechanical activation on consolidation of ZnO-SnO_2 powder system, Fundamental problems of Physics and Technology of Materials, Proceedings of Scientific Meeting Physics and Technology of Materials-FITEM'04, 12-15 October 2004, Čačak, Serbia, p. 115-121. (In Serbian)

[28] Ivetić T, Nikolić MV, Nikolić PM, Blagojević V, Đurić S, Srećković T, Ristić MM. Investigation of zinc stannate synthesis using photoacoustic spectroscopy. Science of Sintering. 2007;**39**:153-160

[29] Nikolic N, Marinkovic Z, Sreckovic T. The influence of grinding conditions on the mechanochemical synthesis of zinc stannate. Journal of Materials Science. 2004;**39**:5239-5242

[30] Ivetić T. Synthesis and characterization of the zinc stannate spinel, M. Sc Thesis. Serbia: University of Belgrade, Faculty of Physical Chemistry; 2006 (In Serbian)

[31] Hashemi T, Al-Allak HM, Illingsworth J, Brinkman AW, Woods J. Sintering behaviour of zinc stannate. Journal of Materials Science Letters. 1990;**9**:776-778

[32] Nikolić MV, Ivetić T, Paraskevopoulos KM, Zorbas KT, Blagojević V, Vasiljević-Radović D. Far infrared reflection spectroscopy of Zn_2SnO_4 ceramics obtained by sintering mechanically activated ZnO-SnO_2 powder mixtures. Journal of the European Ceramic Society. 2007;**27**:3727-3730

[33] Nikolić MV, Ivetić T, Young DL, Paraskevopoulos KM, Zorba TT, Blagojević V, Nikolić PM, Vasiljević-Radović D, Ristić MM. Far infrared properties of bulk sintered and thin film Zn_2SnO_4. Materials Science and Engineering B. 2007;**138**:7-11

[34] Ivetić TB, Nikolić MVP, Pavlović VB, Nikolić PM, Ristić MM. Photoacoustic spectroscopy investigation of sintered zinc-tin-oxide ceramics. Hemijska industrija. 2007;**61**:142-146 (In Serbian)

[35] Rosencwaig A, Gersho A. Theory of the photoacoustic effect with solids. Journal of Applied Physics. 1976;**47**:67-69

[36] Ivetić T. Influence of Bi_2O_3 on the sintering of ZnO-SnO_2 ceramics, Ph.D. Thesis. Serbia: University of Belgrade, Faculty of Physical Chemistry; 2008. (in Serbian)

[37] Ivetić T, Nikolić MV, Slankamenac M, Živanov M, Minić D, Nikolić PM, Ristić MM. Influence of Bi_2O_3 on microstructure and electrical properties of ZnO-SnO_2 ceramics. Science of Sintering. 2007;**39**:229-240

[38] Ivetić T, Nikolić MV, Paraskevopoulos KM, Pavlidou E, Zorba TT, Nikolić PM, Ristić MM. Combined FTIR and SEM-EDS study of Bi_2O_3 doped ZnO-SnO_2 ceramics. Journal of Microscopy (Oxford). 2008;**232**:498-503

[39] Slankamenac M, Ivetić T, Nikolić MV, Ivetić N, Živanov M, Pavlović VB. Impedance response and dielectric relaxation in liquid-phase sintered Zn_2SnO_4-SnO_2 ceramics. Journal of Electronic Materials. 2010;**39**:447-455

Chapter 6

Tailoring of the Magnetic and Structural Properties of Nanosized Ferrites

Sijo A. K.

Additional information is available at the end of the chapter

http://dx.doi.org/10.5772/intechopen.72382

Abstract

Spinel ferrites are porous ceramics with remarkable electrical and magnetic properties. They belong to a technologically important class of magnetic materials which have high resistivity and chemical stability. These properties make them suitable for a wide variety of applications, where other magnetic materials cannot be used. Magnetic, electric, and structural properties of ferrites are tunable. These are currently of great research interest due to the ease of tailoring their magnetic properties by systematic substitution of cations and by proper choice of preparation techniques and post preparation treatments. The Cr^{3+}cations have a strong preference to occupy in the B-site and have an affinity for anti-ferromagnetic coupling with Fe ions. Thus, partial or total substitution of one of the cations with Cr^{3+} induces magnetic frustrations in the spinel ferrite system, which leads to interesting magnetic properties. Therefore, it is very interesting to study variation in magnetic properties on replacement of Cr in the place of Fe in spinel ferrites. This chapter explains tailoring of magnetic and structural properties of some spinel ferrites via solution-self-combustion, fuel-to-oxidizer ratio substitution, and proper substitution.

Keywords: spinel ferrite, chromites, solution-self-combustion, X-ray diffraction, DC magnetization studies

1. Introduction

Spinel ferrites are porous magnetic ceramics. Ferrite nanoparticles have extensive scope in the fundamental and applied research area. They have tunable electrical and magnetic properties that have wide practical applications. Recently, much attention has been paid on the magnetic oxide nanoparticles because they have wide range of applications such as magnetic storage media, gas sensors, ferrofluid technology, semiconductors, batteries, solar energy

transformation, heterogeneous catalysis, magnetocaloric refrigeration, and medical diagnosis [1]. Nanoparticles are much more active than larger bulk particles because of their higher surface area, and they display unique physical and chemical properties [2]. Spinel oxides have general formula DFe_2O_4, where D is a divalent cation like Co, Ni, Zn, Mn, Mg, Cu, etc. Spinel oxides can be prepared by various techniques such as forced hydrolysis, microwave synthesis, sol-gel method, co-precipitation, polyol, self-combustion reaction, and sonochemical [3–7] methods. Among these methods, the self-combustion method, particularly solution self-combustion, is one easy method through which highly pure crystalline and homogenous material can be prepared with high yield [8]. In solution self-combustion method, it is easy to control the stoichiometry and crystallite size, through preparation conditions and post treatments, which have an important direct influence on the magnetic properties of the ferrite.

In solution self-combustion, there are two components, nitrate and fuel. The fuel helps in the combustion of nitrates. The powder characteristics such as crystallite size, surface area, and size distribution are governed by enthalpy or flame temperature generated during combustion which itself depends on the nature of the fuel and fuel-to-oxidizer ratio [9]. There are number of different fuels active in self-combustion such as glycine, citric acid, tartaric acid, urea, etc. Among these fuels, citric acid is a good one to initiate combustion reaction due to its negative combustion heat, −2.76 kcal/g [10].

The Cr^{3+}cations have strong preference to occupy in the B-site and have an affinity for antiferromagnetic coupling with Fe ions. The partial or total substitution of one of the Fe^{3+} cations with Cr^{3+} cations induces magnetic frustrations in the spinel ferrite system, which leads to interesting magnetic properties. Therefore, it is very interesting to study variation in magnetic properties on doping of chromium ion in the place of Fe ion in spinel system [11].

Highly pure and identical nanoparticles are essential for excellent performance of the materials. By tuning of structural and magnetic properties, we can have highly pure and identical nanoparticles with exact physical and chemical properties suitable for particular application. In application level, large-scale synthesis at low cost is needed. With these aims, this work presents low cost synthesis of highly pure nanospinel ferrites via solution self-combustion technique, and the tuning of structural and magnetic properties is undertaken in terms of fuel-to-nitrate ratio and Cr doping. This synthesizing process neither requires sophisticated instruments nor a high sintering temperature.

2. Experimental

Nanosized $NiCrFeO_4$, $CoCrFeO_4$, and Zn $CrFeO_4$ fuel lean, stoichiometric and fuel rich samples, and fuel rich $CoCr_xFe_{2-x}O_4$ (with x = 0, 0.2, 0.4, 0.6, 0.8 and 1.0) were prepared by solution self-combustion technique using analytical grade corresponding to high purity metal nitrates (Merck-Germany) and citric acid ($C_6H_8O_7H_2O$) as oxidizing agents and fuel, respectively. The ratio of citric acid to metal nitrate (F/N ratio) was taken as 0.65 for fuel lean sample, 1 for stoichiometric sample, and 1.35 for fuel rich samples. The solutions of three nitrates (Fe, Cr, Co/Ni/Zn) and citric acid were prepared separately, mixed, and stirred completely to form a

homogenous solution using magnetic stirrer. The homogenous solution was evaporated on a magnetic hot plate. On evaporation, solution gets thickened to a thick gel. The temperature was then increased to 200°C to start the auto-ignition process, which resulted in the formation of a fluffy residue [12–16]. It was powdered and used for further studies.

The X-ray diffraction spectrum of the samples was taken by an X-ray diffractometer (Rigaku MiniFlex) with Cu-K_α radiation. The X-ray diffraction (XRD) patterns of all the samples were fitted with MAUD Rietveld refinement program. DC magnetization measurements were obtained using vibrating sample magnetometer (VSM- Lake Shore 7304) with a maximum applied field of 10 kOe [16].

3. Tuning via fuel-to-oxidizer ratio

XRD spectra of all $CoCrFeO_4$, $NiCrFeO_4$, and $ZnCrFeO_4$ samples are shown in **Figures 1–3**, respectively. Well-defined characteristic reflections in powder X-ray diffraction patterns clearly indicate the formation of the spinel structure. XRD pattern of all the stoichiometric and fuel rich samples shows that they have single-phased cubic spinel structure, whereas fuel lean samples show a small percentage of impurity phases, α-Ni in fuel lean $NiCrFeO_4$, α-Co in fuel lean $CoCrFeO_4$, and α-Fe_2O_3 in $ZnCrFeO_4$. Average crystallite sizes (D) for the samples are calculated by substituting the FWHM values of the maximum intensity (311) peaks in the Scherrer formula:

$$\text{Crystallite sizes (D)} = \frac{0.9\lambda}{\beta \text{Cos}\theta} \tag{1}$$

where λ is the wavelength of X-rays and β is the width of the most intense peak in the XRD after correction for instrumental broadening. Actual density (ϱ) of the samples is determined

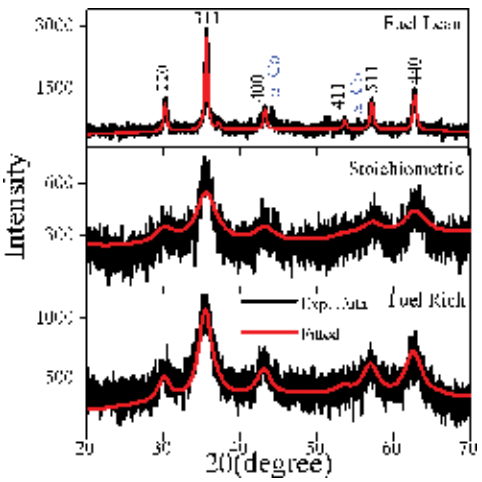

Figure 1. Powder XRD of $CoCrFeO_4$ samples with Rietveld fitting, reprinted from Sijo [15], with permission from Elsevier.

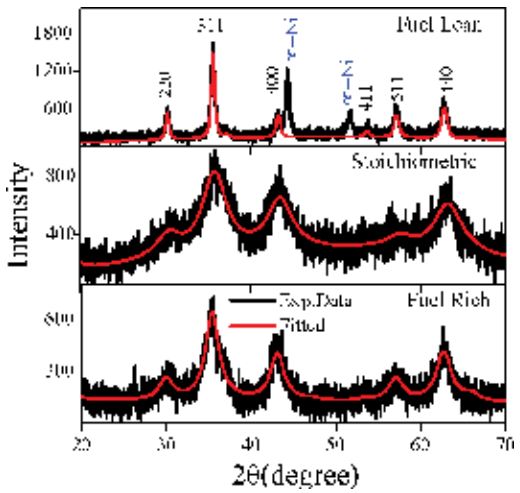

Figure 2. Powder XRD of $NiCrFeO_4$ samples with Rietveld fitting, reprinted from Sijo [15], with permission from Elsevier.

using Archimedes principle. Porosity of the samples is calculated from the actual and x-ray densities. Crystallite size (D), density (ϱ), and porosity of all samples are given in **Table 1**.

It is seen from **Table 1** that the crystallite size of fuel lean sample is many times greater than that of the stoichiometric samples and fuel rich samples. Presence of the impurity phase creates lattice

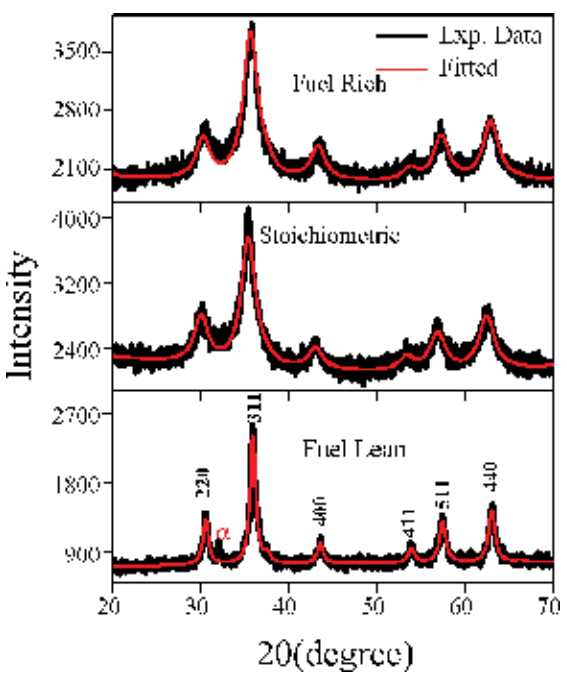

Figure 3. Powder XRD of $ZnCrFeO_4$ samples with Rietveld fitting [14].

Sample name	F/N ratio (φ)	Crystallite size (nm) (±1)	Density (gm/cm^3)	Porosity (%)	M_R (emu/g) (±0.1)	M_S (emu/g) (±0.1)	H_C (Oe) (±1)
$CoCrFeO_4$	0.65	29.5	4.0	22	5.9	28.5	352
$CoCrFeO_4$	1;1	3.4	4.6	12	0.3	4.8	580
$CoCrFeO_4$	1.35;1	5.7	4.7	10	0.5	5.5	645
$NiCrFeO_4$	0.65	30.1	2.8	46	6.4	27.8	182
$NiCrFeO_4$	1;1	3.2	3.6	32	0.25	2.3	192
$NiCrFeO_4$	1.35;1	5.7	4.1	23	0.6	5.5	118
$ZnCrFeO_4$	0.65	15	2.3	57	0.05	1.43	51
$ZnCrFeO_4$	1;1	5	3.4	35	0.02	0.83	49
$ZnCrFeO_4$	1.35;1	6	4.2	23	0.001	0.73	16

Source: Sijo [15] and Sijo et al. [14].

Table 1. Structural and magnetic parameters for the influence of fuel-to-nitrate ratio.

defects in the form of vacancies in the spinel ferrite phase and leads to an expansion of the lattice, which in turn makes the material porous and increases the crystallite size. In fuel lean samples, the amount of fuel is not adequate enough to react completely with metal nitrates and to release enough heat to form well-developed nanosized grains. Since the combustion reaction is incomplete, impurity phases of α-Ni, α-Co and α-Fe_2O_3 are also formed along with the spinel phase in samples prepared under the fuel lean condition. From these results, it is clear that stoichiometric fuel-to-oxidizer ratio results finest single-phased nanoparticles [14–17].

The variation of crystallite size with fuel content is plotted in **Figure 4**. From the figure, it is clear that the finest particles are obtained for stoichiometric fuel-to-nitrate ratio, and there is a small increase of crystallite size in the sample prepared under the fuel rich condition.

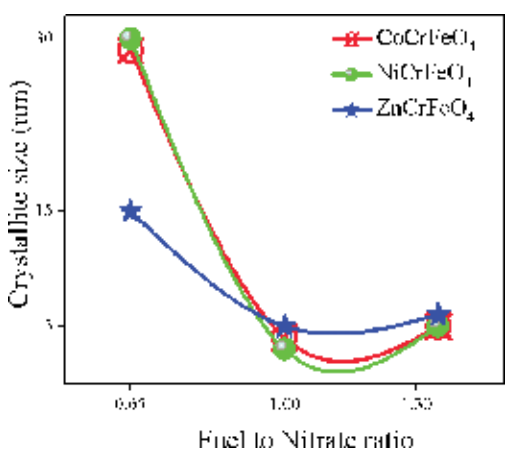

Figure 4. Crystallite size with fuel-to-nitrate ratio: modified from Sijo [15] and Sijo et al. [14].

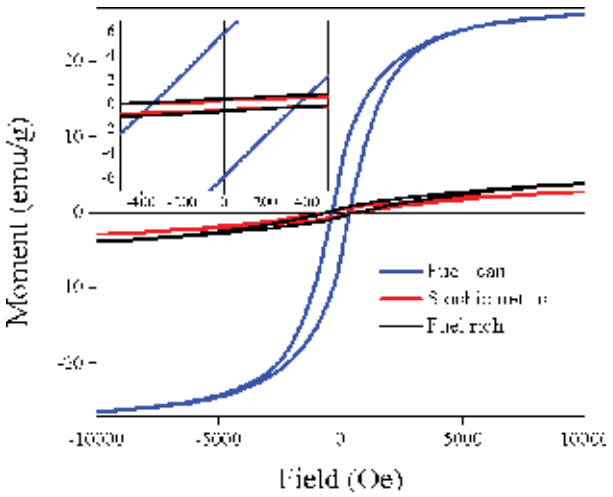

Figure 5. Room temperature magnetization curve of $CoCrFeO_4$ samples.

Smaller crystallite sizes of samples prepared under stoichiometric ratio may be due to the fact that more gaseous products are formed under this condition, leading to the breaking up of particles on escaping and resulting in finer particles. The superior powder properties present in $CoCrFeO_4$, $ZnCrFeO_4$, and $NiCrFeO_4$ samples prepared on stoichiometric ratio is due to the dominant effect of the number of gas molecules over the flame temperature [14–17].

Room temperature (RT) M-H loops of $CoCrFeO_4$, $NiCrFeO_4$, and $ZnCrFeO_4$ samples are shown in **Figures 5–7**, respectively. The coercivity and remenance are obtained directly from the M-H loops. Some of the samples show nonsaturating behavior, and hence, the value of saturation

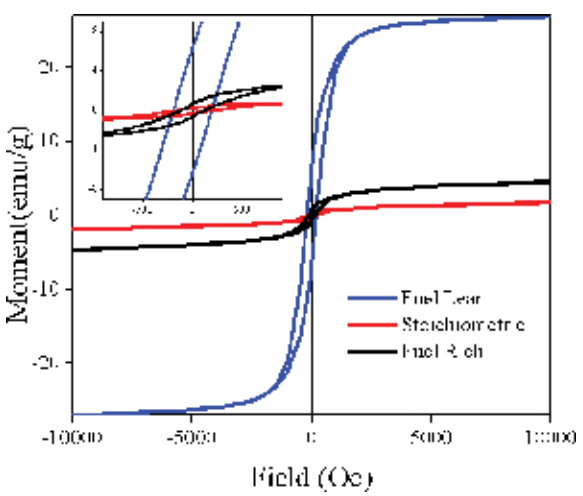

Figure 6. RT magnetization curve of $NiCrFeO_4$ samples. **Figures 5** and **6** are reprinted from Sijo [15], with permission from Elsevier.

http://dx.doi.org/10.5772/intechopen.72382

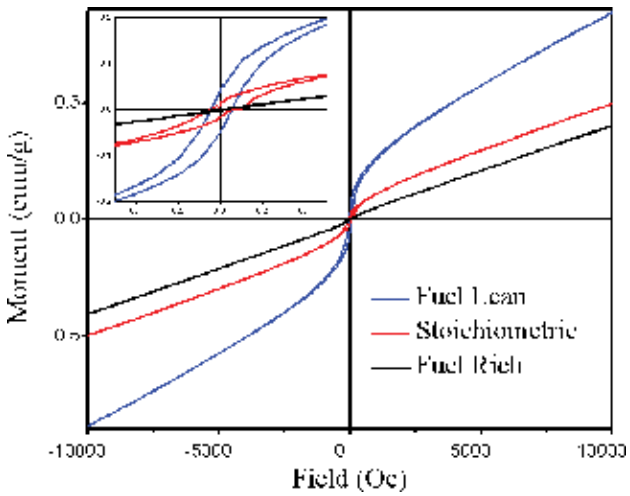

Figure 7. Room temperature magnetization curve of $ZnCrFeO_4$ samples [14].

magnetization of these samples is estimated by plotting M vs. 1/H for 1/H tending to zero. All the DC magnetization parameters are listed in **Table 1**. As seen from structural characterization using Rietveld fitted XRD, the $CoCrFeO_4$, $NiCrFeO_4$, and $ZnCrFeO_4$ samples prepared at fuel lean condition have the presence of a small amount of impurity phases α-Co, α-Ni, and α-Fe_2O_3, respectively. The higher magnetic moments observed in these samples can be attributed to the presence of impurity phases. The saturation magnetization depends on the average crystallite size. As the size increases, the saturation magnetization is also increased. From **Table 1**, we can conclude that the behavior of saturation magnetization (M_S), coercivity (H_C), and remenance (M_R) are highly dependent upon the fuel-to-nitrate ratio, and we can tune the structural and magnetic properties of spinel ferrites by changing fuel-to-oxidizer ratio.

4. Tuning via Cr^{3+} substitution

We can tune the structural and magnetic properties of spinel ferrites by suitable substitution also. For this, consider the samples $CoCrxFe_{2-x}O_4$ (with x = 0, 0.2, 0.4, 0.6, 0.8 and 1.0). The combined X-ray diffraction spectra for Cr doped powder are shown in the **Figure 8(a)**. These diffraction spectra provide clear evidence of the formation of ferrite spinel phase in all the samples. The broad XRD line indicates that the ferrite particles are of nanosize. The crystallite size for each composition was calculated from Rietveld fitting of spectra and given in **Table 2**. Room temperature magnetization measurements are taken for all samples and shown in **Figure 8(b)**. The magnetic parameters of all the samples are obtained and tabulated in **Table 2**, the value of remanence and coercivity obtained directly from individual M-H loops, while saturation magnetization obtained by plotting 1/H vs. M and extrapolating to zero.

From **Table 2**, the crystallite size, remanence, saturation magnetization, and coercivity were plotted vs. Cr content of $CoCr_xFe_{2-x}O_4$ samples and are shown in **Figure 9**. From this figure, we

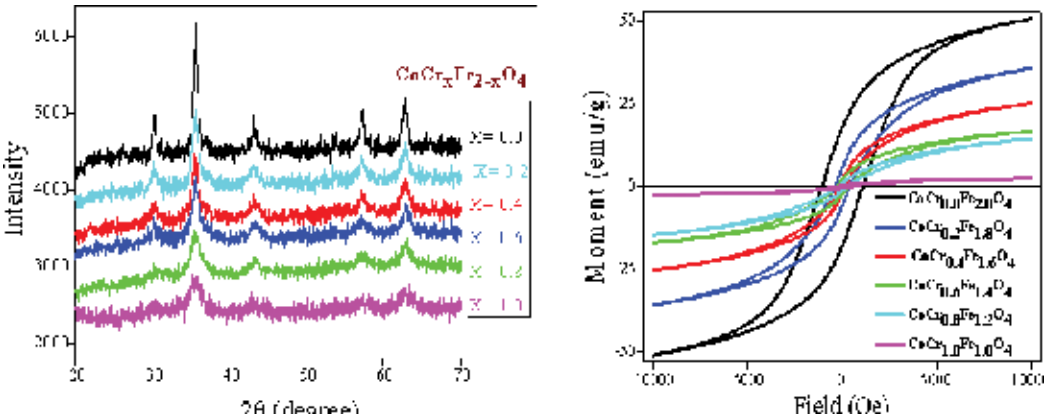

Figure 8. X-ray diffractograms (a) and RT magnetization curves (b) of Cr-doped powder samples. Reprinted from Sijo [13], with permission from Elsevier.

can clearly observe that crystallite size, remanence, saturation magnetization, and coercivity decreases, as chromium content increases. The area of hysteresis curve linearly decreases with increase in Cr content. That is, $CoFe_2O_4$ has the largest area, and $CoCrFeO_4$ has the smallest area inside the hysteresis loop. This indicates that the increased Cr substitution has made the material magnetically soft [14–17].

5. Conclusion

High-purity magnetic spinel ferrites can easily prepare by solution self-combustion method. It provides energy and cost-saving advantages over other methods. The finest nanoparticles obtained for stoichiometric fuel-to-nitrate ratio in solution self-combustion method. Increased Cr substitution in ferrites has made the material magnetically soft. That is, the structural and magnetic properties of ferrites are function fuel content and doping content, and therefore, they are highly tuneable via selection of proper preparation method, proper fuel content,

Sample name	Crystallite size (nm) (±1)	M_R (emu/g)(±0.1)	M_S (emu/g) (±0.1)	H_C (Oe) (±1)
$CoCr_{0.0}Fe_{2.0}O_4$	21	17.9	50.8	1080
$CoCr_{0.2}Fe_{1.8}O_4$	12	5.7	35.8	377
$CoCr_{0.4}Fe_{1.6}O_4$	11	1.9	25.3	192
$CoCr_{0.6}Fe_{1.4}O_4$	09	2.1	16.9	291
$CoCr_{0.8}Fe_{1.2}O_4$	07	1.1	14.6	227
$CoCr_{1.0}Fe_{1.0}O_4$	05	0.4	2.6	378

Table 2. Structural and magnetic parameters of $CoCr_xFe_{2-x}O_4$ samples [13].

http://dx.doi.org/10.5772/intechopen.72382

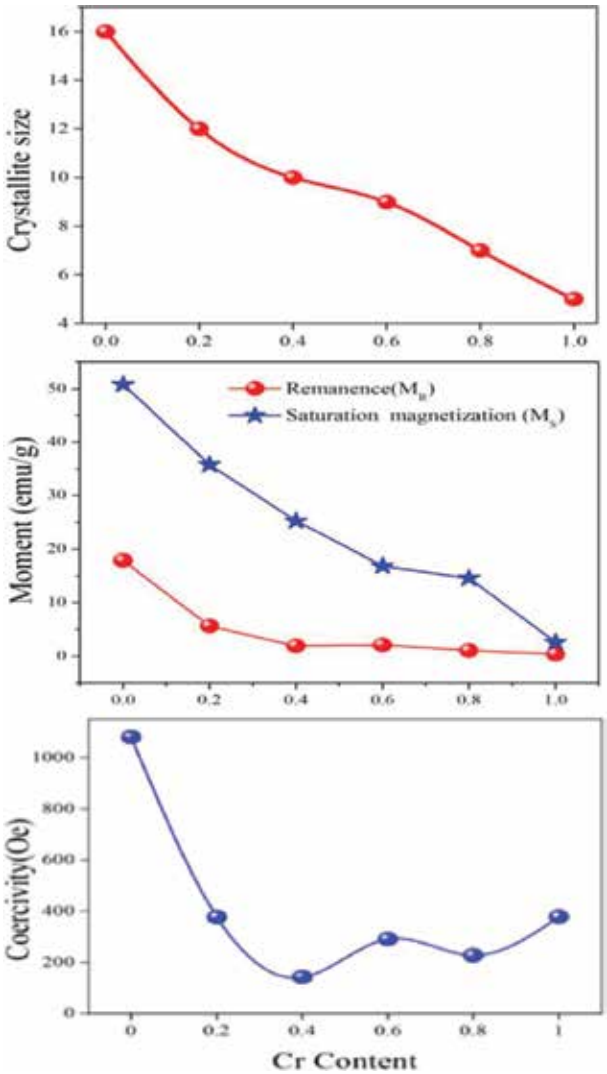

Figure 9. Crystallite size, remanence, saturation magnetization and coercivity vs. Cr content of $CoCr_xFe_{2-x}O_4$ powder samples. Reprinted from Sijo [13], with permission from Elsevier.

and via proper substitution. Therefore, we can desirably modify properties of spinel ferrites according to the requirement and can use in wide range of applications.

Acknowledgements

I acknowledge DAE-BRNS, Department of Physics, Mohanlal Sukhadia University Udaipur and my PhD supervisor Dr. K. Venugopalan (Late) Mohanlal Sukhadia University Udaipur. The contents of chapters three and four of my PhD thesis titled—*Studies of Magnetic and*

Transport Properties of Some Nanosized Fe and Cr Based Spinels have used for writing this chapter. I also acknowledge Nirmalagiri College, Kannur, Kerala for providing additional facilities for my research.

Author details

Sijo A. K.

Address all correspondence to: sijoaracka@gmail.com

Department of Physics, Mohanlal Sukhadia University, Udaipur, Rajasthan, India

References

[1] Zhao L, Yang H, Yu L, Cui Y, Zhao X, Zou B, Feng S. Structure and magnetic properties of nanocrystalline $CoLa_{0.08}Fe_{1.92}O_4$ ferrite. Journal of Magnetism and Magnetic Materials. 2006;**301**:445-451. DOI: 10.1016/j.jmmm.2005.07.033

[2] Chen CY, Chiang CL. Preparation of cotton with antibacterial silver nanoparticles. Materials Letters. 2008;**62**:3607-3609. DOI: 10.1016/j.matlet.2008.04.008

[3] Duong GV, Hanh N, Linh DV, Groessinger R, Weinberger P, Schafler E, Zehetbauer M. Monodispersed nanocrystalline $Co_{1-x}Zn_xFe_2O_4$ particles by forced hydrolysis: Synthesis and characterization. Journal of Magnetism and Magnetic Materials. 2007;**311**:46-50. DOI: 10.1016/j.jmmm.2006.11.167

[4] Millot N, Le Gallet S, Aymes D, Bernard F, Grin Y. Spark plasma sintering of cobalt ferrite nanopowders prepared by coprecipitation and hydrothermal synthesis. Journal of the European Ceramic Society. 2007;**27**:921-926. DOI: 10.1016/j.jeurceramsoc.2006.04.141

[5] Baldi G, Bonacchi D, Innocenti C, Lorenzi G, Sangregorio C. Cobalt ferrite nanoparticles: The control of the particle size and surface state and their effects on magnetic properties. Journal of Magnetism and Magnetic Materials. 2007;**311**:10-16. DOI: 10.1016/j.jmmm.2006.11.157

[6] Júnior AF, de Oliveira Lima EC, Novak MA, Wells Jr PR. Synthesis of nanoparticles of $Co_xFe_{3-x}O_4$ by combustion reaction method. Journal of Magnetism and Magnetic Materials. 2007;**308**:198-202. DOI: 10.1016/j.jmmm.2006.05.022

[7] Park SI, Kim JH, Kim CG, Kim CO. Effect of substitution elements on magnetization of monodispersed MFe_2O_4 particles. Current Applied Physics. 2008;**8**(6):784. DOI: 10.1016/j.cap.2007.04.025

[8] Costa ACFM, Tortella E, Morelli MR, Kaufman M, Kiminami R. H 159 G a effect of heating conditions during combustion synthesis on the characteristics of $Ni_{0.5}Zn_{0.5}Fe_2O_4$ nanopowders. Journal of Materials Science. 2002;**37**:3569-3572

[9] Salunkhe AB, Khot VM, Phadatare MR, Pawar SH. Combustion synthesis of cobalt ferrite nanoparticles—Influence of fuel to oxidizer ratio. Journal of Alloys and Compounds. 2012;**514**:91-96. DOI: 10.1016/j.jallcom.2011.10.094

[10] Franco A, Pereira Alves TE, Oliveira Lima EC, Silva Nunes E, Zapf V. Enhanced magnetization of nanoparticles of $Mg_xFe_{3-x}O_4$ ($0.5 \leq x \leq 1.5$) synthesized by combustion reaction. Applied Physics A: Materials Science & Processing. 2008;**94**:131-137. DOI: 10.1007/s00339-008-4684-y

[11] Eustace DA, Docherty FT, McComb DW, Craven AJ. ELNES as a probe of magnetic order in mixed oxides. Journal of Physics Conference Series. 2006;**26**(1):165

[12] Sijo AK, Dutta DP, Roy M, Sudheesh VD. Magnetic and dielectric properties of $NiCrFeO_4$ prepared by solution self-combustion method. Materials Research Bulletin. 2017;**94**: 154-159. DOI: 10.1016/j.ceramint.2017.09.093

[13] Sijo AK. Magnetic and structural properties of $CoCr_xFe_{2-x}O_4$ spinels prepared by solution self-combustion method. Ceramics International. 2017;**43**(2):2288-2290. DOI: 10.1016/j.ceramint.2016.11.010

[14] Sijo AK, Lakshmi N, Venugopalan K, Dutta DP, Jain VK. Effect of fuel to oxidizer ratio on structural and magnetic properties of $ZnCrFeO_4$ Nanopowder. Advanced Porous Materials. 2015;**2**(3):189-191. DOI: 10.1166/apm.2014.1071

[15] Sijo AK. Influence of fuel-nitrate ratio on the structural and magnetic properties of Fe and Cr based spinels prepared by solution self-combustion method. Journal of Magnetism and Magnetic Materials. 2017;**441**:672-677. DOI: 10.1016/j.jmmm.2017.06.060

[16] Sijo AK, Dutta DP, Roy M, Dielectric study of $CoCrFeO_4$ nano-powder prepared by solution self-combustion. Ceramics International. 2017;**43**(18):16915-16918. DOI: 10.1016/j.ceramint.2017.09.093

[17] Sijo AK. Studies of magnetic and transport properties of some nanosized Fe and Cr based spinels. [PhD thesis] Chapters 3 and 4, Udaipur: Mohanlal Sukhadia University; 2017

Chapter 7

Microwave Plasmas as a Processing Tool for Tailoring the Surface Properties of Ceramic Coatings

Emmanuel J. Ekoi, Muhammad Awais and Denis P. Dowling

Additional information is available at the end of the chapter

http://dx.doi.org/10.5772/intechopen.71686

Abstract

This chapter reviews the use of low pressure microwave plasmas as a processing technology for both sintering and controlling the surface chemistry of porous ceramic coatings. A particular advantage of microwave processing is its ability to penetrate the surface of the workpiece; enabling rapid volumetric heating and thus reducing the need for external heat sources. The microwave plasma treatments have the ability to sinter materials in minutes rather than the hours taken using conventional furnace processing. This study provides examples of the use of these plasmas to sinter both nickel and titanium nanoparticles. These are used in the fabrication of electrodes for use in dye sensitized solar cells. Further applications of the microwave plasma treatments investigated is for their use in heat treatment to control crystalline phase transitions, as well as a rapid technique to oxidize metal surfaces.

Keywords: microwave plasma, porous ceramics, nickel oxide, titanium oxide, coatings

1. Introduction

Microwaves are electromagnetic waves with wavelengths from 1 mm to 1 m and corresponding frequencies between 0.3 MHz and 300 GHz [1, 2]. The use of microwave treatments (non-plasma), as an energy source for the heat treatment of metals, ceramics and composites has been reported to be more effective than conventional furnace heating methods, due to the improved microstructure and properties, reduction in processing time, etc. [1–3]. These microwave treatments are usually carried out at 0.915 GHz, 2.45 GHz and 20–30 GHz frequencies in agreement with the industrial, scientific and medical (ISM) radio bands set aside for non-communication purposes [2, 4]. During microwave processing, energy is supplied

by an electromagnetic field directly to the material by the interaction of the molecules of the material with electromagnetic field. In contrast, conventional thermal processing involves the transfer of energy by conduction, convection and radiation [5].

Clark et al. [1] reviewed the effectiveness of microwave heating and found it to be substrate material dependant. Materials were, thus, grouped into categories (depending on the electromagnetic field-material interaction) as: transparent (low dielectric loss materials); opaque (conductors); absorbing (high dielectric loss materials); and mixed absorbing where there is selective absorption due to differences in dielectric loss in the materials.

Several researchers have demonstrated the capability of using microwave to process metallic and ceramic materials [6–11]. It has been reported that a distinction in the microstructure and porosity distribution can be made between conventional and microwave sintered materials with respect to the pore shape. Microwave sintered samples exhibit pores with more rounded edges than the conventionally sintered materials. The sphericity of pore is reported to be critical in the ductility and strength of the sintered material [11].

In addition to the use of microwaves directly, a plasma discharge can also be formed using the microwave energy, if the appropriate conditions (gas type, pressure, resonator, etc.) are in place. Briefly by way of introduction to this technique, a plasma is described as a collection of unbound charged particles, photons and neutral atomic or molecular species which are electrically neutral on average [12, 13]. Plasma generation arises from the excitation and ionization of gases by energy transfer from various sources to the gases to form excited, charged and neutral species [14]. There are a range of plasma types including high frequency, DC and low frequency discharges [15, 16]. The latter include systems such as glow discharge, corona discharge, hollow cathode discharge [16], while the high frequency consists of radio frequency (RF) and microwave plasma discharges [17].

Microwave plasma systems are usually electrodeless systems and thus, differ from DC and RF systems which mostly use electrodes to generate plasma. In these systems, microwaves are usually guided using waveguide into the chamber where energy is impacted to the gas to form plasma by partially ionizing the gas [18, 19]. A typical example of microwave plasma system is the circumferential antenna plasma (CAP) microwave reactor, which operates at 2.45 GHz (**Figure 1**). In this CAP system, a cylindrical quartz ring window, 345 mm in diameter, embedded in the wall of the plasma chamber guides the microwaves into the plasma chamber. The microwaves are directed to the plasma chamber through a coaxial waveguide, and expands radially as it moves towards the cylindrical quartz ring window. A perfect rotational symmetry is obtained when the microwave which has uniform amplitude and phase distribution passes through the quartz window [20]. The cylindrical geometry of the configuration ensures that the formation of microwave power density at the window is lower than in the center of the chamber; thus, no plasma is formed adjacent to the window [21].

The use of microwave plasma source for surface and bulk treatment of metal and ceramics has the potential to be more effective than DC and RF plasmas, because of the higher density of active atomic species that can be generated using this type of discharge [22]. Microwave discharges generally have higher electron kinetic temperature and number density because

http://dx.doi.org/10.5772/intechopen.71686

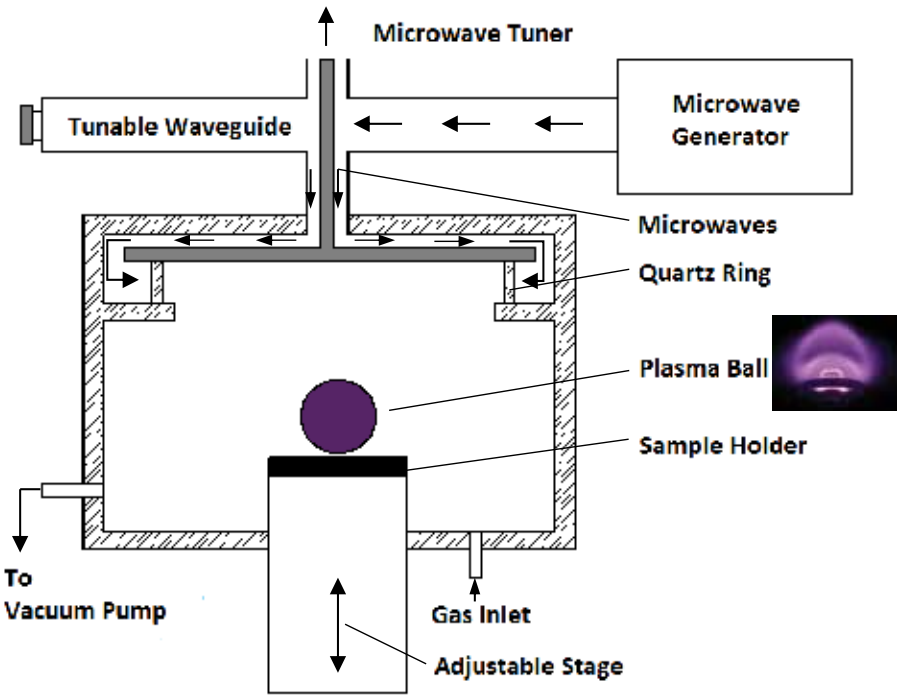

Figure 1. Schematic representation of CAP microwave plasma system.

the power is usually coupled through radiation and thus, bypasses sheath losses [17, 23]. A further advantage of these plasmas is that they can be operated in a wide gas pressure range [24, 25], which combine with the higher electron temperature generally obtained, makes them capable of providing a higher fraction of ionization and dissociation [24].

Metal oxide layers can be obtained using a range of techniques including sol-gel, hydrothermal synthesis, electrophoretic deposition, sputtering, electrochemical treatments (anodic oxidation), chemical vapor deposition (CVD), physical vapor deposition and ion implantation, etc. [26–32]. Most of the techniques (except sputtering and direct metal oxide growth on metal surfaces) require sintering to enhance the packing density, porosity and the adhesion of the deposited coatings. A range of characterisation techniques usually applied includes a FEI Quanta 3D FEG DualBeam scanning electron microscope (SEM) (Morphology); a focused ion beam (FIB)(Thickness); Energy-dispersive X-ray spectroscopy (EDX) (Elemental data); Veeco NT1100 optical profilometer (Surface roughness). Siemens D500 XRD system (Phase identification), a LASCON QP003 and LPC03 ratio pyrometers from Dr. Mergenthaler GmbH & Co. KG. (Temperature measurements) and a J.A. Woollam ellipsometer with a Tauc-Lorentz fitting via completeEASE® software (Band gap and coating thickness).

Having provided an introduction to microwave plasma treatments along with the associated characterization techniques, the following sections firstly provide an overview of the use of microwave plasmas for the sintering of metal oxide powders. The use of microwave plasma treatments for sintering, has previously been described as rapid discharge sintering (RDS).

The specific focus is on the sintering of nanoparticles of nickel oxide (NiO) and titanium dioxide (TiO_2), used as electrodes in dye sensitized solar cells (DSSCs). The effect of the plasma treatments on thermal sensitive crystalline phase changes, is also discussed. A further application reported is that of the use of microwave plasma treatments for the oxidation of metal surfaces, in order to produce porous oxide ceramic (TiO_2) layers on the metal surface.

2. Microwave plasma sintering of nanoparticles

Considerable research has been carried out to understand the interaction of microwave radiation with materials [33, 34]. The ability of microwaves to penetrate work pieces enables volumetric heating at a rapid rate, thus avoiding the need of external heat sources [33]; this makes it an attractive technique in material processing. However, poor coupling in non-plasma microwave processing may result in a non-uniform heating of the substrates [35]. One of the advantages of microwave plasma treatment is the combined advantage inherent in microwave and plasma heating in terms of volumetric, homogeneous and rapid heating [2, 36, 37]. For example, the work of Twomey et al. [37] demonstrates that homogenous heating of substrates could be achieved using microwave plasma treatments including considerably lower cycle times [38] compared to non-plasma microwave and furnace heating. In this section, the use of microwave plasma processing for the sintering of Nickel oxide (NiO) and Titanium dioxide (TiO_2) particles is presented.

2.1. Sintering of nickel oxide (NiO) nanoparticles

NiO coatings are used extensively as a photocathode in the construction of *p*-type DSSCs [39–42] due to their *p*-type semiconductivity [43], and well defined electrical and optical properties [44]. Furthermore, its bandgap energy which range from 3.6 to 4.0 eV helps to make it a model semiconductor substrate [43]. Also, it is considered a good electron donor for numerous photo sensitizers due to its valance bond potential; thus, the NiO coatings are readily quenched with many dye sensitizers [45]. In this section, the use of microwave plasma processing for the sintering of NiO particles to produce coatings for use in DSSC electrodes is discussed [42, 46].

2.1.1. Rapid discharge sintering vs. conventional furnace sintering

In order to process NiO using the RDS technique, a spray technique is used to deposit solvent slurry of NiO nanoparticles onto conductive glass substrates (**Figure 2**). The spray technique involves suspending the NiO nanoparticles in alcohol; the mixture is then applied via spraying onto fluorine-doped tin oxide (FTO) coated glass substrates to form the coating. A subsequent step is carried out after spraying in order to enhance the interconnectivity between the NiO particles by sintering, as well as an increased level of adhesion to the conductive glass substrate. This sintering step was investigated using both microwave plasma and furnace treatments [42, 46]. The latter was carried out using a CWF 1200 Carbolite tube air furnace. Typical furnace sintering temperatures in the range of 300–450°C have been reported

http://dx.doi.org/10.5772/intechopen.71686

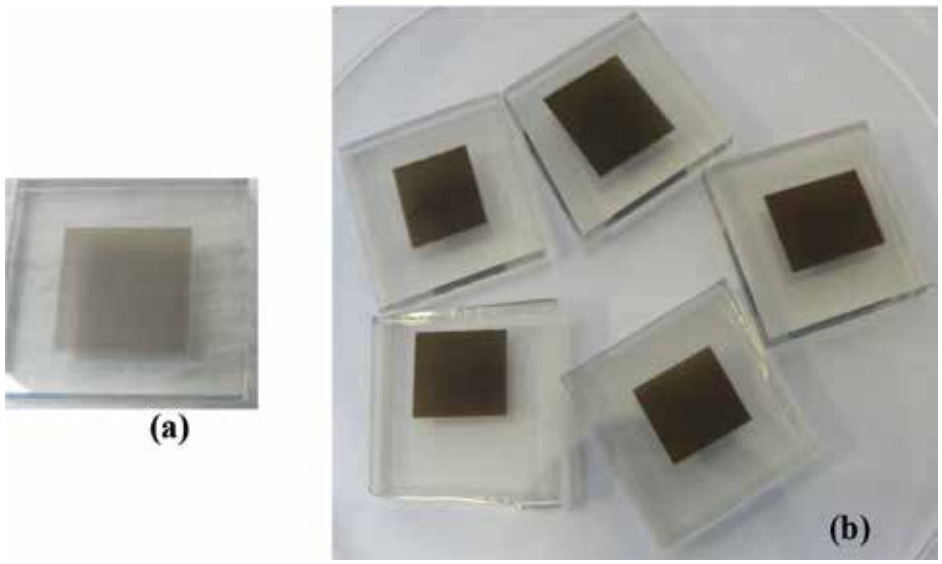

Figure 2. (a) 0.6 (b) 2.5 μm thick NiO coatings deposited using spray technique.

previously [47–51]. In this study, a treatment temperature of approximately 450°C was used for a 5-min period for both the furnace and RDS treatments. This treatment time was chosen because it yielded the best photovoltaic performance for RDS treatment. Overall, a cycle time of ~120 min was required for the furnace sintering including heat up, maintenance at the max 450°C temperature and cool down. In contrast, the RDS processing required only 15 min, included all stages such as pump down, plasma treatment, and cooling.

In this Section, the properties of the furnace sintered coatings, such as morphology, crystal structure, dye adsorption, chemical composition and photovoltaic performance are compared with the NiO coatings treated for 5 min, using the RDS technique.

2.1.1.1. Morphological analyses of porous NiO coatings

A typical SEM micrograph of the morphology of RDS and furnace treated coatings is given in **Figure 3**. A higher level of interconnectivity with reduced grain growth for the RDS treated coatings when compared with the furnace sintered coatings can be observed. The increased grain growth in the furnace sintered coatings could be due to a slower cooling rate (10°C/min) used in the furnace process. In contrast, the RDS technique requires only a 5-min cooling time following the plasma treatment.

A further examination of NiO coatings using an FIB/SEM cross section micrograph (**Figure 4**) indicated that the RDS treated coating displays an improved level of porosity as well as interfacial connection between the NiO coating and FTO substrate. This could be due to the difference in the type of heating mechanisms in both sintering techniques. RDS treatment encompasses volumetric heating, which delivers more efficient heating inside the NiO coating matrix than that obtained with furnace sintering where a conductive type of heating is

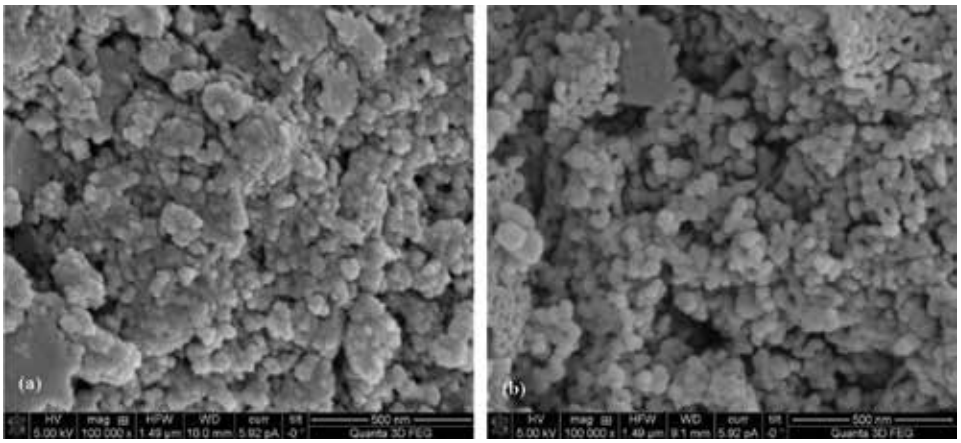

Figure 3. SEM images of ~2.5 μm thick NiO coatings treated using (a) RDS (b) furnace sintering [52].

present. Also, furnace sintering could have resulted in inhomogeneous heating of coatings' surface to yield a heat affected zone [53]; thus, a more open structure is observed for the RDS treated coatings when compared with the furnace sintered samples.

2.1.1.2. Crystal structure, crystallite size and dye adsorption evaluations of NiO coatings

As shown in **Figure 3**, the NiO grain size obtained using the RDS process was smaller than that obtained after treatment using the furnace. A measurement of the crystallite size of NiO coatings obtained using similar sintering techniques to **Figure 3** indicated that the sizes were approximately 6.5 and 14.0 nm, respectively [42]. Thus, the RDS technique results in a finer grain size, in addition to a more uniform heating/sintering of the NiO nanoparticles.

The effect of a smaller grain size and a more open structure (**Figures 3** and **4**) obtained using the RDS technique may be observed in the UV-vis absorption spectra of the NiO coatings obtained using the two sintering techniques (**Figure 5**). The level of dye adsorption increased up to 44% for the case of RDS treated NiO coatings when compared with the furnace sintered coatings of the same thickness.

2.1.1.3. Comparison of photovoltaic performance of porous NiO coatings

Another parameter which can be used to portray the performance of the porous NiO structure is its photovoltaic performance (*I-V* characteristic) when evaluated as part of a *p*-type DSSCs. A comparison of the photovoltaic performance of NiO coatings prepared by various researchers is given in **Table 1**. From this Table, it is clear that the light-to-current conversion efficiency increase of almost 10-fold for the RDS treated NiO coatings (1–2 μm and 2.5 μm thick), when compared with the furnace sintered coatings. The conversion efficiency of the furnace treated coatings (1–2 μm thick) is comparable to the values reported in the literature [42, 46]. A notable observation is that a 2.5 μm thick NiO coatings, prepared using the RDS treatment, exhibited the best performance; it is likely due to improved dye adsorption with enhanced active sites, which results in better photochemical reaction.

http://dx.doi.org/10.5772/intechopen.71686

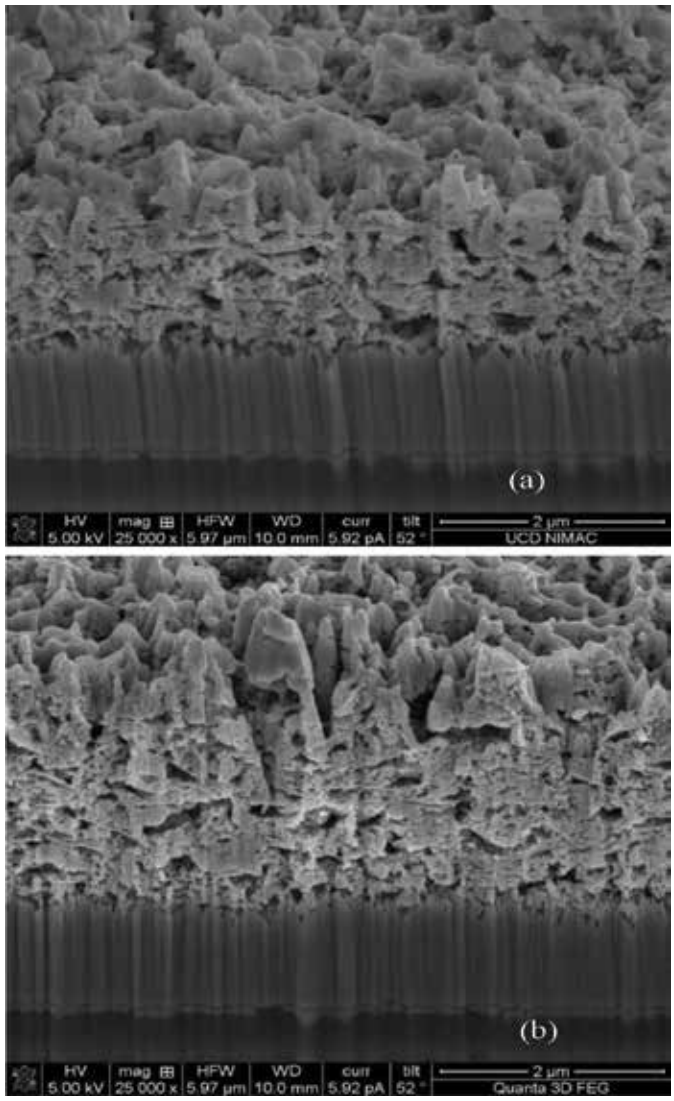

Figure 4. FIB/SEM cross section images of NiO coatings obtained after 5 min sintering using (a) the furnace and (b) the RDS technique. Both coating thicknesses were approximately 2.5 μm. Reprinted from [42] with permission from Elsevier.

2.2. Sintered titanium dioxide (TiO_2) nanoparticles

Since the use of TiO_2 as a photoanode in the fabrication of a DSSC in 1991 by O'Regan and Grätzel [55], many researchers employ TiO_2 for DSSC and other related applications. The phase transformation of TiO_2 coatings is generally carried out using furnace sintering, however, as discussed earlier, it is time consuming. In this section, we will present the use of RDS as viable unconventional sintering technique to convert amorphous TiO_2 to crystalline phase(s). The effect of carbon doping on the resultant coating is also discussed. In this review, the TiO_2 coating of interest with respect to sintering will be that obtained by Dang et al. [56],

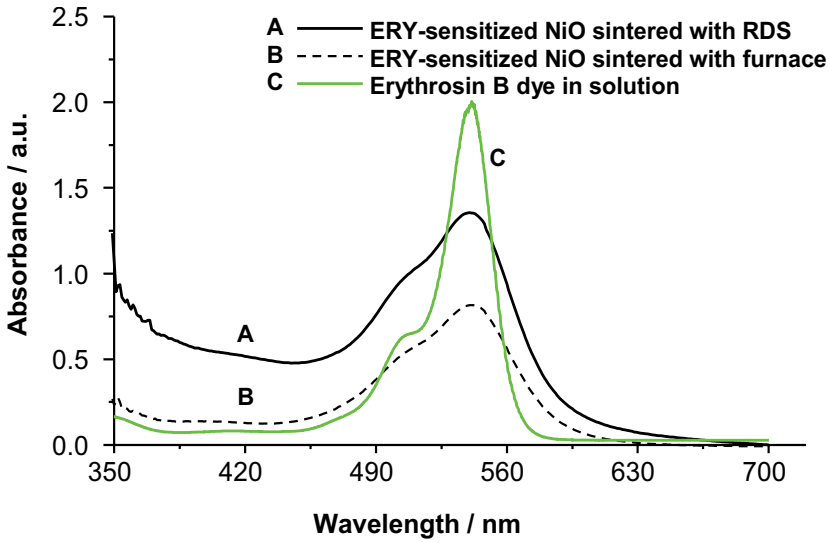

Figure 5. UV-vis absorbance spectra dye sensitized NiO coatings of 1–2 μm thickness (RDS and furnace sintered) and ERY dye in solution. Reprinted from [42] with permission from Elsevier.

Awais et al. [42, 46]/*Reported data* (NiO thickness)	**Treatment time (min)**	**V_{oc} (mV)**	**J_{sc} (mAcm^{-2})**	**FF**	**Efficiency (η)**
RDS treated (~2.5 μm thick)	5	120.00	1.05	36	0.0450
Furnace sintered (~2.5 μm thick)	5	84.00	0.22	25	0.0050
Furnace sintered (~2.5 μm thick)	30	35.29	0.21	26	0.0023
RDS treated (~1–2 μm thick)	5	72.14	0.53	28	0.0118
Furnace sintered (~1–2 μm thick)	5	50.30	0.24	28	0.0037
He et al. [54] (~1 μm thick)	*60*	*83.00*	*0.20*	*27*	*0.0070*
Nattestad et al. [48] (~1.6 μm thick)	*20*	*120.00*	*0.36*	*26*	*0.0110*

Table 1. Photovoltaic performance of RDS and furnace NiO coatings used as photocathode in construction of p-type DSSC (compared with the literature). AM 1.5 solar simulator (*I*: 870 W m^{-2}), 0.5 M LiI and 0.05 M I_2 in propylene carbonate as an electrolyte [52]. Values in italics represent reported literature data.

for example. The following type of coatings are analyzed for their performance: furnace sintered C-doped, RDS treated undoped and C-doped RDS treated.

2.2.1. Comparison of RDS and air furnace treatments of porous TiO_2

TiO_2 coatings were also used to fabricate DSSC electrodes. TiO_2 and carbon-doped TiO_2 were deposited as coatings onto unheated titanium and silicon wafer substrates using a DC closed-field magnetron sputtering system [56]. The C-doped TiO_2 coatings were

http://dx.doi.org/10.5772/intechopen.71686

obtained by introducing low concentrations of carbon dioxide into the argon/oxygen plasma during the sputtering of the metal. The resultant coatings had an amorphous structure and a post-deposition heat treatment is required to convert this amorphous structure into the photoactive crystalline phase(s) of TiO_2. This was achieved using the CAP microwave plasma heat treatment using a nitrogen plasma. During the plasma treatment, the substrate temperature was about 550°C. At this temperature and for treatment times as short as 1 min, 0.25 μm thick coatings converted into the anatase crystalline phase of TiO_2. Further treatments of the coatings at higher temperatures resulted in anatase-to-rutile crystalline phase transformation [56]. As reported earlier for the NiO layers the use of microwave plasma heat treatments facilitated a much more rapid processing compared with furnace heat treatments. It was also observed that the plasma treated TiO_2 coatings also exhibited higher photocurrent density. This is possibly as a result of higher level of surface roughness and consequently a higher available surface area observed for these coatings [56].

As for the plasma treated TiO_2 coatings, C-doped coatings also exhibited a higher roughness when plasma treated compared to furnace treated (**Figure 6**). To investigate the phase transformation efficiency of the two treatment methods as well as the effect of carbon doping, an XRD profile of undoped and C-doped TiO_2 coatings was obtained. As shown in **Figure 7(a)**, anatase phase peaks were observed for coatings treated between 550 and 850°C. As the temperature is increased to 875°C, peaks indicative of the rutile phase could be observed. Interestingly, for the C-doped TiO_2 coatings, the rutile phase can be observed at 750°C (**Figure 7(b)**); thus, it is possible that carbon doping lowered the transitional phase change temperature of anatase to rutile.

In order to evaluate the effect of doping on the efficiency of the TiO_2 coated electrodes, photocurrent density (I_{Ph}) measurements were obtained, as presented in **Table 2**. The highest value

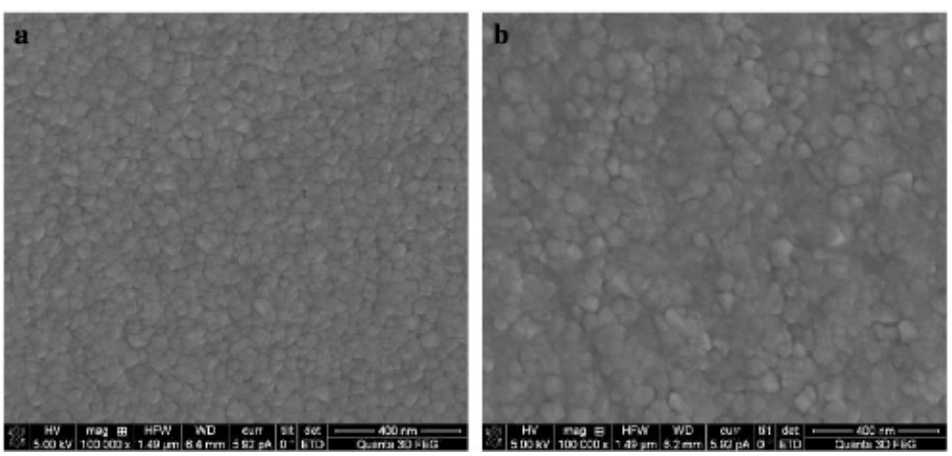

Figure 6. Surface morphology of 2.2% C-doped TiO_2 (a) furnace-treated and (b) MW plasma-treated at 750°C for 3 min. Reprinted from [56] with permission from Elsevier.

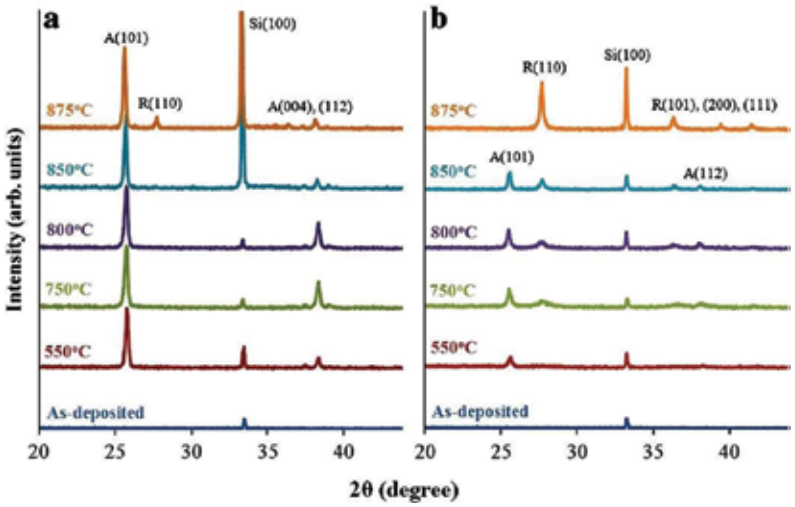

Figure 7. XRD profile of as deposited (a) undoped and (b) 2.2% C-doped TiO_2 upon RDS treatment. Reprinted from [56] with permission from Elsevier.

TiO_2 coatings	Photocurrent density values, I_{Ph} ($\mu A/cm^2$)
As-deposited (C-doped)	108
Furnace sintered (C-doped)	181
RDS treated (un-doped)	167
RDS treated (C-doped)	216

Table 2. Photocurrent density values for different TiO_2 coatings.

of photocurrent density was obtained for the case of carbon doped plasma treated TiO_2 coatings. There was a 19% increase in the I_{Ph} value in comparison to those treated in the furnace. Possible reasons for the superior performance could be due to the enhanced porosity level of plasma treated coatings, which may have provided more active sites for charge production [56]. A further factor could be that the retention of more doped carbon in the RDS-treated TiO_2 coatings further reduced the band gap of RDS-treated compared to the furnace-treated TiO_2 coatings (See **Figure 8**).

2.3. Conclusion and potential of the RDS sintering technique

RDS-treated NiO coatings were found to exhibit a light-to-current conversion efficiency increase of almost a 10-fold, compared with that obtained for the furnace treated oxide coating. Amongst the likely reasons for the enhanced performance is the smaller grain size, along with the more open structure obtained using the RDS technique.

http://dx.doi.org/10.5772/intechopen.71686

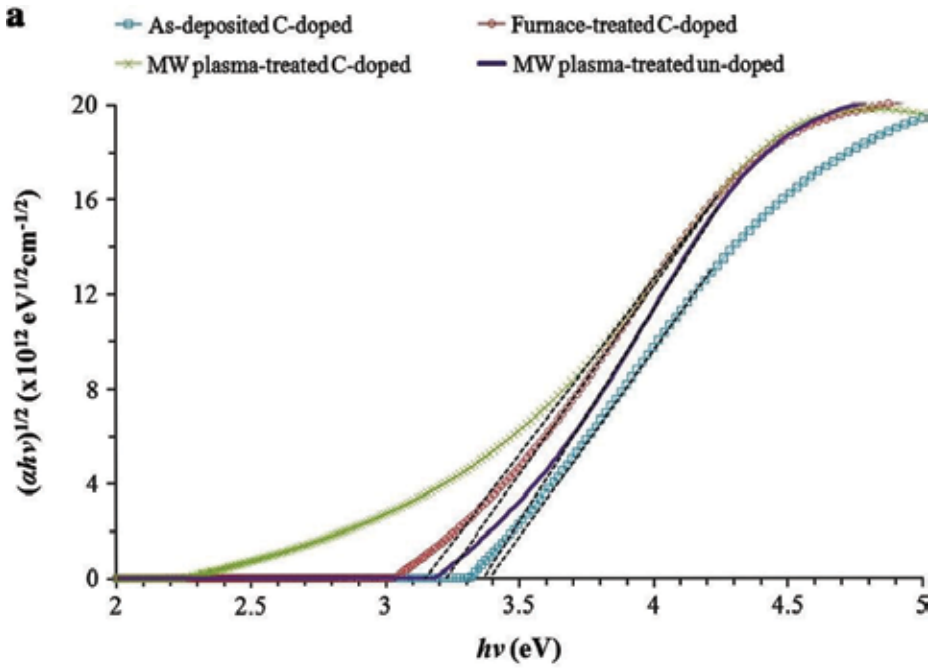

Figure 8. Band gap measurements for as-deposited, furnace treated, RDS treated (2.2% carbon doped) and undoped RDS treated TiO_2 coatings. Reprinted from [56] with permission from Elsevier.

3. Direct porous ceramics growth from metal substrates

In this study, the performance of microwave plasma treatments as a technique for the oxidation of metallic surfaces is investigated. Oxides of titanium formed either on the metal surface or alternatively as TiO_2 coatings (discussed in Section 2.2) have found applications in areas ranging from medical devices (cell attachment), solar cells (light capture), air and water purification, gas sensing, wear protective coatings, etc. [57–62]. This is due to the oxide's photocatalytic, biocompatibility properties, as well as its physical and chemical stability. These properties would depend on the morphology, surface roughness and porosity of the oxides.

Compared to furnace heat treatments, microwave plasma-treated TiO_2 coatings discussed in Section 2.2 possess higher level of surface roughness and hence photoactivity. However, the enhanced surface roughness is still only in the order of a few nanometers and thus, the photoactivity of the resulting coatings is relatively limited [63]. An alternative fabrication method which has been investigated to address this shortcoming is presented in this section.

3.1. RDS oxidation of titanium metal substrates

The plasma treatments were carried out as before using the CAP microwave reactor, in this case using an oxygen discharge [63, 64]. Prior to plasma oxidation, the titanium disc test

substrates were polished to a mirror finish and then solvent cleaned. The oxidized substrates exhibited a white appearance, as shown in **Figure 9**; this is in contrast to the metallic appearance of the non-oxidized titanium metal.

A typical FIB/metallography SEM cross-section image of a RDS treated TiO_2 structure obtained using a focused ion beam (FIB) and metallographic technique for comparison is shown in **Figure 10**. It can be observed that the two sample preparation methods (FIB and metallography) did not alter the porous structure of the ceramics.

3.2. Influence of substrate temperature on the pore structure morphology in a RDS grown oxide-layer

The porosity of the oxide-layer structure was found to generally increase with increase in thickness and treatment temperature (**Figure 11**). Examination of the porous oxide structures indicates that oxide-layers grown at temperature below 880°C exhibits a relatively porous structure, in the upper oxide layer compared to that closer to the metal substrate. Oxides fabricated above 880°C exhibited a further increase in porosity levels throughout the oxide layer. It is well known that α to β phase transformation of titanium occurs at approximately 882°C; this may have influenced porosity distribution observed in the oxide-layers grown on titanium substrates above 880°C [64].

3.3. Comparison of the porosity of sintered TiO_2, air furnace and RDS grown oxide-layer

Figure 12 shows the oxide layer morphology of a RDS and air furnace grown ceramic structures. The structure in **Figure 12(a)** was obtained after 5-hours furnace treatment in air and its thickness was found to be 4.17 μm. In contrast, after treatment in an oxygen microwave plasma for 10 min, the thickness obtained was 6.96 μm (**Figure 12(b)**). It can be observed that the oxide-layer obtained using the microwave plasma oxidation exhibited a relatively

Figure 9. Photograph of oxide-layer formed on the 25-mm diameter titanium disc using microwave plasma and air furnace. Reprinted from [64] with permission from Elsevier.

http://dx.doi.org/10.5772/intechopen.71686

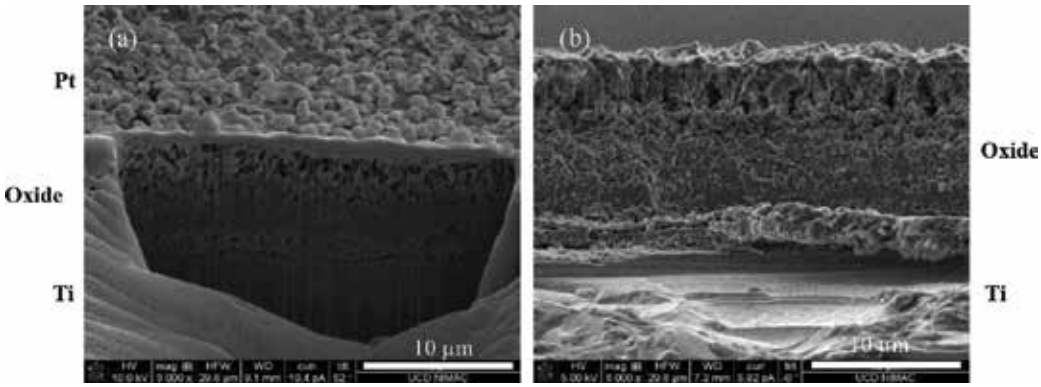

Figure 10. SEM images of oxide cross-section prepared using the FIB (a) and metallographic technique (b). The images were obtained using an FEI Quanta 3D FEG DualBeam system. The average oxide-layer thickness for both techniques is 9.89 μm. (Note a 52° tilt angle is used for the FIB image.) Reprinted from [64] with permission from Elsevier.

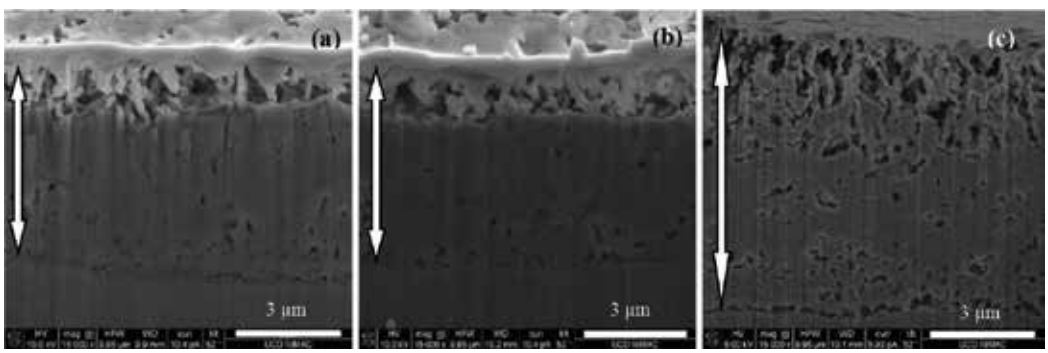

Figure 11. Oxide-layers (demonstrated using the arrows), which were grown on titanium substrates at temperature: (a) 855°C, (b) 880°C and (c) 910°C showing porosity distribution. Note the increased porosity obtained at the higher oxidation temperature. Reprinted from [64] with permission from Elsevier.

rough morphology, with large grains. In contrast, the slower growing oxide formed using the furnace oxidation exhibited a much denser morphology with little or no porosity observed. A possible reason for the increased porosity obtained for the RDS treatments is a result of a preferential grain growth in specific directions due to a van der Drift type of competition with increasing thickness of oxide layer [64].

To conclude it is interesting to compare the morphology of two TiO_2 oxide layers obtained as part of this study as shown in **Figure 13**. **Figure 13(a)** was obtained by oxidation of metal oxide nanoparticles and **Figure 13(b)** by the oxidation of the titanium metal. Both were obtained using the microwave plasma treatments. It is clear from **Figure 13** that the sintering of the TiO_2 nanoparticles yields a much more homogeneous oxide pore structure. Its fabrication, however, involves two steps (spray deposition and sintering), compared with the single microwave plasma oxidation step. Both treatments, however, demonstrate the flexibility of the microwave plasma treatments.

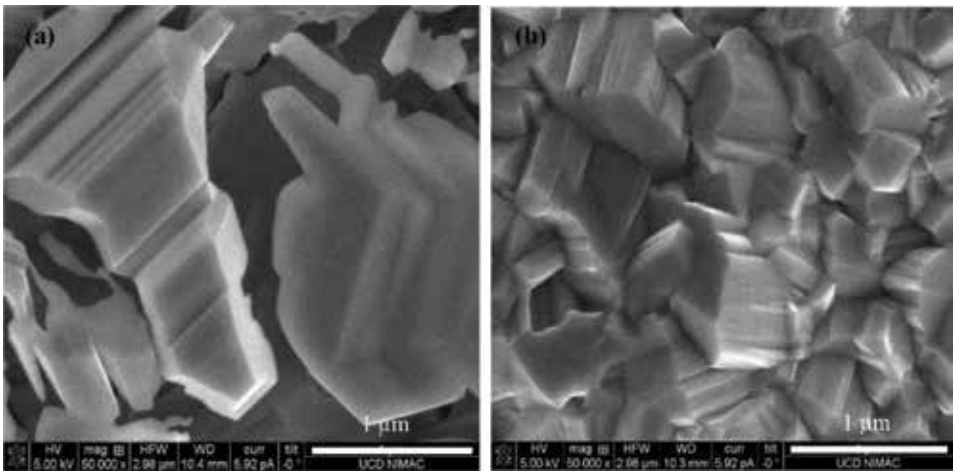

Figure 12. Typical SEM images of oxide-layers grown using a RDS (a); and air furnace (b), demonstrating differences in the grain structure obtained (samples both prepared at a treatment temperature of 790°C). Reprinted from [64] with permission from Elsevier.

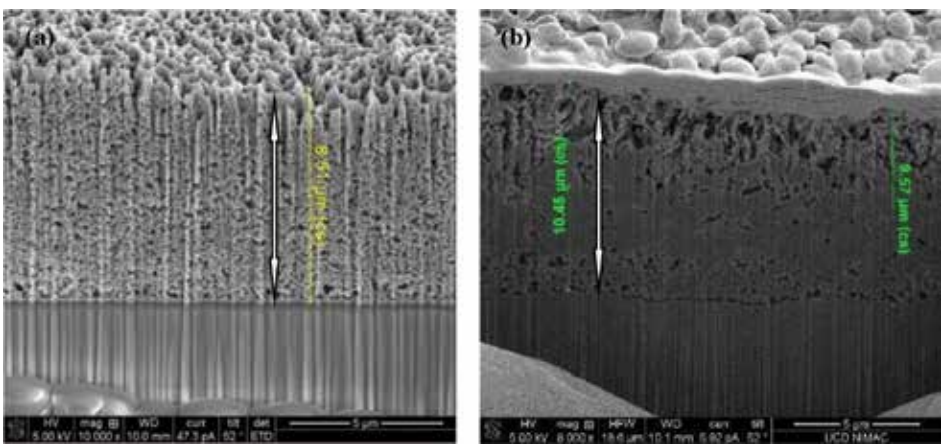

Figure 13. FIB cross-sections of an 8.5 μm thick TiO_2 coating (a) fabricated by sintering TiO_2 nanoparticles. The FIB cross section (b) shows a 10.45 μm TiO_2 oxide-layer obtained by oxidizing the Cp titanium metal (reprinted from [64] with permission from Elsevier).

4. Conclusions

The use of microwave plasma treatments has been reviewed both for sintering nanoparticles (referred to as rapid discharge sintering (RDS), as a thermal processing route for crystalline phase changes, as well as for the oxidation of metal surfaces. For the fabrication of porous ceramics, the plasma treatments have the advantage of being rapid and flexible allowing for the tailoring and control of pore structures with processing conditions. Compared to the conventional methods such as air furnace treatment, the plasma treatments were demonstrated

http://dx.doi.org/10.5772/intechopen.71686

to yield improved results in terms of shorter treatment time, lower energy requirement and enhanced performance. The latter was demonstrated in the case of metal oxide layers (NiO and TiO_2), when evaluated for use in solar energy applications.

Author details

Emmanuel J. Ekoi[1]*, Muhammad Awais[2] and Denis P. Dowling[1]

*Address all correspondence to: emmanuel.ekoi@ucdconnect.ie

1 School of Mechanical and Materials Engineering, University College Dublin, Dublin 4, Ireland

2 Department of Industrial Engineering, Taibah University, Medina, Saudi Arabia

References

[1] Clark DE, Folz DC, West JK. Processing materials with microwave energy. Materials Science and Engineering: A. 2000;**287**(2):153-158

[2] Das S, Mukhopadhyay AK, Datta S, Basu D. Prospects of microwave processing: An overview. Bulletin of Materials Science. 2009;**32**(1):1-13

[3] Sutton WH. Microwave processing of ceramics-an overview. In: MRS Proceedings. Vol. 269. Cambridge University Press; Cambridge, UK, 1992. p. 3

[4] Agrawal D. Microwave sintering of metal powders. In: Chang I, Zhao Y, editors. Advances in Powder Metallurgy. Woodhead Publishing Ltd; Sawston, UK, 2013. p. 361-379

[5] Thostenson ET, Chou TW. Microwave processing: Fundamentals and applications. Composites Part A: Applied Science and Manufacturing. 1999;**30**(9):1055-1071

[6] Roy R, Agrawal D, Cheng J, Gedevanishvili S. Full sintering of powdered-metal bodies in a microwave field. Nature. 1999;**399**(6737):668-670

[7] Sethi G, Upadhyaya A, Agrawal D. Microwave and conventional sintering of premixed and prealloyed Cu-12Sn bronze. Science of Sintering. 2003;**35**(2):49-65

[8] Takayama S, Saiton Y, Sato M, Nagasaka T, Muroga T, Ninomiya Y. Microwave sintering for metal powders in the air by non-thermal effect. In: Proceedings of the 9th Conference on Microwave and High Frequency Heating; 2003. pp. 369-372

[9] Gupta M, Wong WLE. Enhancing overall mechanical performance of metallic materials using two-directional microwave assisted rapid sintering. Scripta Materialia. 2005; **52**(6):479-483

[10] Saitou K. Microwave sintering of iron, cobalt, nickel, copper and stainless steel powders. Scripta Materialia. 2006;**54**(5):875-879

[11] Agrawal D. Microwave sintering of ceramics, composites and metallic materials, and melting of glasses. Transactions of the Indian Ceramic Society. 2006;**65**(3):129-144

[12] Lieberman MA, Lichtenberg AJ. Principles of Plasma Discharges and Materials Processing. John Wiley & Sons; New Jersey, USA, 2005

[13] Möller W. Fundamentals of Plasma Physics. University of Technology Dresden; Dresden, Germany, 2014

[14] Conrads H, Schmidt M. Plasma generation and plasma sources. Plasma Sources Science and Technology. 2000;**9**(4):441

[15] Bellan PM. Fundamentals of Plasma Physics. Cambridge University Press; Cambridge, UK, 2008

[16] Go D. Gaseous Ionization and Ion Transport: An Introduction to Gas Discharges. Department of Aerospace and Mechanical Engineering University of Notre Dame; Indiana, USA, 2012

[17] Moisan M, Barbeau C, Claude R, Ferreira CM, Margot J, Paraszczak J, et al. Radio frequency or microwave plasma reactors? Factors determining the optimum frequency of operation. Journal of Vacuum Science & Technology B: Microelectronics and Nanometer Structures Processing, Measurement, and Phenomena. 1991;**9**(1):8-25

[18] Kabouzi Y, Calzada MD, Moisan M, Tran KC, Trassy C. Radial contraction of microwave-sustained plasma columns at atmospheric pressure. Journal of Applied Physics. 2002;**91**(3):1008-1019

[19] Tendero C, Tixier C, Tristant P, Desmaison J, Leprince P. Atmospheric pressure plasmas: A review. Spectrochimica Acta Part B: Atomic Spectroscopy. 2006;**61**(1):2-30

[20] Pleuler E, Wild C, Füner M, Koidl P. The CAP-reactor, a novel microwave CVD system for diamond deposition. Diamond and Related Materials. 2002;**11**(3):467-471

[21] McConnell ML, Dowling DP, Pope C, Donnelly K, Ryder AG, O'Connor GM. High pressure diamond and diamond-like carbon deposition using a microwave CAP reactor. Diamond and Related Materials. 2002;**11**(3):1036-1040

[22] Kakizaka S, Sakamoto T, Matsuura H, Akatsuka H. Titanium oxidation by microwave discharge oxygen plasma and relationship with plasma parameters. Journal of Advanced Oxidation Technologies. 2007;**10**(2):253-259

[23] Ganguli A, Tarey RD. Understanding plasma sources. Current Science. 2002;**83**(3):279-290

[24] Toumanov IN. Plasma and High Frequency Processes for Obtaining and Processing Materials in the Nuclear Fuel Cycle. Nova Publishers; New York, USA, 2003. p. 64

[25] Eliasson B, Kogelschatz U. Nonequilibrium volume plasma chemical processing. IEEE Transactions on Plasma Science. 1991;**19**(6):1063-1077

[26] Lu G, Bernasek SL, Schwartz J. Oxidation of a polycrystalline titanium surface by oxygen and water. Surface Science. 2000;**458**(1):80-90

[27] Del Pino AP, Serra P, Morenza JL. Oxidation of titanium through Nd: YAG laser irradiation. Applied Surface Science. 2002;**197**:887-890

[28] Gemelli E, Camargo NHA. Oxidation kinetics of commercially pure titanium. Matéria (Rio de Janeiro). 2007;**12**(3):525-531

[29] Li LH, Kong YM, Kim HW, Kim YW, Kim HE, Heo SJ, Koak JY. Improved biological performance of Ti implants due to surface modification by micro-arc oxidation. Biomaterials. 2004;**25**(14):2867-2875

[30] Diefenbeck M, Mückley T, Schrader C, Schmidt J, Zankovych S, Bossert J, et al. The effect of plasma chemical oxidation of titanium alloy on bone-implant contact in rats. Biomaterials. 2011;**32**(32):8041-8047

[31] Kofstad P, Hauffe K, Kjollesdal H. Investigation on the oxidation mechanism of titanium. Acta Chemica Scandinavica. 1958;**12**(2):239-266

[32] Orii Y, Masumoto H, Honda Y, Anada T, Goto T, Sasaki K, Suzuki O. Enhancement of octacalcium phosphate deposition on a titanium surface activated by electron cyclotron resonance plasma oxidation. Journal of Biomedical Materials Research Part B: Applied Biomaterials. 2010;**93**(2):476-483

[33] Agrawal DK. Microwave processing of ceramics. Current Opinion in Solid State and Materials Science. 1998;**3**(5):480-485

[34] Bykov YV, Rybakov KI, Semenov VE. High-temperature microwave processing of materials. Journal of Physics D: Applied Physics. 2001;**34**(13):R55

[35] Campana DM, Ubal S, Giavedoni MD, Saita FA. A deeper insight into the dip coating process in the presence of insoluble surfactants: A numerical analysis. Physics of Fluids. 2011;**23**(5):052102

[36] Bennett CEG, McKinnon NA, Williams LS. Sintering in gas discharges. Nature. 1968;**217** (5135):1287-1288

[37] Twomey B, Breen A, Byrne G, Hynes A, Dowling DP. Rapid discharge sintering of nickel–diamond metal matrix composites. Journal of Materials Processing Technology. 2011;**211**(7):1210-1216

[38] Breen AP, Twomey B, Byrne G, Dowling DP. Comparison between microwave and microwave plasma sintering of nickel powders. In: Materials Science Forum. Vol. 672. Trans Tech Publications; Zürich, Switzerland, 2011. p. 289-292

[39] Awais M, Dini D, Vos JG, Dowling DP. Nickel oxide photocathodes prepared using rapid discharge sintering for p-type dye-sensitized solar cells. Journal of the Chemical Society of Pakistan. 2016;**38**(4):615-615

[40] Awais M, Gibson E, Vos JG, Dowling DP, Hagfeldt A, Dini D. Fabrication of efficient NiO photocathodes prepared via RDS with novel routes of substrate processing for p-type dye-sensitized solar cells. ChemElectroChem. 2014;**1**(2):384-391

[41] Gibson EA, Awais M, Dini D, Dowling DP, Pryce MT, Vos JG, et al. Dye sensitised solar cells with nickel oxide photocathodes prepared via scalable microwave sintering. Physical Chemistry Chemical Physics. 2013;**15**(7):2411-2420

[42] Awais M, Rahman M, MacElroy JD, Dini D, Vos JG, Dowling DP. Application of a novel microwave plasma treatment for the sintering of nickel oxide coatings for use in dye-sensitized solar cells. Surface and Coatings Technology. 2011;**205**:S245-S249

[43] Sato H, Minami T, Takata S, Yamada T. Transparent conducting p-type NiO thin films prepared by magnetron sputtering. Thin Solid Films. 1993;**236**(1):27-31

[44] Lu YM, Hwang WS, Yang JS, Chuang HC. Properties of nickel oxide thin films deposited by RF reactive magnetron sputtering. Thin Solid Films. 2002;**420**:54-61

[45] Odobel F, Le Pleux L, Pellegrin Y, Blart E. New photovoltaic devices based on the sensitization of p-type semiconductors: Challenges and opportunities. Accounts of Chemical Research. 2010;**43**(8):1063-1071

[46] Muhammad Awais, Denis P. Dowling, Franco Decker, Danilo Dini. Electrochemical Characterization of Nanoporous Nickel Oxide Thin Films Spray-Deposited onto Indium-Doped Tin Oxide for Solar Conversion Scopes. Advances in Condensed Matter Physics, vol. 2015, Article ID 186375, 18 pages, 2015. DOI:10.1155/2015/186375

[47] Nakasa A, Usami H, Sumikura S, Hasegawa S, Koyama T, Suzuki E. A high voltage dye-sensitized solar cell using a nanoporous NiO photocathode. Chemistry Letters. 2005; **34**(4):500-501

[48] Nattestad A, Ferguson M, Kerr R, Cheng YB, Bach U. Dye-sensitized nickel (II) oxide photocathodes for tandem solar cell applications. Nanotechnology. 2008;**19**(29):295304

[49] Tachibana Y, Hara K, Sayama K, Arakawa H. Quantitative analysis of light-harvesting efficiency and electron-transfer yield in ruthenium-dye-sensitized nanocrystalline TiO_2 solar cells. Chemistry of Materials. 2002;**14**(6):2527-2535

[50] Grätzel M. Conversion of sunlight to electric power by nanocrystalline dye-sensitized solar cells. Journal of Photochemistry and Photobiology A: Chemistry. 2004;**164**(1):3-14

[51] McConnell RD. Assessment of the dye-sensitized solar cell. Renewable and Sustainable Energy Reviews. 2002;**6**(3):271-293

[52] Awais M. Deposition and evaluation of nickel oxide coatings for dye-sensitized solar cell application [Doctoral dissertation]. University College Dublin; Dublin, Ireland, 2011

[53] Twomey B, Breen A, Byrne G, Hynes A, Dowling D. Plasma power can slash small run sintering times. Metal Powder Report. 2010;**65**(2):10-13

[54] He J, Lindström H, Hagfeldt A, Lindquist SE. Dye-sensitized nanostructured tandem cell-first demonstrated cell with a dye-sensitized photocathode. Solar Energy Materials and Solar Cells. 2000;**62**(3):265-273

[55] O'Regan B, Grätzel M. A low-cost, high-efficiency solar cell based on dye-sensitized colloidal TiO_2 films. Nature. 1991;**353**(6346):737-740

[56] Dang BH, Rahman M, MacElroy D, Dowling DP. Conversion of amorphous TiO_2 coatings into their crystalline form using a novel microwave plasma treatment. Surface and Coatings Technology. 2011;**205**:S235-S240

[57] Liu X, Chu PK, Ding C. Surface modification of titanium, titanium alloys, and related materials for biomedical applications. Materials Science and Engineering: R: Reports. 2004;**47**(3):49-121

[58] Fujishima A, Honda K. Electrochemical photolysis of water at a semiconductor electrode. Nature. 1972;**238**(5358):37-38

[59] Hanaor DA, Sorrell CC. Sand supported mixed-phase TiO_2 photocatalysts for water decontamination applications. Advanced Engineering Materials. 2014;**16**(2):248-254

[60] Kuciauskas D, Freund MS, Gray HB, Winkler JR, Lewis NS. Electron transfer dynamics in nanocrystalline titanium dioxide solar cells sensitized with ruthenium or osmium polypyridyl complexes. The Journal of Physical Chemistry B. 2001;**105**(2):392-403

[61] Boccaccini AR, Karapappas P, Marijuan JM, Kaya C. TiO_2 coatings on silicon carbide and carbon fibre substrates by electrophoretic deposition. Journal of Materials Science. 2004;**39**(3):851-859

[62] Shen GX, Chen YC, Lin CJ. Corrosion protection of 316 L stainless steel by a TiO_2 nanoparticle coating prepared by sol–gel method. Thin Solid Films. 2005;**489**(1):130-136

[63] Dang BH, Rahman M, MacElroy D, Dowling DP. Evaluation of microwave plasma oxidation treatments for the fabrication of photoactive un-doped and carbon-doped TiO_2 coatings. Surface and Coatings Technology. 2012;**206**(19):4113-4118

[64] Ekoi EJ, Stallard C, Reid I, Dowling DP. Tailoring oxide-layer formation on titanium substrates using microwave plasma treatments. Surface and Coatings Technology. 2017; **325**:299-307

Chapter 8

Preparation and Numerical Modelling of Ceramic Foam Insulation for Energy Saving in Buildings

Ru Ji, Xidong Wang and Yang He

Additional information is available at the end of the chapter

http://dx.doi.org/10.5772/intechopen.71393

Abstract

For the purpose of energy saving in buildings, a foam ceramic insulation (FCI) was prepared by using fly ash (FA) and ceramic waste (CW) as the main raw materials for its matrix part and foam part, respectively. The effects of the sintering temperature and the additive agent on the macroscopic performances were systematically measured and investigated. The experiment results indicate that for the matrix sample 5% quartz addition makes the rupture modulus at 1200°C reach high to 34.28 MPa, while the corresponding water absorption capacity is only 0.83%. In addition, for the foam sample with 1 wt% silicon carbide, the lowest measured bulk density and thermal conductivity at 1200°C are 0.471 g/cm^3 and 0.1184 W/(m•K), respectively. Furthermore, the proposed simulation model predicts that the effective thermal conductivity of FCI decreases with the decrease of the bulk density. Moreover, the simulation results calculated by EnergyPlus software indicate that the synthetic FCI can efficiently reduce the building's heating and cooling loads and exerts excellent energy conservation effect.

Keywords: ceramic foam insulation, solid waste, numerical modelling, thermal conductivity, energy saving in buildings

1. Introduction

It is well known that as the society and economy is developing at a high rate, about 35% of the total energy is consumed by buildings [1–4]. For the sake of energy saving in buildings, all over the world, there are many different concepts of energy-efficient buildings, such as passive houses, near-zero-energy buildings, and even active houses [5]. According to the requirements of these houses' design, the energy use in these buildings needs to be strictly reduced to a very certain small range. Therefore, an appropriate thermal insulation material is necessary to

realise the energy saving in buildings [6]. As ceramic foam insulation (CFI) is one of the notable methods to reduce the energy use in buildings, it has been widely developed in recent years.

As we all know, the building insulation materials are generally sorted into two groups, organic insulation materials and inorganic insulation materials. Organic insulation materials, such as polystyrene foam, often lead to a series of problems related to combustion, environmental toxicity, and adhesive incompatibility with cement and ceramic structures. In addition, organic insulation materials usually exert short working life, for instance, foam plastic only can ensure the required heat resistance in about 8 years. However, inorganic materials, such as CFI, are excellent building insulation materials, which have many advantages compared with other thermal insulation materials, including chemically inactive, noncombustible, low moisture absorption, chemically stable, long-time stable in physical properties, environmental friendly, and long use life [7]. For the above reasons, this study is motivated to propose a novel FCI for saving energy in buildings.

On the other hand, according to the investigation in literature, it is known to us that the traditional manufacture of ceramic materials often requires massive amount of natural raw materials, such as clay and feldspar [8–10]. However, recently, taking into consideration the big challenges in environmental protection and energy saving, nontraditional raw materials are needed in the synthesis process of the ceramic materials. Therefore, the development of innovative ceramic materials by using huge amounts of alternative raw materials, especially solid waste, will be important to the environmental protection.

Hence, in this research, according to our previous work [11–13], two solid wastes were applied as the main raw materials for the synthesis of FCI. Firstly, fly ash (FA), a by-product of thermal generation in coal power stations, is used as the main raw material in the matrix part of the FCI [14]. According to the statistics, more than 750 million tonnes of FA are generated each year, but only less than 50% of FA is utilised. In China, the annual output of FA reached almost 600 million tonnes, which results in very serious environmental pollution, such as groundwater contamination [15–17]. Secondly, the reclaimed waste is the ceramic waste (CW). Statistics show that in the ceramic industry about 30% of the daily production will turn into solid waste. As we all know, CW is not recycled in any form at present [18]. Therefore, both solid wastes will cause serious environmental pollution [19–20]. So it is necessary to develop an effective way to recycle FA and CW.

Based on the previous work of our research [11–13], we are therefore motivated to prepare FCI by using FA and CW as the main raw materials. Moreover, since the study of heat transfer behaviour of FCI and its energy-saving function in buildings was important to guide the synthesis process of FCI, in this study, the foaming behaviour, the thermal conductivity, and its energy-saving function were investigated experimentally and were modelled by simulative method.

2. Experimental methods

2.1. Materials

For the manufacture of CFI boards the raw materials can be divided into two kinds, matrix raw materials and foam raw materials. Firstly, the matrix raw materials were composed of

FA, clay, feldspar, and quartz, which were all driven from the same region in China. Secondly, the foam raw materials included CW and other additives. Here, CW was used as a main raw material and SiC was applied as a foaming agent. The chemical characteristics of the main raw materials were measured by X-ray fluorescence (XRF) scan and are shown in **Table 1**. It can be seen that for all main raw materials, SiO_2 and Al_2O_3 possess the dominating proportions with the total proportion of 81.87, 71.53, 86.10, 95.77 and 84.01 wt%. It is interesting to note that for feldspar the total contents of K_2O and Na_2O are high: 11.72 wt%.

In addition, the crystalline phases of the raw materials are determined by X-ray diffraction (XRD) (D/MAX-PC 2500, Rigaku), and the XRD patterns are presented in **Figure 1**. It can be seen that FA is a heterogeneous material. Firstly, the major crystalline phases of FA are quartz and mullite with a small amount of gypsum. Secondly, it is interesting to note that parts of FA belong to the amorphous phase due to the observed low and broad diffraction bands in the range of 20–30°. Moreover, for CW, the main structure is quartz.

2.2. Preparation

In this research, for the matrix part, 50 wt% FA will be used as the main raw material in all batches. While, for the foam part, only CW will be utilised as the raw material with only 1% SiC. In this study, according to the previous work, the detailed steps of the preparation are shown as follows.

Firstly, all raw materials were thoroughly mixed and milled in the proportion as shown in **Table 2**. Here, quartz content in the batches 1–5 varied from 0 to 20 wt%. Then, mixtures were wet ground in two ball mills for 15 h to obtain the homogeneous slurries. The slurries were sieved to pass through a 200-mesh screen and dried at 110°C for 12 h. Subsequently, the two mixtures were granulated in a moist condition and samples were hydraulically compacted using uniaxial pressing at 10 MPa. Finally, the shaped samples were dried at 105°C for 3 h, followed by calcination in a muffle furnace at the preset sintering temperature, and the sintered samples were cooled naturally.

2.3. Characterisation

For the matrix part, the obtained samples were measured for moisture absorption (MA) capacity and rupture modulus.

Content (wt%)	SiO_2	Al_2O_3	K_2O	Na_2O	CaO	Fe_2O_3	MgO	TiO_2	S	LOI
Fly ash	41.97	39.90	0.50	0.20	6.41	1.96	0.60	1.20	3.15	3.64
Clay	34.96	36.57	0.39	0.09	0.49	0.82	0.22	1.47	—	24.38
Feldspar	68.60	17.50	7.74	3.98	0.53	0.41	0.17	0.04	—	0.83
Quartz	91.30	4.47	1.76	1.19	0.42	0.17	0.15	0.01	—	0.44
Ceramic waste	65.18	18.83	1.61	4.10	1.61	0.45	3.22	0.21	—	4.13

Table 1. Chemical composition of main raw materials.

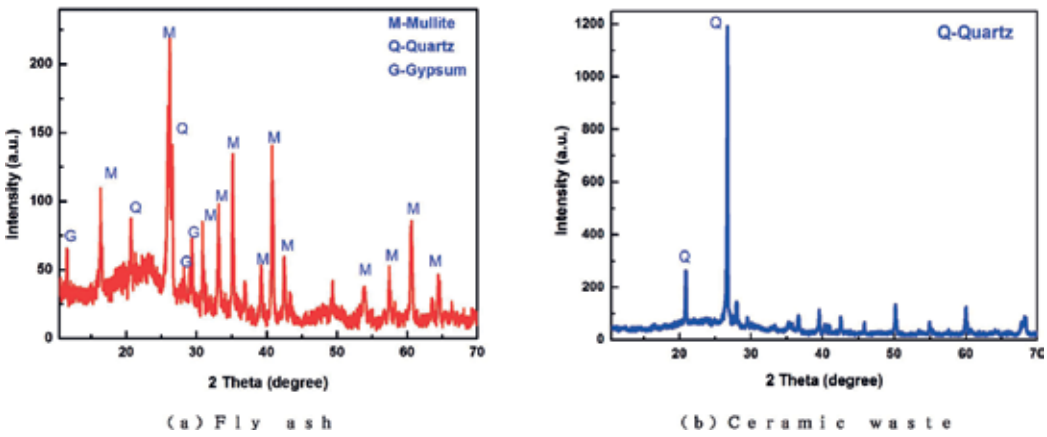

Figure 1. XRD patterns of the main raw materials.

The moisture absorption (MA) capacity was tested according to the following method. Firstly, the dried mass of the sintered sample (M_d, *kg*) was measured. Secondly, the sample was put into boiled water for 5 h and then was soaked for another 24 h. Finally, in water, the mass of the suspended sample (M_{s1}, *kg*) was determined, and the saturated mass (M_{s2}, *kg*) was measured. So M*A* (%) can be obtained as follows:

$$MA = \frac{M_{s2} - M_d}{M_d} \times 100 \tag{1}$$

The rupture modulus, *R* (*MPa*), is calculated by the following formula:

$$R = \frac{3Fl}{2bh^2} \tag{2}$$

where *F* is the failing load (*N*); *l* is the distance between two support bars (mm); *b* is the width of the specimen (mm); and *h* is the minimum thickness of the sample (mm).

For the foam part, the sintered samples were tested regarding bulk density and measured thermal conductivity.

		No. 1	No. 2	No. 3	No. 4	No. 5	No. 6
Matrix part	Fly ash	50	50	50	50	50	—
	Clay	20	20	20	20	20	—
	Feldspar	30	25	20	15	10	—
	Quartz	—	5	10	15	20	—
Foam part	Ceramic waste	—	—	—	—	—	100
	SiC	—	—	—	—	—	1

Table 2. Batch compositions of the samples (wt%).

The bulk density (ρ_b) of final sintered sample was determined by referencing the Chinese Standards Specifications. In particular, three parameters were detected. Firstly, the sintered samples were dried at 110°C for 24 h and then restored to room temperature in a balance desiccator. In this status, the specimen's weight was accurately measured, $M_{a.}$ Secondly, the samples were immersed in boiled water for 3 h, then removed the heating and made samples to still stay in the water for 1 h. Samples' weight M_b in the water was measured by hanging on the hook of the precision electronic balance. Thirdly, after the above process, samples were taken out of the water and the redundant water on the surface was wiped using a wet cloth. Then, the weight M_c of the sample was measured. Finally, the bulk density was calculated by using the following formula, in which ρ_{water} was the density of water.

$$\rho_b = \frac{M_a}{M_b - M_c} \times \rho_{water} \tag{3}$$

For thermal conductivity measurements, a series of rectangular briquettes were prepared separately. The thermal conductivities of the samples were measured in a vapour-tight envelope by using a guarded hotplate apparatus (IMDRY3001-II). For the experiment, the hotplate of the apparatus was set to 33°C and the cold plate was cooled by water at 17°C. The sample was mounted between the two plates, and then, the thermal conductivity of the sample was tested when the temperatures of the two plates became stable. Here, the measurement uncertainty and repeatability of GHP were controlled within ±3% and ±1%, respectively.

3. Simulation methods

Firstly, the effective thermal conductivity (k_e) was simulated by a simulation model developed by our research group. In this simulation, k_e can be obtained as follows:

$$k_e = \frac{Q_{total} \times L}{(T_h - T_l) \times A} \tag{4}$$

where Q_{total} is the total heat flow through the sample, W; T_h and T_l were the known temperatures of the two surfaces perpendicular to the direction of heat flow, K; L is the thickness of the sample, m; and A is the area of the sample, m^2.

In our simulation, by comparing several grids and the results, the whole sample was finally meshed as a grid of $X \times Y \times Z$. For each axis, the grid numbers are $X = A^{0.5}$, $Y = L$, and $Z = A^{0.5}$. In addition, each unit's dimension is equalled to 0.001 m.

Then, by using the thermal conductivity matrix (*TCM = ones (X, Y, Z)*), each unit's thermal conductivity value was determined. For the matrix part of the sample, the thermal conductivity value of each unit is set as the thermal conductivity of the matrix board. For the foam part, the unit thermal conductivity value is set randomly. For example, there were two thermal conductivity values in the foam sample, from thermal conductivity value of the solid material and the thermal conductivity value of the air. Firstly, the volume fractions of the solid material and the air were calculated. Secondly, for each unit, a random number (r*n*) was generated to decide which thermal conductivity value would be endowed. For instance, for one unit,

if *rn* was smaller than the solid material's volume fraction, the thermal conductivity of the solid material would be endowed. Otherwise, this unit would be endowed with the thermal conductivity of the air (k_a = 0.026 W/(m•K) [21]).

In this simulation programme, the steady-state energy equation for three-dimensional heat transfer was established as the control equation. For each unit, the sum of heat flow towards this unit was equal to that away from it. In addition, the solution conditions were defined by using the temperature field matrix: *T = ones (X, Y, Z).* For the surfaces perpendicular to the heat flow direction, they belonged to the first-class boundary condition and the temperatures of these two surfaces were equalled to 33°C and 17°C. As in the experiment, the sample panel was surrounded by thermal insulation fibre; similarly, the four surfaces that surrounded the panel were insulated perfectly. Finally, k_e will be obtained through the iterative calculation.

Secondly, the energy-saving effect of FCI was evaluated by EnergyPlus software [22–24]. In this research, an ideal building is applied as the calculation model for energy consumption. In addition, the energy consumption of buildings with different kinds of external walls was compared systematically.

4. Results and discussions

4.1. The properties of FCI

For the matrix part samples, the sintering temperature will have an important effect on macroscopic properties, including the moisture absorption capacity and rupture modulus, which are shown in **Figures 2** and **3**, respectively.

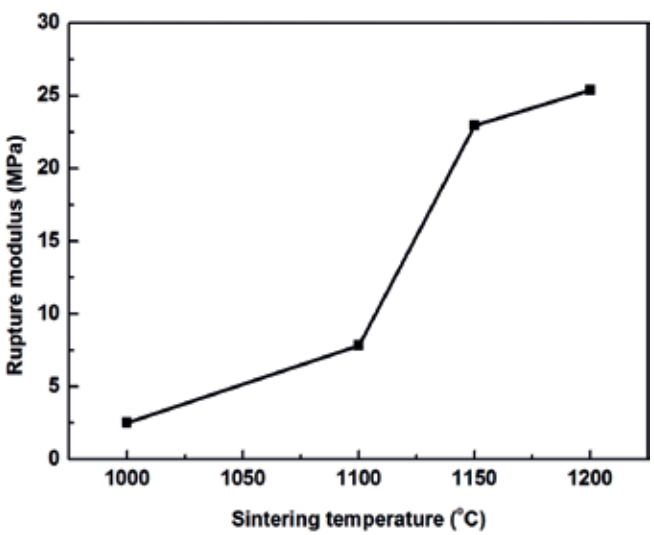

Figure 2. Rupture modulus values of the sample no. 1 versus sintering temperatures.

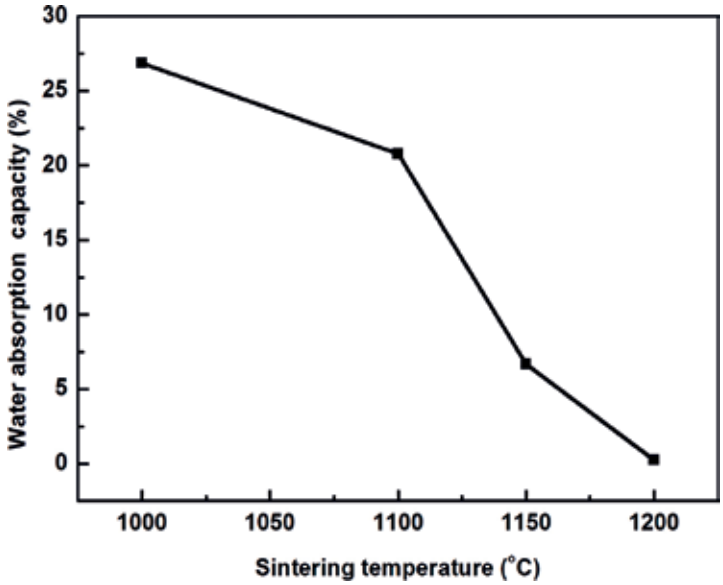

Figure 3. Moisture absorption capacity values of the sample no. 1 versus sintering temperatures.

First, the characteristic curve in **Figure 2** indicates that for the sample no.1 the rupture modulus increases with the increase of the sintering temperature. When the sintering temperature is 1000°C, the rupture modulus is only 2.52 MPa. Moreover, when the sintering temperature is increased to 1100°C, the corresponding rupture modulus increases to 7.82 MPa, indicating that there is the liquid generation in the sample no.1. Furthermore, when the sintering temperature is over 1200°C, the rupture modulus value reaches to 25.38 MPa. Second, it is interesting to note that in the investigated temperature range (1000–1200°C), the moisture absorption capacity dramatically decreases from 26.85% to 0.25% at the sintering temperature of 1000–1200°C.

It can be concluded that when the sintering temperature is 1200°C the samples have excellent properties (moisture absorption capacity and the rupture modulus), which satisfy the requirements of fine stoneware tiles [25].

In addition, the quartz was chosen as an addition to the sample no. 1. **Figures 4** and **5** show the effects of quartz addition on the sample's properties (moisture absorption capacity and rupture modulus). It can be seen that, for the sample no. 2 and no. 3, at 1200°C, the 5% and 10% quartz additions enhance the samples' strength with a little increase in moisture absorption capacity. For instance, for the sample no. 2, the highest rupture modulus reaches 34.28 MPa at 1200°C, which drastically exceeds the property of the sample no. 1 without quartz (25.38 MPa). According to the literature [26], it may be explained that, for the sample no. 2, 5% quartz addition is a benefit to the increase of mullite formation, which will promote the sample's rupture modulus. **Figure 5** shows that 5% quartz addition increases the moisture absorption capacity from 0.25 to 0.83%, but it still satisfies the standards for stoneware porcelain tiles [25].

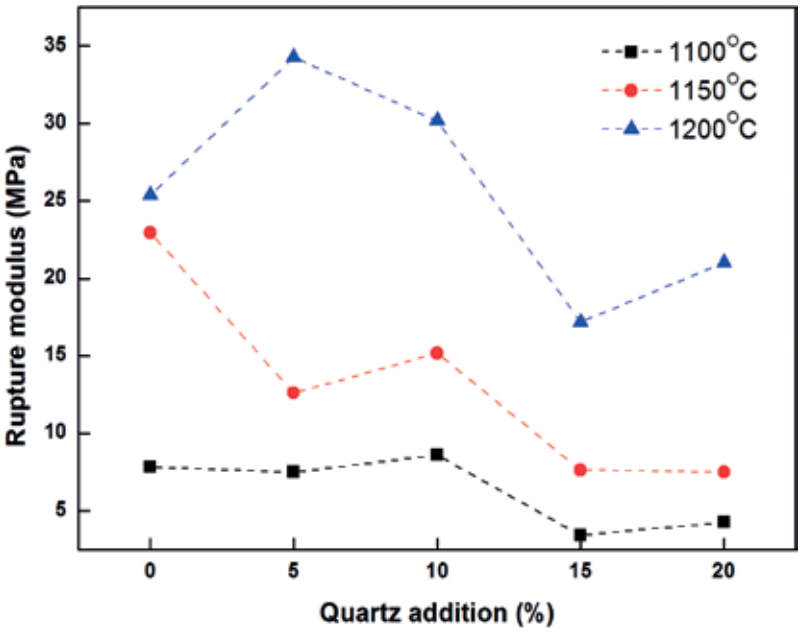

Figure 4. Rupture modulus values of the sample nos. 1–5 with different quartz addition.

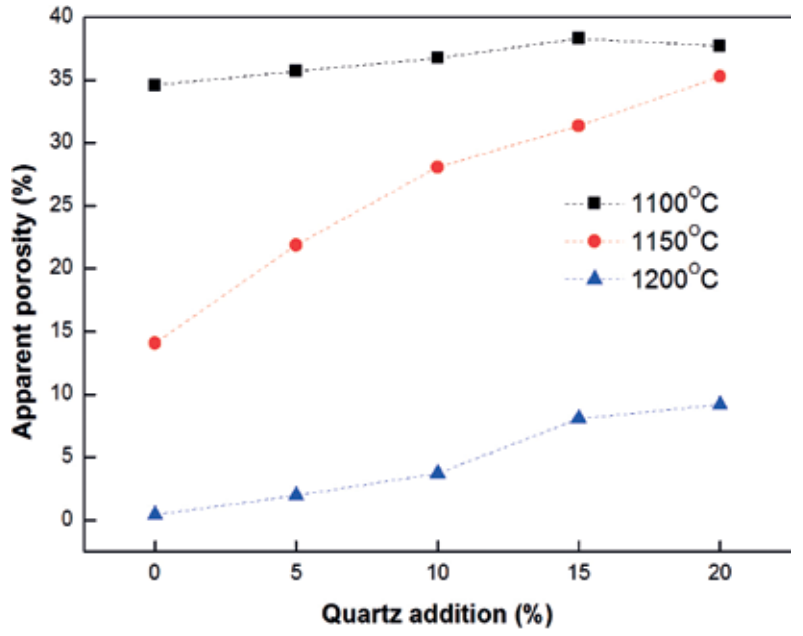

Figure 5. Moisture absorption capacity values of the sample nos. 1–5 with different quartz addition.

In order to explain the above phenomenon, the ternary diagram of sample no. 2 was calculated by FactSage. From **Figure 6**, it can be seen that the new sample's raw materials belong to SiO_2-Al_2O_3-CaO-K_2O system, as shown in red. Therefore, unlike the conventional ternary

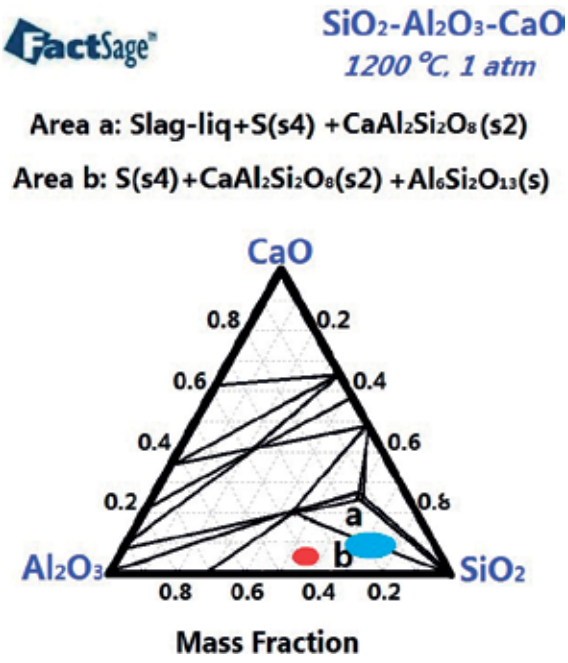

Figure 6. Ternary diagram of the traditional ceramic and sample no. 2 (blue indicates the traditional ceramic crystal phase area and red shows the phase area of sample no. 2).

ceramic system, the new sample broadens the traditional ceramic crystal phase area (blue) to a new phase area. This change of the ceramic system is due to the increase of Al_2O_3 and CaO obtained from FA.

In addition, the powder of both raw materials and sintered sample no. 2 is separately analysed by XRD. Firstly, XRD patterns in **Figure 7** depict that there is none or only a small amount of glass phase in the sintered sample no. 2, which is a benefit to the improvement of its mechanical property. The previous research [27] has shown that in the traditional porcelain stoneware tiles, glass is one of the major phases in addition to quartz and mullite. Therefore, compared to the traditional ceramic tile, the matrix part tile prepared by our research has better mechanical property. In addition, it is interesting to note that there is no quartz in sintered sample no. 2; it is replaced by a large amount of mullite, which will further promote its strength.

Moreover, **Figure 8** shows the DTA-TG curve of the sample. At 200°C, the mass loss is caused by the dehydroxylation of gypsum with an exothermic peak. At the temperature of 400–600°C, the mass loss is caused by the dehydroxylation process of boehmite (with an endothermic peak at 450°C) and kaolinite (with an endothermic peak at above 550°C). Finally, an exothermic peak at about 1000°C is attributable to mullite crystallisation [28].

Secondly, for the foam sample no. 6, the sintering temperature likewise has an important effect on the foam sample's properties, including the bulk density and volume, which are shown in **Figure 9**.

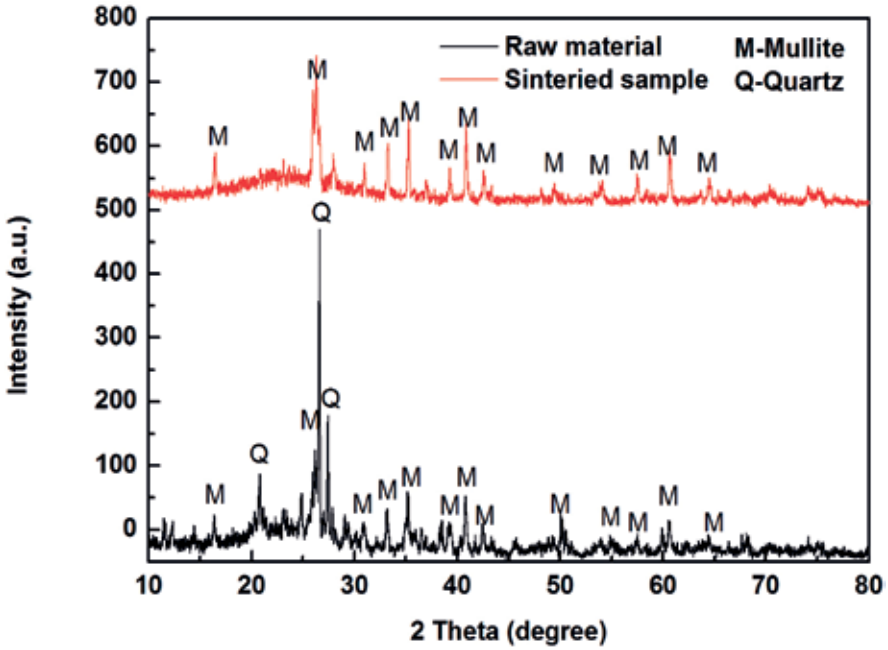

Figure 7. XRD patterns of the sample no. 2.

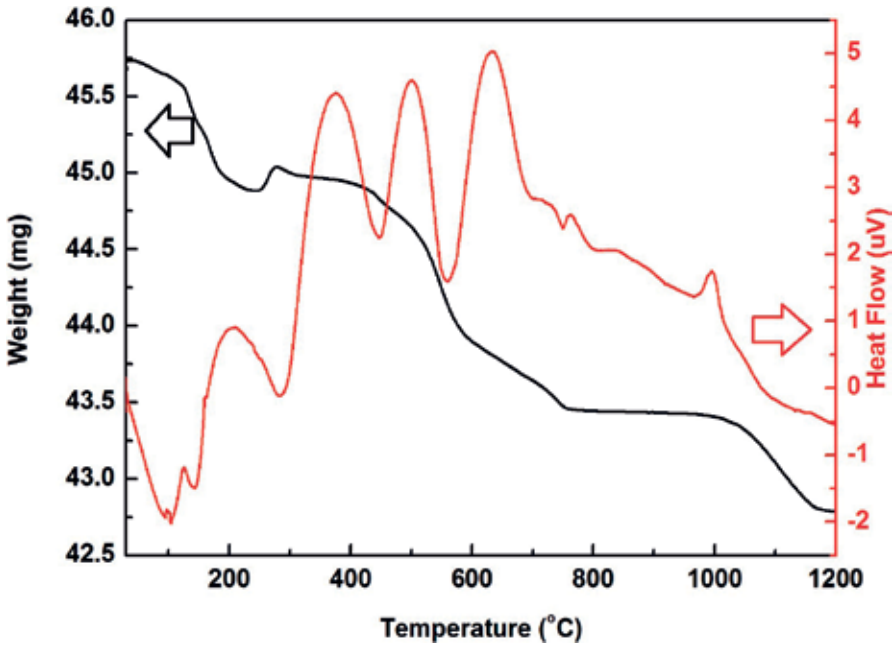

Figure 8. DTA-TG curve of the green sample no.2.

http://dx.doi.org/10.5772/intechopen.71393

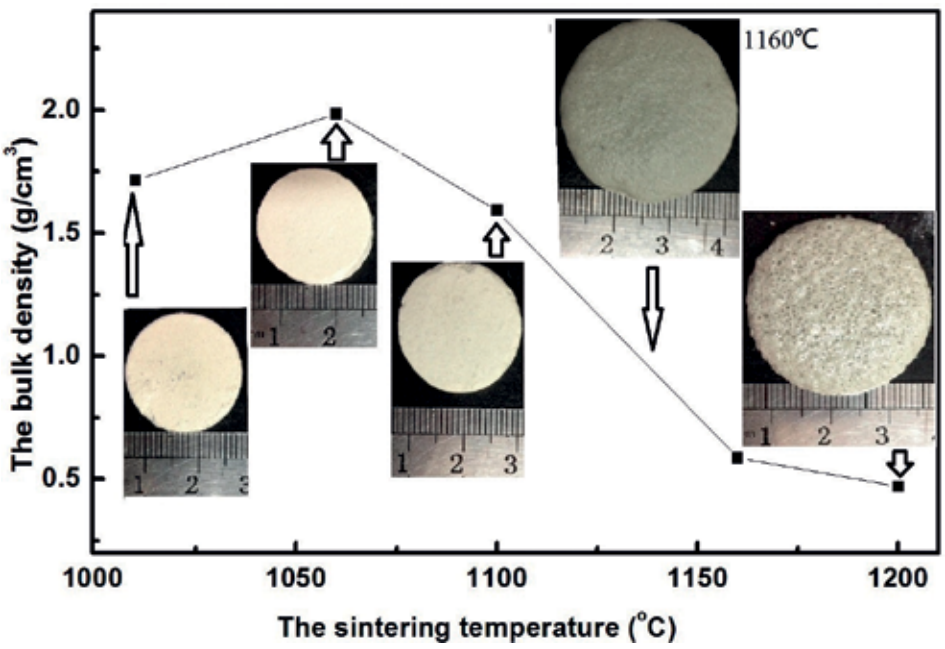

Figure 9. The volume results and the bulk density values of the sample no. 6 at different sintering temperature.

Figure 9 indicates the effect of sintering temperature on the volume results and the bulk density values of the sample no. 6 with 1% SiC as a foaming agent. It can be seen that the volume results of the sample no. 6 first shrank and then expanded with the increase in the sintering temperature from 1010–1200°C. Therefore, it is noted that the corresponding bulk density of sample no. 6 shows a consistent trend. At 1010°C, the bulk density is 1.714 g/cm^3, and then, it increases up to 1.984 g/cm^3 at 1060°C, followed by a rapid decrease with further increasing sintering temperature, and reaches the minimum value of 0.471 g/cm^3 at 1200°C, which is decreased by 76%.

This phenomenon is attributed to two typically changing processes in the sintering of foamed ceramics, which are matrix densification and closed-pore generation. Firstly, in the sintering process, with the increase in sintering temperature, liquid phase is generated, which led to the matrix densification [29]. Secondly, there is SiC in CW and so with the sintering temperature increase SiC began to decompose, resulting in the closed-pore generation. In the process of SiC decomposition, the gas (CO_2 or CO) is generated in the presence of oxygen, which is shown in **Figure 10** [30–32].

Moreover, the measured thermal conductivity of the sample no. 6 as a function of the bulk density is demonstrated in **Figure 11**. It can be seen that the measured thermal conductivity decreases from 0.3876 W/(m•K) to 0.1184 W/(m•K) with the increase in the bulk density of the sample no. 6. It is concluded that the sample no. 6 at high sintering temperature (1200°C) has an excellent heat insulation performance, indicating that it can be utilised as the foam part of FCI.

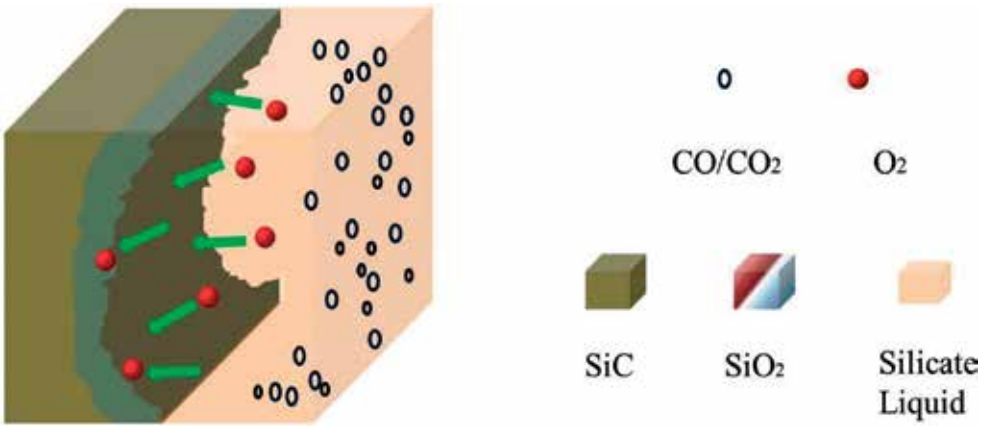

Figure 10. The reaction principle of SiC as a foaming agent.

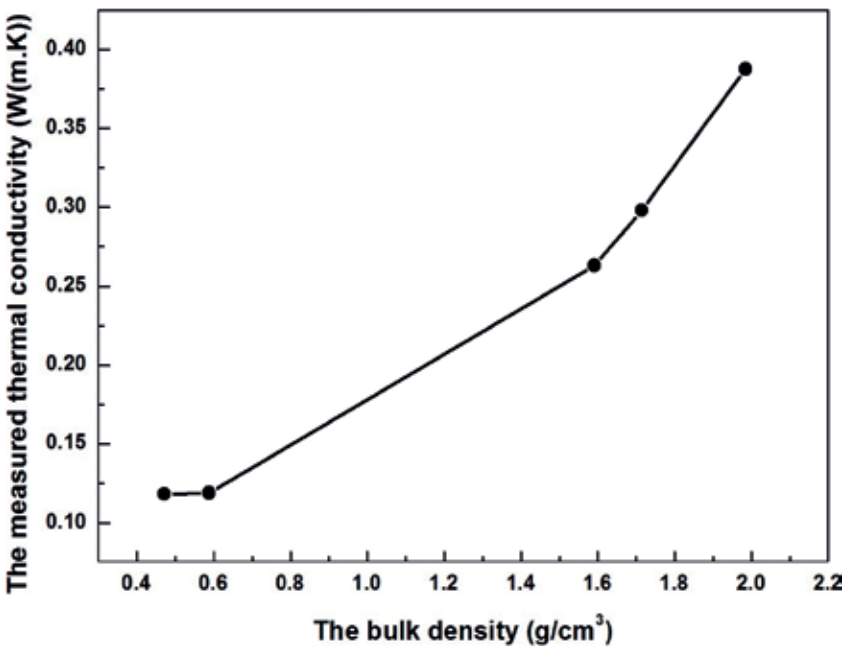

Figure 11. The measured thermal conductivity of the sample no. 6 as a function of the bulk density.

4.2. The forecast of the thermal conductivity and energy saving of FCI

4.2.1. Numerical simulation results of the effective thermal conductivity

The relationship between the effective thermal conductivity and the bulk density can be calculated through the present proposed model. The results of the effective thermal conductivity, k_e, as a function of the bulk density, are indicated in **Figure 12**. It can be seen that the effective thermal conductivity decreases with the decrease of the bulk density. It is interesting

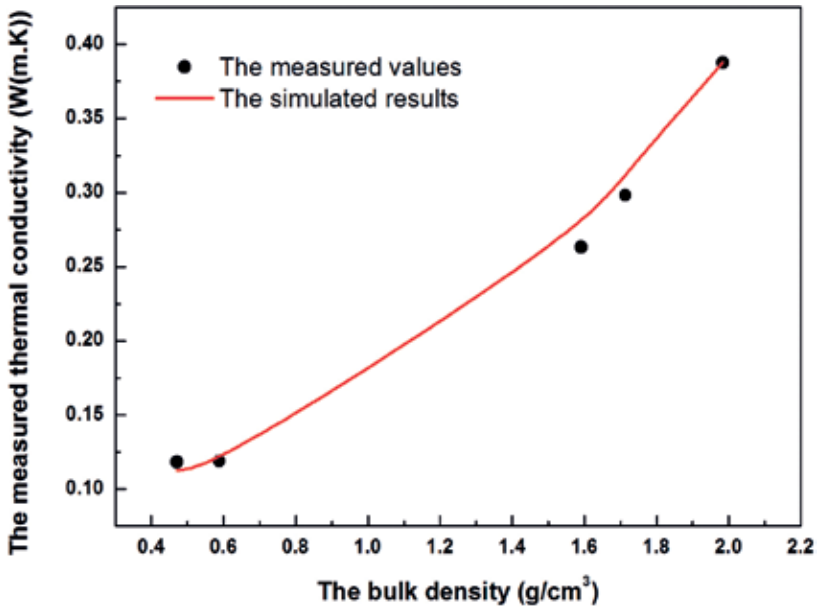

Figure 12. The simulation results of the effective thermal conductivity of the sample no. 6 as a function of the bulk density.

to note that, when the bulk density continues decreasing to a certain level (1.600 g/cm^3), the decrease rate of the effective thermal conductivity becomes small. In addition, it can be seen that the simulated effective thermal conductivities are well in agreement with the measured effective thermal conductivities, with the average deviation of 4%.

From **Figure 12**, we can also get the following relationship between the effective thermal conductivity and the bulk density for the foam sample at 25°C.

$$k_e = 0.15002\text{-}1.25 \times 10^{-4} \rho_b + 1.23 \times 10^{-7} \rho_b^2 \quad (5)$$

4.2.2. The forecast of the energy saving of FCI in an ideal building

In this part, a building (3 m*3 m*2.8 m) in Beijing is used as the calculation model for energy consumption (**Figure 13(a)**). In this building model, there are two kinds of external walls, traditional wall and foam ceramic insulation wall. As shown in **Figure 13(b)**, the foam ceramic insulation wall is composed of four layers: the cement mortar (20 mm, 0.97 W/(m•K)), the matrix part of the foam ceramic insulation (200 mm), the foam part of the foam ceramic insulation (50 mm), and the composite mortar (20 mm, 0.65 W/(m•K)). For the traditional wall, the matrix and foam parts of the foam ceramic insulation were removed and were replaced with a 250-mm reinforced concrete with the thermal conductivity of 1.95 W/(m•K).

Figure 14 shows the annual energy consumption for the ideal building with different external walls. It can be seen that, compared with the traditional wall, the FCI wall significantly reduces the annual energy consumption by 44–57%. In addition, for the building with FCI wall, the annual average heating and cooling rate decreases with the decrease in the bulk

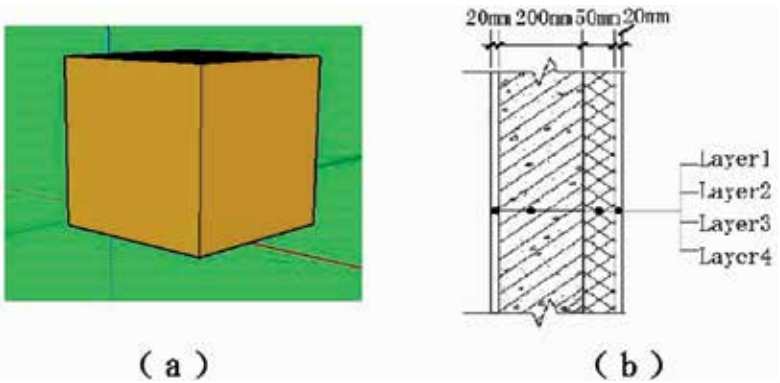

Figure 13. The ideal calculation building model.

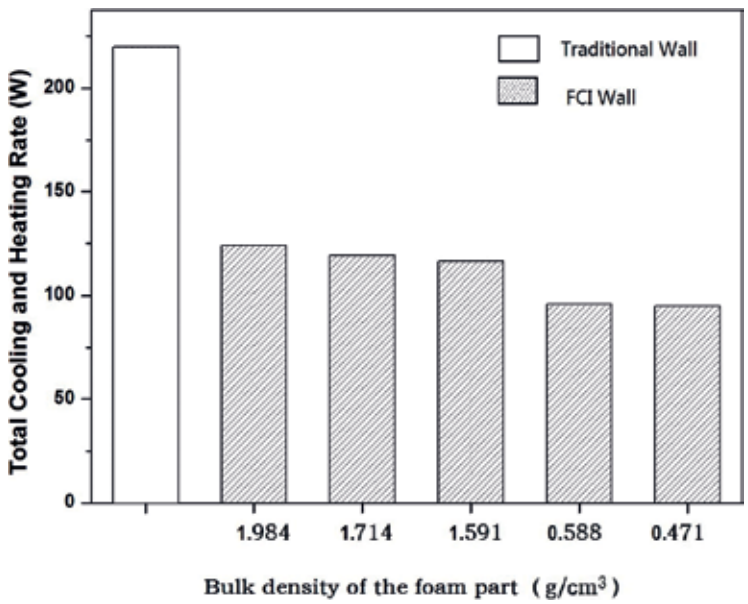

Figure 14. Heating and cooling annual loads in ideal building with different external walls.

density of the foam part of FCI. For instance, when ρ_b = 0.471 g/cm^3, for the ideal building the annual average heating and cooling rate is only 95 W, and compared with that of the building with a traditional wall, the rate is reduced by 57%. Therefore, the energy conservation of the FCI wall is especially pronounced.

5. Conclusion

In this research, solid wastes, such as FA and CW, were effectively utilised for the manufacture of FCI, leading to low-cost and environmental protection. The experiment and

simulation methods are applied to study the effects of sintering temperature and the additive agent on properties of the samples.

For the matrix part of FCI, at 1200°C, the sample with 50 wt% FA and 5 wt% quartz addition shows the best complex properties. The rupture modulus is 34.28 MPa, and the corresponding moisture absorption capacity is only 0.83%. In addition, for the foam sample with 1 wt% silicon carbide, the lowest bulk density and thermal conductivity at 1200°C are 0.471 g/cm^3 and 0.1184 W/(m•K), respectively.

Moreover, the thermal conductivities of CFI and its effect on energy saving in buildings were simulated by a simulation model and EnergyPlus, respectively. Firstly, the proposed simulation model was applied to predict the effective thermal conductivity of the sample no. 6 as a function of bulk density. The simulation results show that the effective thermal conductivity of the sample no. 6 decreases with the decrease in its bulk density, and the simulation values are in good agreement with the measured results, with an average deviation of 4%. These simulation methods are desirable not only for the practical purpose of predicting the thermal properties of CFI, but also for the fundamental knowledge required in developing other new porous ceramics. Furthermore, the EnergyPlus results indicate that FCI can efficiently reduce the thermal load caused by the heat loss of the external construction, so the proposed FCI exhibits excellent energy conservation effect.

Acknowledgements

This chapter was supported by the Fundamental Research Funds for the Central Universities (FRF-TP-15-085A1) and China Postdoctoral Science Foundation (2016 M600927). The authors gratefully acknowledge financial support by the Key Projects in the National Science & Technology Pillar Program (2013BAC14B07). Supports by the National Natural Science Foundation of China (51708022, 51522401 and 51472007) and National Key R&D Plan of China (2017YFC0702600) are acknowledged.

Author details

Ru Ji[1]*, Xidong Wang[2] and Yang He[3]

*Address all correspondence to: jiru@ustb.edu.cn

1 School of Civil and Resource Engineering, University of Science and Technology Beijing, Beijing, The People's Republic of China

2 Department of Energy and Resources Engineering and Beijing Key Laboratory for Solid Waste Utilization and Management, College of Engineering, Peking University, Beijing, The People's Republic of China

3 Nuclear Power (Bidding) Dept. 1, China Nuclear Energy Industry Corp., Beijing, The People's Republic of China

References

[1] Domínguez A, Domínguez MI, Ivanova S, et al. Recycling of construction and demolition waste generated by building infrastructure for the production of glassy materials. Ceramics International. 2016;**42**(14):15217-15223

[2] Hsu D. Comparison of integrated clustering methods for accurate and stable prediction of building energy consumption data. Applied Energy. 2015;**160**:153-163

[3] Huebner GM, Hamilton I, Chalabi Z, et al. Explaining domestic energy consumption: The comparative contribution of building factors, socio-demographics, behaviours and attitudes. Applied Energy. 2015;**159**:589-600

[4] Taurino R, Barbieri L, Bondioli F. Surface properties of new green building material after TiO2–SiO2, coatings deposition. Ceramics International. 2015;**42**(4):4866-4874

[5] Dan D, Tanasa C, Stoian V, et al. Passive house design-an efficient solution for residential buildings in Romania. Energy for Sustainable Development. 2016;**32**:99-109

[6] Al-Homoud MS. Performance characteristics and practical applications of common building thermal insulation materials. Building and Environment. 2005;**40**(3):353-366

[7] Bobkova NM, Barantseva SE, Trusova EE. Production of foam glass with granite siftings from the Mikashevichi deposit. Glass and Ceramics. 2007;**64**(1-2):47-50

[8] Fraga D, Lyubenova TS, Martí R, et al. Ecologic ceramic substrates for CIGS solar cells. Ceramics International. 2016;**42**(6):7148-7154

[9] Andreola F, Barbieri L, Lancellotti I, et al. Recycling of industrial wastes in ceramic manufacturing: State of art and glass case studies. Ceramics International. 2016;**42**(12): 13333-13338

[10] Pérez JM, Romero M. Microstructure and technological properties of porcelain stoneware tiles moulded at different pressures and thicknesses[J]. Ceramics International. 2014;**40**(1):1365-1377

[11] Zhu M, Ji R, Li Z, et al. Preparation of glass ceramic foams for thermal insulation applications from coal fly ash and waste glass. Construction and Building Materials. 2016;**112**: 398-405

[12] Ji R, Zhang Z, He Y, et al. Synthesis, characterization and modelling of new building insulation material using ceramic polishing waste residue. Construction and Building Materials. 2015;**85**:119-126

[13] Ji R, Zhang Z, Yan C, et al. Preparation of novel ceramic tiles with high Al 2 O 3, content derived from coal fly ash. Construction and Building Materials. 2016;**114**:888-895

[14] Lizarazo-Marriaga J, García F, Higuera C. Preliminary electrochemical cementation of high volume fly ash mortars. Construction and Building Materials. 2016;**122**:54-62

[15] Zhu M, Ji R, Li Z, et al. Preparation of glass ceramic foams for thermal insulation applications from coal fly ash and waste glass. Construction and Building Materials. 2016;**112**: 398-405

[16] Luo Y, Ma S, Zhao Z, et al. Preparation and characterization of whisker-reinforced ceramics from coal fly ash. Ceramics International. 2016;**43**(1):1-11

[17] Zhu L, Dong Y, Li L, et al. Coal fly ash industrial waste recycling for fabrication of mullite-whisker-structured porous ceramic membrane supports. RSC Advances. 2015;**5**(15): 11163-11174

[18] Silvestre R, Medel E, García A, Navas J. Using ceramic wastes from tile industry as a partial substitute of natural aggregates in hot mix asphalt binder courses. Construction and Building Materials. 2013;**45**:115-122

[19] Higashiyama H, Yamauchi K, Sappakittipakorn M, Sano M, Takahashi OA. Visual investigation on chloride ingress into ceramic waste aggregate mortars having different water to cement ratios. Construction and Building Materials. 2013;**40**:1021-1028

[20] Pereira-de-Oliveira LA, Castro-Gomes JP, Santos P. The potential pozzolanic activity of glass and red-clay ceramic waste as cement mortars components. Construction and Building Materials. 2012;**31**:197-203

[21] Bomberg M, Klarsfeld S. Semi-empirical model of heat transfer in dry mineral fiber insulations. Journal of Building Physics. 1983;**6**(3):156-173

[22] Crawley DB, Lawrie LK, Winkelmann FC, Buhl WF, Huang YJ, Pedersen CO. EnergyPlus: Creating a new-generation building energy simulation program. Energy and Buildings. 2001;**33**(4):319-331

[23] Fumo N, Mago P, Luck R. Methodology to estimate building energy consumption using EnergyPlus benchmark models. Energy and Buildings. 2010;**42**(12):2331-2337

[24] Miyazaki T, Akisawa A, Kashiwagi T. Energy savings of office buildings by the use of semi-transparent solar cells for windows. Renewable Energy. 2005;**30**(3):281-304

[25] State general administration of the People's Republic of China for quality supervision and inspection and quarantine. Ceramic tiles, GB/T4100-2006. Beijing: Standards Press of China; 2006 [Chinese]

[26] Mah T-I, Mazdiyasni KS. Mechanical properties of Mullite. Journal of the American Ceramic Society. 1983;**66**(10):699-703

[27] Martín-Márquez J, Rincón JM, Romero M. Effect of firing temperature on sintering of porcelain stoneware tiles. Ceramics International. 2008;**34**(8):1867-1873

[28] Lee WE, Souza GP. Mullite formation in clays and clay-derived vitreous ceramics. Journal of the European Ceramic Society. 2008;**28**(2):465-471

[29] Amorós JL, Orts MJ, García-Ten J, Gozalbo A, Sánchez E. Effect of the green porous texture on porcelain tile properties. Journal of the European Ceramic Society. 2007;**27**(5): 2295-2301

[30] García-Ten J, Saburit A, Bernardo E, Colombo P. Development of lightweight porcelain stoneware tiles using foaming agents. Journal of the European Ceramic Society. 2012;**32**(4):745-752

[31] Bernardin AM, Silva MJ, Riella HG. Characterization of cellular ceramics made by porcelain tile residues. Materials Science and Engineering A. 2006;**437**(2):222-225

[32] Orts MJ, Amorós JL, Escardino A, Gozalbo A, Feliu C. Kinetic model for the isothermal sintering of low porosity floor tiles. Applied Clay Science. 1993;**8**(2):231-245

Chapter 9

Physical Properties of Porous Pure and Zr/Sn-Doped Nanocrystalline $BaTiO_3$ Ceramics

Umaru Ahmadu, Alhassan Muazu and Sadiq Umar

Additional information is available at the end of the chapter

http://dx.doi.org/10.5772/intechopen.75500

Abstract

Polycrystalline $BaTiO_3$ and $Ba(Ti_{0.96}SnxZr_{0.04-x})O_3$ ceramics (x = 0.02-0.04) were prepared by a combination of solid-state and mechanochemical process and characterized at room temperature by X-ray diffraction for phase composition. Their crystal structures were found to be of the cubic and tetragonal symmetries, respectively. The grain size and porosity which were determined using Field Emission Scanning Electron Microscope (FESEM) and densitometer, respectively showed decrease and increase of relative density respectively, with increase in doping concentration. The variations of dielectric constant and loss with frequency and temperature show a maximum dielectric constant of 1660 at room temperature for $Ba(Ti_{0.96}Sn_{0.03}Zr_{0.01})O_3$. The remnant polarization (P_r) and coercive field (E_c) of BT were found to be 581.73 V/cm and 0.27 μC/cm^2. Increase in Sn content led to an increase in Pr of 0.58, 3.07, 3.73 C/cm^2, and Ec of 1766.8, 2855.7, 2661.1 V/cm, respectively and are expected to lead to a significant reduction in the thickness of the multilayer ceramic capacitors. Impedance spectroscopy of polycrystalline Ba $(Ti_{0.96}Sn_{0.02}Zr_{0.02})$ O_3 in a wide frequency and temperature range showed Nyquist plots with presence of grain and grain boundary at 400°C and a negative temperature coefficient of resistance (NTCR) for $Ba(Ti_{0.96}Sn_{0.02}Zr_{0.02})O_3$. The dielectric relaxation showed a non-Debye character.

Keywords: porous ceramics, barium titanate, doping, ferroelectrics, MLCC

1. Introduction

1.1. $BaTiO_3$ and $Ba(Ti_{0.96}Sn_xZr_{0.04-x})O_3$

Barium titanate (BT) is one of the most basic and widely applied ferroelectric oxide materials with a perovskite-ABO_3 type crystalline structure. It is chemically and mechanically remarkably stable and exhibits ferroelectric properties from room temperature to just below the transition

temperature (T_c). It is easily prepared and used in polycrystalline ceramic form [1]. Due to its excellent dielectric, ferroelectric, piezoelectric, pyroelectric and optoelectric properties, it is extensively used in multilayer ceramic capacitors (MLCC), positive temperature coefficient of resistance (PTCR) thermistors, piezoelectric sensors, actuators, ferroelectric random access memories (FRAM) and electro-optic devices [2, 3]. Pure BT is an electric insulator with a large energy gap of 3.05 eV at room temperature. However, when doped with small metals, it becomes semiconducting and leads to possibilities of tailoring its properties for specific technological applications. Modified BT compositions are widely used in MLCCs due to its high dielectric constant and low loss [4]. Among the doped BT compositions, $Ba(Ti_{1-x}Sn_x)O_3$ (BST) system has drawn wide attention due to its manifestation of diffuse-type phase transition [5–7] and many dielectric applications with reduction of phase transition temperature toward room temperature [8, 9]. Zirconium-doped barium titanate with general formula $Ba(Zr_xTi_{1-x})O_3$ (BZT) has attracted great attention for its potential applications due to its high dielectric constant, relatively low dielectric losses, large voltage tunability of the dielectric constant, as well as a good chemical stability [10–12]. Partial replacement of titanium by tin, zirconium or hafnium generally leads to a reduction in T_c and an increase in the permittivity maximum (ε_{max}) with increase in dopant content [13]. The substitution of isovalent cations Zr^{+4} and Sn^{+4} for Ti^{+4} lead to the formation of barium titanate stannate zirconate compound which belongs to the class of complex perovskite structure having the general formula $ABB''_xB''_{4-x}O_3$ (A,B, are the cation, $B''_xB''_{4-x}$ are the isovalent cation dopants and O_3 anion). These compounds have been widely studied owing to their very high and broad relative permittivity at the ferroelectric Curie point. Therefore, codoping of BT with two tetravalent ions Zr^{+4} and Sn^{+4} would be a good strategy to tailor the properties of porous BT ceramics.

There are challenges, however, one of which is in developing a dielectric layer of fewer than 10 μm with a large capacitance, a major requirement for MLCC miniaturization and electronic/microelectronic devices [14]. Reduction of the grain size of BT ceramics to the micron level leads to an increase in permittivity at room temperature. Further reduction of grain size to less than few hundred nanometers leads to a further decrease in permittivity. On the other hand, the presence of porosity can lead to dielectric permittivity that is lower than that of the solid material. It is thus one strategy to achieve lower dielectric constants for microelectronics devices. Thus, controlling porosity can yield a spectrum of dielectric constants from a single material [15]. Porosity plays a role in decreasing the Curie point for barium titanate ceramics with apparent density below 90% [16]. Manipulation of the volume ratio of porosity can lead to appropriate dielectric constant being obtained in a wide range. These advantages have been harnessed in the fabrication of materials with highly anisotropic dielectric constants with simultaneous introduction of aligned pores [17]. High material porosity is considered as an advantage only in few cases such as in materials that have resistance to temperature changes.

Various techniques have been introduced to make mesoporous and porous $BaTiO_3$ some of which include, development of soft-chemistry routes to produce nanoparticles or specially shaped materials, such as one-dimensional nanowires; sonochemical methods to prepare size-tunable $BaTiO_3$ crystals [18] and the introduction of biosynthesis methods to prepare $BaTiO_3$ nanopowders [19]. Mesoporous and porous materials have important features such as the

possession of large surface areas and nano size porous structures [20]. These features make the materials widely used in photo electronics, catalytic reactions and semiconductors among others [21, 22]. However, the high costs and difficulty in process control in these routes necessitated the development of alternative options for the synthesis of porous $BaTiO_3$ nanoparticles.

Mechanochemical synthesis can be used to reduce the grain size of porous $BaTiO_3$ and Ba $(Ti_{0.96}Sn_xZr_{0.04-x})$ O_3 (x = 0.02−0.04) powder to nanosize. This is predicated on the fact that mechanical technique is superior to both the conventional solid-state reaction and wet-chemistry-based processing routes for several reasons as it uses low-cost and widely available oxides as starting materials compared to wet chemical routes which are extremely sensitive to environmental conditions such as moisture, light and heat [23, 24].

Complex impedance spectroscopy is a nondestructive method [25] that uses to distinguish the grain boundary from the grain-electrode effects which are usually the sites for trapping oxygen vacancies and other defects. Within a wide range of ceramics, an ionic, ionic plus electronic or electronic conduction is shown in these sites. It is also useful in establishing space charge polarization and its relaxation mechanism, by appropriately attributing different values of resistance and capacitance to the grain and grain boundary effects. It allows the contributions to the overall electrical property by various components in the material to be easily separated. Other workers have used impedance spectroscopy to study other materials [26, 27] to gain insight into electrical conduction mechanisms of the materials. In this work, we report the structural and electrical properties of porous $BaTiO_3$ and $Ba(Ti_{0.96}Sn_xZr_{0.04-x})O_3$ (x = 0.02−0.04) ceramics prepared by solid-state and mechanochemical technique. The effect of porosity on the ceramics material will be used to evaluate the materials and serve as guide in the choice for MLCC and thermistor applications.

1.2. Mechanochemical synthesis

Mechanochemical synthesis or high-energy milling is the preparation of powder by high-energy ball milling of elemental mixtures. The most important feature of this technique is that the formation of the product compounds flows from the reactions of oxide precursors by mechanical energy activation, rather than the heat energy necessitated in the conventional solid-state reaction process.

The solid-state reactions initiated by intensive milling in high-energy ball mills could be a good choice for the ceramic powder preparation. The area of contact between the reactant powder particles increases with the intensive milling. This is the consequence of reduction in particle size and permits fresh surfaces to come into contact. This permits the reduction to continue without the requirement for diffusion through the product layer. Alternatively, the particle refinement and consequent reduction in diffusion distances (due to microstructural refinement) can at least reduce the reaction temperatures significantly, even if they do not occur at room temperature. In general, the procedure of sintering is improved by liquid-phase sintering with titanium-rich composition at the temperature above 1320°C or by mechanical activation of precursors ($BaCO_3$ and TiO_2) [28–30]. In addition, particle size of ceramic powders is reduced by mechanical

treatment and produces nanostructured powders which are of primary interest in the current trend of miniaturization and integration of electronic components [31, 32].

1.3. Barium titanate ($BaTiO_3$) perovskite structure

The perovskite, ABO_3 type structure of BT is cubic (above 120°C) with Ba ion (larger A cation) located at the cube corners, Ti ion (smaller B cation) at the body center, and oxygen at the face centre, forming octahedra around each Ti ion. It is considered an FCC-derivative structure in which the larger A cation and oxygen together form an FCC lattice, while the smaller B cation occupies the octahedral interstitial sites in the FCC array. The Ba ion occupies the space formed between eight neighboring octahedra, giving the Ba, Ti and the oxygen ions coordination number of 12, 6 and 6, respectively. $BaTiO_3$ can accept the substitution of foreign cations on two distinct sites, the A-site (Ba) and the B-site (Ti). The stability of the perovskite compounds arises mainly from the electrostatic charge of the ions when perfectly integrated.

1.4. Structural phase transitions in barium titanate

BT undergoes a series of structural phase transitions upon cooling from high temperature. In the temperature range of 1430–1620°C, barium titanate assumes a hexagonal structure. In the 130–1430°C range, BT is cubic and nonpolar (space group *Pm3m),* thus centrosymmetric and nonpiezoelectric. When the temperature is below the Curie temperature (130°C), the cubic structure (paraelectric) is slightly distorted to a tetragonal *(P4mm)* structure (ferroelectric) which is noncentrosymmetric, with an accompanying movement of Ti atoms inside the O_6 octahedra. In turn, oxygen ions all shift in the opposite direction [100]. Not only does this result in distortion of oxygen octahedron, but the opposite displacement of negative and positive charges within the unit cell leads to the formation of an electric dipole moment, and hence to the appearance of spontaneous polarization and ferroelectric properties. In the tetragonal phase, the direction of the vector of spontaneous polarization Ps (i.e., polar direction) lies parallel to the direction of one of the original cubic [100] directions. When the temperature is below 5°C, the tetragonal structure transforms to an orthorhombic ferroelectric phase *(C2mm)* with the polar axis parallel to a face diagonally, and the direction of spontaneous polarization transfers to a pseudocubic [110]. At as low as −90°C, it further transforms to a rhombohedral structure *(R3m)* with the polar axis along a body diagonal and is spontaneously polarized along a [111] direction.

The Goldschmidt tolerance factor for a perovskite structure (ABO_3) is given by the formula:

$$t = \frac{r_A + r_O}{\sqrt{2}(r_B + r_O)} \tag{1}$$

where r_A r_B and r_O are the A-site, B-site, and oxygen ionic radii, respectively. There are three possible values of 't': (1) $t \geq 1$: show ferroelectricity. (2) $t < 1$: This antiferroelectric perovskite. (3) $t = 1$: perfect cubic structure.

http://dx.doi.org/10.5772/intechopen.75500

2. Experimental

2.1. Sample preparation

All samples used in this study were prepared by the conventional solid state and mechano-chemical technique from fine powders of metal oxides or metal carbonates. The nominal purity of the initial powders, as well as their manufacturers are given in **Table 1**.

2.2. Synthesis of barium titanate ($BaTiO_3$) and Zr- and Sn-doped barium titanate

$BaTiO_3$and $Ba(Ti_{0.96}Sn_xZr_{0.04-x})O_3$ (x = 0.02−0.04) nanocrystalline powders were synthesized by a combination of solid-state reaction and high-energy ball milling technique. The starting materials were analytical grade high-purity (99·9%) oxide precursors, $BaCO_3$, ZrO_2, TiO_2 and SnO_2. Stoichiometric amounts of the oxides were weighed according to nominal composition and ball-mixed for 12 h in alcohol. The mixture was dried in an oven and calcined in an alumina crucible at 1050°C for 4 h in the air to yield $BaTiO_3$, $Ba(Ti_{0.96}Sn_{0.02}Zr_{0.02})O_3$, $Ba(Ti_{0.96}Sn_{0.03}Zr_{0.01})O_3$, and $Ba(Ti_{0.96}Sn_{0.04})O_3$ powders. The calcined powders were ball-milled in an isopropyl alcohol as wetting medium using SPEX 8000 Mixer/Mills (60 Hz model) at room temperature for 7 h. The milling was stopped for 15 min after every 60 min of milling to cool down the system. The slurry was put in an oven and dried at 90°C for 24 h. The milled powder was compacted at 5 ton to make pellets of size 15 mm in diameter and 1.5 mm in thickness using polyvinyl alcohol (PVA) as a binder. After burning off the binder (PVA), the pellets were sintered in a programmable furnace at temperatures of 1190°C for 2 h in alumina crucibles.

2.3. Characterization

Phase identification of calcined and sintered powders was carried out using X-ray diffractometer with monochromatic Cu-Kα radiation (λ = 1.54178 Å) under 40 kV/30 mA—over a 2θ range from 20 to 80° at a scanning rate of 2°/min. The experimental densities of the samples were calculated using Electronic Densimeter MD-3005 ALFAMIRAGE. The morphological studies of the sintered sample were carried out using field-emission scanning electron microscopy (FE-SEM) (JEOL 7600F) operated at 15 kV. The polarization-electric field (P–E) hysteresis

Starting materials	Manufacturers	Purity
$BaCO_3$	Merck, Germany	99.9%
TiO_2	Aldrich Chemical Company, Inc.,U.S.A	99.9+%
SnO_2	Strem, Chemicals, U.S.A.	99.9%
ZrO_2	Strem, Chemicals, U.S.A	99.9%

Table 1. Precursors, purity level and manufacturers.

characteristics of the samples were determined using a Precision LC material analyzer (Radiant, U.S.A). The dielectric and impedance measurement was carried out for the sintered sample using an Agilent 4294 A Impedance Analyzer in the frequency and temperature range of 40 Hz–1 MHz and 30–400°C, respectively.

3. Structural and electrical properties

3.1. Structural properties

Structural and dielectric properties were evaluated for both $BaTiO_3$ and $Ba(Ti_{0.96}Sn_xZr_{0.04-x})O_3$ (x = 0.02−0.04) ceramic, while thermistor application is explored in Ba $(Ti_{0.96}Sn_{0.02}Zr_{0.02})O_3$ ceramic

3.1.1. XRD analysis

Figure 1 shows the room temperature XRD patterns of $BaTiO_3$ and $Ba(Ti_{0.96}Sn_xZr_{0.04-x})O_3$ (x = 0.02−0.04) ceramics. It is seen that all the compositions are of single-phase perovskite structure without any trace of secondary phase and imply that Sn^{+4} and Zr^{+4} entered the unit cell and maintained the perovskite structure as a solid solution. The enlarged XRD patterns of the ceramics in the range of 2θ of 44–46.5° clearly show that the crystal structure of the ceramic is cubic for BT with JCPDS file no. 96-150-7758 and space group *Pm-3 m* (**Figure 2a**). This is because the (200) and (002) peaks are not split [33] as reported by other workers [34, 35], whereas it is tetragonal for $Ba(Ti_{0.96}Sn_xZr_{0.04-x})O_3$ (x = 0.02−0.04) (**Figure 2b**–**d**) with the splitting of the (200) and (002) characteristic peaks which are in agreement with the **j**oint **c**ommittee on **p**owder **d**iffraction **s**tandards (JCPDS file no.98-00-2020), similar result was obtained for x = 0.04 using conventional method by other workers [36]. It can also be noticed from **Figure 2a**–**d** that the positions of the diffraction peaks of the ceramics shift slightly to lower angle with increasing Sn content in the range of 2θ from 44 to 46.5°. This is attributed to the larger ionic radius of Sn^{+4} (0.69 Å) and Zr^{+4} (0.72 Å) as compared with that of Ti^{+4} (0.60 Å) with results in a slight enlargement of crystal cell volumes and hence a shift of diffraction peaks toward lower angles.

3.1.2. Microstructure

Figures 3–**6** show the FE-SEM images of porous $BaTiO_3$ and $Ba(Ti_{0.96}Sn_xZr_{0.04-x})O_3$ (x = 0.02−0.04) ceramic sintered at 1190°C for 2 h. All the samples are dense and have varying microstructural features with the presence of voids. The presence of voids in the FE-SEM images indicates that the pellets have a certain amount of porosity. The grain size and grain boundary can be seen very clearly in a nonagglomerated region and the grain size decreases with increasing Sn content. The difference among these four samples is attributed to the difference in Sn and Zr content since all of them have been processed under the same conditions. Further substitution of Sn caused the grain size to become smaller with more porous regions between them compared to porous $BaTiO_3$ sample. The average grain size of $BaTiO_3$ and $Ba(Ti_{0.96}Sn_xZr_{0.04-x})O_3$ (x = 0.02−0.04) ceramics determined by using linear intercept technique is shown in **Table 2**. The

http://dx.doi.org/10.5772/intechopen.75500

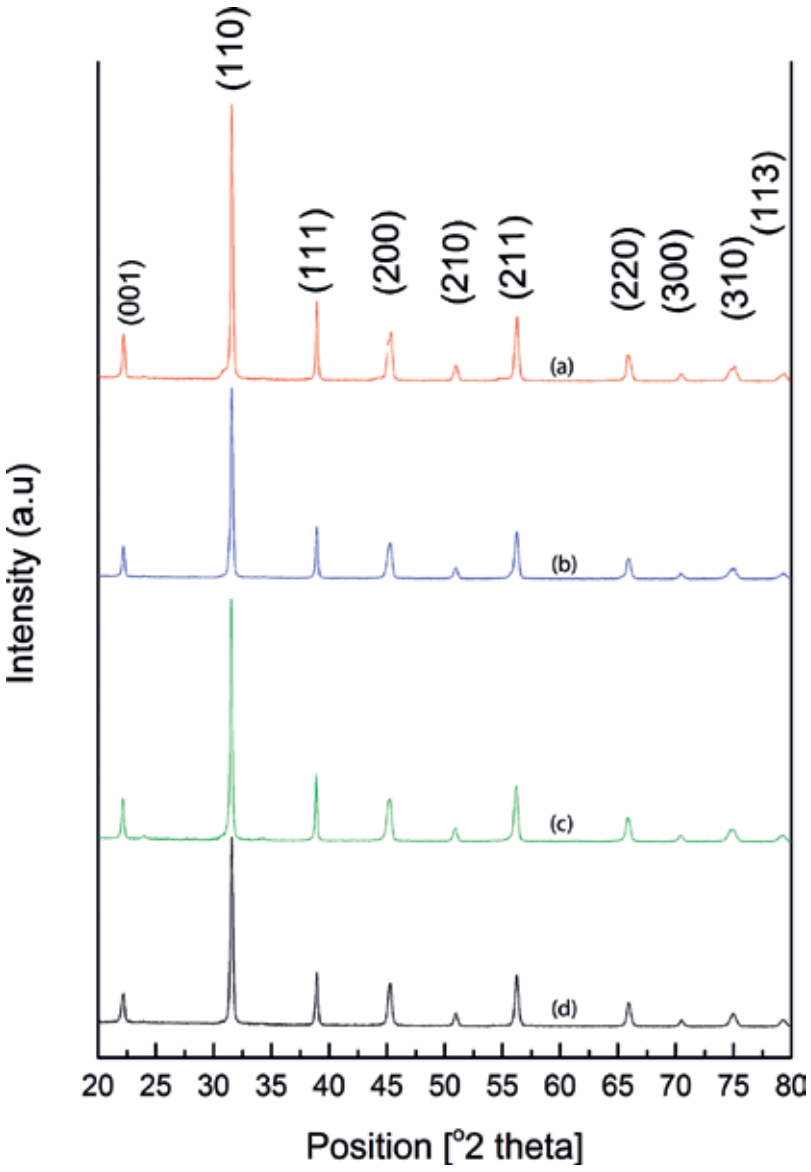

Figure 1. XRD patterns of $BaTiO_3$ and $Ba(Ti_{0.96}Sn_xZr_{0.04-x})O_3$ ceramics (a) BT, (b) 0.02, (c) 0.03 and (d) 0.04 sintered at 1190°C.

grain size decreased from 199.65 to 89.28 nm with increase in Sn and this indicates that Sn is a grain growth inhibitor.

3.1.3. Density

The experimental or observed density of each sample was calculated using the Archimedes principle from (Eq. (2)):

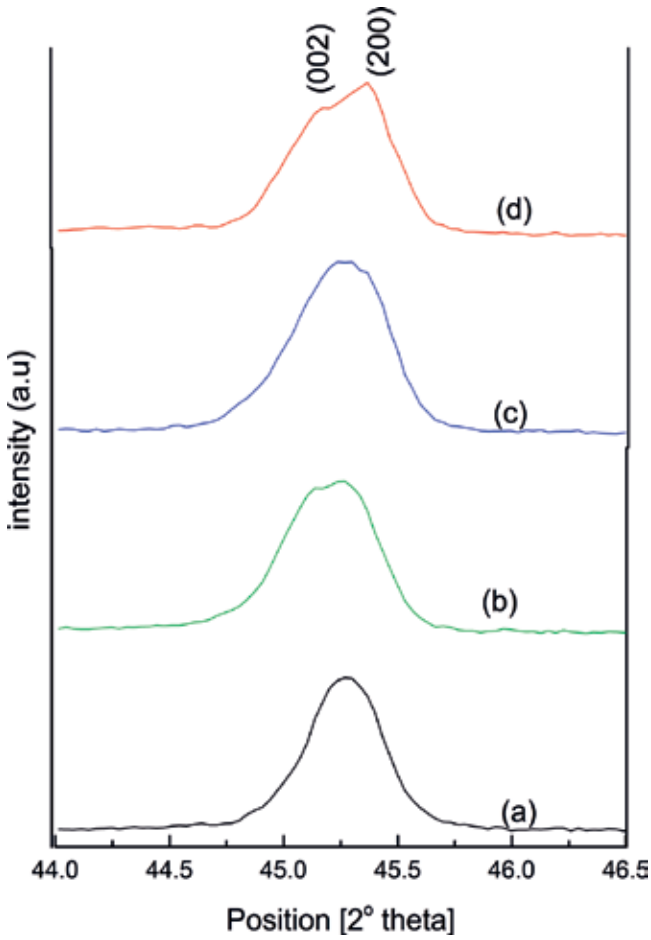

Figure 2. XRD patterns of $BaTiO_3$ and $Ba(Ti_{0.96}Sn_xZr_{0.04-x})O_3$ ceramics in the range of 2θ from 44 to 46.5° (a) BT, (b) 0.02, (c) 0.03 and (d) 0.04 sintered at 1190°C.

$$\rho_{exp} = \frac{M_a \rho_w}{M_a - M_w} \tag{2}$$

where *Ma* and *Mw* are the respective weights in gram of the pellet measured in air and in water. $\rho_{w\ is}$ the density of pure water in g/cm^3. The theoretical density of the material was calculated using (Eq. (3)):

$$\rho_{xrd} = \frac{cell\ mass}{cell\ volume} = \frac{\frac{n \times M \times 1.66 \times 10^{-24}}{V} g}{cm^3}, \tag{3}$$

where n is the number of atoms per unit cell, M is the molecular weight of atoms constituting one unit of the chemical formula, and V is the unit cell volume.

http://dx.doi.org/10.5772/intechopen.75500

The experimental densities of the porous $BaTiO_3$ and $Ba(Ti_{0.96}Sn_xZr_{0.04-x})O_3$ (x = 0.02−0.04) ceramics prepared by High Energy Mechanochemical (HEM) method and conventional sintering vary from 93.6% to 89.0%of theoretical density. The relative density of $BaTiO_3$ is higher compared to the Sn-/Zr-doped samples. The increase of the tin content to x = 0.04 induced further densification which tends to inhibit the grain growth [37]. This increase in density is also evident in FESEM microstructures of **Figures 3–6** which show a decreasing presence of porosity with increasing Sn content.

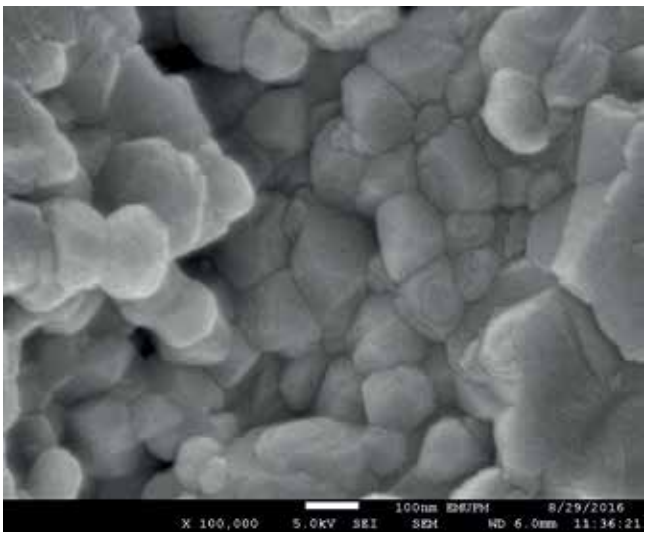

Figure 3. FESEM images of nanocrystalline BT sample at magnification of ×200,000.

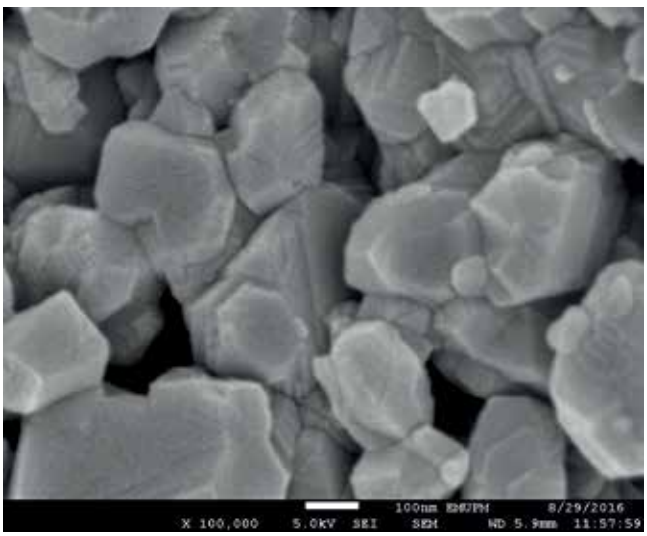

Figure 4. FESEM images of nanocrystalline $Ba(Ti_{0.96}Sn_xZr_{0.04-x})O_3$ (x = 0.02) sample at magnification of ×200,000.

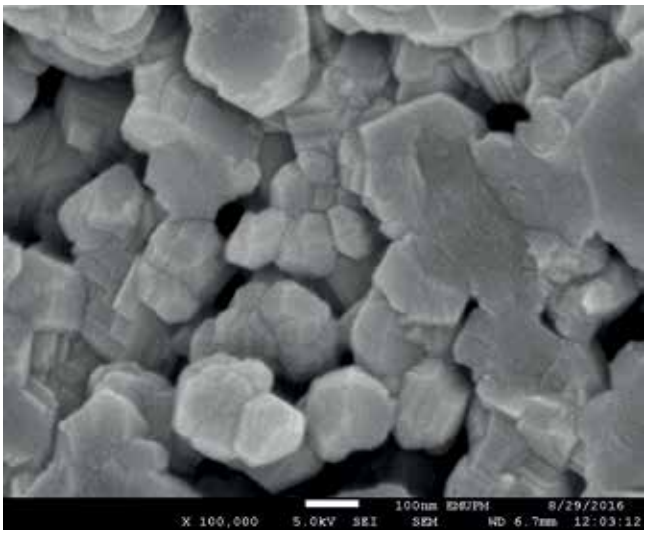

Figure 5. FESEM images of nanocrystalline $Ba(Ti_{0.96}Sn_xZr_{0.04-x})O_3$ (x = 0.03) sample at magnification of ×200,000.

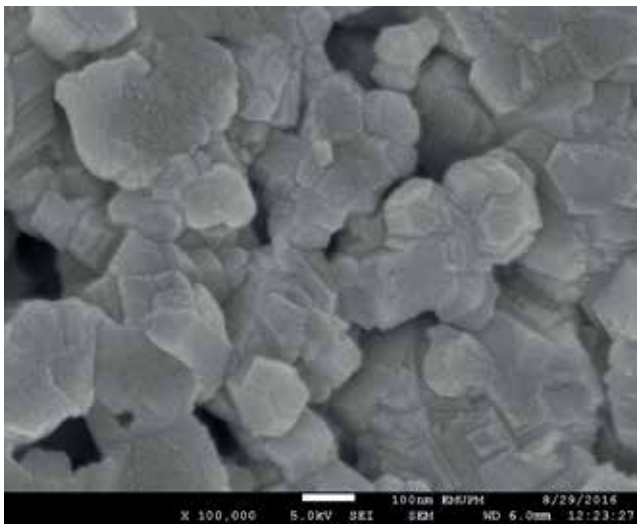

Figure 6. FESEM images of nanocrystalline $Ba(Ti_{0.96}Sn_xZr_{0.04-x})O_3$ (x = 0.04) sample at magnification of ×200,000.

3.1.4. Porosity

The porosity of $BaTiO_3$ and $Ba(Ti_{0.96}Sn_xZr_{0.04-x})O_3$ (x = 0.02−0.04) ceramics was calculated using (Eq. (4)):

$$\text{Porosity} = \left(\boldsymbol{d_{xrd}} - \boldsymbol{d_{\exp}}\right) \times \frac{\mathbf{100}}{\boldsymbol{d_{xrd}}} \tag{4}$$

The macroporous structure of $BaTiO_3$ and $Ba(Ti_{0.96}Sn_xZr_{0.04-x})O_3$ (x = 0.02−0.04) ceramics exhibited a porosity of 6.3–10.9% **Table 2**. Porosity increased from 6.3 to 12.8% at $Ba(Ti_{0.96}Sn_{0.02}Zr_{0.02})O_3$ and then decreased to 10.9% with increase in Sn concentration, respectively. The increase of the relative density and decrease of porosity with Sn concentration enhance the density of the ceramics with reduction of pores. It can be seen from the FESEM image in **Figures 3–6** that the pores vary in sizes in all the samples. Pores are composed of macropores in the grain boundary or nanopores in the grains, but in all the samples, only macropores are visible.

3.1.5. Effect of porosity on dielectric properties

Porosity in BT ceramics can be considered as a secondary phase and indicates its degree of densification. Pores in BT ceramics are usually formed by incomplete sintering or using sacrificial pore formers and exist in between the grains. Porosity decreases strength, because pores reduce the true cross section area of a BT ceramics and also pores act as stress concentrating notches. In many cases, different densities within a ceramic are used to provide a wide continuous range of dielectric constants. The relative permittivity decreases with increasing material porosity as reported by other workers [38]. Porosity of a ceramic material is a serious defect in high-voltage insulating systems [39]. Enhanced electric field in the pores increases the probability of bond breakage on the pore walls and leads to the lowering of the overall breakdown strength [40].

3.2. Dielectric properties

3.2.1. Variation of dielectric constant and loss tangent with frequency

The real (ε′) part of relative permittivity and tan δ in the frequency range of 40 Hz–1 MHz of porous $BaTiO_3$ and $Ba(Ti_{0.96}Sn_xZr_{0.04-x})O_3$ (x = 0.02−0.04) ceramics at room temperature is shown in **Figures 7** and **8**, respectively. It can be seen that the value of dielectric constant is higher at lower frequencies and decreases with increase in frequency. The decrease of dielectric constant with increasing frequency means that the response of the permanent dipoles decreases as the frequency increases and the contribution of the charge carriers (ions) toward the dielectric constant decreases [41, 42].

Sample	Theoretical density (d_{xrd}) (g/cm^3)	Experimental density (d_{exp}) (g/cm^3)	Relative density (%)	% porosity	Grain size (nm)
$BaTiO_3$	6.02	5.639	93.6	6.3	144.53
$Ba(Ti_{0.96}Sn_{0.02}Zr_{0.02})O_3$	6.17	5.382	87.2	12.8	199.65
$Ba(Ti_{0.96}Sn_{0.03}Zr_{0.01})O_3$	6.19	5.418	87.5	12.4	84.54
$Ba(Ti_{0.96}Sn_{0.04})O_3$	6.18	5.502	89.0	10.9	89.28

Table 2. Physical properties of $BaTiO_3$ and $Ba(Ti_{0.96}Sn_xZr_{0.04-x})O_3$ (x = 0.02–0.04) ceramics.

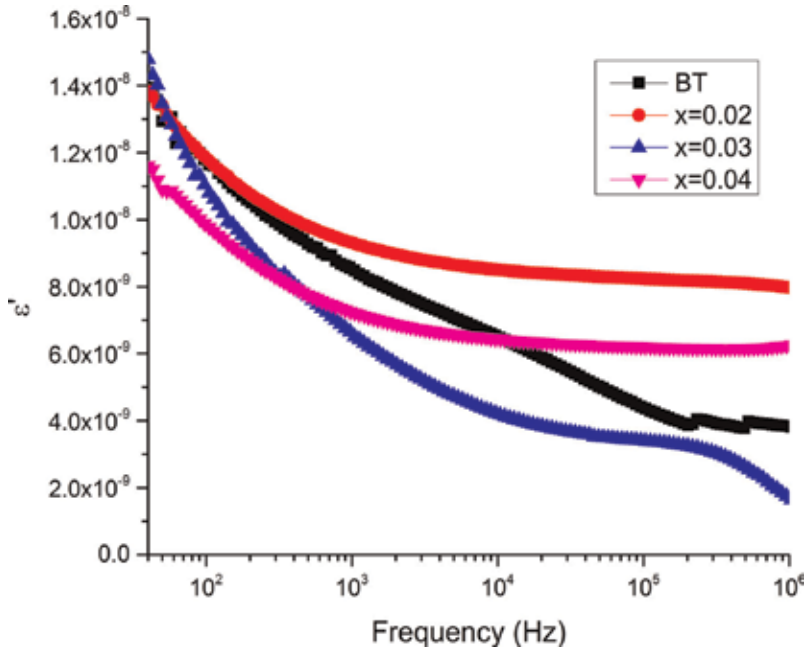

Figure 7. Variation of the real part of relative permittivity (ε′) of nanocrystalline $BaTiO_3$ and $Ba(Ti_{0.96}Sn_xZr_{0.04-x})O_3$ (x = 0.02–0.04) at 30°C.

The ε′ for BT has a value of only 1550 at room temperature which is lower than that of the sample prepared by conventional solid-state reaction route [43, 44]. The observed lower value is as a result of the smaller grain size of the ceramics [45, 46]. With the reduction of crystallite size that corresponds to the width of the domain wall, pinning would be formulated inside the grains and the domain wall motion would be inhibited. The domain wall mobility reduction leads to the decrease of the switching rate, hence lowering the dielectric constant. The presence of tin in the material also decreases the dielectric constant of $Ba(Ti_{0.96}Sn_{0.04})O_3$ [47, 48]. The observed lowering of the dielectric constant for $Ba(Ti_{0.96}Sn_{0.04})O_3$ could be considered as a combined effect of the presence of Sn and the nanocrystalline nature of the grains.

The increase of dielectric constant from 1563 to 1671 (**Table 3**) in porous $Ba(Ti_{0.96}Sn_{0.02}Zr_{0.02})O_3$ and $Ba(Ti_{0.96}Sn_{0.03}Zr_{0.01})O_3$, respectively, may be as a result of decrease of grain size and porosity of the sample. The frequency-independent behavior of è for $Ba(Ti_{0.96}Sn_{0.02}Zr_{0.02})O_3$ and $Ba(Ti_{0.96}Sn_{0.04})O_3$ beyond 1000 Hz indicates the reduction of the contribution of the charge carriers toward the dielectric permittivity ε′ and tends to a static value at all temperatures as a result of absence of space charge effects [49]. Further, the ε′ exhibits high value which reflects the effect of space charge polarization and/or conducting ion motion. The best sample is $Ba(Ti_{0.96}Sn_{0.03}Zr_{0.01})O_3$ because it exhibited high real dielectric relative permittivity of 1671, loss of 1.63 and low porosity of 12.4% among the doped samples. This shows that the sample $Ba(Ti_{0.96}Sn_{0.03}Zr_{0.01})O_3$ can be used for MLCCs and energy storage application.

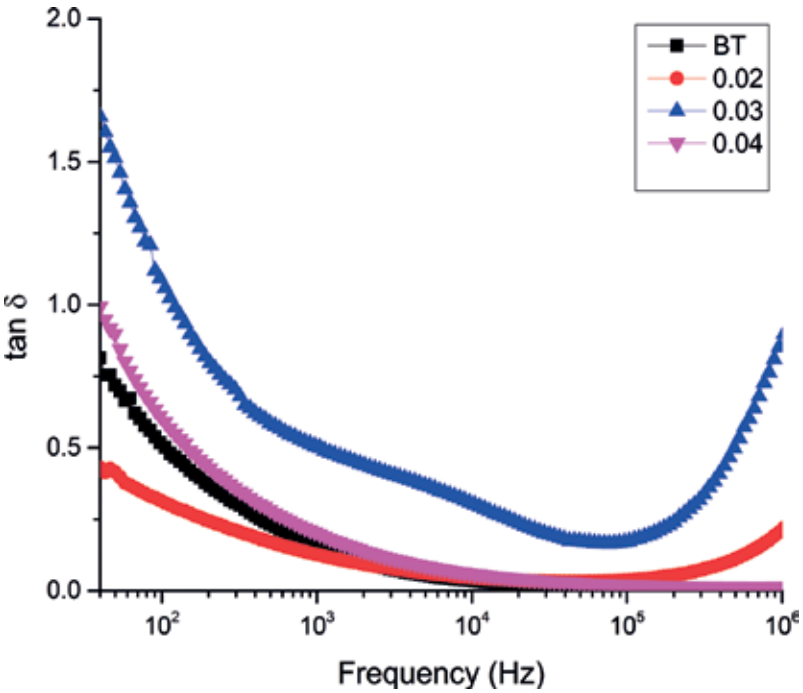

Figure 8. Frequency dependence of dielectric loss (tan δ) of $BaTiO_3$ and $Ba(Ti_{0.96}Sn_xZr_{0.04-x})O_3$ (x = 0.02–0.04) at 30°C.

Samples	E_c (kV/cm)	P_r (μC/cm^2)	P_s (μC/cm^2)
BT	0.592	0.295	1.934
BTSZ1	1.766	0.576	1.411
BTSZ2	2.930	3.117	4.680
BTSZ3	2.894	3.726	5.120

Table 3. Ferroelectric properties of the samples at room temperature.

The variation of tan δ with frequency is shown in **Figure 8**. Similar to the behavior of ε′ with frequency, the dielectric loss exponentially decreases with decreasing frequency to almost zero for porous $BaTiO_3$ and $Ba(Ti_{0.96}Sn_{0.04})O_3$ but rises beyond 10^5 Hz for $Ba(Ti_{0.96}Sn_{0.02}Zr_{0.02})O_3$ and $Ba(Ti_{0.96}Sn_{0.03}Zr_{0.01})O_3$, respectively. In the lower frequency region, a decrease in the value of tan δ is observed which is due to the dominance of space charge polarization and interface effects at lower frequencies. However, for porous $BaTiO_3$ and $Ba(Ti_{0.96}Sn_{0.04})O_3$ at a frequency of 10^4Hz, frequency-independent behavior of these parameters is observed. The values of tan δ of $BaTiO_3$ and $Ba(Ti_{0.96}Sn_xZr_{0.04-x})O_3$ (x = 0.02−0.04) are shown in **Table 3**. The decrease of tan δ in $BaTiO_3$ from 0.8 to 0.43 and from 1.6 at x = 0.03 to 0.43 at x = 0.02 clearly indicates that loss tangent shows a decreasing tendency with increase of zirconium content in agreement with literatures [50]. The dielectric losses were a combined result of electrical conduction and orientational polarization of the matter [51].

3.2.2. Variation of dielectric constant and tangent loss with temperature

The variation of dielectric constant and tangent loss as a function of temperature for porous $BaTiO_3$ and $Ba(Ti_{0.96}Sn_xZr_{0.04-x})O_3$ (x = 0.02−0.04) ceramics measured from room temperature to 150°C at the frequency of 100 Hz is shown in **Figures 9** and **10**, respectively. From **Figure 9**, it is clear that the maximum dielectric constant of porous $BaTiO_3$ and $Ba(Ti_{0.96}Sn_xZr_{0.04-x})O_3$ (x = 0.02−0.04) is at room temperature and decreases with increase in temperature, though less than that reported in CuO-modified $Ba(Ti_{0.96}Sn_xZr_{0.04-x})O_3$ (x = 0.02−0.04) ceramics synthesized using solid-state reaction [44] except for porous BT where the dielectric constant was observed to decrease from 30 to 70°C and then increased sharply at 90°C. Thereafter, it falls to the lowest level at 110°C, thus indicating a phase transition. For porous $Ba(Ti_{0.96}Sn_xZr_{0.04-x})O_3$ (x = 0.02−0.04) ceramics, the phase transition seems to be shifted toward lower room temperature with increase in doping concentration as reported by other workers [52]. The shifting of transition temperature (*Tc*) to a lower value can be explained by the larger radius of Sn^{4+} (0.69 Å) and Zr^{+4} (0.72 Å), compared to Ti^{4+} (0.605 Å). Uchino et al. have suggested that with decreasing grain size, T_c was shifted downward toward room temperature, eventually tending toward 0 K at some critical particle size [53].

In **Figure 10**, the dielectric loss of $Ba(Ti_{0.96}Sn_xZr_{0.04-x})O_3$ (x = 0.02−0.04) beyond 70°C becomes almost independent and later merges at higher temperature, except for $BaTiO_3$ which rapidly increases with increase in temperature beyond 90°C. This sharp increase in dielectric loss in the

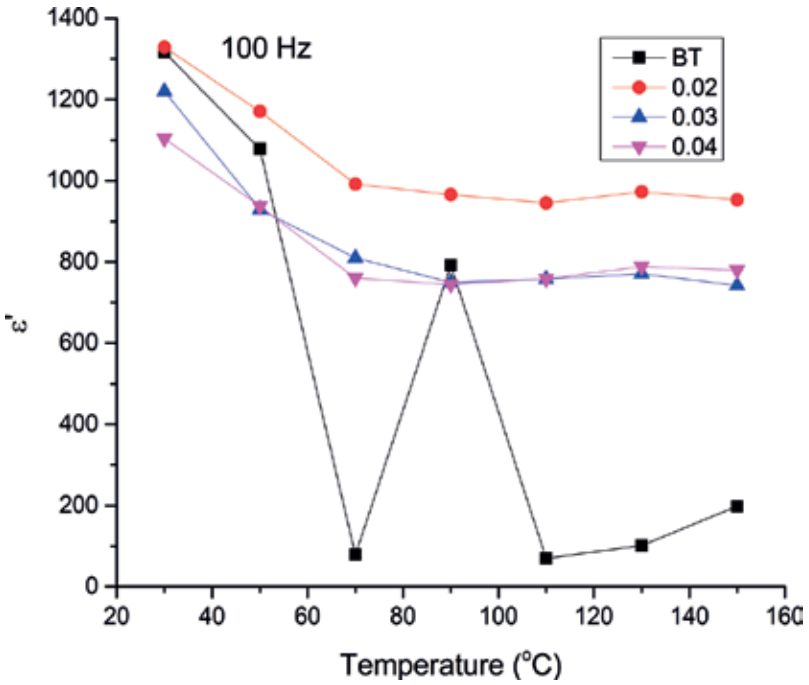

Figure 9. Temperature dependence of dielectric constant of nanocrystalline $BaTiO_3$ and $Ba(Ti_{0.96}Sn_xZr_{0.04-x})$ O_3(x = 0.02–0.04) ceramics measured at 100 kHz.

http://dx.doi.org/10.5772/intechopen.75500

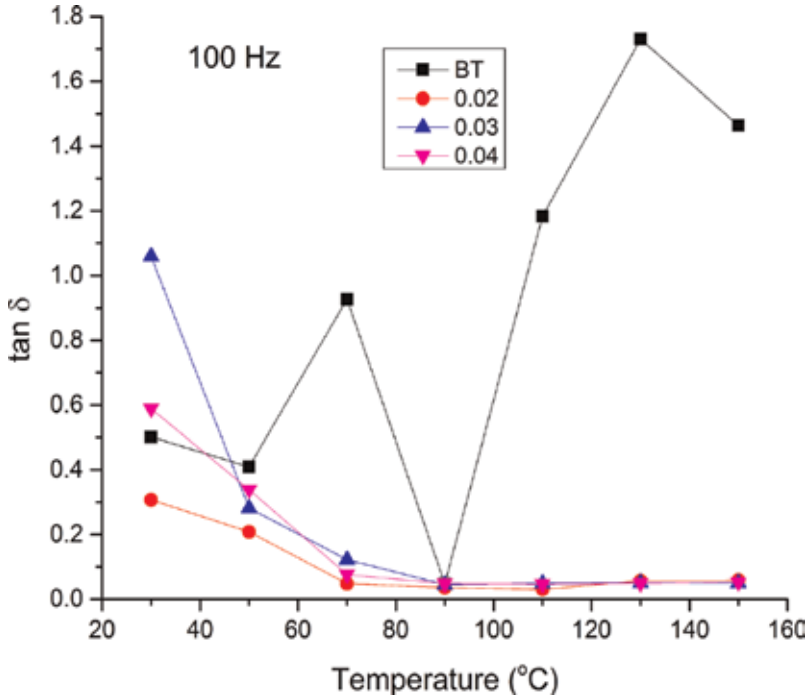

Figure 10. Temperature dependence of dielectric loss of nanocrystalline $BaTiO_3$ and $Ba(Ti_{0.96}Sn_xZr_{0.04-x})O_3$ (x = 0.02–0.04) ceramics measured at 100 kHz.

high temperature region in $BaTiO_3$ may be attributed to the increased mobility of charge carriers arising from defects or vacancies in the sample [54]. In porous $BaTiO_3$ sample, the minimum in the dielectric loss is coincident with the maximum of dielectric anomaly. Therefore, we conclude that porous $BaTiO_3$ sample undergoes a structural phase transition. The loss tangent of porous $Ba(Ti_{0.96}Sn_xZr_{0.04-x})O_3$ (x = 0.02−0.04) ceramics decreases with increasing Zr content due to the chemical stability of Zr^{4+} compared to that of Ti [55].

3.3. Ferroelectric properties

The polarization versus electric field (P-E) hysteresis loops of $BaTiO_3$ and $Ba(Ti_{0.96}Sn_xZr_{0.04-x})O_3$ (x = 0.02−0.04) ceramics measured at room temperature and 1 kHz with different Sn concentrations are shown in **Figure 11**. The results are presented in **Table 3**. The polarization hysteresis loop is not fully saturated which may be due to leakage current. The *P-E* loops become larger and broader as the Sn content (x) increases which show the ferroelectricity of the $Ba(Ti_{0.96}Sn_xZr_{0.04-x})O_3$ (x = 0.02−0.04). The increase in Remnant polarization is due to the increase in the dielectric property and decrease of the porosity of the sample with an increase in Sn doping [56]. The performance parameter of BT is very close to that of the reported values (P_s of 2.0 μC/cm^2, E_c of 5 kV/cm) for the ceramic sample [57] and lower than the one obtained by the same synthesis route (P_r of 2.0μC/cm^2, and coercive field (E_c) of 1060 V/cm) [35]. The decrease of E_c for 2.8 to 2.6 kV/cm for $Ba(Ti_{0.96}Sn_{0.03}Zr_{0.01})O_3$ to $Ba(Ti_{0.96}Sn_{0.04})O_3$ may be

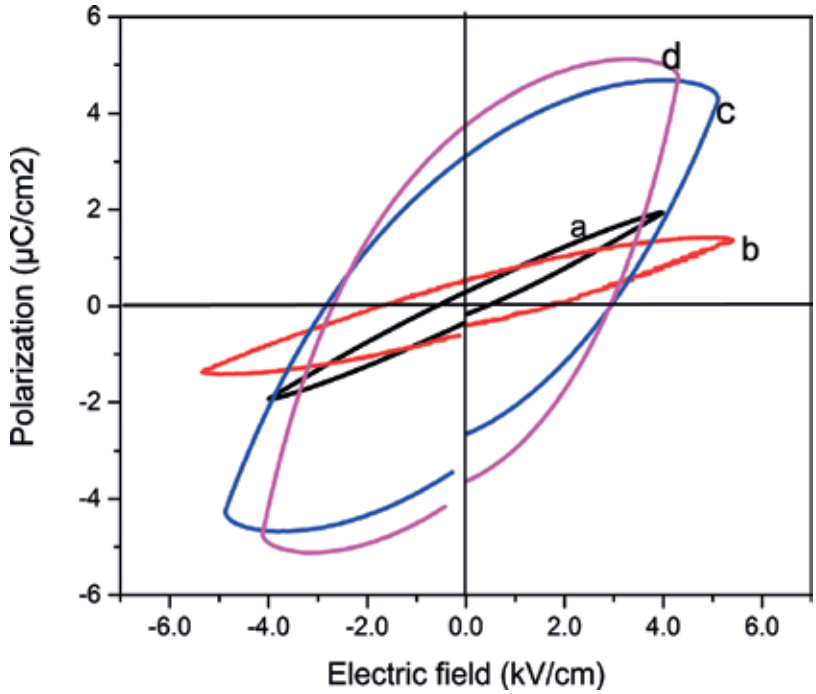

Figure 11. P-E hysteresis loop of nanocrystalline ceramics synthesized at 1190°C: (a) BT, (b) 0.02, (c) 0.03, and (d) 0.04.

attributed to the reduction in grain size and indicates that $Ba(Ti_{0.96}Sn_{0.04})O_3$ may be useful for switching applications. $BaTiO_3$ samples have cubic phase and ferroelectric tetragonal phase ($Ba(Ti_{0.96}Sn_{0.02}Zr_{0.02})O_3$, $Ba(Ti_{0.96}Sn_{0.03}Zr_{0.01})O_3$ and $Ba(Ti_{0.96}Sn_{0.04})O_3$) as evident from XRD result. Polarization reversal of a ferroelectric domain is much easier inside a larger grain the comparison to that in a smaller grain [58]. Oxygen vacancies may affect domain wall motion by a screening of the polarization charge. A formation ion of mechanical barriers against the domain walls by oxygen vacancies, that is, domain wall pinning, might also stabilize the domain configuration.

3.4. Complex impedance

Figure 12 shows the variation of the real (Z') and imaginary (Z'') part of impedance (inset) with frequency from 200 to 400°C. It is observed that the magnitude of Z' decreases with increase in frequency at different temperatures which is an indication of an increase in dc conductivity. The coincidence of Z' and Z'' values at higher frequencies at all temperatures indicates a possible release of space charge [59] and a consequent lowering of the barrier properties of the material [60]. Further, at low frequencies, the Z' values decrease with rise in temperature, that is, they show negative temperature coefficient of resistance (NTCR) behavior similar to semiconductors [61].

http://dx.doi.org/10.5772/intechopen.75500

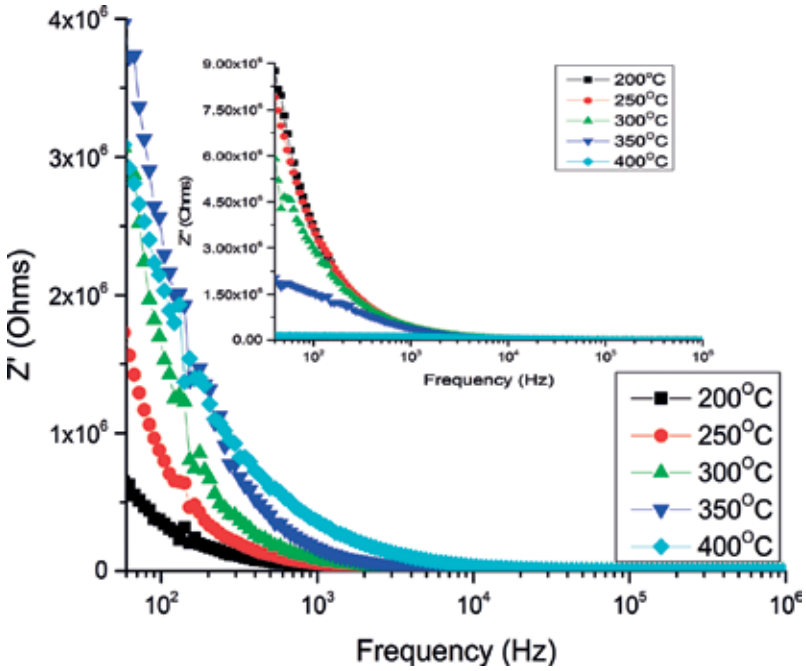

Figure 12. Frequency dependences of real (Z′) and imaginary (Z″) part of impedance (inset) of nanocrystalline Ba $(Ti_{0.96}Sn_{0.02}Zr_{0.02})O_3$ sample at 200–400°C.

Figure 13 shows the complex impedance plots (Z^*) or Cole-Cole plots, that is, plotting imaginary part Z'' against the real part Z' of complex impedance $Z^* = Z' + jZ''$ of BTSZ ceramic, performed at 200, 250, 300 and 350°C over a wide frequency range (40 Hz to 1 MHz). From **Figure 13**, it is observed that with the increase in temperature, the slope of the lines decreases and the curve moves toward real (Z') axis indicating an increase in conductivity of the sample.

At temperature 400°C, two semicircles are formed (**Figure 14**) representing resistance for grain (R_g) and grain boundary (R_{gb}) effect in the material having centers lying below the real axis confirming the presence of the non-Debye type of relaxation phenomenon in the materials [62]. Hence, grain and grain boundary effects in **Figure 14** could be separated at these temperatures. The high-frequency semicircle corresponds to a bulk contribution, and the low-frequency semicircle corresponds to the grain boundary effect [63]. The value of bulk resistance (R_g) in the high-frequency range and grain boundary resistance (R_{gb}) in the low-frequency range obtained from the intercepts of the semicircular arcs formed at 400°C on the real axis (Z') is 44.08 and 148.4 kΩ, respectively (**Figure 14**). The observed data were modeled on an equivalent circuit having a series combination of two parallel resistor-capacitor elements (inset of **Figure 14**) [64, 65]. The real (Z') and imaginary (Z'') parts of total impedance of the equivalent circuit are defined as:

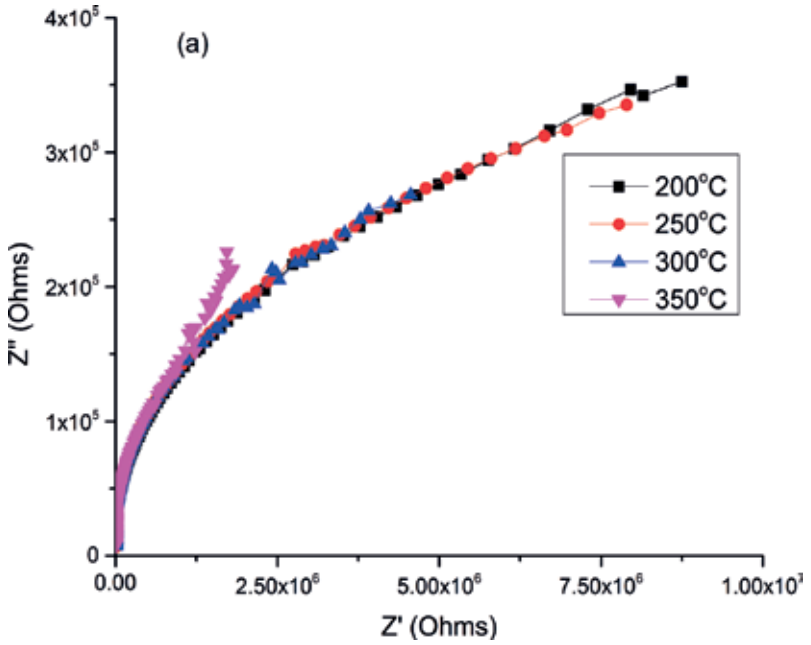

Figure 13. Plot of Z′ versus Z″ (Nyquist or Cole-Cole plots) for nanocrystalline $Ba(Ti_{0.96}Sn_{0.02}Zr_{0.02})O_3$ ceramic data taken over a wide frequency range of 40 Hz to 1 MHz at 200–350°C.

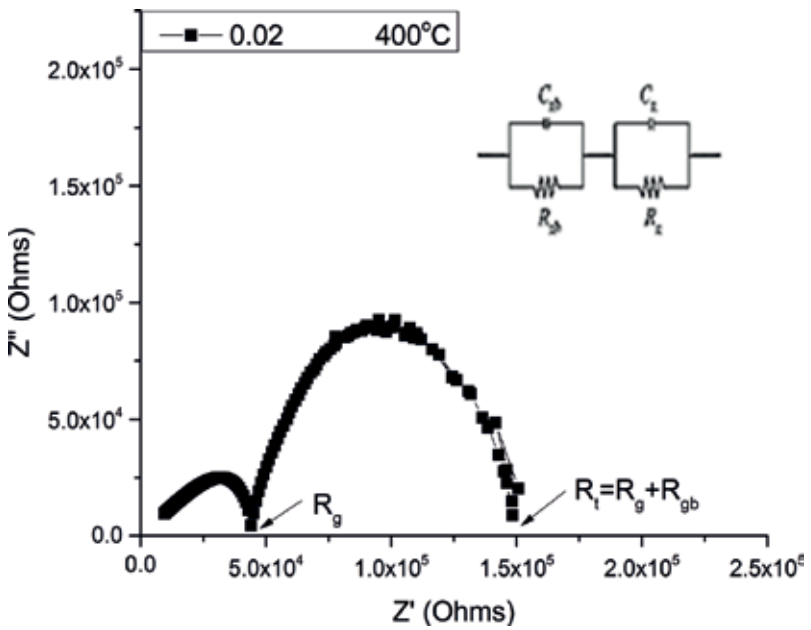

Figure 14. Plot of Z′ versus Z″ (Nyquist or Cole-Cole plots) for nanocrystalline $Ba(Ti_{0.96}Sn_{0.02}Zr_{0.02})O_3$ ceramic data taken over a wide frequency range of 40 Hz to 1 MHz at 400°C.

$$Z' = \frac{R_g}{1 + \left(\omega R_g C_g\right)^2} + \frac{R_{gb}}{1 + \left(\omega R_{gb} C_{gb}\right)^2} \tag{5}$$

$$Z'' = R_g \left[\frac{\omega R_g C_g}{1 + \left(\omega R_g C_g\right)^2}\right] + R_{gb} \left[\frac{\omega R_{gb} C_{gb}}{1 + \left(\omega R_{gb} C_{gb}\right)^2}\right] \tag{6}$$

where R_g and Cg are the grain resistance and grain capacitance, R_{gb} and C_{gb} are the grain boundary resistance and grain boundary capacitance at the interfacial regions, respectively, and ω is the angular frequency. The semicircles in the impedance spectrum have a characteristic peak occurring at a unique relaxation frequency ($\omega_{max} = 2\pi f_{max}$) which can be expressed as $\omega_{max}RC = \omega_{max}\ \tau = 1$, where "$f$ max" is the frequency at the maximum of semicircle. Therefore,

$$f_{max} = \frac{1}{2\pi\tau} = \frac{1}{2\pi RC} \tag{7}$$

where τ is the relaxation time. The respective capacitances (C_b and C_{gb}) due to the grain and grain boundary effects can be calculated using Eq. 7. The values of R_g, R_{gb}, C_g and C_{gb} obtained from Cole-Cole plots at 400°C are 44.17 kΩ, 148.43 kΩ, 3.23×10^{-10} Farad and 1.71×10^{-8} Farad, respectively. The corresponding relaxation times due to both the bulk and grain boundary effect (τ_g and τ_{gb}) have been calculated using Eq. 7 to be 1.42×10^{-5} s and 2.55×10^{-3} s, respectively.

Moreover, the results showed a higher value of R_{gb} as compared to R_g as a result of a lower concentration of oxygen vacancies and trapped electrons in grain boundaries. This is due to the loss of oxygen during high temperature sintering process which again greatly influenced the conduction and dielectric relaxation behavior of the material. High temperature sintering leads to the formation of oxygen vacancies as $2O_o^x \rightarrow O_2(g) + 2V\ddot{o} + 4e^-$. Nevertheless, when the temperature is slowly cooled to room temperature in air, a reoxidation process occurs as $2V\ddot{o} + O_o^x + 4e^- \rightarrow O_2(g)$ and leads to the formation an insulating grain boundary and highly conductive oxygen-deficient grains [66].

4. Conclusion

In this study, porous $BaTiO_3$ and $Ba(Ti_{0.96}Sn_xZr_{0.04\text{-}x})O_3$ (x = 0.02−0.04) ceramics with nanocrystalline structure were obtained by mechanochemical synthesis method. The effects of the porosity of the ceramics on their microstructural and dielectric properties were investigated. It was found that porosity of the ceramics could be tailored by varying the dopant content. With increase of Sn content, porosity decreased from 12.8 to 10.9%. X-ray analysis confirms the cubic and tetragonal structure at room temperature for pristine and Zr and Sn codoped barium titanate, respectively. FESEM images indicated that the particles possess a porous structure. The temperature dependence dielectric study revealed a normal ferroelectric behavior in the material. Room temperature dielectric constant increased with Sn and Zr content, while

dielectric loss decreased. Electrical parameters such as the real part of impedance (Z'), the imaginary part of impedance (Z'') as a function of both frequency and temperature have been studied through impedance spectroscopy. Nyquists plots of $Ba(Ti_{0.96}Sn_{0.02}Zr_{0.02})O_3$ ceramic show both bulk and grain boundary effects at 400°C which indicates the NTCR behavior of the sample. Therefore, $Ba(Ti_{0.96}Sn_{0.02}Zr_{0.02})O_3$ ceramic is considered as a promising low-cost material for thermistor applications. The electrical relaxation process occurring in the material has been found to be temperature dependent.

Author details

Umaru Ahmadu[1]*, Alhassan Muazu[2] and Sadiq Umar[3]

*Address all correspondence to: u.ahmadu@yahoo.com

1 Department of Physics, Federal University of Technology, Minna, Nigeria

2 Department of Physics, Federal College of Education (T), Bichi, Kano, Nigeria

3 Department of Physics, Ahmadu Bello University, Zaria, Nigeria

References

[1] Stojanovic BD, Mastelaro VR, Paiva Santos CO, Varela JA. Structure study of donor doped barium titanate prepared from citrate solutions. Science of Sintering. 2004;**36**:179-188

[2] Haertling GH. Ferroelectric ceramics: History and technology. Journal of American Ceramic Society. 1999;**82**(4):797-818

[3] Uchino K. Ferroelectric Devices. New York: Marcel Dekker; 2000

[4] Jaffe B, Cook WR, Jaffe H. Piezoelectric Ceramics. London: Academic Press Limited; 1971

[5] Shi T, Xie L, Gu L, Zhu J. Why Sn doping significantly enhances the dielectric properties of $Ba(Ti_{1-x}Sn_x)O_3$. Scientific Reports. 2015;**5**:8606. DOI: 10.1038/srep08606

[6] Lu SG, Xu ZK, Chen H. Tunability and relaxor properties of ferroelectric barium stannate titanate ceramics. Applied Physics Letters. 2004;**85**(22):5319-5321

[7] Wei X, Yao X. Preparation, structure and dielectric property of barium stannate titanate ceramics. Material and Science Engineering, B. 2007;**137**:184

[8] Kumar SU, Reddy VR, Bag P, Rawat R, Gupta SM, Gupta A. Electro-caloric effect in lead-free Sn doped $BaTiO_3$ ceramics at room temperature and low applied fields. Applied Physics Letters. 2014;**105**:112907. DOI: 10.1063/1.4896044

[9] Xie L, Li YL, Yu R, Cheng ZY, Wei XY, Yao X, Jia CL, Urban K, Bokov AA, Ye Z-G, Zhu J. Static and dynamic polar nanoregions in relaxor ferroelectric $Ba(Ti_{1-x}Sn_x)O_3$ system at high temperature. Physical Review B. 2012;**85, 014118**

[10] Zhi Y, Guo R, Bhalla AS. Dielectric behavior of $Ba(Ti_{1-x}Zr_x)O_3$ single crystals. Journal of Applied Physics. 2000;**88**(1):410. DOI: 10.1063/1.373674

[11] Stojanovic BD, Foschini CR, Pavlovic VB, Pablovic VM, Pejovic V, Varela JA. Barium titanate screen-printed thick films. Ceramics International. 2002;**28**(3):293-298. DOI: 10.1016/S0272-8842 (01)00093-1

[12] Zhao J, Li L, Wang Y, Gui Z. DC bias properties of $Ba(Ti_{1-x}Zr_x)O_3$ ceramics. Material Science and Engineering, B. 2003;**99**(1–2):207-210

[13] Jiang JZ, Poulsen FW, Mørup S. Structure and thermal stability of nanostructured iron-doped zirconia prepared by high-energy ball milling. Journal of Materials Research. 1999; **14**:1343-1352

[14] Martin L, Chu Y, Ramesh R. Advances in the growth and characterization of magnetic, ferroelectric, and multiferroic oxide thin films. Materials Science and Engineering R. 2010; **68**:89-133. DOI: 10.1016/j.mser.2010.03.001

[15] Gong X, She WH, Hoppenjans EE, Wing ZN, Geyer RG, Halloran JW, Chappell WJ. Tailored and anisotropic dielectric constants through porosity in ceramic components. IEEE Transactions on Microwave Theory and Techniques. 2005;**53**:3638-3647

[16] Fang TT, Hsieh HL, Shiau F. Effects of pore morphology and grain size on the dielectric properties and tetragonal–cubic phase transition of high-purity barium titanate. Journal of the American Ceramic Society. 1993;**76**(5):1205-1211. DOI: 10.1111/j.1151-2916.1993. tb03742.x

[17] Wing ZN, Wang B, Halloran JW. Permittivity of Porous Titanate Dielectrics. Journal of the American Ceramic Society. 2006;**89**:3696. https://doi.org/10.1111/j.15512916.2006.01323.x

[18] Dang ZM, Zhou T, Yao SH, Yuan JK, Zha JW, Song HT, Li JY, Chen Q, Yang WT, Bai J. Advanced calcium copper titanate/polyimide functional hybrid films with high dielectric permittivity. Journal of Advanced Materials. 2009;**21**(20):2077-2082. DOI: 10.1002/ adma.200803427

[19] Jhaa AK, Prasad K. Ferroelectric $BaTiO_3$ nanoparticles; biosynthesis and characterization. Colloids and Surfaces, B: Biointerfaces. 2010;**75**:330-334

[20] Larsen G, Lotero E, Nabity M, Petkovic LM, Shobe DS. Surfactant-assisted synthesis of mesoporous zirconia powders with high surface areas. Journal of Catalysis. 1996;**164**:246-248. DOI: 10.1006/jcat.1996.0379

[21] Corma A. From microporous to mesoporous molecular sieve materials and their use in catalysis. Chemical Reviews. 1997;**97**(6):2373-2420. DOI: 10.1021/cr960406n

[22] Victor F, Stone J, Davis R. Synthesis, characterization, and photocatalytic activity of titania and niobia mesoporous molecular sieves. Chemistry of Materials. 1998;**10**(5):1468-1474. DOI: 10.1021/cm980050r

[23] German RM. Sintering Theory and Practice. New York: Wiley; 1996

[24] Wang S, Ding J, Shi Y, Chen YJ. High coercivity in mechanically alloyed $BaFe_{10}A_{l2}O_{19}$. Journal of Magnetism and Magnetic Materials. 2000;**219**:206-212

[25] Macdonald JR. Impedance Spectroscopy—Emphasizing Solid Materials and Systems. New York: Wiley-Interscience; 1987

[26] Ahmadu U, Tomas Ŝ, Jonah SA, Musa AO, Rabiu N. Equivalent circuit models and analysis of impedance spectra of solid electrolyte $Na_{0.25}Li_{0.75}Zr_2(PO_4)_3$. Advanced Materials Letters. 2013;**4**(3):185-195

[27] Jacob R, Harikrishnan Nair G, Isac J. Impedance spectroscopy and dielectric studies of nanocrystalline iron doped barium strontium titanate ceramics. Processing and Application of Ceramics. 2015;**9**(2):73-79

[28] Gomez-Yanez C, Benitez C, Ramirez HB. Mechanical activation of the synthesis reaction of $BaTiO_3$ from a mixture of $BaCO_3$ and TiO_2 powders. Ceramics International. 2000;**26**: 271-277

[29] Berbenni V, Marini A, Bruni G. Effect of mechanical milling on solid state formation of $BaTiO_3$ from $BaCO_3$-TiO_2 (rutile) mixtures. Thermochimica Acta. 2001;**374**:151-158

[30] Brzozovski E, Castro MA. Lowering the synthesis temperature of high-purity $BaTiO_3$ powders by modifications in the processing conditions. Thermochimica Acta. 2003;**398**: 123-129

[31] Ding JS, Suzuki T, McCormic PG. Ultra fine particles prepared by mechanical/thermal processing. Journal of the American Ceramic Society. 1996;**79**:2956-2958

[32] Giri AK. Nanocrystalline materials prepared through crystallization due to instability in amorphous materials after grinding. Advanced Materials. 1997;**9**:163-166

[33] Buttner RH, Maslen EN. Structural parameters and electron difference density in $BaTiO_3$. Acta Crystallographica Section B. 1992;**B48**:764-769

[34] Burtr L, Jianping Z. Preparation, structure evolution and dielectric properties of barium titanate thin fim and powder by an aqueous sol-gel process. Thin Solid Films. 2001;**388**:107

[35] Lazarevi ZZ, Vijatovi M, Doh MZ, Rom NZ, Rom MJ, Paunovi N, Stojanovi BD. The characterization of the barium titanate ceramic powders prepared by the Pechini type reaction route and mechanically assisted synthesis. Journal of the European Ceramic Society. 2010;**30**:623-628

[36] Pengrong R, Zicheng L, Qian W, Biaolin P, Shanming K, Huiqing F, Gaoyang Z. Large nonlinear dielectric behavior in $BaTi_{1-x}Sn_xO_3$. Scientific Reports. 2017;**7**:6693. DOI: 10.1038/s41598-017-07192-x

[37] Al-Naboulsia T, Boulos M, Tenailleau C, Dufour P, Zakhour M, Sophie G-F. Elaboration and characterization of barium titanate powders obtained by the mechanical activation of barium nitrate and titanate oxide, and electrical properties of the ceramics sintered by SPS. Journal of Ceramic Processing Research. 2016;**17**(8):870-875. ISSN 1229-9162

[38] Hou YD, Chang LM, Zhu MK, Song XM, Yan H. Effect of $Li_2CO_3Li_2CO_3$ addition on the dielectric and piezoelectric responses in the low-temperature sintered 0.5PZN–0.5PZT systems. Journal of Applied Physics;**102**:2007, 084507. DOI: 10.1063/1.2800264

[39] Srikanth KS, Singh VP, Vaish R. Enhanced pyroelectric figure of merits of porous $BaSn_{0.05}Ti_{0.95}O_3$ ceramics. Journal of the European Ceramic Society. 2017;**37**(13):3943-3950. DOI: 10.1016/j.jeurceramsoc.2017.05.015

[40] Yang KY, You WJ, Krishnamurthy A. Effect of porosity on electrical stability of hydrocarbon polymeric low-k dielectric. IEEE Transactions on Electron Devices. 2005;**52**(10):2333-2336

[41] Graca M, Valente MA, Ferreira da Silva MG. Electrical properties of lithium niobium silicate glasses. Journal of Non-Crystalline Solids. 2003;**325**(1–3):267-274

[42] Bergo P, Pontuschka WM, Prison JM. Dielectric properties of P_2O_5-$N_{i2}O$-L_{i2} glasses containing WO_3, CoO or Fe_2O_3. Solid State Communicaions. 2007;**141**(10):545-547

[43] Shao SF, Zhang JL, Zhang Z, Zheng P, Zhao ML, Li JC, Wang CL. High piezoelectric properties and domain configuration in $BaTiO_3$ ceramics obtained through the solid-state reaction route. Journal of Physics and Dielectric: Applied Physics. 2008;**41**(12):125408

[44] Tan YQ, Zhang JL, Wang CL. High piezoelectric properties and good temperature stabilities of CuO-modified $Ba(Ti_{0.96}Sn_xZr_{0.04-x})O_3$ ceramics. Journal of Advanced Dielectrics. 2013;**3**(2):1350014

[45] Wu K, Schulze W. Aging of the weak-field dielectric response in fine- and coarse-grain ceramic $BaTiO_3$. Journal of the American Ceramic Society. 1992;**75**(12):3390-3395. DOI: 10.1111/j.1151-2916.1992.tb04439.x

[46] Frey MH, Payne DA. Grain-size effect on structure and phase transformations for barium titanate. Physics Review. 1996;**B54**:3158-3168

[47] Isupov VA. Some p5roblems of diffuse ferroelectric phase transitions. Ferroelectrics. 1989; **90**(1):113-118. DOI: 10.1080/00150198908211278

[48] Nath AK, Medhi N. Density variation and piezoelectric properties of $Ba(Ti_{1-x}Sn_x)O_3$ ceramics prepared from nanocrystalline powders. Bulletin of Materials Science. 2012; **35**(5):847-852

[49] Ahmadu U, Tomas Ŝ, Musa AO, Isah KU. Electrical and dielectric characterization of $Na_{0.5}Li_{0.5}Zr_2(PO_4)_3$. Open Journal of Physical Chemistry. 2011;**1**:94-103

[50] Zheng P, Zhang JL, Shao SF, Tan YQ, Wang CL. Piezoelectric properties and stabilities of CuO-modified $Ba(Ti,Zr)O_3$ ceramics. Applied Physics Letters. 2008;**94**:032902. DOI: 10.1063/1.3072347

[51] Gattu S, Dasari KS, Kocharlakota VR. Structural and dielectric properties of Sn doped barium magnesuim zirconium titanate perovskite ceramics. World Journal of Condensed Matter Physics. 2015;**5**:346-352. DOI: 10.4236/wjcmp.2015.54035

[52] Alkathya MS, Joseph A, Raju KCJ. Dielectric properties of Zr substituted barium strontium titanate. Materials Today: Proceedings. 2016;**3**:2321-2328

[53] Uchino K, Sadanaga E, Hirose T. Dependence of the crystal structure on particle size in barium titanate. Journal of the American Ceramic Society. 1989;**72**(8):1555-1558. DOI: 10.1111/j.1151-2916.1989.tb07706.x

[54] Ganguly P, Jha AK. Journal of Alloys and Compound. 2010;**495**:7-12

[55] Sagar R, Hudge P, Madolappa S, Kumbharkhane AC, Raibagkar RL. Electrical properties and microwave dielectric behaviour of holmium substituted barium zirconium titanate ceramics. Journal of Alloys and Compound. 2012;**537**:197

[56] Yadav KL, Sharma P. Indian Journal of Engineering & Materials Sciences. 2008;**15**:61

[57] Deshpande SB, Potdar HS, Patil MM, Deshpande VV, Khollam YB. Dielectric properties of $BaTiO_3$ ceramics prepared from powders with bimodal distribution. Journal of Industrial and Engineering Chemistry. 2006;**12**(4):584-588

[58] Leu CC, Chen CY, Chien CH. Domain structure study of $SrBi_2Ta_2O_9$ ferroelectric thin films by scanning capacitance microscopy. Applied Physics Letters. 2003;**82**(20):3493-3495. DOI: 10.1063/1.1576308

[59] Plocharski J, Wieczoreck W. PEO based composite solid electrolyte containing NASICON. Solid State Ionics. 1988;**979**:28-30

[60] Kumar A, Singh BP, Choudhary RNP, Thakur AK. Characterization of electrical properties of Pb-modified $BaSnO_3$ using impedance spectroscopy. Materials Chemistry and Physics. 2006;**99**(1):150-159

[61] Sarangi S, Badapanda T, Behera B, Anwar S. Frequency and temperature dependence dielectric behavior of barium zirconate titanate nanocrystalline powder obtained by mechanochemical synthesis. Journal of Materials Science: Materials in Electronics. 2013; **24**:4033-4042. DOI: 10.1007/s10854-013-1358-0

[62] Ranjan R, Kumar N, Behera B, Choudhary RNP. Investigations of Impedance and Electric Modulus Properties of Pb1-xS mx$(Zr_{0.45}Ti_{0.55})$1x/4O_3ceramics. Advanced Materials Letters. 2014;**5**(3):138-142

[63] Ganguly P, Jha AK, Deori KL. Complex impedance studies of tungsten–bronze structured $Ba_5SmTi_3Nb_7O_{30}$ ferroelectric ceramics. Solid State Communications. 2008;**146**(11-12):472-477

[64] Hirose N, West AR. Impedance spectroscopy of undoped $BaTiO_3$ ceramics. Journal of the American Ceramic Society. 1996;**79**:1633-1641. DOI: 10.1111/j.1151-2916.1996.tb08775.x

[65] Dutta A, Bharti C, Sinha TP. AC conductivity and dielectric relaxation in CaMg1/3Nb2/3O_3. Materials Research Bulletin. 2008;**43**(5):1246-1254

[66] Morrison FD, Sinclair DC, West AR. Characterization of lanthanum doped barium titanate ceramics using impedance spectroscopy. Journal of the American Ceramic Society. 2001;**84**:531-538

Chapter 10

Mechanical Properties of Porous Ceramics

Vânia Regina Salvini, Victor C. Pandolfelli and
Dirceu Spinelli

Additional information is available at the end of the chapter

http://dx.doi.org/10.5772/intechopen.71612

Abstract

It is widely known that increasing interest in porous ceramics is due to their special properties, which comprise high volumetric porosity (up to 90%) with open or closed pores, and a broad range of pore sizes (micropores: d < 2 nm; mesopores: 50 nm > d > 2 nm and macropores: d > 50 nm). These properties have many uses comprehending macroscaled devices, mesoscaled materials and microscaled pieces. During their usage, these materials are usually submitted to thermal and/or mechanical loading stresses. Therefore, it is a premise to understand how these porous structures behave under thermomechanical stresses to design materials that show adequate properties for the required application. In this context, the aim of this chapter is to review the mechanical properties of macroporous ceramics.

Keywords: porous ceramics, foams, mechanical properties, elastic modulus, fracture energy

1. Introduction

It is widely known that increasing interest in porous ceramics is due to their special properties, which comprise high volumetric porosity (up to 90%) with open and interconnected or closed and isolated pores, and a broad range of pore sizes (micropores: d < 2 nm; mesopores: 50 nm > d > 2 nm and macropores: d > 50 nm). These properties have many uses comprehending macroscaled devices (filters for liquid metals [1, 2], thermal insulating refractories [3, 4], bioceramics for bone regeneration [5–7], filters for water treatment [8], acoustic insulating tiles [9]),

mesoscaled materials (membranes for catalysis [10], drug release substrates [11, 12]) and microscaled pieces (e.g., multifunctional materials where gravimetric properties are critical as batteries [13] and electronic sensors [14]).

During their usage, these materials are usually submitted to thermal and/or mechanical loading stresses. Therefore, it is a premise to understand how these porous structures behave under thermomechanical stresses to design materials that show adequate properties for the required application.

Despite the importance of porosity for application of these materials, there is not a general consensus about the dependence of mechanical properties on porosity parameters. In other words, the real data of the mechanical properties of these materials indicate that their mechanical behavior depends on more than just porosity of the materials.

Since its introduction to the ceramic community in the 1970s, the area of fracture mechanics has made significant contributions to improving ceramics. As an example, the combination of fracture toughness, fracture statistics and fractography has made it possible to identify critical flaws in material and, consequently develop better and reliable advanced ceramics. In addition, the contribution of fracture mechanics was fundamental in understanding the fracture process in brittle materials.

Recognizing that the area behind a crack was responsible for the increase in the R-curve in ceramics was particularly relevant. One issue concerning the uses of brittle ceramics is associated with the statistical and size-dependence of their fracture properties, which can make reliable prediction, a difficult task. Two other problems are the absence of design methodology for brittle ceramics and the high costs of producing the ceramic components [15].

Nowadays, the ceramic community is witnessing a "boom" of nature inspired materials using hierarchical structures that should have the same behavior or qualities as the natural ones. Various papers [16–20] in the literature show beautiful structures of natural materials and their mimicked copies by researchers. The capacity of a human being's observation, also a characteristic controlled by nature, has been the driving force to imitate natural hierarchical structures and their qualities.

In this context, the aim of this chapter is to review the mechanical properties of macroporous ceramics. The following issues are of particular interest to this chapter:

1. Which microstructural parameters affect the mechanical strength of the porous ceramic material besides its porosity?
2. To what extent do the pores affect the fracture toughness of the porous ceramic material? Does it make sense to measure the fracture toughness of porous material knowing that the stress intensity factor at the notch tip is decreased by the presence of surrounding pores? Or, instead of this, would the total fracture energy be a more realistic measure?
3. What is the elastic modulus behavior of porous ceramics as a function of temperature?

All these questions need to be considered in order to advance not only the processing of porous ceramic materials but also to design their structures for specific applications.

2. Influence of microstructural parameters on the mechanical strength of porous ceramic materials

The objective here is not to carry out an extensive revision of the fracture of brittle porous materials, but to present results which serve as a basis to the authors´ proposal in this chapter.

First of all, fracture of porous ceramics is better described by the quasi-brittle behavior as their ultimate fracture is triggered by many local events (different from essentially brittle behavior of glass ceramics), yet they are not preceded by highly dissipative processes associated with plastic deformation and strain hardening (as observed in ductile metals) [21]. Quasi-brittle fracture behavior is also observed in rocks, bones and ceramic composites.

As mentioned earlier, the real data of the mechanical properties of porous materials indicate that their mechanical behavior depends on more than just porosity of the materials.

Questions have been raised about the models proposed by Gibson and Ashby (GA) [22, 23], which indicate that the relative strength of a porous material is a function of its relative density as follows:

$$\frac{\sigma}{\sigma_s} = C\left(\frac{\rho}{\rho_s}\right)^m \tag{1}$$

where σ and ρ are, respectively, the fracture strength and the density of porous material; σ_S and ρ_S are the fracture strength and the density of solid material, respectively; C is a dimensionless constant and the exponent m depends on the pore morphology (m = 3/2 for open pores or m = 2 for closed ones). The Gibson and Ashby (GA) models are based on the bending or buckling of cell edges.

Figure 1 shows the relative strength predicted by the Gibson and Ashby models plotted together with experimental data of porous ceramics from different researchers. It can be seen a disagreement between the theoretical curves of GA models and the experimental results.

Colombo et al. [24] attributed microstructural factors for the lack of fitting data to the Gibson and Ashby models, as shown in **Figure 1**, as they do not consider the distribution of pore sizes, neither have mixed pores (open and closed) nor flaws in the pore wall (struts).

Seeber et al. [25] also noted that the drop in mechanical properties of foamed ceramics was disproportionately greater than what was to be expected solely from increasing the porosity. These authors suggested this behavior must be an influence of the pore size or the strut thickness, as reported by Brezny and Green [26] in a previous paper.

Nevertheless, Salvini et al. [27] suggested that a parameter which expresses the processing method to produce the porous structure should be considered by the mechanical models. For instance, porous ceramics with similar porosity and density ranges can be produced using different ceramic methods such as sacrificial fugitives, replica templates and directing foaming. However, each method provides a different number of struts (ligaments) of distinct solid particle packing, which influences the final mechanical behavior of the material.

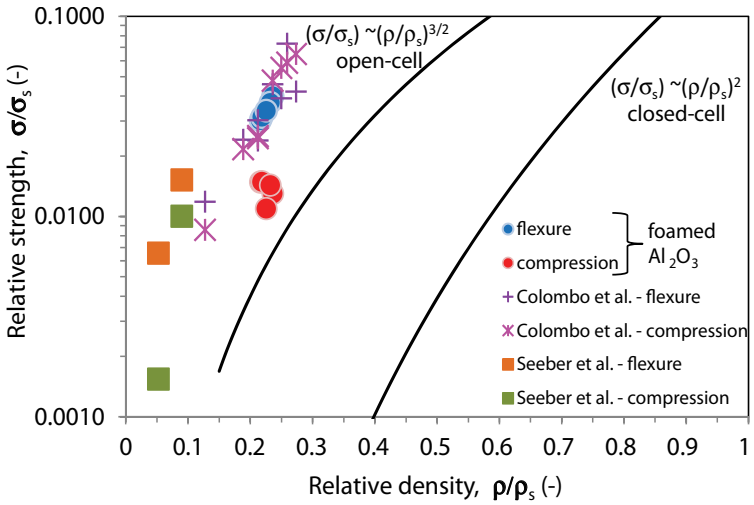

Figure 1. Plot of relative strength as a function of relative porosity for Gibson and Ashby (GA) models [22, 23] and for experimental data obtained by Salvini et al. [27], Colombo et al. [24] and Seeber et al. [25].

In this context, Lichtner et al. [28] produced porous ceramics of same porosity but different pore arrangement using the freeze casting and the slip casting processing methods. They have noted a strong influence of processing on the mechanical properties, and attributed to the differences of orientation and connectivity of macropores.

Brezny et al. [29] also reported that strength of the struts is an important parameter controlling the properties of porous ceramics. According to them, an increase in the strut strength would be expected as a result of the reduced probability of finding a critical flaw in a smaller volume of material as predicted by Weibull, the weakest link hypothesis for strength variability.

Additionally, Genet et al. [21] pointed out that the Gibson and Ashby's approach cannot directly deal with the statistical and size-dependent aspects of fracture.

In 1996, Rice [30] had already drawn attention to this debate considering some problems with micromechanics-based models. The first concern mentioned by Rice was the assumption that porous bodies are represented by packing of hollow spherical particles of an infinite range of sizes. Then, it is assumed the application of a hydrostatic pressure is uniformly distributed in all particles so the resulting strain response can be calculated. Moreover, a common approach to improving the agreement between these models is to let some parameter, for example, the Poisson ratio, depends on the porosity, that is, using it as an adjustable parameter. Another concern is that these models assume that porosity will remain fixed during applications.

Then, Rice has proposed that the mechanical strength of porous ceramics should depend not only on the relative density but also on the minimum solid area fraction, as depicted in **Figure 2**. That is because the solid area is required for transmission of mechanical stresses and thermal and electrical fluxes. This concept is schematically presented in **Figure 3**.

As can be seen in **Figure 2**, each specific model has the following three characteristics: (1) a nearly linear slope of the first half to three-quarters of the porosity range, (2) the approximate

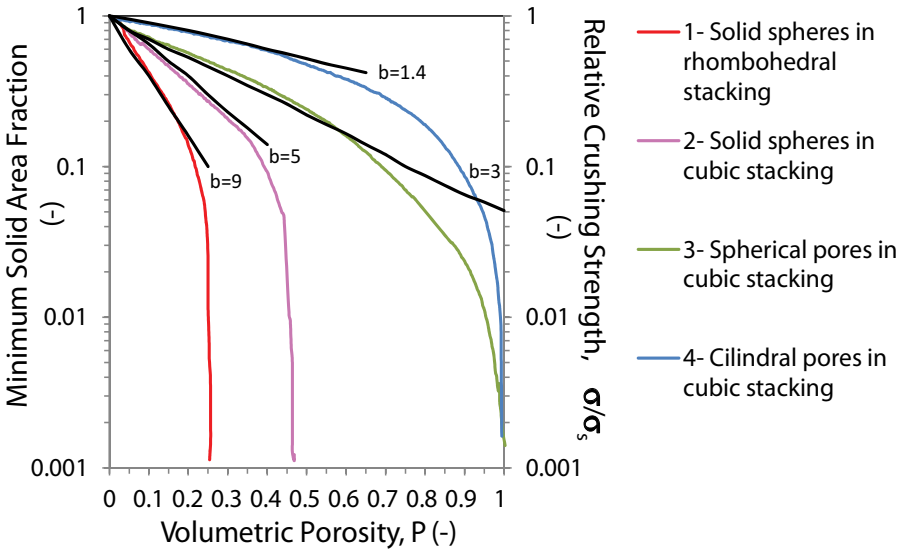

Figure 2. Models from the literature showing the effects of the minimum solid area and porosity on the strength for three basic sphere stackings (cubic, rhombohedral and a mixture of them) and for cylindrical or spherical pores, as well as their mixture, in cubic stacking. The nearly linear portion of curves is represented by the semilogarithmic expression $\sigma = \sigma_S\, e^{-bP}$, with b values ranging from 1 to 3 for stacked pores and from 3 to 9 for stacked particles [30].

porosity value where properties start to be damaged more significantly than the linear slope and (3) the critical porosity P_C where properties go to zero.

However, as pointed out by Rice, these characteristics are useful in distinguishing the basic porosity character of each stacking model, but their utility varies. For instance, P_C values can be accurately defined theoretically, but obtaining reliable experimental data can be a difficult task.

Moreover, the approximated linear slopes are unique for the basic stacking models, and they have been the most widely available factor for polycrystalline materials. However, as clearly shown in **Figure 2**, they can be applied for the restricted porosity range only.

More recently, Bruno et al. [31] reviewed micromechanics aiming the development of microstructure-property relations for porous microcracked ceramics. They focused on specific issues for porous ceramics as the nonlinear stress–strain behavior and the thermal-induced microcracking.

Zheng et al. [32] considered that the fracture strength of brittle porous material is nonlinear and, therefore, there is a percolation failure phenomenon at the fracture of these materials. Therefore, their model considers the porosity (P) and the elastic percolation (ϕ), which depends on the Poisson's ratio of material, as shown:

$$\frac{\sigma}{\sigma_S} = \left[\left(\frac{\phi - P}{\phi}\right)^{1+\nu} \cdot \left(1 - \phi^{2/3}\right)\right]^{1/2} \tag{2}$$

$$\phi = 1 - \left[\frac{1+\upsilon}{3(1-\upsilon)}\right] = \frac{2(1-2\upsilon)}{3(1-\upsilon)} \tag{3}$$

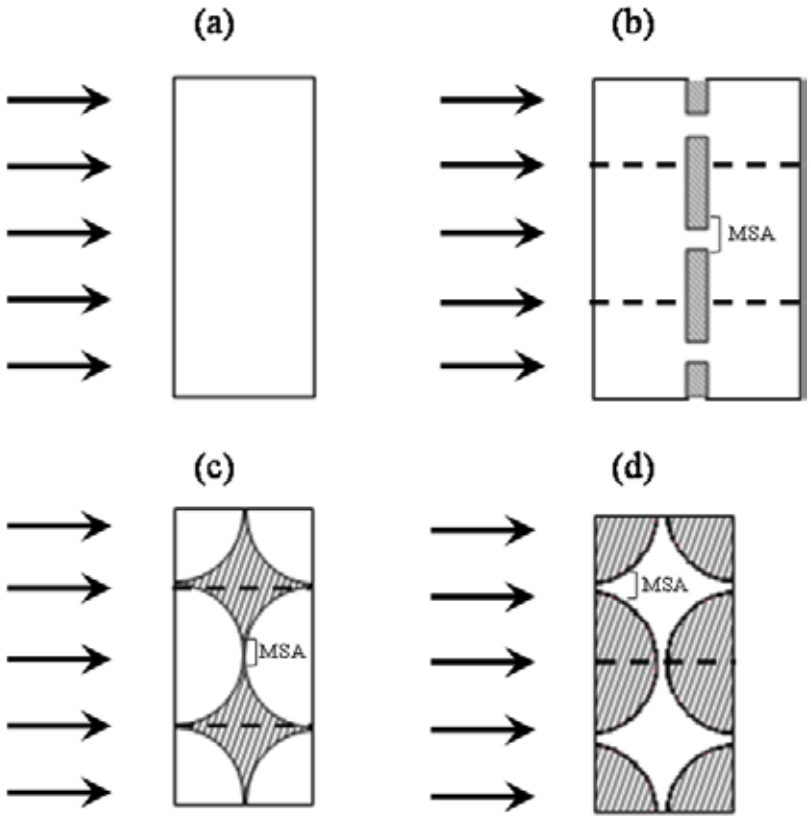

Figure 3. Diagram of the minimum solid area concept. (a) Cross section of a dense material showing the uniform transmission among layers normal to a uniform mechanical stress or conductive flux. (b) Cross section of material showing some layers were removed, leaving only small continuous areas (MSA) for transmission of stress or flux. (c) Cross section of stacked particles and (d) cross section of stacked pores where again the minimum areas of solid will control the transmission of stress or flux normal to the plane of slab [30].

where ν is the scaling exponent for tridimensional solids and υ is the Poisson ratio of materials. In general, for ceramics $\upsilon = 0.2$ and $\phi = 0.5$, for metals $\upsilon = 0.3$ and $\phi = 0.38$, and for polymers $\upsilon = 0.33$ and $\phi = 0.338$. Zheng et al. [32] validated the proposed model for polymers using different porosities and experimentally measured them using the three-point-bending strength test.

In order to check the validity of Zheng's model, Salvini et al. [27] considered the fracture flexure strength data of foamed Al_2O_3 with porosity of 76%. Nevertheless, the results must be interpreted with caution, as Zheng's model overestimated the flexure strength indicating values around 25 MPa, while the average experimental value obtained by Salvini et al. [27] was 10 MPa.

Regarding the failure patterns, Genet et al. [21] investigated the fracture mechanism across scales of porous ceramic scaffold applying a computational method. **Figure 4** shows the

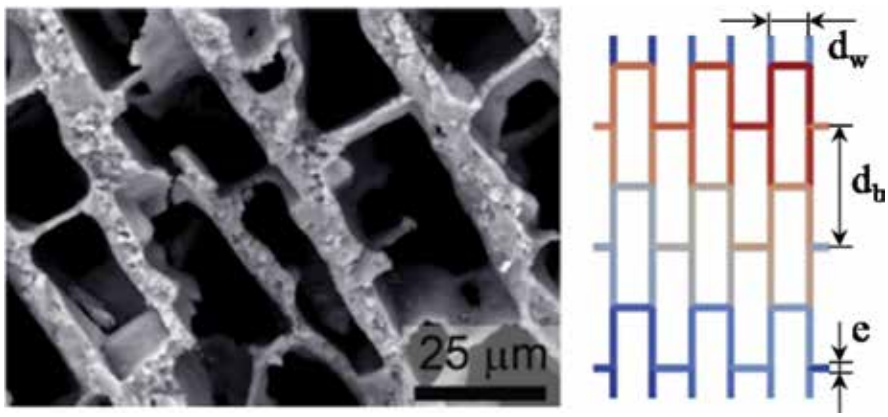

Figure 4. SEM image of a porous ceramic scaffold made by the freeze casting method and its associated idealized geometry, which consists of walls connected by bridges positioned in staggered rows. The geometrical parameters are as follows: The distance between the walls, d_w (d_w = 25 μm), the distance between the bridges, d_b (d_b = 75 μm), and the thickness of the walls and bridges, e (e = 5 μm). A microcell is defined by r × r RVEs (representative volume elements) [21].

scanning electron microscopy (SEM) image of the porous scaffold made by freeze casting and the respective idealized geometry.

Genet et al. [21] found that for very small-sized samples (r = 1 × 1 RVEs), the fracture is brittle and is triggered by the first strut to break. For intermediate-sized samples (r = 5 × 5 RVEs), however, the fracture is controlled by the percolation of several strut breaks, and is mainly governed by the stress redistribution after each break. For large-sized samples (r = 256 × 256 RVEs), they found that the failure process appears to be different, and it is divided into two stages.

The initial stage consists of a widespread development of damage due to the failure of the weakest local defects. But, the stress redistribution caused by these failures is not high enough to make the neighboring cells break or initiate a macrocrack. Instead, a critical defect is activated, rapidly leading to the development of a macrocrack, which leads to the final fracture of the material. Then, the "fatal" macrocrack in large samples does not result from the percolation of previously damaged cells/pores.

Nevertheless, there are some limitations in this study. Firstly, the computational analyses were based on the assumption that porous scaffold material presents isotropic Young's modulus and Poisson's ratio. Another limitation of this study is that the fracture behavior was evaluated under one loading direction only (pure traction).

Although using high resolution tomography to evaluate the failure behavior of porous ceramics, Berek et al. [33] and Petit et al. [34] independently identified the same fracture pattern as proposed by Genet et al. [21]. Recently, Cui et al. [35] also found the nonlinear mechanical behavior due to the accumulation of local damage in porous ceramics.

In different works, Brezny et al. [26] and Morgan et al. [36] studied the effect of the cell size of glassy porous ceramics on their mechanical properties. Both authors reported the mechanical

strength of cellular ceramics increased with decreasing cell sizes. They attributed this behavior to a reduction in the critical flaw size as well as the increasing strut strength in smaller cell sizes.

Meanwhile, Deng et al. [37] investigated the reinforcement mechanisms of fine- and coarse-grain porous SiC and found that the crack-tip blunting mechanism in porous material, as shown in **Figure 5**, increases the fracture toughness of the material. They also noted that the larger the pore size in front of the crack, the more the fracture toughness of the porous ceramic is relative to its fracture strength. However, a detailed discussion about the fracture toughness of porous ceramics is provided in the next section.

Based on the *Stress Concentration Design Factors,* Peterson [38], Deng et al. [37] and Rice [39] attributed this behavior to the interactions between pores. Rice [39] combined Peterson's data in **Figure 6** to show that the stress concentration diminishes significantly as the pores become closer and the pore interactions begin to no longer be negligible when the center-to-center distance between them is around two times their diameter. Specifically, for the case where pores touch each other, in porosity of 78%, **Figure 6** shows that the stress concentrations become very low.

In reviewing the literature about mechanical properties of porous ceramics, it can be summarized which parameters affect, and to what extent, the strength of this class of ceramic materials.

On the one hand, there are researches considering the pores as the stress concentrations for the material fracture. Therefore, these researches consider the mechanical properties of porous ceramics depend only on the relative porosity.

On the other hand, other researches have considered the interactions among pores as low as 10% of porosity, which reduce the stress concentration factor for fracture. Then, they take into account the mechanical properties of porous ceramics depend on pores-stress interactions.

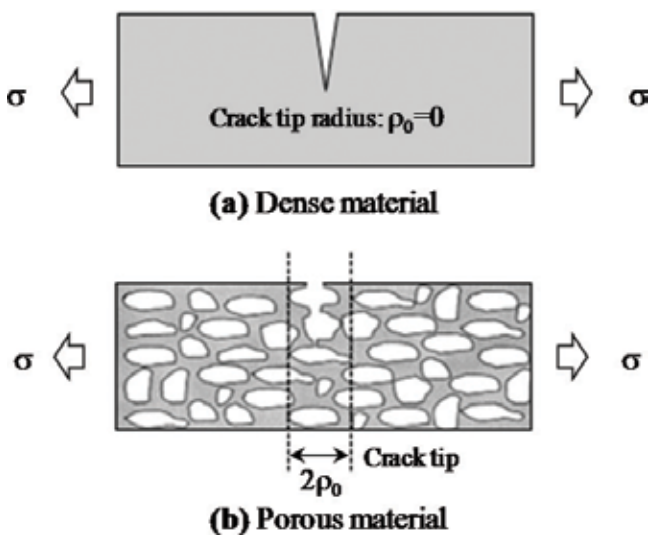

Figure 5. Representation of a crack propagated in (a) dense ceramic with a sharp crack-tip and in (b) porous ceramic where the crack-tip becomes blunt [37].

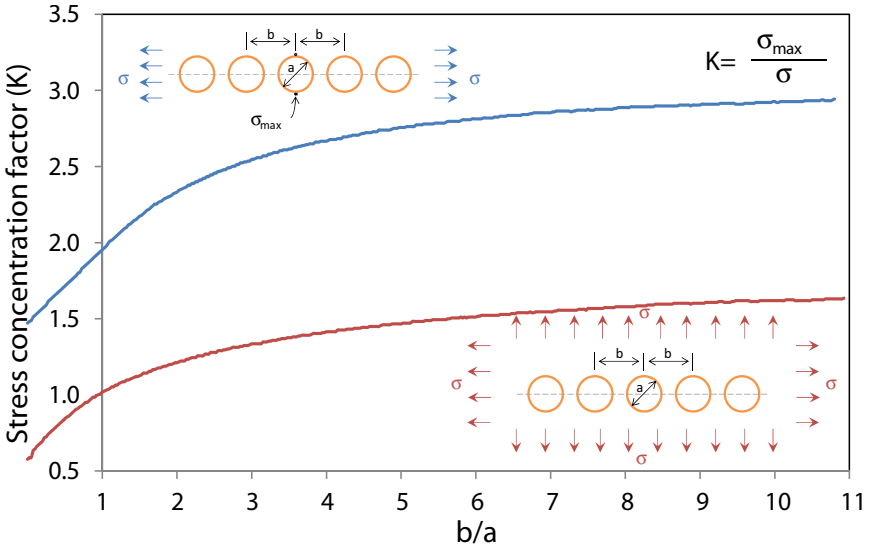

Figure 6. Stress concentration factors for a chain of holes in either uniaxial or in biaxial tension [38].

Regarding pore-stress interactions, there is strong evidence in the literature [40–42] concerning the mechanical behavior of human bones (also a quasi-brittle material) to support the hypothesis that microstructural changes in material may be essential in controlling its strength. The considered microstructural parameters are the porosity, size of pores, number and thickness of struts connecting the pores.

In human bodies, the mechanical properties of natural bone change with their biological location because the crystallinity, porosity and composition of bone adjust to the biological and biomechanical environment. For these materials, the bone volume fraction (bone volume BV/total volume TV) is given as a function of the thickness-to-length ratio, that is, t/ℓ, as shown in the following expression:

$$\frac{BV}{TV} = \frac{33\,\pi}{80\,\sqrt{2}}\left(\frac{t}{\ell}\right)^2 \tag{4}$$

Changes in the microstructure of the vertebral trabecular bone with aging have been quantified by histomorphometric analysis and also simulated by a computer using finite element software in two-dimensional (2D) [41] and three-dimensional (3D) [42] microstructural models. The microstructural changes of the bone include reductions in the trabecular thickness (t) and number (N), as shown in **Figure 7**. Both changes are strongly correlated with reductions in bone volume fraction and represent the two fundamental changes in microstructure associated with reduced bone volume [40–42].

Silva et al. [41] showed, using a 2D model, that once significant numbers of trabeculae (ligaments) are lost, it is impossible to recover the original mechanical properties of bone merely by increasing the trabeculae thickness, indicating the importance of the trabeculae number (N) and the integrity of its microstructure.

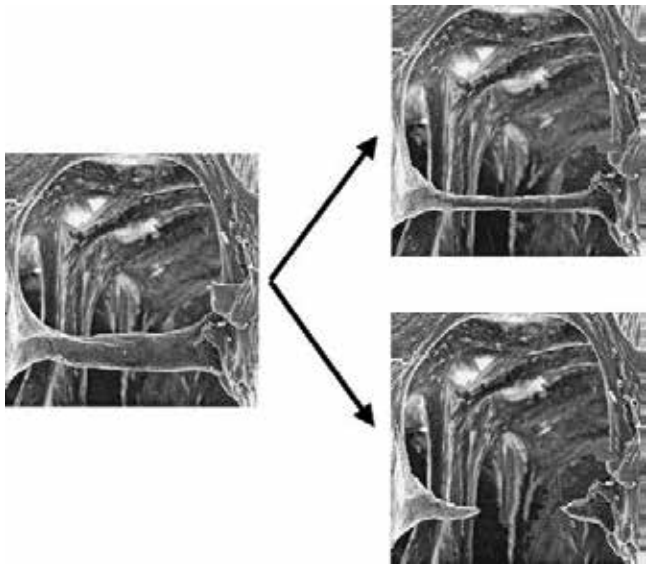

Figure 7. Simulated images of the trabecular bone showing two types of bone loss. Top right: thinning of trabeculae (ligaments) and bottom right: loss of trabeculae [42].

Considering the different types of trabeculae microstructures in 3D (rod-like and plate-like as shown in **Figure 8**), Guo et al. [42] quantified the changes in the Young's modulus and mechanical strength due to the trabecular bone loss. They considered the arrangement of tetrakaidecahedral cells as a 3D model for trabecular bones as shown in **Figure 8**. The cells filled in the 3D space were connected by either all beams (rod-like model) or all plates (plate-like model).

For each case of trabeculae loss simulation, the apparent Young's modulus and mechanical strength were normalized by the values of corresponding initial intact models (E_0 = 15 GPa, σ_0 = 100 MPa, Poisson's ratio of 0.3 at $t/\ell = 0.1$).

Quantitative relationships between mechanical strength and bone volume fraction (BV/TV) for the two types of bone loss in rod-like and plate-like models are presented in **Table 1** and **Figure 9**.

In the case of the rod-like model (**Figure 9a**), the loss of oblique trabeculae showed that the reductions in mechanical strength were more severe when the trabeculae thickness was reduced. In addition, after 13% loss of bone volume fraction (BV/TV), there was a dramatic reduction in strength due to the loss of the horizontal trabeculae.

For the plate-like model (**Figure 9b**), the reductions in mechanical strength due to trabeculae loss were also much more significant than those due to uniform trabeculae thinning. The quantitative relationships between the mechanical strength and bone volume fraction (BV/TV) due to trabeculae loss were dramatically different from those for trabeculae thinning (see **Table 1**).

These results suggest the importance of microstructural integrity such as the connectivity of the trabeculae bone architecture to maintain the mechanical integrity of bones. Besides, the extent of reduction in the mechanical properties due to trabeculae loss depends on the types of microstructures in the bone.

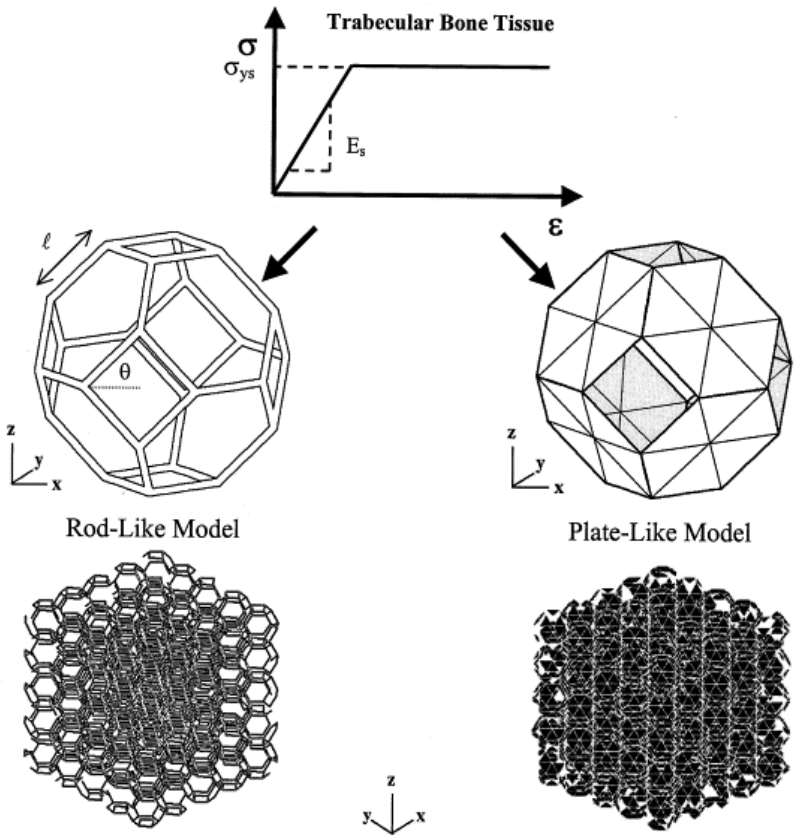

Figure 8. The 3D microstructural model of the trabecular bone. Each single cell has an edge of equal length, ℓ. θ = 45° for an isotropic structure. The entire model consists of arrays of 5 × 5 × 5 cells [42].

Model type	Bone loss type	Mechanical strength
Rod-like	Trabeculae thinning	$\frac{\sigma^*}{\sigma_0} = 0.592\ \left(\frac{BV}{TV}\right)^{1.60}$, $r^2 = 0.99$
Plate-like	Trabeculae thinning	$\frac{\sigma^*}{\sigma_0} = 0.378\ \left(\frac{BV}{TV}\right)^{1.10}$, $r^2 = 0.99$
Rod-like	Horizontal trabeculae loss	$\frac{\sigma^*}{\sigma_0} = 1.65x10^3\ \left(\frac{BV}{TV}\right)^{3.27}$, $r^2 = 0.85$
	Oblique trabeculae loss	$\frac{\sigma^*}{\sigma_0} = 4.69x10^{10}\ \left(\frac{BV}{TV}\right)^{6.94}$, $r^2 = 0.99$
Plate-like	Trabeculae loss	$\frac{\sigma^*}{\sigma_0} = 1.36x10^2\ \left(\frac{BV}{TV}\right)^{3.36}$, $r^2 = 0.99$

Table 1 Relationships between mechanical strength and bone volume (BV/TV) for two types of bone loss in rod-like and plate-like models [42].

Thus, for the natural bones, the number of ligaments (trabeculae) between pores appears to be much more effective to increase the strength of the material in comparison to the ligament thickness.

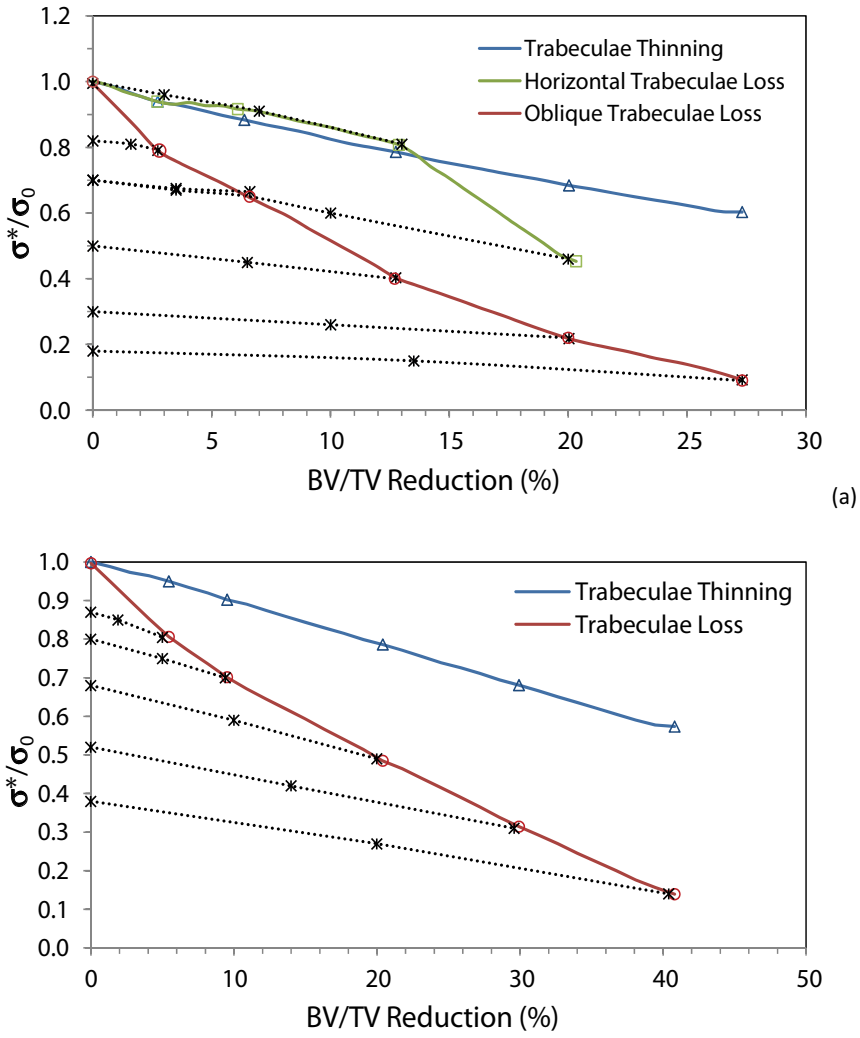

Figure 9. Reduction in the strength (a) of the rod-like model and (b) plate-like model due to bone loss (trabeculae thinning and trabeculae loss) represented by solid lines. Strength recovery by subsequent treatment with thickening trabeculae is represented by the dotted lines [42].

Lichtner et al. [28] also found the mechanical properties of freeze casting porous ceramics that are controlled by the connectivity of pore walls.

Similar mechanical behavior was reported by Salvini [43] for SiC ceramic filters of the same porosity (85%) but with different pores per inch (ppi), number of struts and average pore sizes (**Figure 10**). It can be seen in **Figure 10** that there is a rise in the number of connecting struts when the pore per inch (ppi) increases.

http://dx.doi.org/10.5772/intechopen.71612

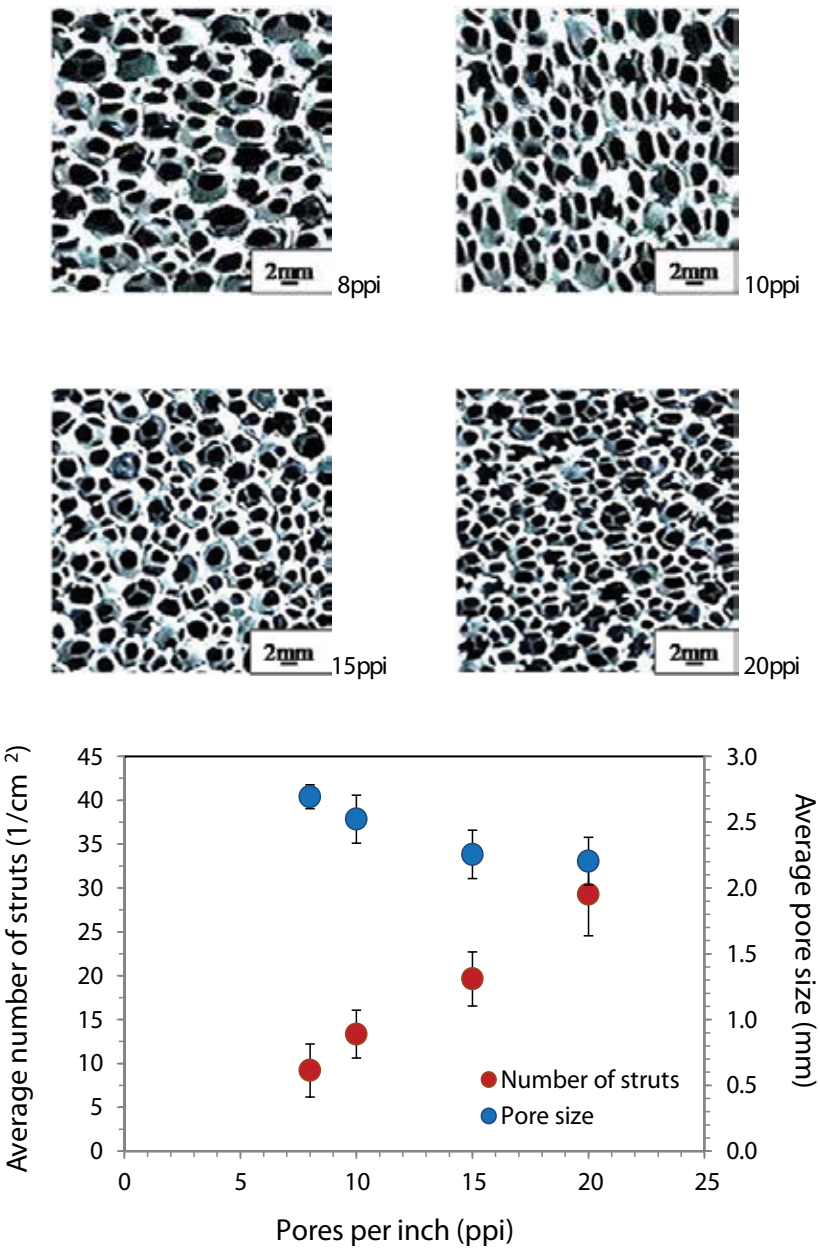

Figure 10. Physical characteristics of SiC ceramic filters of the same porosity (85%) but with different pores per inch (ppi) [43].

Moreover, differences were found between the strut number and pore size tendencies as a function of pores per inch (ppi). Interestingly, the number of connecting struts is sensitive to the variation of the number of pores (ppi).

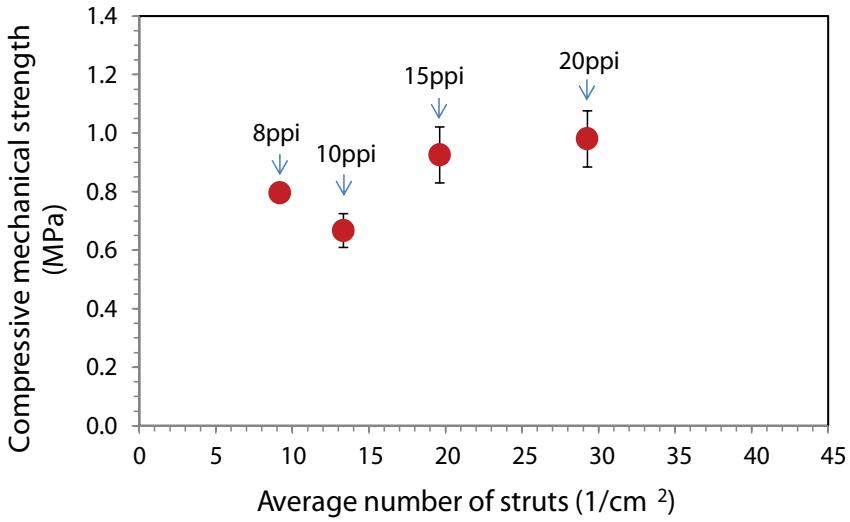

Figure 11. Compressive mechanical strength of SiC ceramic filters of the same porosity level (85%), but with different average pore sizes and number of connecting struts [43].

The high number of connecting struts in the SiC filters of high pores per inch (ppi) is more probably contributed to their increasing mechanical strength, as depicted in **Figure 11**.

A possible explanation for this mechanical behavior in SiC ceramic filters, as well as in trabeculae bones, might be the diminution of the stress concentration factor due to the stress-pore interactions, which is very low for porosity higher than 78% (see **Figure 6**).

One of the more significant findings to emerge from this section is that, in addition to the porosity of porous ceramics, the number of connecting struts between the cells/pores in the microstructure plays a fundamental role in their mechanical strength behavior.

3. Fracture toughness of porous ceramics

A requirement for almost structural materials is that they are both strong and tough yet invariably, in most materials, the properties of strength and toughness are mutually exclusive [44]. Whereas strength of material is a stress indicating its resistance to nonrecovery deformation, toughness is the resistance of material to the propagation of a crack and, then is measured as the energy required to cause fracture.

The ability of material to experience limited plastic deformation is a critical aspect to toughness, as this characteristic enables the local dissipation of high stress that would otherwise cause the fracture of material. That is the reason why the design methodology based on yield strength of materials is a common practice in the engineering [45].

Concerning fracture toughness (K_{IC}) methods for brittle ceramics, there are several tests which have been used such as the precrack by indentation, the single-edge notch beam (SENB) and

Chevron notch (CV) methods, which are the most common tests. All methods involve application of force to a beam test specimen in three or four point flexures.

Each method has limitations and the major problem is that significant effects due to the microstructure, for example, grain size and porosity, are not addressed in the continuum mechanics basis of these tests.

As proposed by Rice [46], the microstructural dependence of fracture energy (γ) comprehends the grain size (G), the composition, the porosity (P) and the combined effects of them.

Concerning the grain size effect, the crystalline structure of material is important when evaluating behavior between G and γ. Overall, the cubic materials present less variation of γ with G.

On the other hand, as shown in **Figure 12** for some noncubic ceramics, they present rising values of fracture energy (γ) until the maximum and, then, there is a decrease as the grain size (G) increases. This effect is attributed to the thermal expansion anisotropy, which occurs only in noncubic materials, but the intensity of it varies among materials [47].

Changes in the ceramic composition can also lead to a similar effect related to the grain size. These changes can be due to chemical composition or by introducing a more compliant grain boundary phase; both changes can modify the thermal expansion anisotropy affecting the fracture energy (γ) behavior of the material. There are several examples in the literature showing this behavior for Al_2O_3-ZrO_2 system, and SiC and Si_3N_4 with additions of oxides.

Although there are more limited data about the relation between fracture energy and porosity ($\gamma \times$ P) in comparison to fracture energy and grain size($\gamma \times$ G), some tendencies can be mentioned.

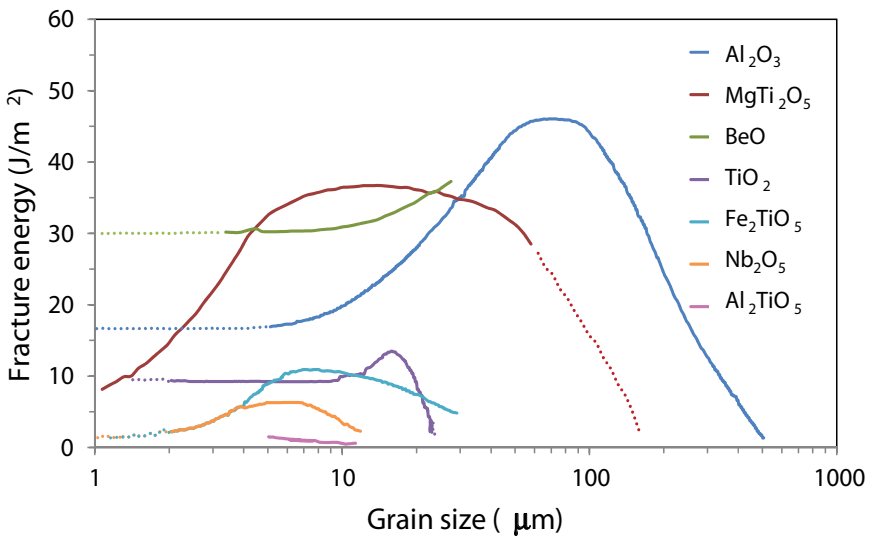

Figure 12. Fracture energy (γ) as a function of grain size (G) for noncubic oxide ceramics at 22°C [47].

At first, in single-phase ceramics with fine-to-medium-grain size, the fracture energy (γ) decreases as porosity (P) increases, following a similar tendency to the one found for mechanical strength (see **Figure 2**). Overall, this tendency has been shown in many advanced ceramics with porosity up to 50% [47].

Nevertheless, there are some works indicating the rate of fracture energy decrease can be reduced or even reversed [37, 47]. For instance, porous-fused SiO_2 (P~13–20%) provided fracture energy (γ) equal to or greater than the obtained value for dense SiO_2 glass.

Additional examples comprehend porous composite SiC-Al_2O_3-C (P~30–40%) and reaction sintered Si_3N_4 (P~45%). However, in all cases, the fracture energy (γ) decreased again at high porosity level (P) because the γ value goes to zero as P achieves 100%.

Considering there is not a consensus concerning the relation between fracture energy and porosity, we would like to propose a discussion about the influence of porosity on the fracture energy measurements of porous ceramics and, consequently, on their fracture toughness values.

Recently, Salvini et al.[43] have shown that fracture energy values for macroporous foamed Al_2O_3 can vary significantly depending on the test conditions. According to them, this is because of the following two factors: (1) the stress intensity factor at the notch tip may be decreased by the presence of surrounding pores (crack-tip blunting mechanism) as shown in **Figure 13** and (2) there is a strong interaction of cracks with the pores in the microstructure.

Although many researchers use a single test sample, Salvini et al. [48] carried out tests on separated notched macroporous samples for the two energy measurements γ_{eff} and γ_{WOF}. The

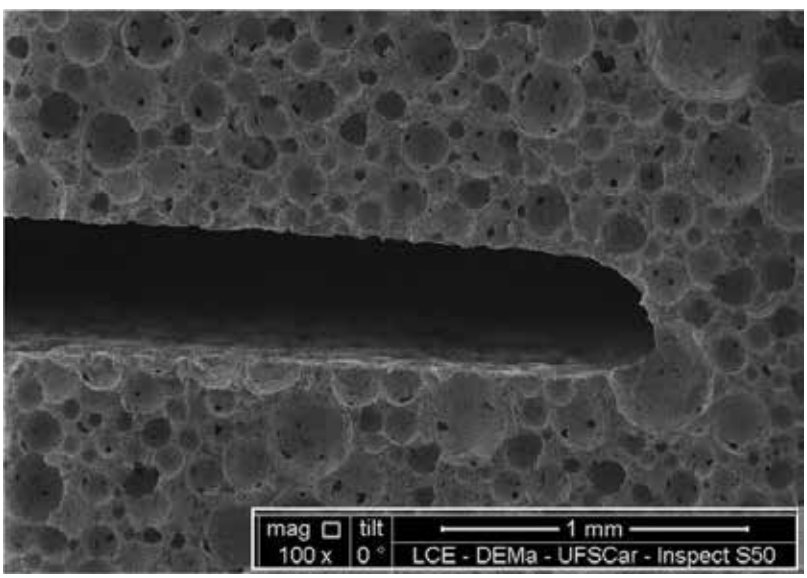

Figure 13. Macroporous foamed Al_2O_3 sample notched with a 300-μm thick diamond blade where the crack-tip blunting mechanism is shown [58].

γ_{eff} represents the fracture surface energy to initiate crack propagation, as proposed by Evans [49], whereas the total work-of-fracture γ_{WOF} expresses the energy to propagate a crack through the specimen thickness, as suggested by Nakayma [50]. A similar approach has been applied in evaluating fracture energy in materials with coarse microstructures, for example, in refractory ceramics [51, 52].

The fracture toughness (K_{IC}) was determined according to the ASTM E-399 at room temperature in a three-point bend test applying the equation:

$$K_{IC} = \frac{F \times S}{B \times W^{3/2}} \times f\left(\frac{a}{W}\right) \tag{5}$$

where F is the fracture load (N), S is the span (m), B is the specimen width, W is the specimen thickness, a corresponds to the crack size, and f (a/W) is obtained by the following expression:

$$f\left(\frac{a}{W}\right) = 3\sqrt{\frac{a}{W}} \times \frac{1.99 - \left(\frac{a}{W}\right) \times \left(1 - \frac{a}{W}\right)\left[2.15 - 3.93\frac{a}{W} + 2.7\left(\frac{a}{W}\right)^2\right]}{2\left(1 + 2\frac{a}{W}\right)\left(1 - \frac{a}{W}\right)^{3/2}} \tag{6}$$

The bar samples were center-notched to one-half of their thickness $(a/W \approx 0.5)$ with a 300-μm thick diamond blade for the K_{IC} measurements. All fracture energy tests were performed on a MTS 180 machine in three-point bending over a span of 125 mm. For K_{IC}, fracture surface energy (γ_{eff}) measurements were carried out at a stress loading rate of 1.5 kN/s.

This measured value of K_{IC} was then used to calculate the energy for crack initiation (γ_{eff}) by the expression:

$$K_{IC} = \left(2\gamma_{eff}E\right)^{1/2} \tag{7}$$

where E is Young's elastic modulus measured by a sonic technique in foamed Al_2O_3 bar samples (E = 18 GPa). Further details about this technique can be found in Ref. [53].

For the total work-of-fracture (γ_{WOF}) measurements, the foamed Al_2O_3 bar samples were also center-notched with a 300-μm thick diamond blade so that one-half of their thickness cross section remained. The samples were loaded in three-point bending at a crosshead speed of 0.001 mm/min to ensure stable crack growth (ASTM C1368–10). The total work-of-fracture (γ_{WOF}) values were then calculated by:

$$\gamma_{WOF} = \frac{\int F\,dx}{2\,A} \tag{8}$$

where $\int F\,dx$ represents the required work for new surfaces' generation and A is the projected area of the new fracture surfaces, as determined directly from the individual specimen notched areas.

Table 2 shows the obtained experimental results of the fracture energies (γ_{eff} and γ_{WOF}) and the fracture toughness (K_{IC}) for the foamed Al_2O_3.

Density, ρ (g/cm^3)	γ_{eff} (J/m^2)	γ_{WOF} (J/m^2)	K_{IC} (MPa.m$^{1/2}$)
0.86 ± 0.02	4.68 ± 0.5	15.81 ± 0.8	0.42 ± 0.03
0.87 ± 0.01	3.62 ± 0.3	14.46 ± 0.95	0.35 ± 0.05
0.90 ± 0.02	3.72 ± 0.6	15.39 ± 1.0	0.37 ± 0.02
0.92 ± 0.02	4.15 ± 0.8	12.27 ± 1.1	0.36 ± 0.02
0.94 ± 0.03	3.55 ± 0.35	13.32 ± 0.9	0.34 ± 0.09

Table 2 Results of fracture energies (γ_{eff} and γ_{WOF}) and the fracture toughness (K_{IC}) for macroporous foamed Al_2O_3 [58].

The K_{IC} values in **Table 2** were the expected ones for highly porous ceramics and they were compatible with data from the literature [24, 54, 55]. However, these results must be interpreted carefully, because of the crack-tip blunting mechanism due to the presence of surrounding pores (see **Figure 13**). This mechanism may decrease the stress intensity factor at the notch tip. Consequently, the crack propagation should not follow the required linear-elastic conditions for the fracture toughness measurement.

Based on that, we would like to raise the following issues: Does it make sense to measure the fracture toughness (K_{IC}) of porous ceramics knowing that the stress intensity factor at the notch tip is decreased by the crack-tip blunting? Or, instead of this, would the total work-of-fracture energy be a more realistic measure for these materials?

The results of total work-of-fracture energy (γ_{WOF}) presented in **Table 2** agree with the values obtained for Al_2O_3 produced using intermediate grain sizes (10–50 μm) [56].

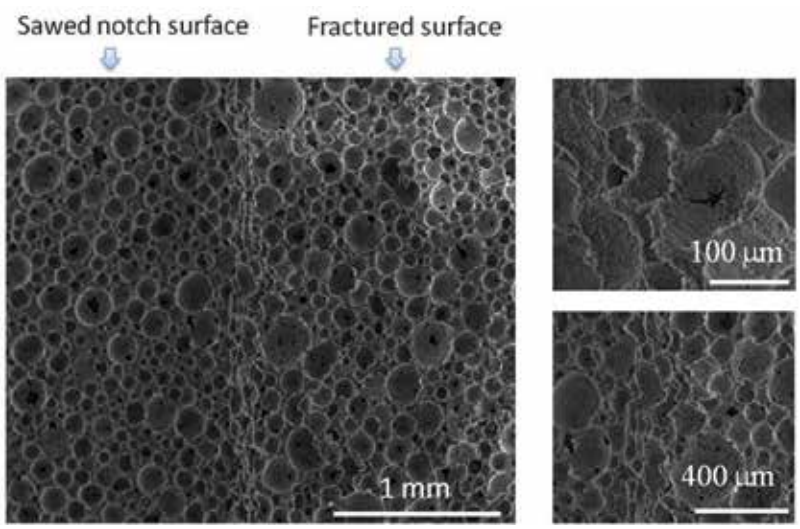

Figure 14. Fracture surface of macroporous foamed Al_2O_3 showing the characteristics of the fracture and notched surfaces [58].

Nevertheless, there is few data in the literature concerning fracture energies of porous ceramics. Kanhed et al. [57] found fracture toughness values in the range of 0.55–0.86 $MPa\ m^{1/2}$ for porous hydroxyapatite.

Considering the fracture surface microstructure of foamed Al_2O_3 presented in **Figure 14**, it seems that the fracture energy increase induced by porosity and the fracture energy reduction caused by decreased solid concentration are combined to describe the total work-of-fracture energy of material. However, more research on this topic is therefore recommended.

4. Elastic modulus behavior of porous ceramics

As well known, accurate elastic moduli are measured dynamically by measuring the frequency of natural vibrations of a beam, or by measuring the velocity of sound waves in the material. Both depend on $\sqrt{E/\rho}$, so if density (ρ) is known, E can be determined. These properties (ρ, E) reflect the mass of atoms, the way they are packed in material and the stiffness of the bonds that hold them together. For instance, **Table 3** presents the literature data of elastic modulus for several synthetic and natural porous brittle materials.

Considering that microscaled damage in ceramics can be caused in processing as well as during their application, a technique that detects the in situ microcracks evolution is important to estimate the life operation of them [65].

The *in situ* elastic modulus measurement as a function of temperature may identify the causes of microcracks in material, which is very helpful to adjust ceramic processing and design the material microstructure for an extended period of use.

Material	Porosity (%)	Elastic modulus (GPa)
Porous hydroxyapatite (HA) [5]	82–86	0.002–0.83
Cortical bone [5, 59, 60]	5–15	7–18
Cancellous bone [5, 59, 60]	~90	0.1–5
Cordierite diesel particulate filter (DPF) [54]	~50	12–13
Porous clay ceramics [55]	35–50	1–3
Silicon oxycarbide ceramic foams [24]	70–85	1–7
Porous SiC preforms [61]	30–65	30–120
Porous Si_3N_4 [62, 63]	35–55	45–105
Gelcasting Al_2O_3 foams [63]	60–85	10–65
Foamed Al_2O_3 [48]	76–80	15–18
SiC filters for metals [64]	85–92	2–3

Table 3. Elastic modulus values for porous and brittle materials.

In this context, this section is divided into two parts. In the first part, a review about theoretical models to describe the effect of porosity on the elastic modulus of porous ceramics is presented. Then, the second part presents and discusses the elastic modulus behavior as a function of temperature for the foamed Al_2O_3 ceramics.

Much research over the last decades was dedicated to understanding the influence of the porosity on the elastic modulus of ceramics. **Table 4** shows the most common theoretical models concerning the elastic modulus (E) and the porosity (P) correlations.

The Knudsen [66] and Rice [28] models fit well with real data of materials with porosity lower than 50%, as reported by Boccaccini et al. [67] and Ohji et al. [62, 63].

The model proposed by MacKenzie [68] and Kingery [69] is also defined for a lower level of closed pores.

Gibson and Ashby (GA) models [22, 23] indicated that the elastic modulus of a porous material depends only on its relative density and pore morphology.

Boccaccini model [67] introduced the *s* parameter to indicate the porosity geometry effect on the elastic modulus, that is, the pore shape and its orientation. However, it is valid only for low porosity level (P < 0.4) of closed pores.

In another work Boccaccini et al. [70] also included the topological parameters of highly porous microstructure to the model, besides the geometrical ones. Topological characterization comprehends the separation, the separated volume and the degree of contact and separation in two-phase microstructures. However, an issue that was addressed by the authors in this model is the necessity of a well-characterized porous structure of material, besides its porosity, to achieve rigorous verification of the model.

Model	**Characteristics**	
$E = E_0 e^{-bP}$ Refs. [28, 66]	Dependent on P and on extent of contact between solids	Valid for $P < 0.5$ and isotropic material
$E = E_0\ (1 - 1.9P + 0.9P^2), P \leq 0.5$ Refs. [67, 68]	Dependent on the closed pores' concentration	Valid for $P < 0.5$ and isotropic material
$E = C\,E_0\left(\frac{\rho}{\rho_s}\right)^n, C \approx 1\ and\ 1 < n < 2$ Refs. [22, 23]	Dependent on relative density and pore type	Valid for open porous and isotropic material
$E = E_0\left(1 - P^{2/3}\right)^s$ $s = 1.21\left(\frac{z}{x}\right)^{1/3}\left\{1 + \left[\left(\frac{z}{x}\right)^{-2} - 1\right]\right\}^{1/2}\cos^2\theta$ Ref. [67]	Dependent on P and on porosity geometry of closed pores	Valid for $P < 0.4$ and anisotropic material
$E = E_0\ \frac{(1-P)^2 R}{P+(1-P)R}$ $R = \frac{d_\beta}{d_\alpha}$, size ratio Ref. [69]	Dependent on P, on geometry and on topology of porosity	Valid for $R < 1$ and anisotropic material

Table 4 Summary of the elastic modulus (E) and porosity (P) models, where E_0 refers to the elastic modulus of solid material.

Overall, little research in the literature considers porous ceramics as anisotropic material in the evaluation of their elastic modulus behavior.

For instance, Rodrigues et al. [71] compared experimental data of the elastic moduli of Al_2O_3 foams (P: 60–90%) to several models proposed in the literature, as depicted in **Figure 15**. These authors considered the Al_2O_3 foams as isotropic material and, therefore, the experimental data fitted well with the MacKenzie [68] and Gibson and Ashby (GA) [22, 23] models.

This analysis, however, needs to be considered carefully because the foamed ceramics of high porosity (P > 60%) are usually anisotropic material and the mentioned models are valid only for homogeneous and isotropic ones.

Roy et al. [61], Wu et al. [59] and Lichtner [28] clearly showed that the extent of anisotropy, and its effect on the elastic modulus measurements, is strongly dependent on the porosity level, mainly for porosities higher than 40%, which is the case of the most foamed ceramics and natural porous materials.

Moving to the elastic modulus behavior at heating, Salvini et al. [48] evaluated the *in situ* elastic modulus behavior of foamed Al_2O_3 to identify the changes at the curing, drying and sintering stages of material.

The tests of elastic modulus were carried out in the range of temperature from 50 to 1400°C in air with heating and cooling rates of 2°C/min and a holding time of 4 h at 1400°C. After that, additional thermal cycles of elastic modulus measurements were carried out up to 1400°C.

Green bar samples (25 mm × 25 mm × 150 mm) of foamed Al_2O_3 containing 5 wt% of high alumina cement were considered for the *in situ* elastic modulus evaluation. The measurements

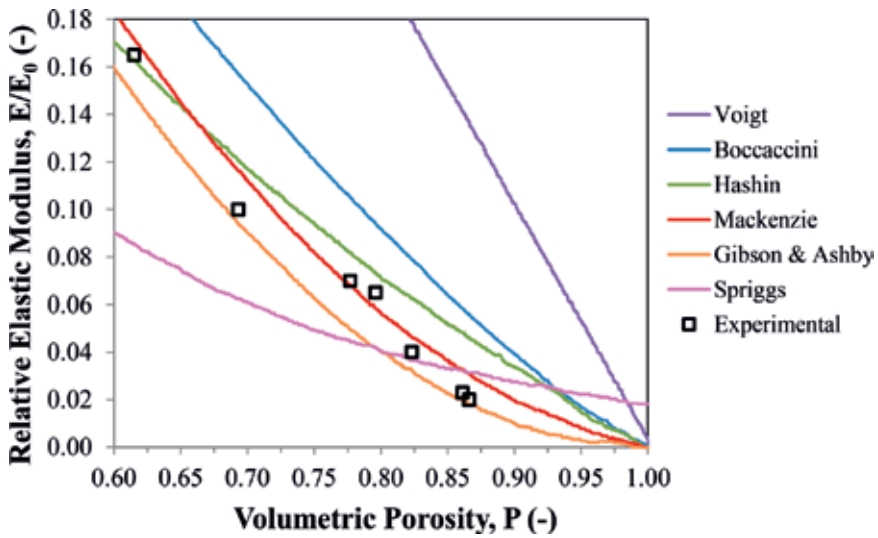

Figure 15. Theoretical models predicting the effect of porosity on the relative Young's modulus (continuous lines) and experimental data of gelcasting Al_2O_3 foams [71].

were carried out according to ASTM C1198–91 using the resonance bar technique (Scanelastic equipment, ATCP, Brazil).

Figure 16 depicts the in situ elastic modulus evolution (first and second cycles) up to 1400°C, in addition to results of the as-sintered foamed Al_2O_3 at 1500°C/4 h. **Table 5** presents the crystalline phase changes obtained by X-ray diffraction as a function of temperature for ceramic composition.

The foaming and casting processes of Al_2O_3 suspension were carried out at room temperature (~25°C). As reported by the literature [72], the main cement hydrate phase formed at room temperature is CAH_{10} ($CaO.Al_2O_3.10H_2O$). When the temperature increases, this phase partially dehydrates ~110°C into a mixture of gibbsite, AH_3 ($Al_2O_3.3H_2O$) and tricalcium aluminate hydrate, C_3AH_6 ($CaO.Al_2O_3.6H_2O$). This suggests that the drop of

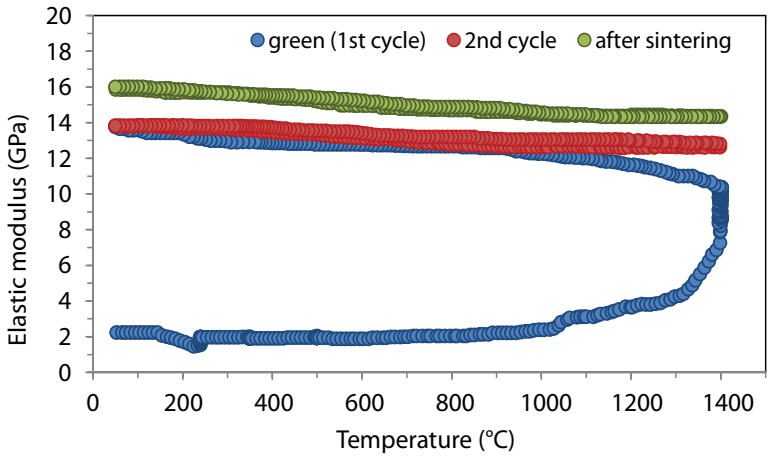

Figure 16. In situ elastic modulus of macroporous Al_2O_3: blue curve corresponds to the first cycle up to 1400°C of the green sample; the red curve is the measurement after the first cycle, and the green curve corresponds to the measurement after sintering up to 1500°C/4 h. The arrows indicate the discontinuities in the curve caused by decomposition or formation reactions of specific ceramic phases [48].

Crystalline phases	110°C	1000°C	1200°C	1400°C	1500°C
α-Al_2O_3	******	******	******	******	******
Al2O3.3H2O, AH3	**				
CaO. $Al_2O_3.6H_2O$, C_3AH_6	**				
$CaO.Al_2O_3$, CA		***	*		
$CaO.2Al_2O_3$, CA_2		*	***	****	*
$CaO.6Al_2O_3$, CA_6					***

Table 5 Phase changes obtained by X-ray diffraction in alumina composition containing 5 wt% of high alumina cement. The concentration of phases is qualitatively defined by the number of asterisks (*) displayed [48].

modulus curve observed in the initial stage of heating of the first cycle was caused by the conversion of CAH_{10}.

At higher temperatures, the discontinuities in the temperature range of 200–400°C were probably due to dehydration of the phases AH_3 ($Al_2O_3.3H_2O$) and C_3AH_6 ($CaO.Al_2O_3.6H_2O$), besides the decomposition of the organic additives (surfactants).

After dehydration, the elastic modulus remains stable at a low value until sintering starts at ~900°C. After 1100°C, the modulus increases rapidly due to sintering involving phase changes and formation of strong atomic bonds, which are characteristics of ceramic compositions.

At ~900°C, the CA ($CaO.Al_2O_3$) is the first crystalline phase formed, then it reacts with Al_2O_3 giving CA_2 ($CaO.2Al_2O_3$) at around 1100°C. The formation of CA_2 from CA and Al_2O_3 is expansive as a result of anisotropic growth of crystals [72].

At higher temperatures, the following two competitive phenomena occur: (1) expansion due to the formation of CA_2 phase and (2) shrinkage due to sintering of Al_2O_3 particles.

In the second cycle of measurement, no significant difference in the modulus curve was found in comparison with the first one.

In contrast, in case of sintering at 1500°C/4 h, the calcium hexa-aluminate CA_6 ($CaO.6Al_2O_3$) phase is additionally formed due to a reaction of CA_2 with Al_2O_3, which starts at ~1450°C. The formation of CA_6 is also expansive, leading to a superior elastic modulus of material.

Finally, when cooling the modulus curves remained stable without discontinuities, indicating an absence of microcracking of material.

These findings enhance the understanding not only about the role of specific additives (surfactants and inorganic binders) but also about the crystalline phase transformations and corresponding dimensional changes at sintering of macroporous ceramics. These results have important implications for developing porous ceramics with superior mechanical properties.

5. Summary

This chapter reviews the mechanical properties of porous ceramics with special interest on the mechanical strength, fracture toughness and elastic modulus of these materials.

One of the more significant findings to emerge from analysis of mechanical strength section is that, in addition to the porosity of porous ceramics, the number of connecting struts between the cells/pores in the microstructure plays a fundamental role in their mechanical strength behavior. Data from the literature support that once the connecting struts are lost in the porous structure, it is impossible to recover the original mechanical strength of it by merely increasing the struts thickness.

Regarding to fracture toughness of porous ceramics, two factors appear to control this property: the presence of surrounding pores at the crack front and the interaction of cracks with the pores in the microstructure.

Finally, the in situ hot elastic modulus analysis appears as an important method to better understand the processing steps as well as for predicting the life operation of this class of ceramic materials.

Author details

Vânia Regina Salvini[1]*, Victor C. Pandolfelli[2] and Dirceu Spinelli[3]

*Address all correspondence to: vr.salvini@gmail.com

1 College of Technology FATEC Sertãozinho, Sertãozinho, Brazil

2 Materials Engineering Department, Materials Microstructure Engineering Group GEMM, Federal University of São Carlos UFSCar, São Carlos, Brazil

3 Materials Engineering Department, EESC-USP São Carlos, São Carlos, Brazil

References

[1] Salvini VR, Innocentini MDM, Pandolfelli VC. Optimizing permeability, mechanical strength of ceramic foams. The American Ceramic Society Bulletin. 2000;**79**(5):49-54

[2] Sutton WH, Palmer JC, Morris JC. Development of ceramic foam materials for filtering high temperature alloys. AFS Transactions. 1985;**51**:339-346

[3] Salvini VR, Luz AP, Pandolfelli VC. High temperature Al_2O_3-CA_6 insulating foamed ceramics: Processing and properties. Interceram. 2012;**6**:335-339

[4] Sato M, Tomohide T, Kohji K, Akihiro S. Energy saving of slab reheating furnaces by improvements of refractories. In: Proceedings of the ACerS Unified International Technical Conference of Refractories (UNITCER´13); 10–13 September. Victoria Island, Canada: ACerS; 2013. pp. 333-338

[5] Rezwan K, Chen QZ, Blaker JJ, Boccaccini AR. Biodegradable and bioactive porous polymer/inorganic composite scaffolds for bone tissue engineering. Biomaterials. 2006;**27**:3413-3431. DOI: 10.1016/j.biomaterials.2006.01.039

[6] Jones JR, Hench LL. Regeneration of trabecular bone using porous ceramics. Current Opinion in Solid State and Materials Science. 2003;**7**:301-307. DOI: 10.1016/j.cossms.2003.09.012

[7] Teraoka K, Kato T, Hattori K, Ohgushi H. Evaluation of the capacity of mosaic-like porous ceramics with designed pores to support osteoconduction. Journal of Biomedical Materials Research Part A. 2013;**101**(12):3571-3579. DOI: 10.1002/jbm.a.34663

[8] Oyanedel-Craver VA, Smith JA. Sustainable colloidal-Silver-impregnated ceramic filter for point-of-use water treatment. Environmental Science & Technology. 2008;**42**(3):927-933. DOI: 10.1021/es071268u

[9] Pia G, Canedi L, Ionta M, Sanna U. On the elastic deformation properties of porous ceramic materials obtained by pore-forming agent method. Ceramics International. 2015; **41**:11097-11105. DOI: 10.1016/j.ceramint.2015.05.057

[10] Yang C, Zhang G, Xu N, Shi J. Preparation and application in oil-water separation of ZrO_2/α-Al_2O_3 MF membrane. Journal of Membrane Science. 1998;**142**:235-243. DOI: 10.1016/S0376-7388(97)00336-0

[11] Arcos D, Vallet-Regí M. Bioceramics for drug delivery. Acta Materialia. 2013;**61**:890-911. DOI: 10.1016/j.actamat.2012.10.039

[12] Treccani L, Klein T Y, Meder F, Pardun K, Rezwan K. Functionalized ceramics for biomedical, biotechnological and environmental applications. Acta Biomaterialia. 2013;**9**(7):7115-7150. DOI: 10.1016/j.actbio.2013.03.036

[13] Warren SC, Perkins MR, Adams AM, Kamperman M, Burns AA, Arora H, Herz E, Suteewong T, Sai H, Li Z, Zwanziger JW, Graetzel M, Disalvo FJ, Wiesner U. A silica sol-gel design strategy for nanostructured metallic materials. Nature Materials. 2012;**11**:460-467. DOI: 10.1038/nmat3274

[14] Suzuki Y, Hwang H J, Kondo N, Ohji T, In situ processing of a porous calcium Zirconate/Magnesia composite with Platinum nanodispersion and its influence on nitride oxide decomposition. Journal of the American Ceramic Society. 2001;**84**(11):2713-2715. DOI: 10.1111/j.1151-2916.2001.tb01079.x

[15] Bradt RC. Fracture mechanics of brittle ceramics – 30 years of progress. In: Salem A, Quinn GD, Jenkins MG, editors. Fracture Resistance of Monolithic and Composite Brittle Materials. West Conshohocken, PA: ASTM; 2002. pp. 3–13

[16] Zhang D, Zhang W, Gu J, Zhu S, Su H, Liu Q, Fan T, Ding J, Guo Q. Bio-inspired functional materials templated from nature materials. KONA Powder and Particle Journal. 2010;**28**:116-130. DOI: 10.14356/kona.2010011

[17] Ritchie RO. Armoured oyster shells. Nature Materials. 2014;**13**:435-437. DOI: 10.1038/nmat3956

[18] Meyers MA, Mckittrick J, Chen P-Y. Structural biological materials: Critical mechanics-materials connections. Science. 2013;**339**:773-779. DOI: 10.1126/science.1220854

[19] Fukasawa T, Ando M, Ohji T, Kanza S. Synthesis of porous ceramics with complex pore structure by freeze-dry processing. Journal of the American Ceramic Society.2001;**84**(1):230-232. DOI: 10.1111/j.1151-2916.2001.tb00638.x

[20] Launey ME, Munch E, Alsem DH, Barth HB, Saiz E, Tomsia AP, Ritchie RO. Designing highly toughened hybrid composites through nature-inspired hierarchical complexity. Acta Materialia. 2009;**57**:2919-2932. DOI: 10.1016/j.actamat.2009.03.003

[21] Genet M, Couégnat G, Tomsia AP, Ritchie RO. Scaling strength distributions in quasi-brittle materials from micro- to macro-scales: A computational approach to modeling nature-inspired structural ceramics. Journal of Mechanics and Physics of Solids. 2014;**68**:93-106. DOI: 10.1016/j.jmps.2014.03.011

[22] Ashby MF. The mechanical properties of cellular solids. Metallurgical Transactions A. 1983;**14**(9):1755-1769. DOI: https://doi.org/10.1007/BF02645546

[23] Gibson LJ, Ashby MF. Cellular solids – Structure and properties. 2nd ed. Cambridge: Cambridge University Press; 1999. ISBN-13: 978-0521499118

[24] Colombo P, Hellmann JR, Shelleman DL. Mechanical properties of silicon oxycarbide ceramic foams. Journal of the American Ceramic Society. 2001;**84**(10):2245-2251. DOI: 10.1111/j.1151-2916.2001.tb00996.x

[25] Seeber BSM, Gonzenbach UT, Gauckler LJ. Mechanical properties of highly porous alumina foams. Journal of Materials Research. 2013;**28**(17):2281-2287. DOI: 10.1557/jmr.2013.102

[26] Brezny R, Green DJ. The effect of cell-size on the mechanical behavior of cellular materials. Acta Metallurgica et Materialia. 1990;**38**(12):2517-2526. DOI: 10.1016/0956-7151(90)90263-G

[27] Salvini VR, Spinelli D, Pandolfelli VC. Mechanical behavior of foamed insulating ceramics. In: Ohji T, Matyás J, Manjooran NV, Pickrell G, Jitianu A, editors. Advances in Materials Science for Environmental and Energy Technologies III. New Jersey, USA: John Wiley & Sons; 2014. pp. 89-99. ISBN: 978-1-118-99668-3

[28] Lichtner A, Roussel D, Jauffres D, Martin CL, Bordia RK. Effect of macropore anisotropy on the mechanical response of hierarchically porous ceramics. Journal of the American Ceramic Society. 2016;**99**(3):979-987. DOI: 10.1111/jace.14004

[29] Brezny R, Green DJ, Dam CQ. Evaluation of strut strength in open-cell ceramics. Journal of the American Ceramic Society.1989;**72**(6):885-889. DOI: 10.1111/j.1151-2916.1989.tb06239.x

[30] Rice RW. Evaluation and extension of physical property-porosity models based on minimum solid area. Journal of Materials Science. 1996;**31**:102-118. DOI: 10.1007/BF00355133

[31] Bruno G, Kachanov M. Microstructure-property connections for porous ceramics: The possibilities offered by micromechanics. Journal of the American Ceramic Society. 2016;**99**(12):3829-3852. DOI: 10.1111/jace.14624

[32] Zheng M, Zheng X, Luo ZJ. Fracture strength of brittle porous materials. International Journal of Fracture. 1992;**58**:51-55. DOI: 10.1007/BF00015623

[33] Berek H, Halkova J, Aneziris CG. Characterization of cellular ceramics and MMC by in situ computed tomography. In: Presentation at the International Conference on Modern Materials and Technologies (13th CIMTEC), 8–13 June, Montecatini Therme, Italy: ECerS. 2014

[34] Petit C, Meille S, Maire E, Tadier S, Adrien J. Mechanical behavior of β-TCP ceramic with a random porosity: Study of the fracture path with X-ray tomography. Journal of the European Ceramic Society. 2016;**36**:3225-3233. DOI: 10.1016/j.jeurceramsoc.2016.05.001

[35] Cui Z, Huang Y, Liu H. Predicting the mechanical properties of brittle porous materials with various porosity and pore sizes. Journal of the Mechanical Behavior of Biomedical Materials. 2017;**71**:10-22. DOI: 10.1016/j.jmbbm.2017.02.014

[36] Morgan JS, Wood JL, Bradt RC. Cell size effects on the strength of foamed glass. Materials Science and Engineering. 1981;**47**:37-42. DOI: 10.1016/0025-5416(81)90038-0

[37] Deng Z-Y, She J, Langaki Y, Yang J-F, Ohji T, Tanaka Y. Reinforcement by crack-tip blunting in porous ceramics. Journal of the European Ceramic Society. 2004;**24**:2055-2059. DOI: 10.1016/S0955-2219(03)00365-0

[38] Peterson RE. Stress Concentration Design Factors. New York: John Wiley Inc.; 1953

[39] Rice RW. Limitations of pore-size concentrations on the mechanical properties of porous materials. Journal of Materials Science. 1997;**32**:4731-4736. DOI: 10.1023/A:101867471

[40] Morgan EL, Bouxsein ML. Biomechanics of bone and age-related fractures. In: Bilezikian JP, Raisz LG, Martin TJ, editors. Principles of Bone Biology. Vol. I. 3rd ed. Academic Press; 2008. pp. 29-51. ISBN: 0-12-098653-1

[41] Silva MJ, Gibson LJ. Modeling the mechanical behavior of the vertebral trabecular bone: Effects of age-related changes in microstructure. Bone. 1997;**21**(2):191-199. DOI: 10.1016/S8756-3282(97)00100-2

[42] Guo XE, Kim CH. Mechanical consequence of trabecular bone loss and its treatment: A three-dimensional model simulation. Bone. 2002;**30**(2):404-411. DOI: 10.1016/S8756-3282(01)00673-1

[43] Salvini VR. Processing and evaluation of fluid dynamic and thermomechanical properties of ceramic filters in the Al_2O_3-SiC system [thesis]. São Carlos: Federal University of São Carlos; 2000

[44] Ritchie RO. The conflicts between strength and toughness. Nature Materials. 2011;**10**:817-822. DOI: 10.1038/nmat3115

[45] Ashby MA, Sherliff H, Cebon D. Materials Engineering, Science, Processing and Design. 1st ed. Burlington, UK: Butterwoth-Heinemann; 2007. pp. 164-181

[46] Rice RW. Test-microstructural dependence of fracture energy measurements in ceramics in Fracture Mechanics for Ceramics. In: Freiman SW, Fuller Jr ER, editors. Rocks and Concrete. West Conshohocken: ASTM; 1982

[47] Rice RW. Grain size and porosity dependence of ceramic fracture energy and toughness at 22°C. Journal of Materials Science. 1996;**31**:1969-1983

[48] Salvini VR, Lasso PRO, Luz AP, Pandolfelli VC. Nontoxic processing of reliable macroporous ceramics. International Journal of Applied Ceramic Technology. 2016;**13**(3):522-531. DOI: 10.1111/ijac.12521

[49] Evans AG. Energies for crack propagation in polycrystalline MgO. Philosophical Magazine. 1970;**22**(178):841-852. DOI: 10.1080/14786437008220952

[50] Nakayama J, Abe H, Bradt RC. Crack stability in the work-of-fracture test: Refractory applications. Journal of the American Ceramic Society. 1981;**64**(11):671-675. DOI: 10.1111/j.1151-2916.1981.tb15868.x

[51] Sakai M, Ichikawa H. Work-of-fracture of brittle materials with microcracking and crack bridging. International Journal of Fracture. 1992;**55**:65-79

[52] Salvini VR, Pandolfelli VC, Bradt RC. Extension of Hasselman's thermal shock theory for crack/microstructure interactions in refractories. Ceramics International. 2012;**38**:5369-5375. DOI: 10.1016/j.ceramint.2012.03.046

[53] Pickett G. Equations for computing elastic constants from flexural and torsional resonat frequencies of vibration of prisms and cylinders. In: Proceedings of the Portland Cement Association ASTM. 1945;**45**:846-865

[54] Shyam A, Lara-Curzio E, Watkins TR, Parten RJ. Mechanical characterization of diesel particulate filter substrates. Journal of the American Ceramic Society. 2008;**91**(6):1995-2001. DOI: 10.1111/j.1551-2916.2008.02381.x

[55] Yakub I, Du J, Soboyejo WO. Mechanical properties, modeling and design of porous clay ceramics. Materials Science & Engineering A. 2012;**558**:21-29. DOI: 10.1016/j.msea.2012.07.038

[56] Doerre E, Huebner H, Alumina: Processing, Properties, and Applications. 1st ed. Berlin: Springer-Verlag Press; 1984. 329 p. ISBN: 3-540-13576-6

[57] Kanhed S, Awasthi S, Goel S, Pandey A, Sharma R, Upadhyaya A, Balani K. Porosity distribution affecting mechanical and biological behavior of the hydroxyapatite bioceramic composite. Ceramics International 2017,**43**:10442–10449. DOI:10.1016/j.ceramint.2017.05.083

[58] Salvini VR, Spinelli D, Pandolfelli VC. Thermomechanical properties of macro-porous alumina. In: Presentation at the ECerS International Conference on Modern Materials and Technologies (13th CIMTEC), 8–13 June, Montecatini Therme, Italy: ECerS; 2014

[59] Wu S, Liu X, Yeung KWK, Liu C, Yang X. Biomimetic porous scaffolds for bone tissue engineering. Materials Science and Engineering R. 2014;**80**:1-36. DOI: 10.1016/j.mser.2014.04.001

[60] Dong XN, Guo XE. The dependence of transversely isotropic elasticity of human femoral cortical bone on porosity. Journal of Biomechanics. 2004;**37**:1281-1287. DOI: 10.1016/j.jbiomech.2003.12.011

[61] Roy S, Schell K G, Bucharsky E C, Weidenamann K A, Wanner A, Hoffman M J. Characterization of elastic properties in porous SiC performs fabricated using polymer waxes as pore formers. Journal of the American Ceramic Society. 2013;**96**(7):2269-2275. DOI: 10.1111/jace.12341

[62] Yang J-F, Ohji T, Kanzaki S, Díaz A, Hampshire S. Microstructure and mechanical properties of silicon nitride ceramics with controlled porosity. Journal of the American Ceramic Society. 2002;**85**(6):1512-1516. DOI: 10.1111/j.1151-2916.2002.tb00305.x

[63] Ohji T. Microstructural design and mechanical properties of porous silicon nitride ceramics. Materials Science and Engineering A. 2008;**498**:5-11. DOI: 10.1016/j.msea.2007.09.104

[64] ERG Materials and Aerospace Corporation. 2017. Available from http://www.ergaerospace.com/SiC-properties.htm [Accessed: 2017-11-01]

[65] Yonezy A, Chen X. Micro-scale damage characterization in porous ceramics by an acoustic emission technique. Ceramics International. 2014;**40**(7):9859-9866. DOI: 10.1016/j.ceramint.2014.02.079

[66] Knudsen FP. Dependence of mechanical strength of brittle polycrystalline specimens on porosity and grin size. Journal of the American Ceramic Society. 1959;**42**(8):376-387. DOI: 10.1111/j.1151-2916.1959.tb13596.x

[67] Boccaccini AR, Fan Z. A new approach for the Young's modulus – Porosity correlation of ceramic materials. Ceramics International. 1997;**23**:239-245. DOI: 10.1016/S0272-8842(96)00033-8

[68] Mackenzie JK. The elastic constants of a solid containing spherical holes. Proceedings of Physical Society B. 1950;**63**(1):2-11. DOI: 10.1088/0370-1301/63/1/302

[69] Kingery WD, Bowen HK, Uhlmann DR. Introduction to Ceramics. 2nd ed. USA: John Wiley & Sons; 1976. pp. 773-781. ISBN: 0-471-47860-1

[70] Boccaccini DN, Boccaccini AR. Effect of pore shape on the ultrasonic velocity-porosity correlation in sintered materials. Journal of Materials Science Letters.1997;**16**:623-625. DOI: 10.1023/A:101850703

[71] Rodrigues JA, Ortega FS, Paiva AEM, Villaboim ELG, Pandolfelli VC. The relation between porosity and elastic moduli of gelcast ceramic foams. Cerâmica. 2004;**50**:209-216. DOI: 10.1590/S0366-69132004000300007

[72] Nonmet E, Lequeux N, Boch P. Elastic properties of high alumina cement castables from room temperature to 1600°C. Journal of the European Ceramic Society.1999;**19**:1575-1583

Chapter 11

Shock Compression of Porous Ceramics

Yin Yu and Hongliang He

Additional information is available at the end of the chapter

http://dx.doi.org/10.5772/intechopen.72246

Abstract

Shock compression is a challenge for porous ceramics in application. In this chapter, numerical simulation and experimental observation have been introduced, which reveals generation of crack, damage, and fracture within porous ceramics upon shock wave loading. Simulation of a two-dimensional lattice-spring model explains the effects of voids and grain boundaries on the mesoscopic deformation features of shocked porous ceramics. Experiments confirm the fracture and fragmentation evolution in the post-shock ceramics. These understandings are conducive to the design, manufacture and usage of the porous ceramics under rapid impulsive loading. Furthermore, the concept of controllable fracture is proposed, which is a strategy to modulate the propagation of shock fracture in porous ceramics for the avoidance or delay of the shock-induced functional failure. It is evidenced that a "shielded region," i.e., free of severe shock fracture, could be formed with the sacrifice of a "damaged region" in the porous ceramics.

Keywords: porous ceramics, shock compression, lattice-spring model, deformation mechanisms, damage shielding

1. Introduction

Shock wave loading is generated often at impact, collision, and blast. A shock wave is a powerful amplifier of defects in that it activates pre-existing defects (e.g., microvoids, cracks, and grain boundaries), extends cracks, and breaks media. The main challenge of porous ceramics in the application upon shock wave loading is its nonstationary behavior due to crack, damage, and fracture of the heterogeneous structure [1–4]. Mechanical, electrical, and optical properties of ceramics are severely affected by shock waves, and consequently, it may deteriorate the designed functions of shocked ceramics, such as in the cases of high-strength ceramics for armor [5], piezoelectric and ferroelectric ceramics for converting mechanical energy to electrical energy [6–8] and transparent ceramics for optical measurements in shock experiments [9].

Hence, a good understanding of the dynamic response of porous ceramics under rapid impulsive loading is vital to the design, manufacture, and usage of these materials. To this objective, a two-dimensional lattice-spring model (LSM) has been newly established, and the shock compression behavior of porous ceramics is explored and the mechanisms and strategies for improving robustness are discussed.

2. Model of porous ceramics under shock wave compression

Dynamic response of porous ceramics under rapid impulsive loading relates to evolution of a crack network following the shock wave. Although some pioneer works have been conducted on modeling ceramic shock fracture via mesh-based computational methods [10–13], such methods encounter significant difficulties when dealing with fracture and fragmentation induced by shock wave compression. The reason is that partial derivatives are used in mesh-based methods to represent the relative displacement and force between any two neighboring particles [14]. But, the necessary partial derivatives with respect to the spatial coordinates are undefined along the cracks and need to be redefined. However, the redefinition requires us to know where the discontinuity is located. This limits the usefulness of these methods in addressing problems involving the spontaneous formation of cracks, in which one might not know their location in advance [14]. In contrast, as a particle method, the lattice-spring model (LSM, also known as discrete-element method) [15–20] could avoid various numerical difficulties caused by displacement discontinuity. In this section, details of the LSM model (lattice interactions, spring mapping procedure, fracture criterion, microstructures, loading) and its validation are introduced.

2.1. Lattice-spring model

A two-dimensional LSM was established to explore the shock behavior of porous ceramics. In the LSM, continuum medium is described as discrete material particles. The nearest neighboring particles are interconnected and interact through springs. Evolution of this network can represent the global response of macroscopic materials, if the interactions of material particles are described accurately. Through simplifications of real materials and the model's discrete nature, LSM has the advantage in treating fracture, fragmentation, and other dynamic damage processes of brittle materials subjected to tension, compression, shear, and other complex loading [17].

The model established here has an elastic-brittle interaction, which ignores the small plasticity contribution to the response that possibly exists in brittle materials; only a linear elastic interaction is used. Particle interaction is shown in **Figure 1**. Between pairs of nearest-neighbor particles, indexed by i and j, there are the central potential forces f_{ij}^{n} and the shear resistance forces f_{ij}^{τ}. They could be visualized as forces provided by a normal spring that lies along the normal direction and a shear spring that lies along the tangent direction.

An energy threshold based on Griffith's energy balance principle [21] has been used as the fracture criterion. The summation of the deformation energy induced by tension in the normal spring and shear in the shear spring is calculated when the relative position between two neighboring particles changes. And the two springs break irreversibly to create a microcrack between the two

http://dx.doi.org/10.5772/intechopen.72246

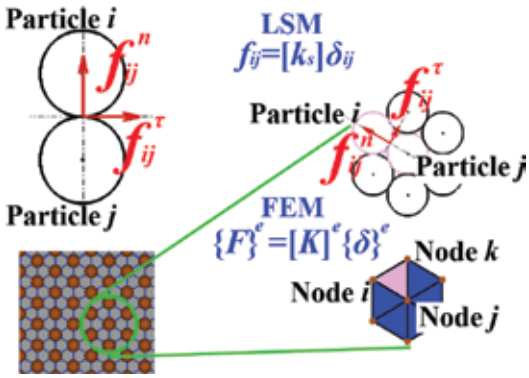

Figure 1. Particle interaction in the LSM model and schematic of the parameter mapping procedure.

particles, when the sum exceeds a certain threshold corresponding to the fracture energy. The deformation energy induced by compression in the normal spring will not be counted in this criterion, because it is assumed that hydrostatic compression would not cause fracture in the homogeneous media. When the microcrack forms between two particles, tension and shear interactions are removed; however, repulsion and friction interactions exist, when the broken particles come into collision.

2.2. Parameter mapping procedure

The parameters used in the interaction formulae of LSM were usually given empirically, resulting in a qualitative representation of mechanical properties of target materials. Several outstanding studies have been done to overcome this shortcoming [14–16, 22–25]. Gusev proposed a parameter mapping procedure between finite-element method (FEM) and LSM [26]: consider a network that is both a LSM lattice and a FEM mesh; first, elastic constants of the target material are transformed into stiffness matrix of the FEM mesh; next, using the same network, the interaction-parameter conversion between FEM and LSM is performed (**Figure 1**).

To obtain the deformation state for the FEM mesh, the force-displacement equations assembled from all elements need to be solved, that is,

$$\{F\} = [K]\{\delta\} \tag{1}$$

where $\{F\}$ and $\{\delta\}$ are the respective column vectors formed from the external forces and displacements of all nodes. The so-called global stiffness matrix $[K]$ is a sparse symmetric matrix, which is determined by elastic constants of the material and geometrical structure of the mesh. Under the equilibrium state, the internal force f_i acting on node i can be written, according to Eq. (1), as

$$f_i = -F_i = -\left(K_{i1}\times\delta_1 + K_{i2}\times\delta_2 + \cdots + K_{ii}\times\delta_i + \cdots + K_{ij}\times\delta_j + \cdots + K_{iN}\times\delta_N\right) \tag{2}$$

Since motion of translation would not change the strain energy of the whole system, Eq. (3) holds between elements of the matrix $[K]$ [26],

$$K_{ii} = -\sum_{\substack{x=1 \\ x\neq i}}^{N} K_{ix} \tag{3}$$

Using K_{ii}, Eq. (3) could be rearranged as

$$\begin{aligned} f_i &= -\left[K_{i1}\times\delta_1 + K_{i2}\times\delta_2 + \cdots + \left(-\sum_{\substack{x=1 \\ x\neq i}}^{N} K_{ix}\times\delta_i\right) + \cdots + K_{ij}\times\delta_j + \cdots + K_{iN}\times\delta_N\right] \\ &= -\left\{\left[K_{i1}\times(\delta_1-\delta_i)\right] + \left[K_{i2}(\delta_2-\delta_i)\right] + \left[K_{ij}(\delta_j-\delta_i)\right] + \left[K_{iN}(\delta_N-\delta_i)\right]\right\} \\ &= \sum_{\substack{x=1 \\ x\neq i}}^{N} K_{ix}(\delta_i-\delta_x) = \sum_{\substack{x=1 \\ x\neq i}}^{N} f_{ix} \end{aligned} \tag{4}$$

The resultant internal force f_i is the sum of the forces from all the neighbor particles (1, 2,…, j,…, N; i excluded). Hence, the internal force acting on particle i by particle j is

$$f_{ij} = K_{ij}\left(\delta_i-\delta_j\right) = K_{ij}\delta_{ij} \tag{5}$$

where $\delta_{ij} = \delta_i - \delta_j$. Eq. (5) has the form of Hooke's law. The K_{ij} could be taken as the stiffness coefficients of the springs of the LSM.

2.3. Model validation

In order to validate the parameter mapping procedure, dense and porous samples have been built and tested. Young's modulus, E_0 = 250 GPa; shear modulus, G_0 = 104 GPa; and density $\rho = 5\times10^3\,\mathrm{kg/m^3}$ are set into the lattice-spring networks of those samples. Samples with porosity 0, 2, 4, 6, 8, and 10% are subjected to quasi-static compression and tension. The maximum and minimum strains are 0.1 and −0.1%, respectively. Young's modulus of the dense sample is 251 GPa, which is in good agreement with the preset E_0 [17]. In porous samples, Young's modulus decreases with the porosity increasing.

Shear wave speeds (C_s) of dense and porous samples have been obtained via acoustic velocity tests. Then, the shear modulus $G = \rho C_s^2$ could be calculated. For the dense sample, shear modulus is 105 GPa, which is almost the same with the preset G_0 [17]. As the porosity increases, shear modulus decreases. In rock physics, the elastic property of rock with spherical pores could be estimated from [27]

$$\beta_{eff}(\eta) = \beta_s\left(1+\frac{3(1-\nu_s)}{2(1-2\nu_s)}\frac{\eta}{1-\eta}\right) \tag{6}$$

where β_s is the compression coefficient (the inverse of bulk modulus) of the dense medium, β_{eff} the effective compression coefficient of the porous medium, ν_s Poisson's ratio of the dense medium, and η porosity. With

$$G(\eta) = \frac{3E(\eta)}{\left(9 - \beta_{eff}(\eta)E(\eta)\right)} \tag{7}$$

together with $\beta_{eff}(\eta)$ estimated from Eq. (6) and Young's moduli $E(\eta)$ obtained from the simulation, the shear moduli $G(\eta)$ of the porous samples could be worked out. G/G_0 extracted directly from acoustic velocity tests are in good agreement with G/G_0 estimated via Eq. (7) [17]. Thus, the parameter-mapping procedure is verified as having the capability of representing elastic properties of both dense and porous brittle medium quantitatively.

2.4. Microstructures and shock wave loading

To capture the influence of grain boundaries (GBs) on porous ceramics, polycrystalline sketching has been randomly produced using Voronoi tessellation [10]. As shown in **Figure 2(a)**, particles (small circles) in the model are assigned into grains (large polygons). If two particles connected by springs belong to different grains, then the springs are assumed to be a small segment of a GB. Given that media on GBs have higher energy state than media in grains, the deformation energy required for creating a pair of new crack surfaces on GBs is smaller than that in grains. The energy threshold on GBs is given as $U_S^{GB} = U_S^{grain} - E^{GB}$, where U_S^{grain} and E^{GB} are the threshold in a grain and the additional energy that exists on GBs, respectively. **Figure 2(b)** shows the distribution of U_s in grains and GBs. Most GBs are high-angle GBs (red lines), which are much weaker than grains (blue media). A few GBs are low-angle GBs (green, yellow, and brown lines), which have various thresholds according to their relative angles.

Voids are set by removing portions of the model particles (**Figure 2(c)**). In the model, the balance distance between nearest neighbor particles is 1 μm, characteristic size of the grains is 10 μm, and the diameter of a round void is 50 μm. The length of the model along the shock direction is 1.6 mm. The model is illustrated schematically in **Figure 3**. A piston composed of two columns of particles is set on the left-hand side of the model; it moves with piston velocity (v_p) towards the right and produces a shock wave, which propagates from the left to the right. In order to reduce computational cost, periodic boundary conditions are applied on the upper and lower boundaries. Free boundary condition has been applied on the right side. At appointed simulation steps, evolution information such as particles' coordinates, velocities, stresses, springs' forces and connection states will be recorded.

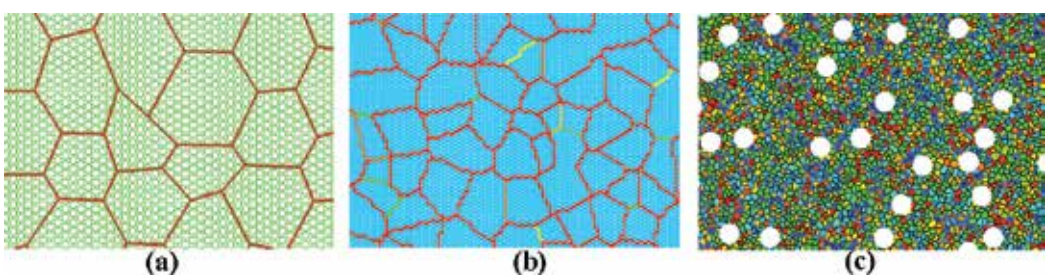

Figure 2. (a) Sketch of polycrystalline model. (b) Fracture energy set in the polycrystalline model. (c) Sketch of porous ceramics. White circles are randomly distributed voids and small colored dots are grains.

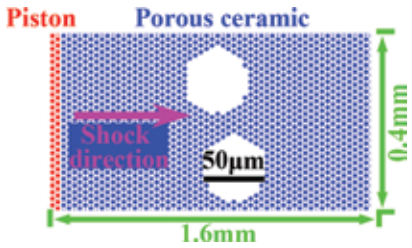

Figure 3. Schematic of the shock wave compression model for porous ceramics.

3. Mechanisms of damage and deformation in shocked porous ceramics

A shock wave relates to a high-power pulse, in which stress and the energy are sufficient to vanquish toughness of ceramics. It would activate pre-existing defects (e.g., microvoids, cracks, and grain boundaries), extends cracks, and breaks media. Mechanical, electrical, and optical properties of ceramics are severely affected by shock waves [28–30], and consequently, it may deteriorate the designed functions of ceramics. Hence, revealing the mechanisms of damage and deformation in shocked porous ceramics would be a foundation for modulation of shock behavior and enhancement of robustness of the porous ceramics involving shock applications. In this section, the effects of voids and grain boundaries on the mesoscopic deformation features of shocked porous ceramics have been explored and compared with shock experiments with the recovery of shocked porous ceramics. Microscope photographs of voids in the recovered sample have been analyzed and compared with computational results. A novel mechanism of slippage and rotation deformation has been revealed, which contributes to and enhances inelastic deformation of the shocked brittle materials. As the pressure increases, the rotational deformation becomes a universal and important mechanism for relieving shear stress and dissipating strain energy.

3.1. Void collapse under shock wave compression

Simulations reveal that void collapse is initiated from severe shear stress concentrations around the void after the shock sweeps through. When media far from the void experience a mild shear stress, media in four corners around the void achieve the fracture criterion. **Figure 4** shows an isolated void that swept by a shock wave. Four shear cracks extend from the void, and broken fragments fill into void along shear cracks and occupy the free volume.

To validate the computational results, shock experiments with the recovery of shocked porous ceramics have been implemented [31]. The lead zirconate titanate (PZT) ceramic has been used, which is a ferroelectric ceramic and generates megawatts of electrical power in a short period of time via a ferroelectric-to-antiferroelectric phase transformation driven by the shock wave from a high-explosive. Unpoled samples have been used, which have no bound charge and charge releasing under the shock experiments. Voids in the ceramics were introduced during fabrication by adding spherical polymethyl methacrylate particles. As shown in **Figure 5(a)**,

http://dx.doi.org/10.5772/intechopen.72246

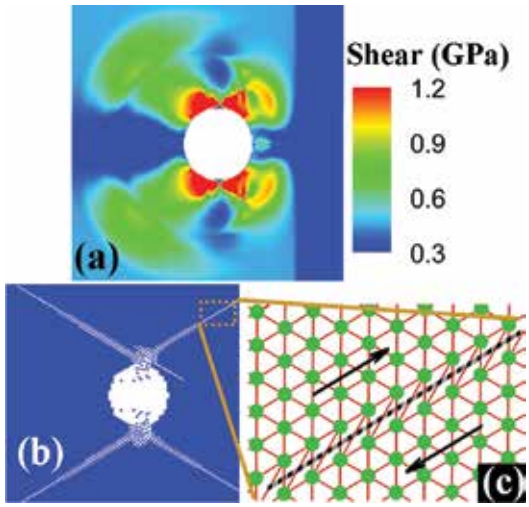

Figure 4. Mesoscopic mechanisms of shock plasticity in porous brittle material. (a) Distribution of the maximum resolved shear stress when shock wave has just swept through a void. (b) A snapshot of shear cracks extension around the void after shock wave has swept through. (c) Relative slippage and rotational deformation revealed in post-shocked region.

the voids in sintered ceramics have diameters of ~50 μm. Bulk density of the samples is determined using the Archimedes method, and the sample porosity is calculated from the ratio of the bulk density to the theoretical density (ρ_0 = 8010 kg/m^3). The sample porosity is 9.3%.

In the recovery experiment, one wants to recover porous ceramic that contains shock compression fracture, and this fracture should only be produced by high-speed impact between the flyer and the target. Therefore, a momentum trap (**Figure 5(b)**), which has the same shock impedance as the ceramic, is needed to bear the intense dynamic tension produced by rarefaction waves and to fly away alone carrying most of the momentum input by the flyer. **Figure 5(c)** shows an incised sample: an integral recovered ceramic (yellow) is conserved in a brown brass packet. Samples are polished and acid etched before scanning electron microscopy (SEM) studies.

Figure 6 shows comparison of void collapse features observed in the model with an isolated void and recovered porous ceramics. Long-distance extended cracks that are emitted from voids are an important feature in the model (**Figure 6(a)**). **Figure 6(b)** shows representative

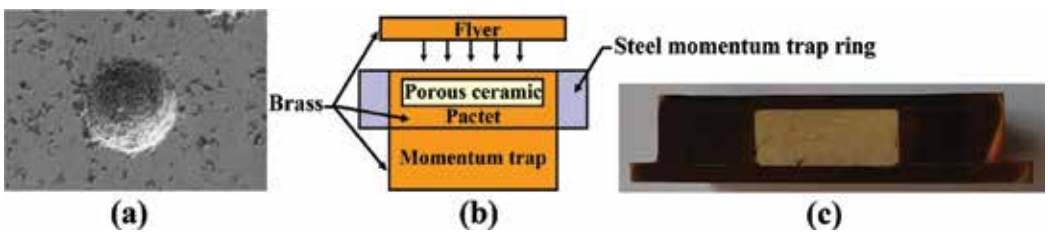

Figure 5. (a) Microscopic observation of a void in initial porous lead zirconate titanate ceramic. (b) A schematic of the shock experiment with recovery of the shocked porous ceramics. (c) Cross section of a recovered sample.

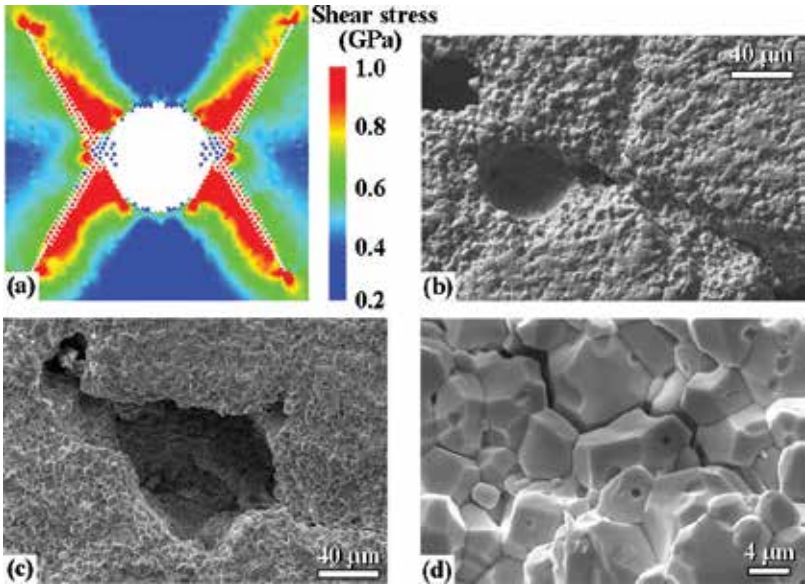

Figure 6. (a) Shear cracks emit from the void because of shear stress concentrations after the exposure to a shock wave. (b) Long-distance extended cracks and (c) thick cranny are observed representative mesoscopic deformation features. (d) Minor crack advances along GBs.

long cracks in the recovery sample subjected to 3.3 GPa compression. The extended crack directions deviate from those around the modeled isolated void (**Figure 6(a)**), and only two cracks are emitted. In **Figure 6(c)**, no long crack exists around this void; instead, a thick crevice forms at the top left corner of the void. It can be deduced that numerous grains in this area were damaged by multicracks and were scaled off during polishing to form such a feature. Many cracks that advance along GBs of porous PZT ceramic have been observed (**Figure 6(d)**). Hence, a more complex model, including multivoid and GBs, would be needed to reproduce these damaged features.

3.2. Characters of shear cracks around collapsing voids

Features of void collapse and shear fracture obtained from the polycrystalline model containing multivoid have been analyzed. In **Figure 7(a)**, fragments of grains fill a damaged void, and long shear cracks extend from the void. All fragments have been removed in **Figure 7(b)** to compare with experimental observations (**Figure 7(c)**). In **Figure 7(d)**, a wide area on the bottom left corner of the void has been damaged during crack evolution. When all fragments have been removed, a thick crevice is visible (**Figure 7(e)**), which is comparable with the deformation feature observed experimentally (**Figure 7(f)**). **Figure 7(g–i)** compares damage features between two voids. A few minor cracks, which are similar to the intergranular crack in **Figure 6(d)**, exist around all the voids in the polycrystalline model.

The polycrystalline model also reveals the evolution of long cracks and thick crevices. For long cracks, an initially transgranular crack translates into an intergranular cracks after a certain propagation range. The translation should occur when the crack-driving force is decreased to a

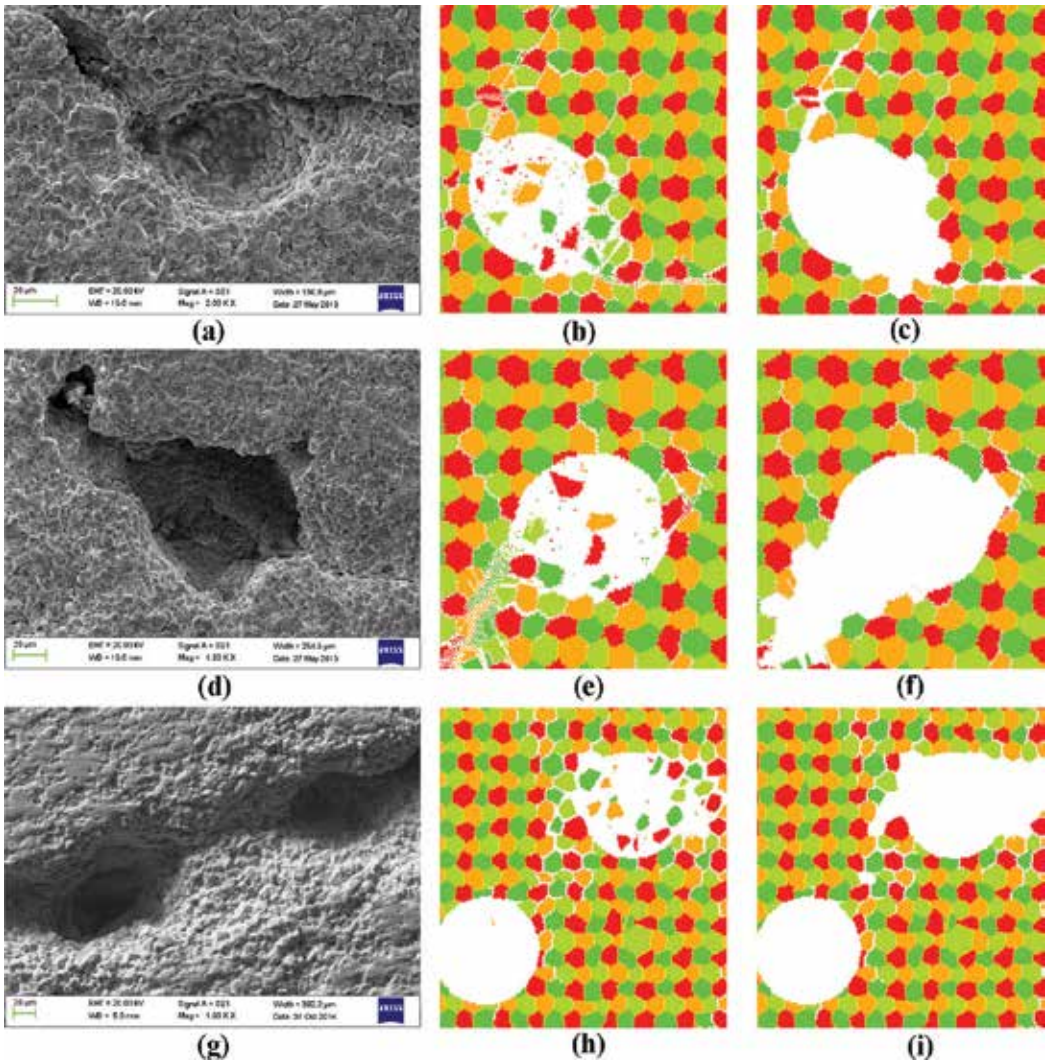

Figure 7. Comparison of deformation features observed in the polycrystalline model and recovery sample. (a)–(c) Representative long-distance extended shear cracks. (d)–(f) Representative thick crevices. (g)–(i) Crack transfixion between two voids.

value that cannot support transgranular fractures. This fracture mode is termed "transgranular-to-intergranular crack mode." However, intergranular cracks branch from the main transgranular crack during main crack propagation to form thick crevices. This fracture mode is termed "main (transgranular) crack and branching (intergranular) cracks mode." Media in a wide area will be damaged in this fracture mode, and a thick crevice becomes visible after fragments have been removed.

What is the dominant factor that leads to these two different fracture modes? As shown in **Figure 7(d)**, the main crack comminutes media in a wide area during its propagation. The thickness of the main transgranular crack is ~10 μm. The violent extension of the main crack

implies that the crack-driving force is very strong. The branching of numerous intergranular cracks from the main transgranular crack may be attributed to the need for more effective shock energy dissipation.

3.3. Slippage and rotational deformation of shatters

A novel mechanism of slippage and rotation deformation, which contributes to and enhances inelastic deformation of the shocked brittle materials, has been revealed by this model. In shocked porous ceramic, numerous shear cracks are emitted during void collapse, forming a crack network. As a consequence, the media are comminuted into scattered tiny shatters by interlaced cracks. When the field of the relative velocity in these comminuted regions is drawn (**Figure 8**), the arrows (which indicated the relative velocities and directions of media) revealed complex vortex structures, showing that the shatters were slipping and rotating under shock [17]. The complex vortex structures indicate that the network composed of shear cracks takes a similar role to that of shear bands in high-strength high-toughness metallic glasses [32, 33]. They provide the precondition for relative slippages of media and irreversible deformation of the sample.

The rotational deformations of different types of materials have been reported in shock and static high-pressure investigations carried out by experiments and simulations [34–38]. For example, nickel nanoparticles were found to rotate in a diamond anvil cell when the pressure rose from 3 GPa to more than 38 GPa. When the particle sizes were various from 500 nm down to 3 nm, the measurements indicated that more active grain rotation occurs in the smaller nickel nanocrystals. Investigations here and in literatures about rotational deformation of various materials and loading conditions indicate that it becomes a universal and important deformation mechanism under high pressure to help the loaded systems to relieve shear stress and dissipate strain energy, when other usual deformations (e.g., dislocation, twinning) are absent or repressed [38, 39].

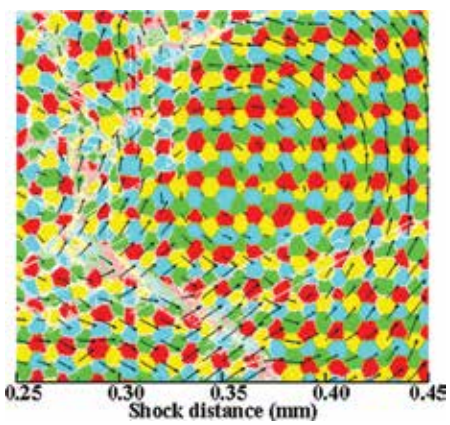

Figure 8. Slippage and rotation of shatters induced by extending shear cracks.

4. Design of energy absorbing and fracture control in shocked porous ceramics

Pre-existing defects in ceramics induce shock wave compression fractures and may lead to the failure of designed functions. One traditional strategy for failure prevention has been by sintering "defect-free" ceramics (e.g., a large, perfect single-crystal sample). However, such treatment by sintering is difficult in practice and costly in expense, and more importantly, it only increases the critical emergence stress of shock fracture rather more than eliminating the probability of shock failure. Adopting an approach that is the opposite of creating defect-free ceramics, one may be able to control shock fracture and avoid the shock failure of ceramics by properly introducing defects. The control of shock fracture by introducing defects may seem counterintuitive. However, under quasi-static loading, there have already been many successful cases in which defects are introduced to avoid catastrophic fracture. In nature, highly mineralized natural materials owe their exceptional toughness and quasi-ductility to microscopic building blocks, weak interfaces and architecture [40–42]. In engineering, the fracture toughness of "hard and brittle" glass and metal glasses has been increased by properly introducing microcracks and voids [43–45]. These mechanisms can be summarized as crack shielding, deflection, and bridging, which effectively reduce the crack-driving force [46]. In shock applications, however, the difference is that a shock wave relates to a high-power pulse. The stress and the energy input are sufficient to vanquish various toughening strategies. Hence, numerous cracks nucleate and grow inevitably. In this case, strategies for toughening brittle materials cannot be duplicated. Instead, a novel approach in addressing shock fracture is proposed, i.e., modulating the propagation of crack network in shocked ceramics by deliberately adding pores.

4.1. Control of the fractured region

Mesoscopic damage and deformation evolutions (void collapse, shear fracture, and rotational deformation) induced significant stress relaxation, leading to macroscopic "plastic" response, although the model particles and springs did not contribute to plasticity (only a linear elastic interaction was set in springs of the model). Note that here plasticity is taken in its broadest sense; it is identified not by dislocation movements, but by the macroscopic stress-strain curve and irreversible deformations. **Figure 9** shows the correlation between macroscopic plasticity and mesoscopic damage evolution. Initially, a steep shock front is induced by the impact of the piston. The shock front broadens and splits into two waves during propagation inside a sample. The precursor wave is an elastic wave, which propagates with longitudinal acoustic speed. The second wave, which corresponds to an irreversible deformation, is usually termed the deformation wave (it is called plastic wave in ductile metals). The propagation speed of the deformation wave is slower than the elastic wave; thus, a plateau is produced between these two waves. After the deformation wave, the final equilibrium state, namely the Hugoniot state, is achieved. The deformation wave and the following plateau (the Hugoniot state) correspond to a "severely fractured state (SFS)," where shear fracture, void collapse, and rotational deformation of comminuted media are processed abundantly [10]. Note that the deformation wave and

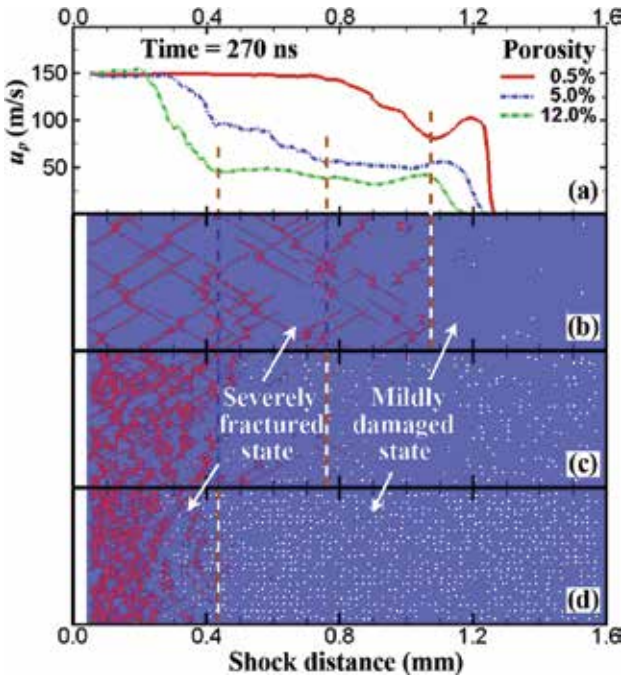

Figure 9. Comparison of (a) shock wave profiles and (b–d) damage distributions in dense, 5, and 12% porous ceramics, respectively.

the SFS propagate synchronously. If the deformation wave is unloaded, then, without enough energy to maintain damage evolution, the SFS would be "frozen." This is the foundation for modulating shock fracture.

Figure 10 shows schematics of controlling shock fracture. A traditional strategy for doing it is sintering "fully dense" ceramics (**Figure 10(a)**). Evolution of a dense sample with only 0.5%

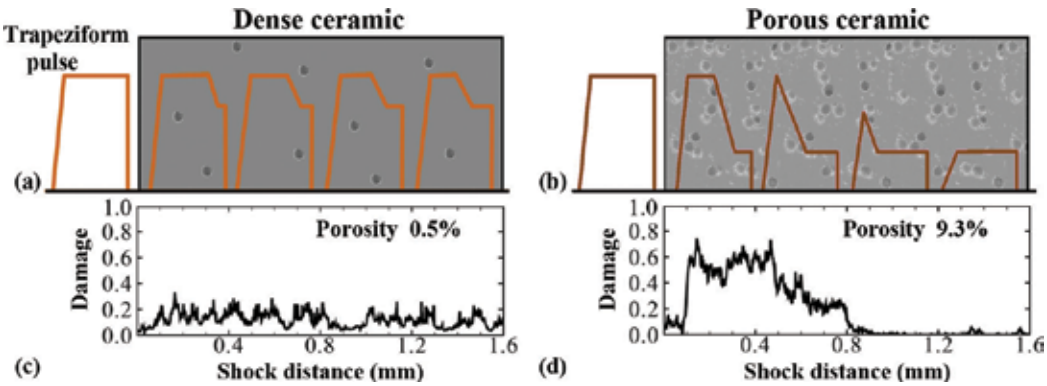

Figure 10. Schematic of short pulse evolutions in (a) dense ceramic (with 0.5% porosity) and (b) porous ceramic (with 9.3% porosity). Degrees of damage of (c) dense and (d) porous samples at 800 ns after impact.

porosity was therefore simulated; **Figure 10(c)** shows that its average degree of damage is reduced to ~0.1, but the damage is distributed throughout the sample. An alternative approach is worth looking for. Instead of sintering fully dense ceramics, a new idea is to make use of the pores. As shown in **Figure 10(b)**, voids are deliberately added in the ceramic; **Figure 10(d)** shows the degree of damage of a porous sample with 9.3% porosity (it is the porosity of PZT ceramics used in experiments) after sufficient evolvement: half of the porous sample has an average damage of ~0.4, and the other half of the sample is almost intact. A "shielded region" is acquired at the cost of severe fracture in the other parts of the sample (the "damaged region").

The design of controlling fractured region is based on the following mechanism: (1) the deformation wave would be slowed down by the deliberately increased porosity; (2) if the pulse is short compared with the thickness of the sample, then a rarefaction wave (the "trailing edge" of a stress pulse of shock) would catch up and unload the slow deformation wave; (3) the SFS would be frozen after the deformation wave vanishes, rather than sweep through the entire sample. After that, the ceramic will undergo elastic compression and stay in a mildly damaged state.

4.2. Validation by LSM simulation

Figure 11(a) shows the configuration of the model to investigate whether voids can protect part of a sample away from the SFS. In one of the simulation runs, the porosity of the sample is 9.3% and the velocity of the flyer v_f=300 m/s, which induces a ~5 GPa shock stress. The ultimate damage distribution after sufficient evolvement is shown in **Figure 11(b)**. Half of the sample is in the SFS, whereas the other half is basically intact. **Figure 11(c)** plots three shock wave profiles at three midterm times. At 130 ns after impact, an elastic wave-deformation wave-rarefaction wave structure has formed; at 240 ns, the rarefaction wave has caught the deformation wave; at 350 ns, the deformation wave has unloaded completely, and the SFS should be frozen at that time. Indeed, the boundary between the damaged region and shielded region at 800 ns in **Figure 11(b)** matches the position where the deformation wave vanished in **Figure 11(c)**.

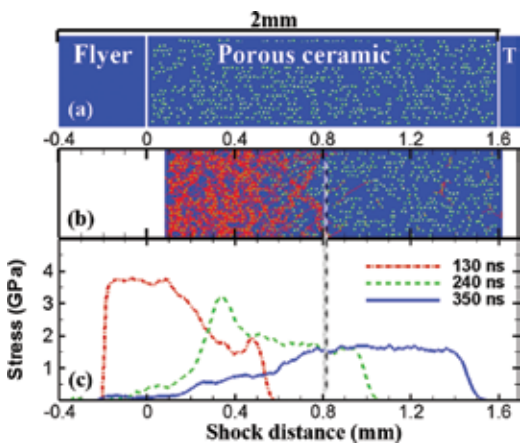

Figure 11. Mechanism of earning a shielded region where the severely fractured state will not enter. (a) Configuration of the model. T refers to a very long momentum trap. (b) Damage distribution in the sample at 800 ns. (c) Stress wave evolution at three midterm times.

Damage evolutions of dense, 5, and 12% porous ceramics have been further simulated and their ultimate damage distributions after the flyer impact at 300 m/s are compared. **Figure 12** plots the void collapse ratio $r_{collapse}$ for all samples. The samples are divided into segments; the $r_{collapse}$ is calculated from the ratio of the number of collapsed voids to the total number of voids in each segment. The boundary between the damaged region and shielded region corresponds to a rise of $r_{collapse}$ from 0 to 1. For the same shock stress and the pulse width, as the porosity increases, the thickness of the shielded region increases accordingly. The dense ceramic has no shielded region, whereas the 12% porous ceramic has a shielded region of about 1 mm.

4.3. Validation by soft recovery experiment

Figure 13(a) and **(e)** shows the fracture characteristics of the sample subjected to a compression of 3.3 GPa and that of 1.4 GPa, respectively. Each image is composed of 19 SEM frames, which are successively scanned along the "scanned area" marked in **Figure 13(b)**. The image has a width of 766 μm and a length of nearly 8 mm. The direction of the shock wave propagation is from the left of the image to the right. The green circles represent the voids that are basically intact. **Figure 13(c)** shows that they are concavities that are almost hemispheric and show no sign of collapse. The red rectangles represent the voids that have collapsed. **Figure 13(d)** shows that they are hollows that are believed to have been voids, but no longer retains their hemispheric shape.

For the sample loaded by a 3.3 GPa shock wave, an elastic wave-deformation wave structure emerged once, then the deformation wave is unloaded. The shield ratio should be r^{shield}≈0.76, which means that ~1/4 of the sample would stay in the SFS and the other ~3/4 of the sample would be shielded. In **Figure 13(a)**, all the voids close to the impact surface have collapsed; but in the other half of the sample, there are numerous voids that are basically intact. While the distribution of the collapsed voids in the experimental samples is not as ideal as that in the modeled sample, this sample can still be divided distinctly into a damaged region and a shielded one. However, for a fully dense (0.5%-porous) sample, the simulation showed that a shielded region did not form under the same condition. For the sample loaded by a 1.4 GPa shock wave, only one elastic wave (which would not cause void collapse) emerged. And in **Figure 13(e)**, basically intact voids can be found throughout the sample.

The results obtained from simulations and experiments have a similar trend, except that about 40% of the voids were identified as collapsed void in the shielded region of the experimental

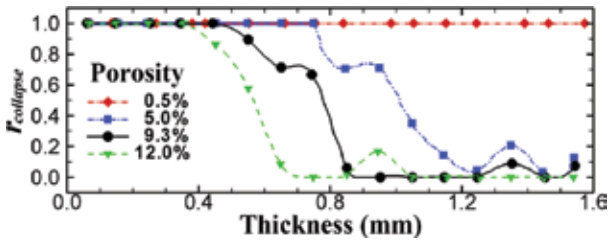

Figure 12. Comparison of collapse ratios of dense and porous samples with different porosities under the same shock stress and pulse width. $r_{collapse}$ represents collapse ratio.

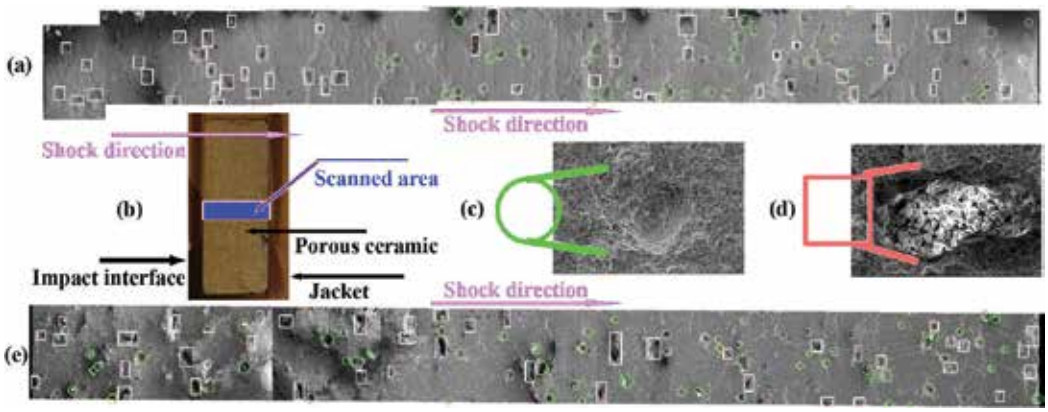

Figure 13. Fracture character of porous ceramics in recovery experiments. (a) Voids evolution in the sample subjected to compression of 3.3 GPa. (b) Cross section of recovery sample. (c) Green circle represents basically intact void. (d) Red rectangle represents void which has collapsed. (e) Voids evolution in the sample subjected to compression of 1.4 GPa.

sample. We attribute this "additional damage" in the shielded region of the recovered sample to two main reasons. First, there is roughness on the rear interface between the ceramic and the packet, which induced dynamic tensile stress after the shock wave has swept through and resulted in additional void damage. Second, the PZT ceramic is soft; a lot of grains are scaled off during polishing, which has a significant influence on the results counting. If one deducts the additional damage, then the experimental result is in good agreement with the simulation result.

5. Conclusion

With the lattice-spring model simulation and the shock recovery experiment, mechanisms of damage evolution, including void collapse, shear fracture, and rotational deformation, are illuminated, and their contributions to the damage toleration of the shocked porous ceramics are demonstrated, which would be beneficial to the understanding of porous ceramics in application upon shock wave loading.

Here, adding pores deliberately does not mean to fabricate "foam ceramic." As the porosity increases, the length of the shielded region increases accordingly, and it should be considered integrally when one designs porous ceramics.

Author details

Yin Yu and Hongliang He*

*Address all correspondence to: honglianghe@caep.cn

National Key Laboratory of Shock Wave and Detonation Physics, Institute of Fluid Physics, CAEP, Mianyang, Sichuan, People's Republic of China

References

[1] Kanel GI, Zaretsky EB, Rajendran AM, Razorenov SV, Savinykh AS, Paris V. Search for conditions of compressive fracture of hard brittle ceramics at impact loading. International Journal of Plasticity. 2009;**25**:649-670. DOI: https://doi.org/10.1016/j.ijplas.2008.12.004

[2] Grady DE. Shock-wave compression of brittle solids. Mechanics of Materials. 1998;**29**: 181-203. DOI: https://doi.org/10.1016/S0167-6636(98)00015-5

[3] Bourne NK, Millett JCF, Rosenberg Z, Murray N. On the shock induced failure of brittle solids. Journal of the Mechanics and Physics of Solids. 1998;**46**:1887-1908. DOI: https://doi.org/10.1016/S0022-5096(98)00046-5

[4] Graham RA. Shock-induced electrical activity in polymeric solids. A mechanically induced bond scission model. Journal of Physical Chemistry A. 1979;**83**:3048-3056. DOI: 10.1021/j100486a024

[5] Lankford J, Predebon WW, Staehler JM, Subhash G, Pletka BJ, Anderson CE. The role of plasticity as a limiting factor in the compressive failure of high strength ceramics. Mechanics of Materials. 1998;**29**:205-218. DOI: https://doi.org/10.1016/S0167-6636(98)00023-4

[6] Jiang D, Zhang N, Feng Y, Du J, Gu Y. Electric response of $Pb_{0.99}[(Zr_{0.90}Sn_{0.10})_{0.968}Ti_{0.032}]_{0.98}Nb_{0.02}O_3$ ceramics to the shock-wave-induced ferroelectric-to-antiferroelectric phase transition. Materials Science and Engineering B. 2012;**177**:210-216. DOI: https://doi.org/10.1016/j.mseb.2011.12.015

[7] Zeng T, Dong X, Mao C, Zhou Z, Yang H. Effects of pore shape and porosity on the properties of porous PZT 95/5 ceramics. Journal of the European Ceramic Society 2007; **27**: 2025-2029. DOI: http://dx.doi.org/10.1063/1.3525056

[8] Graham RA, Ingram GE. Piezoelectric current from x-cut quartz subjected to short-duration shock-wave loading. Journal of Applied Physics 1972;**43**:826-835. DOI: http://dx.doi.org/10.1063/1.1661289

[9] Li J, Zhou X, Li J. A time-resolved single-pass technique for measuring optical absorption coefficients of window materials under 100 GPa shock pressures. The Review of Scientific Instruments 2008;**79**:123107-123101-6. DOI: http://dx.doi.org/10.1063/1.3046279

[10] Espinosa HD, Zavattieri PD. A grain level model for the study of failure initiation and evolution in polycrystalline brittle materials. Part I: Theory and numerical implementation. Mechanics of Materials. 2003;**35**:333-364. DOI: https://doi.org/10.1016/S0167-6636(02)00285-5

[11] Espinosa HD, Zavattieri PD. A grain level model for the study of failure initiation and evolution in polycrystalline brittle materials. Part II: Numerical examples. Mechanics of Materials. 2003;**35**:365-394. DOI: https://doi.org/10.1016/S0167-6636(02)00287-9

[12] Zavattieri PD, Raghuram PV, Espinosa HD. A computational model of ceramic microstructures subjected to multi-axial dynamic loading. Journal of the Mechanics and Physics of Solids. 2001;**49**:27-68. DOI: https://doi.org/10.1016/S0022-5096(00)00028-4

[13] Silling SA. Reformulation of elasticity theory for discontinuities and long-range forces. Journal of the Mechanics and Physics of Solids. 2000;**48**:175-209. DOI: https://doi.org/10.1016/S0022-5096(99)00029-0

[14] Case S, Horie Y. Discrete element simulation of shock wave propagation in polycrystalline copper. Journal of the Mechanics and Physics of Solids. 2007;**55**:589-614. DOI: https://doi.org/10.1016/j.jmps.2006.08.003

[15] Wang YC, Mora P. Modeling wing crack extension: Implications for the ingredients of discrete element model. Pure and Applied Geophysics. 2008;**165**:609-620. DOI: https://doi.org/10.1007/978-3-7643-8757-0_9

[16] Buxton GA, Care CM, Cleaver DJA. lattice spring model of heterogeneous materials with plasticity. Modelling Simul. Materials Science and Engineering. 2001;**9**:485-497. DOI: http://iopscience.iop.org/article/10.1088/0965-0393/9/6/302/meta

[17] Yu Y, Wang W, He H, Lu T. Modeling multiscale evolution of numerous voids in shocked brittle material. Physical Review E. 2014;**89**:043309-1-8. DOI: https://doi.org/10.1103/PhysRevE.89.043309

[18] Cundall PA. A discrete numerical model for granular assemblies. Geotechnique. 1979;**1**:47-65. DOI: http://www.icevirtuallibrary.com/doi/pdf/10.1680/ege.35362.0025

[19] Alava MJ, Nukala PKVV, Zapperi S. Statistical models of fracture. Advances in Physics 2006;**55**:349-476. DOI: http://dx.doi.org/10.1080/00018730300741518

[20] Pazdniakou A, Adler PM. Lattice spring modles. Transport in Porous Media. 2012;**93**:243-262. DOI: 10.1007/s11242-012-9955-6

[21] Griffith AA. The phenomena of rupture and flow in solids. Philosophical Transactions of the Royal Society of London. 1920;**221**:163-198. DOI: http://www.jstor.org/stable/91192

[22] Zhao GF, Fang JN, Zhao J. A 3D distinct lattice spring model for elasticity and dynamic failure. International Journal for Numerical and Analytical Methods in Geomechanics. 2011;**35**:859-885. DOI: 10.1002/nag.930

[23] Ostoja-Starzewski M. Lattice models in micromechanics. Applied Mechanics Reviews. 2002;**55**:1-26. DOI: 10.1115/1.1432990

[24] Grah M, Alzebdeh K, Sheng PY, Vaudin MD, Bowman KJ, Ostoja-Starzewski M. Brittle intergranular failure in 2D microstructures: Experiments and computer simulations. Acta Materialia. 1996;**44**:4003-4018. DOI: https://doi.org/10.1016/S1359-6454(96)00044-4

[25] Wang Y, Yin XC, Ke FJ, Xia MF, Peng KY. Numerical simulation of rock failure and earthquake process on mesoscopic scale. Pure and Applied Geophysics. 2000;**157**:1905-1928. DOI: https://doi.org/10.1007/PL00001067

[26] Gusev AA. Finite element mapping for spring network representations of the mechanics of solids. Physical Review Letters. 2004;**93**:034302-1-4. DOI: https://doi.org/10.1103/PhysRevLett.93.034302

[27] Walsh JB. The effect of cracks on the compressibility of rock. Journal of Geophysical Research. 1965;**70**:381-389. DOI: 10.1029/JZ070i002p00381

[28] Chen MW, McCauley JW, Dandekar DP, Bourne NK. Dynamic plasticity and failure of high-purity alumina under shock loading. Nature Materials. 2006;**5**:614-618. DOI: 10.1038/nmat1689

[29] Zhang F, He H, Liu G, Liu Y, Yu Y, Wang Y. Failure behavior of Pb(Zr0.95Ti0.05)O3 ferroelectric ceramics under shock compression. Journal of Applied Physics. 2013;**113**:183501-1-7. DOI: https://doi.org/http://dx.doi.org/10.1063/1.4803052"http://dx.doi.org/10.1063/1.4803052

[30] Hao GY, Liu FS, Zhang DY, Zhang MJ. Optical emission of directly contacted copper/sapphire interface under shock compression of megabar. Applied Physics Letters. 2007;**90**:261914-1-3. DOI: http://dx.doi.org/10.1063/1.2751606

[31] Yu Y, Wang WQ, He HL, Jiang TL, Huan Q, Zhang FP, Li YQ, Lu TC. Mesoscopic deformation features of shocked porous ceramic: Polycrystalline modeling and experimental observations. Journal of Applied Physics. 2015;**117**:125901-1-8. DOI: http://dx.doi.org/10.1063/1.4916244

[32] Hofmann DC, Suh JY, Wiest A, Lind ML, Demetriou MD, Johnson WL. Development of tough, low-density titanium-based bulk metallic glass matrix composites with tensile. Nature. 2008;**451**:1085. DOI: 10.1073/pnas.0809000106

[33] Chen LY, Fu ZD, Zhang GQ, Hao XP, Jiang QK, Wang XD, Cao QP, Franz H, Liu YG, Xie HS, Zhang SL, Wang BY, Zeng YW, Jiang JZ. Physical Review Letters. 2008;**100**:075501. DOI: https://doi.org/10.1103/PhysRevLett.100.075501

[34] Yano K, Horie Y. Discrete-element modeling of shock compression of polycrystalline copper. Physical Review B. 1999;**59**:13672-13680. DOI: https://doi.org/10.1103/PhysRevB.59.13672

[35] Mescheryakov YI, Mahutov NA, Atroshenko SA. Micromechanisms of dynamic fracture of ductile high-strength steel. Journal of the Mechanics and Physics of Solids. 1994;**42**:1435-1457. DOI: https://doi.org/10.1016/0022-5096(94)90004-3

[36] Chen B, Lutker K, Lei J, Yan J, Yang S, H-k M. Detecting grain rotation at the nanoscale. Proceedings of the National Academy of Sciences of the United States of America. 2014; **111**:3350-3353. DOI: 10.1073/pnas.1324184111

[37] Ma W, Zhu W, Jing F. The shock-front structure of nanocrystalline aluminum. Applied Physics Letters 2010; **97**: 121903-121901-3. DOI: http://dx.doi.org/10.1063/1.3490643

[38] Schiøtz J, Jacobsen KW. A maximum in the strength of nanocrystalline copper. Science. 2003;**301**:1357-1359. DOI: 10.1126/science.1086636

[39] FDi G, JQ-da F. An experimental study of the polycrystalline plasticity of austenitic stainless steel. International Journal of Plasticity. 2015;**74**:92-109. DOI: https://doi.org/10.1016/j.ijplas.2015.05.012

[40] Yahyazadehfar M, Bajaj D, Arola DD. Hidden contributions of the enamel rods on the fracture resistance of human teeth. Acta Biomaterialia. 2013;**9**:4806-4814. DOI: https://doi.org/10.1016/j.actbio.2012.09.020

[41] Barthelat F, Rabiei R. Toughness amplification in natural composites. Journal of the Mechanics and Physics of Solids. 2011;**59**:829-840. DOI: https://doi.org/10.1016/j.jmps.2011.01.001

[42] Barthelat F, Tang H, Zavattieri PD, Li CM, Espinosa HD. On the mechanics of mother-of-pearl: A key feature in the material hierarchical structure. Journal of the Mechanics and Physics of Solids. 2007;**55**:306-337. DOI: https://doi.org/10.1016/j.jmps.2006.07.007

[43] Mirkhalaf M, Dastjerdi AK, Barthelat F. Overcoming the brittleness of glass through bio-inspiration and micro-architecture. Nature Communications. 2014;**5**:3166-1-9. DOI: 10.1038/ncomms4166

[44] Sarac B, Schroers J. Designing tensile ductility in metallic glasses. Nature Communications. 2013;**4**:3158-1-7. DOI: 10.1038/ncomms3158

[45] RT Q, Zhao JX, Stoica M, Eckert J, Zhang ZF. Macroscopic tensile plasticity of bulk metallic glass through designed artificial defects. Materials Science and Engineering A. 2012;**534**:365-373. DOI: https://doi.org/10.1016/j.msea.2011.11.082

[46] Launey ME, Ritchie RO. On the fracture toughness of advanced materials. Advanced Materials. 2009;**21**:2103-2110. DOI: 10.1002/adma.200803322

Edited by Uday M. Basheer Al-Naib

Porous ceramics have recently gained growing importance in industry because of their many applications like filters, absorbers, dust collectors, thermal insulation, hot gas collectors, dielectric resonators, bioreactors, bone replacement and automobile engine components. Generally, porous ceramics have good properties such as mechanical strength, abrasion resistance, and chemical and thermal stability. These porous network ceramic structures also have relatively low density, low mass and low thermal conductivity. Furthermore, permeability is one of the most important properties of porous ceramics for different applications such as membranes because this property directly relates to the pressure drop during filtration. Pore size control is one key factor in fabrication of porous ceramics. The size of particles and their distribution of the raw materials, manufacturing techniques, types of binder used, distribution of binder, and sintering affect the final porosity and pore connectivity, are important things that must be considered during the manufacturing of a porous ceramic body. Therefore, the development of porous ceramic research requires sufficient mechanical and chemical stability as well as permeability. This book covers a wide range of topics such as porous ceramic structure and properties, preparation, simulation and fabrication, sintering, applications for bioceramics, sensors, magnetics and energy saving.

Published in London, UK

IntechOpen

ISBN 978-1-83881-280-5